A Novel Approach for Designing Integrated Ultra Low Noise Microwave Wideband Voltage-Controlled Oscillators

Vorgelegt von
M. Tech. Ajay Kumar Poddar
aus Fair Lawn, New Jersey, USA

Von der Fakultät IV - Elektrotechnik und Informatik
der Technischen Universität Berlin
zur Erlangung des akademischen Grades

Doktor der Ingenieurwissenschaften
-   Dr.-Ing. –

genehmigte Dissertation

Promotionsausschuß:

Vorsitzender: Professor Dr.-Ing. Ernst Obermeier
Gutachter: Professor Dr.-Ing. Georg Böck
                   Professor Dr.-Ing. Arne Jacob (TU Hamburg- Harburg)

Tag der wissenschaftlichen Aussprache: 14. Dezember 2004

Berlin 2005
D83

Acknowledgement

This work is a result of my design effort at Synergy Microwave Corporation to build a new class of high performance VCOs. I am deeply grateful to Professor Dr.-Ing. Georg Böck for accepting this work as a doctoral dissertation and for his invaluable guidance as my advisor and for his encouragement throughout this effort. The valuable suggestions, extreme patience, and cooperative attitude from supervisors and colleagues have enabled me to carry out the given research work successfully. I am also thankful to Professor Dr.-Ing. Arne Jacob for discussions, cooperative attitude and useful recommendations.

I am indebted to Professor Dr.-Ing. Ulrich L. Rohde, Chairman of Synergy Microwave Corporation, for all his efforts to make this work possible and his wonderful guidance throughout my research. His foresight in identifying this topic and associated problems, as an important research area, and his continued support have made my professional experiences rich and rewarding in the field of low noise, wideband oscillator design.

I would like to thank my parent, my wife Kavita, and my daughters Aditi and Amrita for their support and understanding during our time apart and together, as they are the source of my strength and the reason for my endeavor. A special thanks goes out to my wonderful friend Asha for her encouragement and unfailing confidence in my abilities and me.

My acknowledgements would not be complete without expressing gratitude towards God, our creator and redeemer.

Abstract

As commonly known, oscillators play a very important role in all communication and test equipment. The major differences between oscillator types are the frequency range, the tuning range, and the required specifications for the particular applications. Key requirements are phase noise, output power, harmonic contents, and others like power consumption, size, and cost. A special type of oscillator is the voltage-controlled oscillator (VCO), which can be tuned over ranges, starting from a few percent to a range of almost 1:3. Phase noise and tuning range, to a degree, are opposing requirements. As a general rule, the phase noise gets poorer as the tuning range increases.

This dissertation deals with these topics and introduces several new and important issues. After discussing the oscillator theory and introducing the concept of the voltage-controlled oscillator, the one and two-port oscillators are introduced. Following this, it is shown that a system of coupled oscillators provides better phase noise than single oscillators. While the concept of synchronized oscillators is known, its phase noise calculation and coupling conditions are new. Furthermore, the operating Q is also calculated. It is further shown that by increasing the number of coupled oscillators, the overall performance of the oscillator system can be improved by the factor $1/N$, and this modern circuit minimizes this effect.

In the circuit the components play a major rule and therefore, both active and passive devices are looked at for their suitability.

Since the individual oscillator is the major contributor, two new types of oscillators are introduced:
1) The oscillator using more than one resonator for improved phase noise (1000-2000/2000-4000 MHz and 1500-3000/3000-6000 MHz).
2) An oscillator, which exhibits a very wide tuning range (320-1120 MHz).

This dissertation closes with various validation circuits, which prove that the detailed theory and the actual measurements do agree fully. Detailed insight in all of the design procedures is provided. The dissertation contains 75 literature references and three appendices, which provide additional aspects in the design process.

At microwave frequencies, the actual circuit performance is largely driven by the component values and parasitic elements and the optimum layout minimizes these effects. Intensive studies were conducted to find the optimum layout configuration and a U.S. copyright was obtained for this. This in itself is a somewhat unusual procedure but it shows the importance of physical layout at microwave frequencies.

This work, which was partially supported and funded by the U.S. Government Agency DARPA (Defense Advanced Research Projects Agency) has also resulted in a variety of patents and copyrighted layout structures.

Zusammenfassung

Wie allgemein bekannt, haben Oszillatoren in Kommunikationssystemen und Messgeräten einen extrem großen Einfluss auf deren Eigenschaften. Die wesentlichen Unterschiede zwischen den verschiedenen Oszillator-Typen liegen im Frequenzbereich, im Abstimmbereich und allgemein in den Spezifikationen, die für eine bestimmte Anwendung benötigt werden. Die wichtigsten Eigenschaften sind das Phasenrauschen, die Ausgangsleistung, der Oberwellengehalt sowie Stromverbrauch, Baugröße und Kosten. Eine spezielle Variante des Oszillators ist der spannungsgesteuerte Oszillator (VCO), im Englischen „voltage-controlled oscillator", welcher über einen Bereich von wenigen Prozent bis zu einem Bereich von 1:3 abgestimmt werden kann. Das Phasenrauschen und der Abstimmbereich beeinflussen sich gegenseitig. Man kann generell sagen, dass das Phasenrauschen schlechter wird, wenn der Abstimmbereich größer wird, aber eine neue hier vorgestellte Schaltungsvariante reduziert diesen Effekt.

Die vorliegende Dissertation beschäftigt sich mit diesem Sachverhalt und zeigt wesentliche neue Erkenntnisse. Nach der Diskussion der Oszillatortheorie und dem VCO werden der Ein- und Zweitor-Oszillator vorgestellt. Anschließend wird gezeigt, dass ein System gekoppelter Oszillatoren weniger Rauschen verursacht als der Einzel-Oszillator. Das Prinzip gekoppelter Oszillatoren ist bekannt, neu ist jedoch die Berechnung ihres Rauschverhaltens und die optimale Kopplung. Auch wird erstmalig die Betriebsgüte berechnet. Es wird gezeigt, dass sich mit zunehmender Anzahl von Oszillatoren das Rauschen um den Faktor 1/N verringert.

In allen Schaltungen spielen die verwendeten Bauelemente eine große Rolle und daher werden aktive und passive Komponenten auf ihre Tauglichkeit für diese Applikationen untersucht.

Nachdem der Einzel-Oszillator die dominierende Rauschquelle ist, werden zwei neue und verbesserte Oszillatoren vorgestellt:
1) ein Oszillator mit mehreren Resonatoren für die Frequenzbereiche (1000-2000/ 2000- 4000 MHz und 1500-3000/3000-6000 MHz)
2) ein Oszillator mit extrem großen Abstimmbereich (320-1120 MHz)

Die Arbeit endet mit mehreren Schaltungen, die zum Nachweis der Richtigkeit der Theorie aufgebaut und vermessen wurden, wobei Einzelheiten genauestens wiedergegeben werden. Die Arbeit enthält 75 Literaturstellen und drei Anhänge, die weitere theoretische Aspekte aufzeigen.

Im Bereich der Mikrowellenfrequenzen hängen die Eigenschaften der Schaltungen von den aktiven und passiven Komponenten und dem optimalen Layout ab. Dieser Punkt wurde besonders untersucht und eine Layout-Anordnung gefunden, die beste Ergebnisse zeigte. Dafür wurde ein U.S. Copyright beantragt. Dieser Vorgang ist etwas ungewöhnlich und zeigt, wie wichtig die Layoutfragen genommen wurden. Weiterhin wurden für einige Teile der Schaltungen Patentansprüche eingereicht.

Table of Contents

Chapter 1

Introduction

1.1   Microwave Oscillators and VCOs

One of the greatest achievements of the twentieth century civilization is the maturing and industrialization of wireless communications systems. The popularity of mobile telephones has caused renewed interest in and generated more attention to wireless architectures and circuit techniques. In addition, this popularity has further spawned a revival of interest in the design of low noise and fairly wideband oscillators.

The wireless personal communication market has been growing explosively due to ever emerging new applications and dropping prices. The applications of wireless communication devices include pagers, cordless phones, cellular phones, global positioning systems, and wireless local area networks, transmitting either voice or data and starving for low phase noise power efficient wideband voltage-controlled oscillators (VCOs).

The growing importance of wireless media for voice and data communications is the driving need for higher integration in personal communications transreceivers in order to achieve lower cost and lower power dissipation. One approach to this problem is to integrate the RF functionality in low-cost IC technology together with the VCOs. A low cost, small, long-battery-life solution has been the dream for decades. Many efforts have been devoted to the integration of such circuits in low-cost technology in order to reach the goal.

In fact, the demands of wideband sources have increased enormously because of the explosive growth of the wireless communications and the broadband tunability.   Ultra low phase noise of the VCOs is one of the most fundamental requirements in the VCO's design, impacting both the technology and the topology used. As the frequency band for the wireless communication shifts higher, a generation of the ultra low noise wideband and thermal stable compact signal sources with low cost become more and more challenging due to the frequency limitations of the active devices and broadband tunability of the tuning diode.

The design of ultra low noise octave-band VCOs is challenging and difficult because maintaining more or less of the same Q of the resonator/tuning network for octave-band is a complex phenomenon. It is a major challenge to find ways to realize low phase noise with low Q RF components at a higher operating frequency that supports broadband tunability.

1.2   New Development

Improvements of oscillator/VCO technology have continued over time, yielding ever-smaller circuits with enhanced phase noise and tuning linearity. Two-way radios and cellphones are the largest group of users and in these applications, cleanliness and its freedom of wideband tunability is of utmost importance.

Oscillators/VCOs based on discrete devices have been widely employed for many years in commercial and military radio receiver applications, however, the advancement of SiGe-HBT/GaAs-HBT technology made a dramatic change that has led to fully integrated oscillators/VCOs circuits.

Generally, the overall performance of the present integrated VCO implementation is inferior to the discrete VCO modules because of the lower Q of the integrated components, specifically, the phase noise and tuning characteristics is poorer than what could be routinely achieved in the discrete version of the VCO modules. This shortfall in performance is principally due to the low Q of the integrated inductors and tuning diodes in the present IC technologies. Recent developments have shown promising results with the use of bond wire inductors, yet low phase noise performance has remained elusive and out of reach of monolithic VCOs, IC technology.

1.3   Problem Statement

Despite the continious improvement, VCOs still remain the bottleneck, and thus, the main challenge of RF transreceivers. This is due to the most important and demanding parameters of the VCOs; low phase noise, low power consumption, low thermal drift, and wide frequency tuning range. The frequency tuning range is determined by the usable capacitive tuning ratio of the varactor and the parasitics associated with the tuning network because the parasitics deteriorate and limit the effective tuning capabilities of the varactors at high frequency. Therefore, the wide tuning range varactors, such as hyperabrupt types, are required to guarantee specified center frequencies and frequency tuning ranges.

The dynamic time average Q factor of the resonator, as well as the tuning diode noise contribution, sets the noise performance of the VCOs, and in general, the dynamic loaded Q is inversely proportional to the frequency range of the VCOs. The frequency range over which a resonator/coupled resonator circuit can be tuned by the tuning diode depends on the useful capacitance ratio of the tuning diode and on the parallel and series capacitance present in the circuit.

The research described here explores a topology for wideband oscillators (octave-band tunability) and optimization of the performance of the tuning networks. It will be investigated as to how the capacitance tuning range of varactors can be improved, and

identifying the effects that limit the tuning range, which leads to the development of the several proposed tuning networks. As the loss resistance of the device determines the quality factor, special attention is paid to the resistive behavior. The frequency tuning range, the contribution of the varactors and inductors to the phase noise, and the influence of the variations of power supplies and tuning voltages will be studied.

Furthermore, this work examines a unique research regarding systems of coupled oscillators using N-push/push-push configuration and this dissertation points out the remarkable improvement of the phase noise and opens the door of the high frequency ranges and it enables the realization of integrated SiGe-HBT/GaAs-HBT based systems at higher frequencies for wideband operation.

As the information age progresses higher frequency signals are required for the transmission of larger amounts of information. The coupled resonator and N-push/push-push topology is one of the many techniques used for improving the phase noise and extending the range of the oscillation frequency. The active devices are often pushed near to their physical limits of operation, resulting in degraded noise performance of the integrated oscillator/VCOs circuit. The push-push oscillator basically enhances the even mode harmonics and suppresses the odd mode output, doubling the frequencies, so higher oscillating frequencies can be obtained beyond the limitation caused by the cut-off frequency of the available three terminal active devices and the tuning diodes.

The monolithic VCO implementations suffer from poor phase noise performance partly due to the low quality factor Q of the passive components. A design study has been carried out to optimize the phase noise performance by incorporating the N-push/push-push approach to compensate for the low Q-factor in the integrated VCO implementation.

The paucity of literature on wideband (more than octave-band) tunability of the VCOs, together with a lack of experimental verification of the underlying theories of coupled oscillators in N-push/push-Push configuration for an ultra low noise performance, has been a strong motivator, stirring a need for doing noise analysis for coupled oscillator design. Available publications [1-10] do not contain any analysis that describes the performance or design constraints of wideband N-push/push-push VCOs. The effort under this research describes the dynamically-tuned, integrated coupled resonator-tuned network, negative resistance generating network, phase coupling network, and the second harmonic combiner network for the realization of an ultra low noise octave-band voltage-controlled oscillator. Furthermore, efforts have been taken to increase the loaded quality factor over the frequency band by selecting optimum coupled microstripline resonator structures.

1.4   Definition of the Task

Independent of the improvement of the time average loaded quality factor of the tuning network and resonator circuits for better phase noise, several methods are explored based on following:

- Coupled-oscillator/N-push approach for improvement in phase noise.
- Novel coupled resonator structure, which will support the resonance over an octave-band.
- Novel topology, which provides a constant negative resistance over the octave-band.
- Novel tuning arrangement for wideband tunability without degrading the time average loaded Q of the tuning network over the octave-band.
- Dynamically tuned phase coupling network.

This dissertation deals with the design, fabrication, and testing of various wideband VCOs (320-1120 MHz, 1000-2000/2000-4000 MHz and 1500-3000/3000-6000 MHz frequency band). In addition, this thesis presents the theoretical analysis of the phase noise improvements by implementation of the coupled oscillator topology. Developments in the coupled resonator/oscillator may change the paradigm of the oscillator/VCOs design and suggest a need for the new phase noise equation for the coupled/N-push oscillators/VCOs, which is derived here.

1.5   Research Motivation

The VCOs theory is complex and mystifying. It is still an open issue despite significant gains in practical experience and modern CAD tools for design. To this end, VCO noise theory, how the circuit works, its noise mechanism, optimum drive level and conduction angle, the nature of signals generated, the effect of flicker noise, topology, resonator structure, and coupling to an active device are often held as trade secrets by many manufacturers. This dissertation describes new and interesting opportunities for research in ultra low noise octave-band coupled resonator/oscillators. It produces new information regarding the octave-band tunable resonator without degrading the Q factor over the band and implementation of N-push/push-push topology for improvement in the phase noise.

Wideband oscillators are used in spectrum analyzers, frequency sweepers, and network analyzers. Frequency domain test and measurement systems pose interesting challenges for wideband VCOs design. The test system must be versatile enough to work over a broad range of frequencies, meet or exceed the performance of the device under test (DUT), and must not alter the function or performance of the DUT.

Whether the medium is discrete or integrated, the Colpitts class of resonant oscillators has seen its share of the spotlight for ultra low noise applications, but narrow tuning

range. While the topology can take a number of forms, the defining characteristic of a Colpitts oscillator is the capacitive voltage divider that provides positive feedback around an active gain module, and these oscillator circuits have been shown to offer excellent phase noise performance.

The optimum design of the Colpitts configuration was not well understood until Rohde [11] discussed the discontinuous conduction of the active device which is controlled by the conduction angle and timed via the feedback network such that a current is only supplied to the resonator network during a portion of the period when the oscillator phase is relatively less perturbed, thereby, the noise level is controlled and minimized in the loop.

Rohde [11] has explained a new and efficient method of designing low noise microwave oscillator by incorporating an optimum feedback (capacitance ratio) arrangement, optimum drive level, optimum conduction angle, operating point, and unified noise calculation techniques, but his research is centered on uncoupled free-running oscillators/VCOs and suggest the need for new phase noise equation for coupled/N-push oscillators/VCOs.

The oscillators/VCOs considered in this work are based on the use of commercially available Si and SiGe bipolar transistors. As most designers do not have elaborate and expensive equipment for parameter extraction, the large signal S-parameters are generated using a synthesis-based approach and using data from the manufacturer.

1.6   Overview of the Dissertation

This dissertation is organized in 12 chapters.

Chapter 1 - the Introduction, describes the purpose of the dissertation, new development, and defines the problem.

Chapter 2 - briefly discusses the oscillators/VCOs theory and defines the common oscillator topologies for wideband voltage-controlled oscillators.

Chapter 3 - describes the system of mutually coupled oscillators that is compared with the classical coupled pendulum. In addition, the dynamics of the mutually coupled oscillator and system of the N-coupled oscillators are briefly discussed.

Chapter 4 - describes the oscillator noise model. In addition, the noise analysis of the coupled oscillator is briefly discussed which gives insight in the improvement of the phase noise compared with the single free-running uncoupled oscillator. Finding the relative improvement of the phase noise for N-coupled oscillators with respect to single free running uncoupled oscillator is the objective of the chapter 4.

Chapter 5 - describes the approach and topologies of the practical coupled-mode oscillators/VCOs in N-push/push-push configuration. For better insight and understanding of the coupled oscillator, detailed noise analysis of the push-push topology is discussed.

Chapter 6 - describes the characterization of the device models. The transistor is characterized under the large signal condition. In addition, characterizations of the tuning diode, resonator network and passive components are discussed.

Chapter 7 - deals with the wideband VCO approach and low noise VCO design criteria for wideband applications.

Chapter 8 - shows three selected circuits of wideband oscillators (320-1120 MHz, 1000-2000/2000-4000 MHz, and 1500-3000/3000-6000 MHz), which provide state-of-the-art wideband VCOs. As a result of this work, copyrights for the layout (US Registration No. Vau-603-982 and Vau-603-984) have been awarded and patent disclosures have been submitted for an international patent covering the United States, Asia, and Europe (Provisional Patent Nos. 60/493075, 60/501371, 60/501790, 60/527957, 60/528670, 60/563481, 60/564173, 60/589090, 60/601823 and 60/605791).

Chapter 9 - deals with the accomplishments, conclusions, and future possibilities. Further directions are also pointed out.

Chapter 10 - explains abbreviations and symbols.

Chapter 11 - shows a list of all relevant references used throughout the dissertation.

Chapter 12 - contains Appendices A, B, and C. Appendix A discusses the noise analysis of the N-coupled oscillator coupled through different coupling topology, Appendix B describes the analytical design approach of the wideband oscillators/VCOs for optimum power, and Appendix C discusses the derivation of the noise equation.

Chapter 2

Oscillator/VCO Theory

2.1   Theory of Operation

An oscillator is an autonomous circuit consisting of a frequency selective positive feedback network. The noise present in the active device or power supply turn-on transient leads to the initial oscillation build-up. As a basic requirement for producing a self-sustained, near-sinusoidal oscillation, an oscillator must have a pair of complex-conjugate poles on the imaginary axis i.e. in the right half of an s-plane with $\alpha > 0$.

$$P(p_1, p_2) = \alpha \pm j\beta \tag{2.1}$$

While this requirement does not guarantee an oscillation with a well-defined steady state (squeaking), it is nevertheless a necessary condition for any oscillator. When subjected to an excitation due to the power supply turn-on transient or noise associated with the oscillator circuit, the right half plane RHS-poles in the equation above produce a sinusoidal signal with an exponentially growing envelope given as

$$v(t) = V_0 \exp(\alpha t) \cos(\beta t) \tag{2.2}$$

$$v(t)\big|_{t=0} \rightarrow V_0 \tag{2.3}$$

V_0 is determined by the initial conditions and the growth of the signal amplitude $v(t)$ is eventually limited by the associated nonlinearities of the oscillator circuit.

Oscillators are fundamentally a feedback amplifier with a resonator in the feedback path and if enough gain exists for given oscillation conditions, noise will be amplified sufficiently enough to eventually stabilize the gain via non-linearity effects and create an output signal that consists of narrow band noise. This narrow-band profile of the noise characteristics in the oscillator is the prime issue of the oscillator design. The two methods used for analyzing and understanding noise issues for oscillators are the feedback model approach and the negative resistance model. Using either the feedback model approach or the negative resistance model, one can perform the analysis of the oscillator. Depending on the oscillator topology and characteristics, one approach is preferred over the other. The condition of oscillation build-up and steady state oscillation will be discussed using both approaches. The application of either the feedback model or the negative-resistance model is sufficient for analyzing the linear behavior of the oscillator circuit, and it must be unstable about its bias point or, equivalently, have poles in the RHP if an oscillation buildup is to take place. The feedback model is shown in

Figure 2-1, where an oscillator circuit is decomposed into a frequency-dependent forward loop gain block $H_1(j\omega)$ and a frequency-dependent feedback network $H_2(j\omega)$, both of which are typically multi-port networks. If the circuit is unstable about its operating point (poles in the right half of the s-plane), it can produce an expanding transient when subjects to an initial excitation. As the signal become large, the active device in the circuit behaves nonlinearly and limits the growth of the signal. When oscillation starts up, the signal level at the input of the amplifier (forward loop gain block) is very small, and the amplitude dependence of the forward amplifier gain can be initially neglected until it reaches saturation.
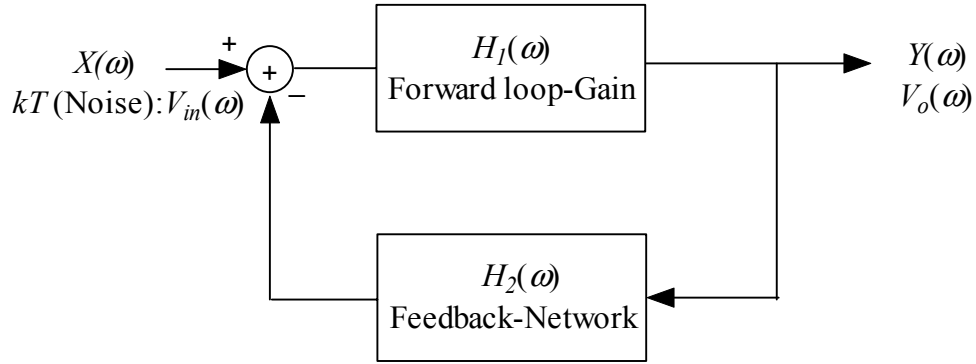

Figure 2-1: Block diagram of basic feedback model-oscillator.

The closed loop transfer function (T.F) and output voltage $V_o(\omega)$ are given by

$$\left[TF(j\omega)\right]_{closed-loop} = \frac{[Y(j\omega)]_{output}}{[X(j\omega)]_{input}} = \frac{V_o(\omega)}{V_{in}(\omega)} = \frac{H_1(j\omega)}{[1 + H_1(j\omega)H_2(j\omega)]} \qquad (2.4)$$

$$[Y(j\omega)]_{output} = V_o(\omega) = \left[\frac{H_1(j\omega)}{[1 + H_1(j\omega)H_2(j\omega)]}\right]V_{in}(\omega) \qquad (2.5)$$

For an oscillator, the output voltage V_o is nonzero even if the input signal $V_i = 0$. This is only possible if the forward loop gain is infinite (which is not practical), or if the denominator $1 + H_1(j\omega)H_2(j\omega) = 0$ at some frequency ω_o; that is the loop gain is equal to unity for some values of the complex frequency $s=j\omega$. This leads to the well-known condition for oscillation (the *Nyquist criterion*), where at some frequency ω_o $H_1(j\omega_o)H_2(j\omega_o) = -1$, and can be mathematically expressed as

$$\left|H_1(j\omega_o)H_2(j\omega_o)\right| = 1 \qquad (2.6)$$

and $\qquad Arg[H_1(j\omega_o)H_2(j\omega_o)] = n\pi \ \ where \ n = 0,1,2... \qquad (2.7)$

When the above *criterion* is met, the two conjugate poles of the overall transfer function are located on the imaginary axis of s-plane, and any departure from that position will lead to an increase or a decrease of the oscillation amplitude of the oscillator output signal in time domain, which is shown in Figure 2-2.
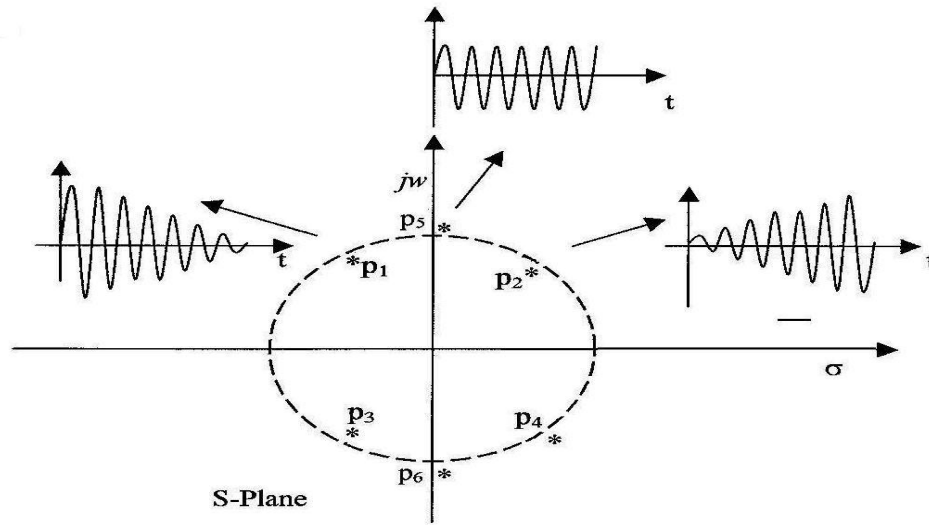

Figure 2-2: Frequency domain root locus and the corresponding time domain response.

In practice, the equilibrium point cannot be reached instantaneously without violating some physical laws. As an example, high Q oscillators take longer than low Q types for full amplitude. The oscillator output sine wave cannot start at full amplitude instantaneously after the power supply is turned on. The design of the circuit must be such that at start-up condition, the poles are located in the right half plane, but not too far from the *Y*-axis. However, the component tolerances and the nonlinearities of the amplifier will play a role. This oscillation is achievable with a small signal loop gain greater than unity, and as the output signal builds up, at least one parameter of the loop gain must change its value in such a way that the two complex conjugate poles migrate in the direction of the *Y*-axis and that the parameter must then reach that axis for the desired steady state amplitude value at a given oscillator frequency. Figure 2-3 shows the general schematic diagram of a one-port negative resistance model. The oscillator circuit is separated into a one-port active circuit, which is a nonlinear time variant (NLTV) and a one-port frequency determining circuit, which is a linear time invariant (LTIV). The frequency determining circuit, or resonator, sets the oscillation frequency, and it is signal-amplitude independent. The function of the active-circuit is to produce a small-signal negative resistance at the operating point of the oscillator and couple it with the frequency-determining circuit while defining the oscillation frequency. Assuming that the steady state current at the active circuit is almost sinusoidal, the input impedance $Z_d(A,f)$ can be expressed in terms of a negative resistance and reactance as

$$Z_d(A,f) = R_d(A,f) + jX_d(A,f) \qquad (2.8)$$

11

where A is the amplitude of the steady state current and f is the resonance frequency. $R_d(A,f)$ and $X_d(A,f)$ are the real and imaginary parts of the active circuit and depend on the amplitude and frequency. Since the frequency determining circuit is amplitude-independent, it can be represented as

$$Z_r(f) = R_r(f) + jX_r(f) \qquad (2.9)$$

where $Z_r(f)$ is the input impedance of the frequency determining circuit, $R_r(f)$ and $X_r(f)$ are the loss resistance and reactance associated with the resonator/frequency determining circuit.
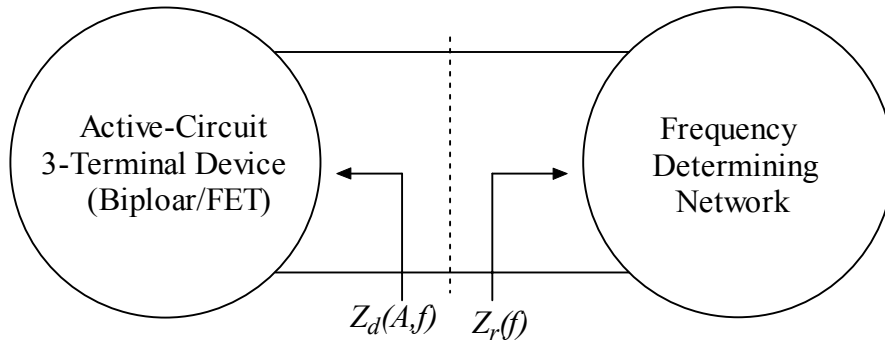

Figure 2-3: Schematic diagram of one-port negative resistance model.

To support the oscillator build-up, $R_d(A,f) < 0$ is required so the total loss associated with the frequency determining circuit can be compensated. Oscillation will start build-up if the product of the input reflection coefficient $\Gamma_r(f_0)$, looking into the frequency determining circuit and the input reflection coefficient $\Gamma_d(A_0,f_0)$ of the active part of the oscillator circuit is unity at $A = A_0$ and $f = f_0$. The steady state oscillation condition can be expressed as

$$\Gamma_d(A,f)\Gamma_r(f)\big|_{f=f_0} \Rightarrow \Gamma_d(A_0,f_0)\Gamma_r(f_0) = 1 \qquad (2.10)$$

Figure 2-4 shows the input reflection coefficient $\Gamma_d(A_0,f_0)$ and $\Gamma_r(f_0)$, which can be represented in terms of the input impedance and the characteristic impedance Z_0 as

$$\Gamma_d(A_0,f_0) = \frac{Z_d(A_0,f_0) - Z_0}{Z_d(A_0,f_0) + Z_0} \qquad (2.11)$$

$$\Gamma_r(f_0) = \frac{Z_r(f_0) - Z_0}{Z_r(f_0) + Z_0} \qquad (2.12)$$

12

$$\Gamma_d(A_0, f_0)\Gamma_r(f_0) = 1 \Rightarrow \left[\frac{Z_d(A_0, f_0) - Z_0}{Z_d(A_0, f_0) + Z_0}\right]\left[\frac{Z_r(f_0) - Z_0}{Z_r(f_0) + Z_0}\right] = 1 \qquad (2.13)$$

$$[Z_d(A_0, f_0) - Z_0][Z_r(f_0) - Z_0] - [Z_d(A_0, f_0) + Z_0][Z_r(f_0) + Z_0] = 0 \qquad (2.14)$$

$$\Rightarrow Z_d(A_0, f_0) + Z_r(f_0) = 0 \qquad (2.15)$$

The characteristic Equation $Z_d(A_0, f_0) + Z_r(f_0) = 0$ can be written as

$$R_d(A_0, f_0) + R_r(f_0) = 0 \qquad (2.16)$$

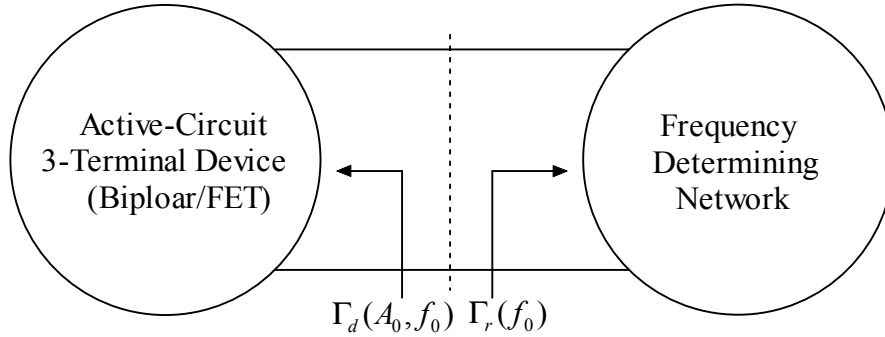and $\quad X_d(A_0, f_0) + X_r(f_0) = 0 \qquad (2.17)$

Figure 2-4: Schematic diagram of one-port negative resistance model.

This means that the one-port circuit is unstable for the frequency range $f_1 < f < f_2$, where $R_d(A, f)|_{f_1 < f < f_2} < 0 \Rightarrow |R_d(A, f)|_{f_1 < f < f_2} > |R_r(f)|$.

At the start-up oscillation, when the signal amplitude is very small, the amplitude dependence of the $R_d(A, f)$ is negligible and the oscillation build-up conditions can be given as

$$[R_d(f) + R_r(f)]_{f=f_x} \Rightarrow R_d(f_x) + R_r(f_x) \le 0 \qquad (2.18)$$

and $\quad [X_d(f) + X_r(f)]_{f=f_x} \Rightarrow X_d(f_x) + X_r(f_x) = 0 \qquad (2.19)$

where f_x denotes the resonance frequency at which the total reactive component equals zero. The conditions above are necessary, but are not sufficient conditions for oscillation build-up, particularly in a case when multiple frequencies exist to support the above-

shown conditions. To guarantee the oscillation build-up, the following condition at the given frequency needs to be met [25]:

$$\frac{\partial}{\partial f}[X_d(f) + X_r(f)]_{f=f_x} > 0 \tag{2.20}$$

$$R_d(f_x) + R_r(f_x) < 0 \tag{2.21}$$

$$X_d(f_x) + X_r(f_x) = 0 \tag{2.22}$$

Alternatively, for a parallel admittance topology [25],

$$Y_d(f_x) + Y_r(f_x) = 0 \tag{2.23}$$

$$G_d(f_x) + G_r(f_x) < 0 \tag{2.24}$$

$$B_d(f_x) + B_r(f_x) = 0 \tag{2.25}$$

$$\frac{\partial}{\partial f}[B_d(f) + B_r(f)]_{f=f_x} > 0 \tag{2.26}$$

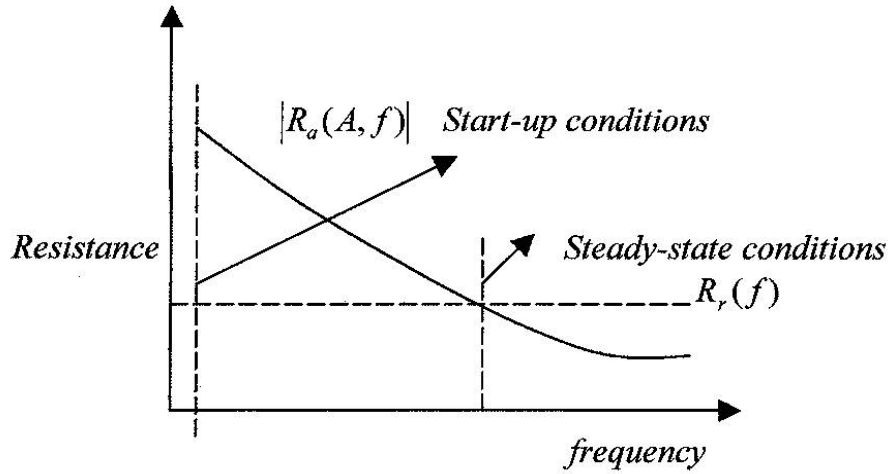Figure 2-5 shows the start-up and steady-state oscillation conditions.

Figure 2-5: Plot of start and steady state oscillation conditions.

As discussed earlier, if the closed-loop voltage gain has a pair of complex conjugate poles in the right half of the s-plane, close to the imaginary axis, then due to an ever-present noise voltage generated in the circuit or power-on transient, a growing, near-sinusoidal voltage appears. As the oscillation amplitude grows, the amplitude-limiting capabilities, due to the change in the transconductance from a small signal [g_m] to the

14

large signal $[g_m(t)=G_m]$ of the amplifier, produce a change in the location of the poles. The changes are such that the complex-conjugate poles move toward the imaginary axis and at some value of the oscillation amplitude; the poles reach to the imaginary axis giving steady-state oscillation

$$\text{as } |G(j\omega_o)H(j\omega_o)| = 1 \tag{2.27}$$

In the case of the negative resistance model, the oscillation will continue to build as long as $R_d(A,f)\big|_{f_1<f<f_2} < 0 \Rightarrow |R_d(A,f)|_{f_1<f<f_2} > |R_r(f)|$.

The frequency of oscillation is determined by $R_d(A_0,f_0)+R_r(f_0)=0$, and $X_d(A_0,f_0)+X_r(f_0)=0$ might not be stable because $Z_d(A,f)$ is frequency and amplitude-dependent. To guarantee stable oscillation, the following condition is to be satisfied as [25]

$$\frac{\partial}{\partial A}\Big[R_d(A)\big|_{A=A_0}\Big]*\frac{\partial}{\partial f}\Big[X_r(f)\big|_{f=f_0}\Big] - \frac{\partial}{\partial A}\Big[X_d(A)\big|_{A=A_0}\Big]*\frac{\partial}{\partial f}\Big[R_r(f)\big|_{f=f_0}\Big] > 0 \tag{2.28}$$

$$\frac{\partial}{\partial A}\Big[R_d(A)\big|_{A=A_0}\Big]*\frac{\partial}{\partial f}\Big[X_r(f)\big|_{f=f_0}\Big] > \frac{\partial}{\partial A}\Big[X_d(A)\big|_{A=A_0}\Big]*\frac{\partial}{\partial f}\Big[R_r(f)\big|_{f=f_0}\Big] \tag{2.29}$$

In the case of an LC resonant circuit, $R_r(f)$ is constant and the equation above can be simplified to

$$\frac{\partial}{\partial A}\Big[R_d(A)\big|_{A=A_0}\Big]*\frac{\partial}{\partial f}\Big[X_r(f)\big|_{f=f_0}\Big] > 0 \tag{2.30}$$

Alternatively, for a paralleled tuned circuit, the steady-state oscillation condition is given as [25]

$$G_d(f_0)+G_r(f_0)=0 \tag{2.31}$$

$$B_d(f_0)+B_r(f_0)=0 \tag{2.32}$$

$$\frac{\partial}{\partial A}\Big[G_d(A)\big|_{A=A_0}\Big]*\frac{\partial}{\partial f}\Big[B_r(f)\big|_{f=f_0}\Big] > 0 \tag{2.33}$$

2.2   Wideband Voltage-Controlled Oscillators

In order for a closed loop system, as shown in Figure 2-1, to be tunable for wideband, some of the modules/elements must be variable to achieve a positive feedback at different frequency of the tuning range over the band. The frequency selective feedback network of an oscillator is usually a resonator circuit, which can be modeled as an LCR equivalent

network in either a parallel or series configuration. A tunable oscillator will vary one of the parameters that set the oscillation condition in order to change the oscillation frequency over the tuning band. This is accomplished either by varying the inductor or capacitor to change the resonance frequency of the resonator circuit.

The frequency of oscillation of a resonator circuit is defined as $\omega_0 = 1/\sqrt{LC}$, and for the octave tuning range the minimum capacitive or inductive tuning range (capacitive or inductive ratio) is required in the order of 4:1. There are two primary constraints, which limit the oscillator circuit topologies; first is the transistor and its package, and second, is the large capacitance change required to tune the oscillator over an octave band.

The common emitter (CE) and common base (CB) are the common topology for the wideband oscillator/VCO design. Figure 2-6 shows the CE topology, uses a capacitive feedback network with C_1 and C_2 to create the negative resistance looking into the base of the transistor [11].
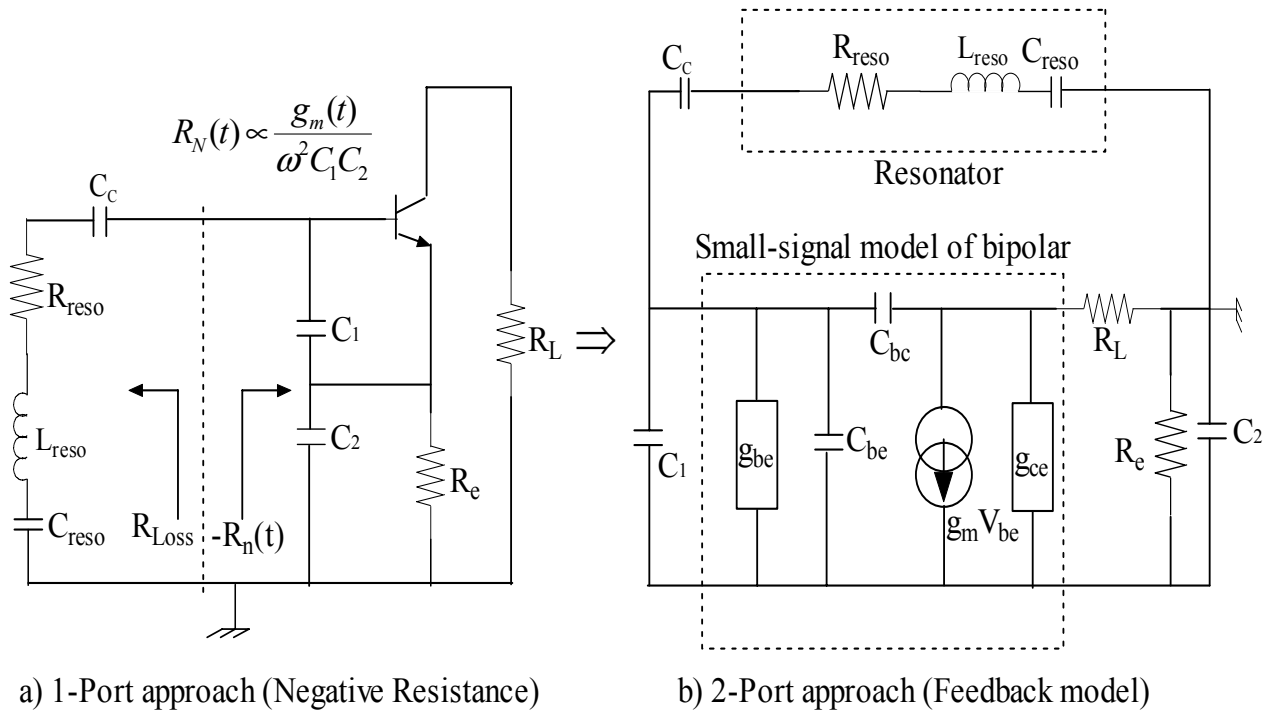

Figure 2-6: a) 1-Port and b) 2-Port approach of the common emitter oscillator.

Figure 2-7 shows the common base (CB) topology, which uses an inductor in the base of the transistor to generate the negative resistance looking into the emitter of the transistor. The frequency selective network (resonator) will have a loss resistance (positive resistance) associated with it, and the oscillation occurs when the negative resistance looking into the active device is greater than the absolute value of the loss resistance of the frequency selective network.

Based on the negative resistance approach, the dynamic load over the tuning range seen by the frequency selective network is negative and the resulting dynamic loaded Q would be infinite if taken in this context [15], and the loaded Q remains the measured quantity, but not predicted, as given by Leeson's model (Equation 4.13).

$$R_n(t) \propto \left[\frac{g_m(t)}{\omega^2 C_{ce} C_{reso} (1 - L_b C_{be} \omega^2)} \right]$$

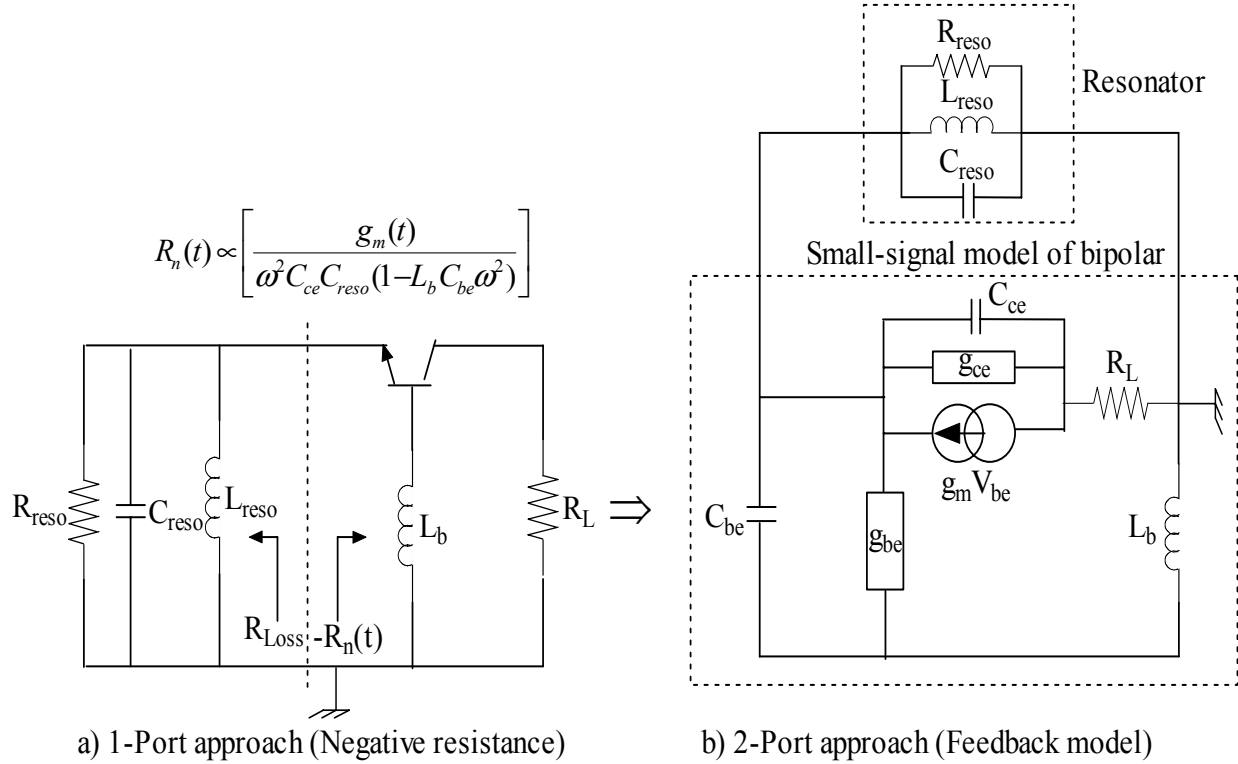a) 1-Port approach (Negative resistance)   b) 2-Port approach (Feedback model)

Figure 2-7: a) 1-Port and b) 2-Port approach of the common base oscillator.

For an ultra low noise and wideband tunability, there is an apriori need to determine the circuit parameters, which influences the dynamic loaded Q over the tuning range, therefore, optimization of the Q can be achieved for the low phase noise performance.

Rearranging the negative resistance oscillator (one-port) to a two-port equivalent configuration, by using small signal model for the active device, enables the approximate analysis of the loaded Q of the frequency selective network (resonator) as shown in Figure 2-6(b) and Figure 2-7(b).

Figure 2-6 (b) shows the effective loading of the resonator for the CE configuration that is due to the series combination of the load resistance, base and emitter resistance, and the parallel capacitance of C_1 and C_2 (influence of C_{be}, C_{bc} and g_{ce} are less in comparison to the other parameters, therefore, neglected for simplification purpose).

17

Small values of the feedback capacitance C_1 and C_2 generate the large negative resistance and allow for a wide tuning range at the cost of heavily loading of the resonator and wide conduction angle, thereby poor phase noise performance [73].

For optimum phase noise performance, the active device is driven at a large signal drive level that corresponds to the narrow conduction angle, and this restricts the lower limit of the values of the feedback capacitor. From [11,73], the drive level is directly proportional to the feedback capacitor C_2; therefore, this topology is best suited for narrow tuning range (10-30%)VCOs because large values of feedback capacitor C_1 and C_2 will raise the loaded Q of the resonator at the expense of lesser tuning ranges and lower negative resistance.

Figure 2-7 (b) shows the effective loading of the resonator for the common base (CB) oscillator configuration, which are due to the series combination of the load resistance, g_{ce} and C_{ce} of the transistor (influence of g_{be} and C_{be} are less in comparison to the other parameters, therefore, neglected for simplification purpose). For $\omega < \sqrt{\dfrac{1}{L_b C_{be}}}$, the loaded Q of the resonator is not much affected by the negative resistance generated by the feedback inductance L_b of the 3-terminal device (Bipolar/FET) and is, therefore, best suited for a wideband (octave-band) VCOs application. For best phase noise performance, the effective load across the resonator is to be kept to the optimum value corresponding to the optimum ratio m ($m = \dfrac{Q_{Loaded}}{Q_{unloaded}}$), equal to 0.5, and the condition for the best phase noise is discussed in Chapter 6 (Equation 6.48).

Chapter 3

System of Coupled Oscillators

3.1   Mutually Coupled Oscillators Using Classical Pendulum Analogy

A system of coupled oscillators/VCOs possesses a wealth of interesting and useful nonlinear dynamical phenomena, and the design of such systems requires a detailed understanding of the behavior of the coupled oscillator systems. The purpose of this analysis is to provide basic understanding and insights for a class of coupled oscillator systems based on the classical analogy of the coupled pendulum and to apply these techniques to practical ultra low phase noise wideband oscillators/VCOs. In this chapter we develop a general analysis for finding synchronized frequency of the coupled oscillator systems in the mutually locked state conditions. Figure 3-1 shows the classic example of pendulum connected with the spring [68].

Swinging in same direction   Swinging in opposite direction
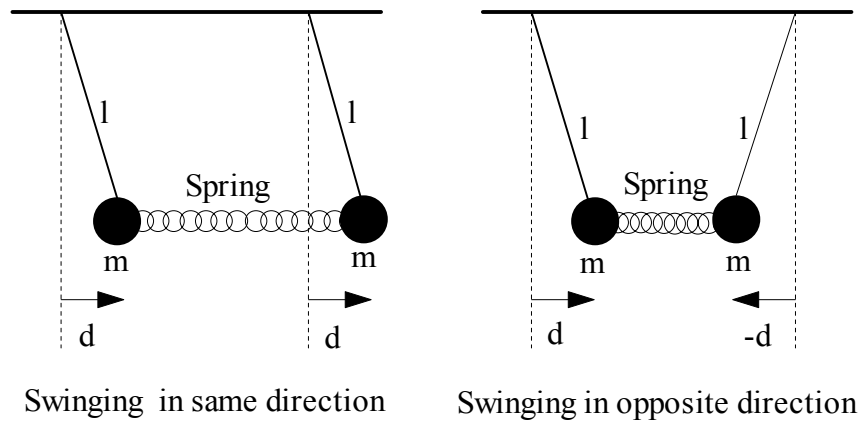
Figure 3-1: Pendulum connected with the spring.

In presence of the initial excitation, one pendulum starts swinging with small amplitude and the other slowly builds up the amplitude as the spring feeds energy from the first pendulum into the second pendulum and then energy flows back into the first and the cycle repeats due to transformation of energy back and forth.
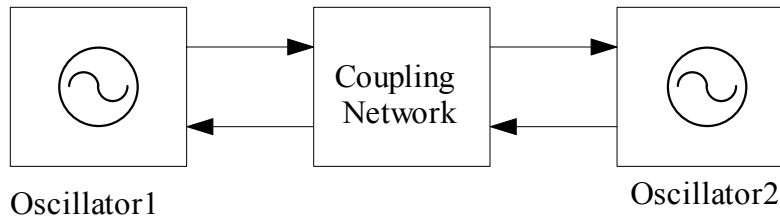

Figure 3-2 (a) : Block diagram of the coupled oscillator.

There can be two modes of motion i.e. swinging together in the same direction and swinging in the opposite directions. If it swings in the same direction, it swings in unison at their natural frequency and if they swing in the opposite direction than they will swing at higher frequency than they if they are uncoupled. When the pendulums are not identical, there are still two normal modes but the motions are more complicated and neither mode is at the uncoupled frequency. Similar analogy is given for coupled oscillator.

Figures 3-2 (a) and (b) show the simplified block diagram and the schematic of the series tuned coupled oscillator circuit for the purpose of the analysis. Oscillator1 and oscillator2 are the series tuned oscillators; L_1, C_1 and L_2, C_2 are the components of the LC resonant circuit of the series tuned oscillator1 and oscillator2. $R_{1\text{-Loss}}$ and $R_{2\text{-Loss}}$ are the loss resistances of the resonator and R_{n1} and R_{n2} are the negative resistance of the active device respectively.
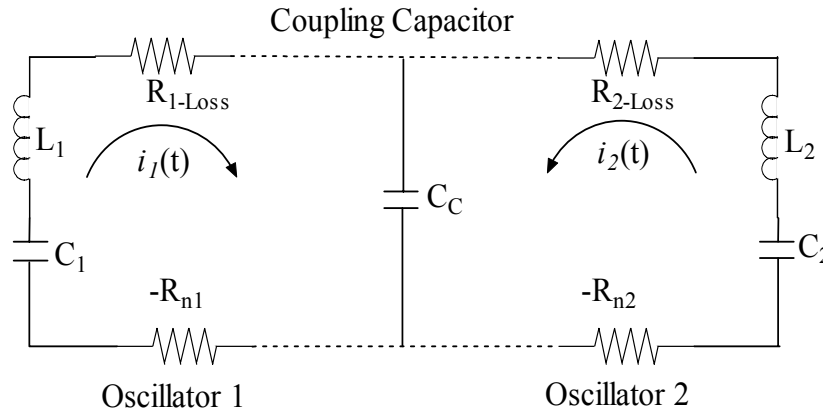

Figure 3-2 (b): Schematic of the coupled oscillator.

The simplest coupling network can be realized by capacitor C_c that couples the two oscillator circuits. The coupling strength depends upon the value of C_c. For the value of $C_c \rightarrow 0$, it corresponds to strong coupling and the circuits behave like a single LC oscillator circuit with and the equivalent values of L and C are given as

$$L = L_1 + L_2 \tag{3.1}$$

$$C = \frac{C_1 C_2}{C_1 + C_2} \tag{3.2}$$

For the value of $C_c \rightarrow \infty$, it corresponds to zero coupling, and the two oscillator circuits are uncoupled and capacitor C_c behaves like short circuit for RF signals. Considering that oscillator1 and oscillator2 are oscillating at their free-running frequencies and the negative resistance of the active devices compensates the corresponding loss resistance of the resonators, then Figure 3-2 (b) is reduced to Figure 3-3.

Figure 3-3 shows the coupled oscillator circuit without the series loss resistance and device negative resistance because negative resistance of the active device compensates the loss resistance if any, at the frequency of the desired oscillation. In real application, intermediate range of the coupling strength ($\infty > C_c > 0$) is more meaningful for the analysis of the mutually coupled oscillator systems.
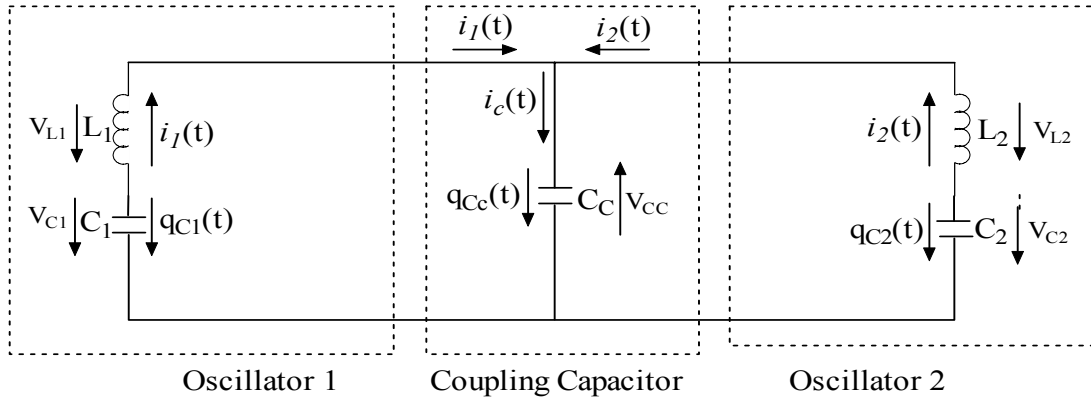

Figure 3-3: Coupled oscillator circuit without the series loss resistance

The circuit equation of the Figure 3-3 is given from the Kirchoff's voltage law (KVL),

$$V_{C_1}(t) + V_{L_1}(t) + V_{Cc}(t) = 0 \tag{3-3}$$

$$\frac{q_{C_1}(t)}{C_1} - L_1\frac{\partial i_1(t)}{\partial t} - \frac{q_{C_c}(t)}{C_c} \Rightarrow \frac{q_{C_1}(t)}{C_1} + L_1\frac{\partial^2[q_{C_1}(t)]}{\partial t^2} - \frac{q_{C_c}(t)}{C_c} = 0 \tag{3-4}$$

$$q_{C_c}(t) + q_{C_1}(t) + q_{C_2}(t) = 0 \Rightarrow q_{C_c}(t) = -[q_{C_1}(t) + q_{C_2}(t)] \tag{3-5}$$

$$i_1(t) + i_2(t) - i_{C_c}(t) = 0 \Rightarrow i_{C_c}(t) = [i_1(t) + i_2(t)] \tag{3-6}$$

From Equations (3-4) and (3-5)

$$\frac{q_{C_1}(t)}{C_1} + L_1\frac{\partial^2[q_{C_1}(t)]}{\partial t^2} + \frac{1}{C_c}[q_{C_1}(t) + q_{C_2}(t)] = 0 \tag{3.7}$$

$$\frac{\partial^2[q_{C_1}(t)]}{\partial t^2} + \left[\frac{1}{L_1 C_1} + \frac{1}{L_1 C_c}\right][q_{C_1}(t)] + \frac{1}{L_1 C_c}[q_{C_2}(t)] = 0 \tag{3-8}$$

$$\frac{\partial^2[q_{C_1}(t)]}{\partial t^2} + \omega_1^2[q_{C_1}(t)] + \omega_{1c}^2[q_{C_2}(t)] = 0 \tag{3-9}$$

where

$$V_{C_1}(t) = \frac{q_{C_1}(t)}{C_1}, \ V_{L_1}(t) = -L_1\frac{\partial i_1(t)}{\partial t}, \ V_{Cc}(t) = -\frac{q_{C_c}(t)}{C_c}, \ i_1(t) = -\frac{\partial q_{C_1}(t)}{\partial t}, \ i_2(t) = -\frac{\partial q_{C_2}(t)}{\partial t}$$

$$\omega_1 = \sqrt{\frac{1}{L_1}\left[\frac{1}{C_1}+\frac{1}{C_c}\right]} \ , \ \omega_2 = \sqrt{\frac{1}{L_2}\left[\frac{1}{C_2}+\frac{1}{C_c}\right]}, \ \omega_{1c} = \sqrt{\frac{1}{L_1 C_c}} \ , \ \omega_{2c} = \sqrt{\frac{1}{L_2 C_c}}$$

Similarly

$$V_{C_2}(t) + V_{L_2}(t) + V_{Cc}(t) = 0 \tag{3.10}$$

$$\frac{q_{C_2}(t)}{C_2} - L_2\frac{\partial i_2(t)}{\partial t} - \frac{q_{C_c}(t)}{C_c} \Rightarrow \frac{q_{C_2}(t)}{C_2} + L_2\frac{\partial^2[q_{C_2}(t)]}{\partial t^2} - \frac{q_{C_c}(t)}{C_c} = 0 \tag{3.11}$$

$$\frac{q_{C_2}(t)}{C_2} + L_2\frac{\partial^2[q_{C_2}(t)]}{\partial t^2} + \frac{1}{C_c}[q_{C_1}(t) + q_{C_2}(t)] = 0 \tag{3.12}$$

$$\frac{\partial^2[q_{C_2}(t)]}{\partial t^2} + \left[\frac{1}{L_2 C_2} + \frac{1}{L_2 C_c}\right][q_{C_2}(t)] + \frac{1}{L_2 C_c}[q_{C_1}(t)] = 0 \tag{3.13}$$

$$\frac{\partial^2[q_{C_2}(t)]}{\partial t^2} + \omega_2^2[q_{C_2}(t)] + \omega_{2c}^2[q_{C_1}(t)] = 0 \tag{3.14}$$

Equations (3.8) and (3.14) are the second order homogeneous differential equations of the mutually coupled oscillator circuit shown in Figure 3-3.

The natural frequencies ω_{r1} and ω_{r2} of the coupled oscillator can be derived by solving the second order homogeneous Equations (3.8) and (3.14). The solutions are

$$q_{C_1}(t) = K_1 \exp[j\omega_{r1}t] + K_2 \exp[j\omega_{r2}t] \tag{3.15}$$

$$q_{C_2}(t) = K_3 \exp[j\omega_{r1}t] + K_4 \exp[j\omega_{r2}t] \tag{3.16}$$

where K_1, K_2, K_3 and K_4 are the coefficients of the $q_{C_1}(t)$ and $q_{C_2}(t)$

After substituting the values of $q_{C_1}(t)$ and $q_{C_2}(t)$ in the Equations (3.8) and (3.14), and equating the coefficient of $\exp[j\omega_{r1}t]$ and $\exp[j\omega_{r2}t]$, we obtain four linear equations as

$$\omega_1^2 K_1 + \omega_{1c}^2 K_3 - \omega_{r1}^2 K_1 = 0 \tag{3.17}$$

$$\omega_1^2 K_2 + \omega_{1c}^2 K_4 - \omega_{r2}^2 K_2 = 0 \tag{3.18}$$

$$\omega_2^2 K_3 + \omega_{2c}^2 K_1 - \omega_{r1}^2 K_3 = 0 \tag{3.19}$$

$$\omega_2^2 K_4 + \omega_{2c}^2 K_2 - \omega_{r2}^2 K_4 = 0 \tag{3.20}$$

After solving Equations (3.17), (3.18), (3.19) and (3.20), the expression of the coefficients K_1, K_2, K_3 and K_4 are

$$K_1 = \left[\frac{\omega_{r1}^2 - \omega_2^2}{\omega_{2c}^2} \right] K_3 \tag{3.21}$$

$$K_2 = \left[\frac{\omega_{r2}^2 - \omega_2^2}{\omega_{2c}^2} \right] K_4 \tag{3.22}$$

$$K_3 = \left[\frac{\omega_{r1}^2 - \omega_1^2}{\omega_{1c}^2} \right] K_1 \tag{3.23}$$

$$K_4 = \left[\frac{\omega_{r2}^2 - \omega_1^2}{\omega_{1c}^2} \right] K_2 \tag{3.24}$$

From Equations (3.21), (3.22), (3.23) and (3.24), the coefficients K_1, K_2, K_3 and K_4 can be eliminated and ω_{r1} and ω_{r2} are

$$(\omega_{r1}^2 - \omega_1^2)(\omega_{r1}^2 - \omega_2^2) - \omega_{1c}^2 \omega_{2c}^2 = 0 \tag{3.25}$$

$$(\omega_{r2}^2 - \omega_1^2)(\omega_{r2}^2 - \omega_2^2) - \omega_{2c}^2 \omega_{1c}^2 = 0 \tag{3.26}$$

$$\omega_{r1}^2 = \frac{1}{2}(\omega_1^2 + \omega_2^2) + \frac{1}{2}\sqrt{[(\omega_1^2 - \omega_2^2) + 4\omega_{1c}^2 \omega_{2c}^2]} \tag{3.27}$$

$$\omega_{r2}^2 = \frac{1}{2}(\omega_1^2 + \omega_2^2) - \frac{1}{2}\sqrt{[(\omega_1^2 - \omega_2^2) + 4\omega_{1c}^2 \omega_{2c}^2]} \tag{3.28}$$

where ω_{r1} and ω_{r2} are natural frequencies of oscillation corresponding to the two normal oscillation modes of the coupled oscillator.

From Equations (3.15) and (3.16) $q_{C_1}(t)$ and $q_{C_2}(t)$ can be expressed as

$$q_{C_1}(t) = K_1 \exp[j\omega_{r1}t] + K_2 \exp[j\omega_{r2}t] \tag{3.29}$$

$$q_{C_2}(t) = K_1\left[\frac{(\omega_{r1}^2 - \omega_1^2)}{\omega_{1c}^2}\right]\exp[j\omega_{r1}t] + K_2\left[\frac{(\omega_{r2}^2 - \omega_1^2)}{\omega_{1c}^2}\right]\exp[j\omega_{r2}t] \qquad (3.30)$$

defining ω_{av} and ω_{diff} as

$$\omega_{av} = \frac{\omega_{r1} + \omega_{r2}}{2} \quad \text{and} \quad \omega_{diff} = \frac{\omega_{r1} - \omega_{r2}}{2}$$

Equations (3.29) and (3.30) can be further simplified to

$$q_{C_1}(t) = \exp[j\omega_{av}t]\left(K_1\exp[j\omega_{diff}t] + K_2\exp[-j\omega_{diff}t]\right) \qquad (3.31)$$

$$q_{C_2}(t) = \exp[j\omega_{av}t]\left(K_1\frac{(\omega_{r1}^2 - \omega_1^2)}{\omega_{1c}^2}\exp[j\omega_{diff}t] + K_2\left[\frac{(\omega_{r2}^2 - \omega_1^2)}{\omega_{1c}^2}\right]\exp[-j\omega_{diff}t]\right) \qquad (3.32)$$

For the case of the identical oscillators $(L=L_1=L_2$ and $C=C_1=C_2)$, the coupled oscillator parameters are reduced to

$$\omega_1^2 = \frac{1}{L}\left[\frac{1}{C} + \frac{1}{C_c}\right] \qquad (3.33)$$

$$\omega_2^2 = \frac{1}{L}\left[\frac{1}{C} + \frac{1}{C_c}\right] \qquad (3.34)$$

$$\omega_{1c}^2 = \frac{1}{LC_c} \qquad (3.35)$$

$$\omega_{2c}^2 = \frac{1}{LC_c} \qquad (3.36)$$

$$\omega_{r1}^2 = \frac{1}{2}(\omega_1^2 + \omega_2^2) + \frac{1}{2}\sqrt{[(\omega_1^2 - \omega_2^2) + 4\omega_{1c}^2\omega_{2c}^2]} \qquad (3.37)$$

$$\omega_{r1}^2 = \frac{1}{2}\left\{\frac{1}{L}\left[\frac{1}{C} + \frac{1}{C_c}\right] + \frac{1}{L}\left[\frac{1}{C} + \frac{1}{C_c}\right]\right\} + \frac{1}{2}\sqrt{4\left(\frac{1}{LC_c}\right)^2} \qquad (3.38)$$

$$\omega_{r1}^2 = \frac{1}{L}\left[\frac{1}{C} + \frac{1}{C_c}\right] + \left(\frac{1}{LC_c}\right) = \left[\frac{1}{LC} + \frac{2}{LC_c}\right] \qquad (3.39)$$

$$\omega_{r2} = \frac{1}{2}(\omega_1^2 + \omega_2^2) - \frac{1}{2}\sqrt{[(\omega_1^2 - \omega_2^2) + 4\omega_{1c}^2\omega_{2c}^2]} \tag{3.40}$$

$$\omega_{r2}^2 = \frac{1}{2}\left\{\frac{1}{L}\left[\frac{1}{C} + \frac{1}{C_c}\right] + \frac{1}{L}\left[\frac{1}{C} + \frac{1}{C_c}\right]\right\} - \frac{1}{2}\sqrt{4\left(\frac{1}{LC_c}\right)^2} = \frac{1}{LC} \tag{3.41}$$

For ($L = L_1 = L_2$ and $C = C_1 = C_2$), Equations (3.31) and (3.32) can be simplified as

$$q_{C_1}(t) = \exp[j\omega_{av}t](K_1\exp[j\omega_{diff}t] + K_2\exp[-j\omega_{diff}t]) \tag{3.42}$$

$$q_{C_2}(t) = \exp[j\omega_{av}t](K_1\exp[j\omega_{diff}t] - K_2\exp[-j\omega_{diff}t]) \tag{3.43}$$

Coupled Oscillator Frequency and Modulation Frequency

Assuming that oscillator 1 starts oscillating first and oscillator 2 starts oscillation due to the injection mechanism from oscillator 1 in the coupled oscillator circuit shown in Figure 3-3. This condition forces zero current at $t = 0$ in the circuit of oscillator 2, and the corresponding classical analogy of this mechanism as shown in Figure 3-1 can be given by pulling one mass aside of the pendulum and release it from rest.

Under this constraints the initial conditions of the charge distribution on the capacitor C_1 and C_2 are given as

$$q_{C_1}(t)\big|_{t=0} \neq 0 \tag{3.44}$$

$$q_{C_2}(t)\big|_{t=0} = 0 \tag{3.45}$$

Assuming $K_1 = K_2 = K$, Equations (3.42) and (3.43) can be rewritten as

$$q_{C_1}(t) = K\exp[j\omega_{av}t](\exp[j\omega_{diff}t] + \exp[-j\omega_{diff}t]) \Rightarrow q_{C_1}(t)\big|_{t=0} = 2K \tag{3.46}$$

$$q_{C_2}(t) = K\exp[j\omega_{av}t](\exp[j\omega_{diff}t] - \exp[-j\omega_{diff}t]) \Rightarrow q_{C_2}(t)\big|_{t=0} \Rightarrow 0 \tag{3.47}$$

Equations (3.46) and (3.47) can be expressed in the form of cosine and sine function as

$$q_{C_1}(t) = 2K\{\cos(\omega_{diff}t)(\cos(\omega_{av}t) + j\sin(\omega_{av}t))\} \tag{3.48}$$

$$q_{C_2}(t) = -2jK\{\sin(\omega_{diff}t)(\cos(\omega_{av}t) + j\sin(\omega_{av}t))\} \tag{3.49}$$

The real and imaginary part of the Equations (3.48) and (3.49) are

$$\text{Re}[q_{C_1}(t)] = 2K[\cos(\omega_{av}\, t)\cos(\omega_{diff}\, t)] \tag{3.50}$$

$$\text{Im}[q_{C_1}(t)] = 2K[\sin(\omega_{av}\, t)\cos(\omega_{diff}\, t)] \tag{3.51}$$

$$\text{Re}[q_{C_2}(t)] = 2K\sin(\omega_{av}\, t)\sin(\omega_{diff}\, t) \tag{3.52}$$

$$\text{Im}[q_{C_2}(t)] = -2K[\cos(\omega_{av}\, t)\sin(\omega_{diff}\, t)] \tag{3.53}$$

The real part of the Equations (3.48) and (3.49) gives the equation of the oscillation for $q_{C_1}(t)$ and $q_{C_2}(t)$ of the mutually identical coupled oscillator. Equations (3.50) and (3.52) show that $q_{C_1}(t)$ and $q_{C_2}(t)$ oscillate at frequency ω_{av}, and that they are modulated by the lower frequency ω_{diff}. From (3.50) and (3.52), we can see that the modulation associated with $q_{C_1}(t)$ and $q_{C_2}(t)$ is 90^0 out of phase, which indicates that the total energy is flowing back and forth between the two coupled oscillator circuits oscillator 1 and oscillator 2 with the analogy of the coupled pendulum shown in Figure 3-1, that oscillates back and forth.

Defining coupled oscillator frequency as ω_c, we obtain

$$\omega_c = \omega_{av} = \frac{\omega_{r1} + \omega_{r2}}{2} \tag{3.54}$$

Defining modulation frequency ω_m, we obtain

$$\omega_m = \omega_{diff} = \frac{\omega_{r1} - \omega_{r2}}{2} \tag{3.55}$$

From (3.54) and (3.55)

$$\frac{\omega_m}{\omega_c} = \frac{\omega_{r1} - \omega_{r2}}{\omega_{r1} + \omega_{r2}} \Rightarrow \omega_m = \left[\frac{\omega_{r1} - \omega_{r2}}{\omega_{r1} + \omega_{r2}}\right]\omega_c \tag{3.56}$$

From (3.38) and (3.41)

$$\omega_m = \left[\frac{(\omega_{r1} + \omega_{r2})(\omega_{r1} - \omega_{r2})}{(\omega_{r1} + \omega_{r2})(\omega_{r1} + \omega_{r2})}\right]\omega_c = \left[\frac{(\omega_{r1}^2 - \omega_{r2}^2)}{(\omega_{r1} + \omega_{r2})(\omega_{r1} + \omega_{r2})}\right]\omega_c \tag{3.57}$$

$$\omega_m = \left[\frac{(\omega_{r1}^2 - \omega_{r2}^2)}{(\omega_{r1} + \omega_{r2})(\omega_{r1} + \omega_{r2})}\right]\omega_{av} = \left[\frac{1}{(\omega_{r1}^2 + \omega_{r2}^2 + 2\omega_{r1}\omega_{r2})}\right]\left[\frac{2}{LC_c}\right]\omega_c \tag{3.58}$$

The modulation frequency, therefore, is

$$\omega_m \approx \frac{C}{2C_c}\sqrt{\frac{1}{LC}} = \left[\frac{C}{2C_c}\right]\omega_c \Rightarrow \omega_m = \omega_c\left[\frac{C}{2C_c}\right] \tag{3.59}$$

From Equation (3.59), oscillator output can be described as

$$V_{out}(t) = A_m \cos(\omega_m t)\cos[\omega_c t + \varphi(t)] = A(t)\cos[\omega_c t + \varphi(t)] \tag{3.60}$$

where $A(t)$ and $\varphi(t)$ are amplitude and phase terms of the oscillator signal.

3.2   Phase Condition for Mutually Locked Coupled Oscillators

Figure 3-4 (a) shows the equivalent circuit of the mutually coupled oscillators (parallel-turned oscillators) coupled through the transmission line as a coupling network. The equivalent model of the oscillator circuit can be given either by series tuned or parallel tuned configuration, and the condition for mutually locking are valid for both the cases. Considering the transmission line acts as a resonant circuit in addition to the coupling network, and for the simplification in the analysis, the loss associated with the transmission line is assumed as a part of the load admittances G_L.
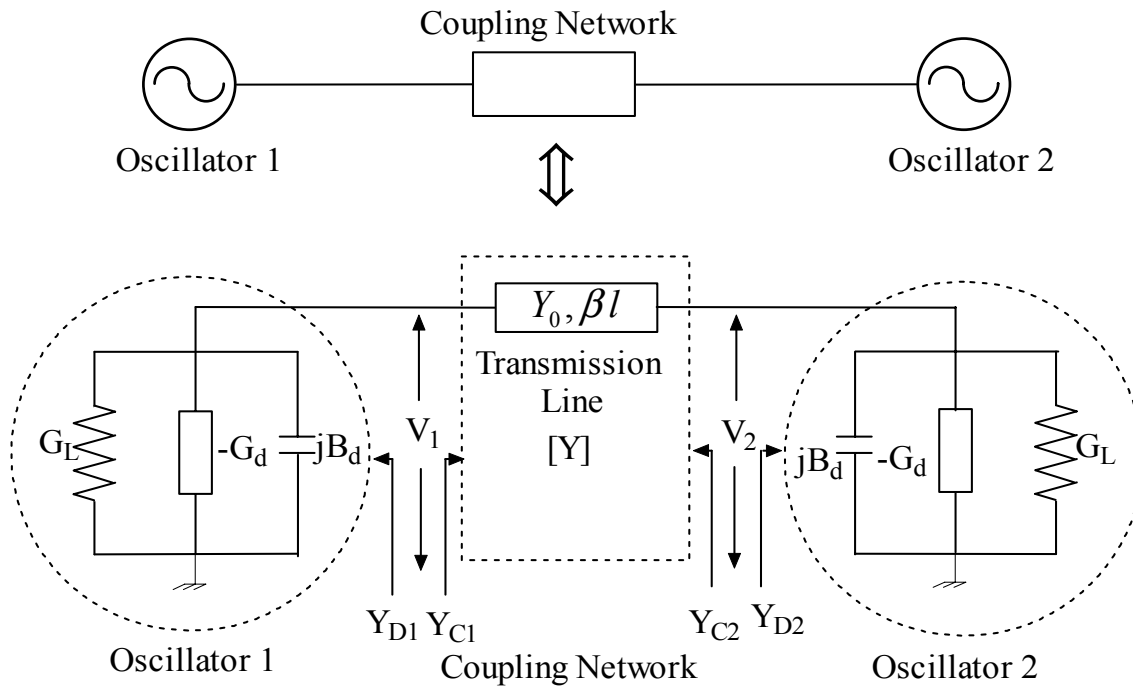

Figure 3-4 (a): Equivalent circuit of mutually coupled oscillators.

In Figure 3-4 (a), Y_{d1} and Y_{d2} represent the equivalent admittance of the two active devices and their loads, while Y_{C1} and Y_{C2} represent the admittance seen by the devices of the mutually-coupled oscillator circuit. Based on the extended resonance technique [12], the length of the transmission line is selected such that the two devices resonate with each other at the common resonance frequency. This can be realized by choosing the length of the transmission line of the coupling network in such a way that each device's susceptance is transformed to a susceptance with the same magnitude, but opposite in sign, and thereby, creating a virtual short circuit at the midpoint of the transmission line, ensuring that the device are injection locked with respect to out of phase.

For analysis purpose, transmission line is characterized as a two-port network with its terminal voltages represented by voltage phasor as $V_1 = |V_1|e^{j\varphi_1}$ and $V_2 = |V_2|e^{j\varphi_2}$, where $|V_1|$, $|V_2|$, φ_1 and φ_2 are the magnitudes and phases of the voltage phasor. The circuit equation for Figure 3-4(a) at the transmission line terminals can be expressed as

$$-Y_{D1}|V_1|e^{j\varphi} = Y_{11}|V_1|e^{j\varphi_1} + Y_{21}|V_2|e^{j\varphi_2} \tag{3.61}$$

$$-Y_{D1}|V_2|e^{j\varphi} = Y_{21}|V_1|e^{j\varphi_1} + Y_{22}|V_2|e^{j\varphi_2} \tag{3.62}$$

Equations (3.61) and (3.62) can be expressed in matrix form as

$$\begin{bmatrix} -Y_{D1}V_1 \\ -Y_{D1}V_2 \end{bmatrix} = \begin{bmatrix} Y_{11} & Y_{12} \\ Y_{21} & Y_{22} \end{bmatrix} \begin{bmatrix} V_1 \\ V_2 \end{bmatrix} \tag{3.63}$$

$$[Y]_{transmission\,line} = \begin{bmatrix} Y_{11} & Y_{12} \\ Y_{21} & Y_{22} \end{bmatrix} = \begin{bmatrix} -jY_0\cot(\beta l) & jY_0\cos ec(\beta l) \\ jY_0\cos ec(\beta l) & -jY_0\cot(\beta l) \end{bmatrix} \tag{3.64}$$

where β, Y_0 and l are the phase constant, characteristic admittance and length of the transmission line.

For identical coupled oscillators: $V_1 = V_2 = V$, $Y_{D1} = Y_{D2} = Y_D$ and $Y_{C1} = Y_{C2} = Y_C$. From Equations (3.61) and (3.62)

$$e^{\pm j(\varphi_2-\varphi_1)} = e^{\pm j(\Delta\varphi)} = \frac{Y_D + Y_{11}}{-Y_{12}} \tag{3.63}$$

The admittance Y_D comprises of the device admittance and load conductance as
$$Y_D = G_L - G_D + jB_D; \ G_D > 0 \tag{3.64}$$

The admittance Y_C is given from the transmission line equation as

$$Y_C = Y_0 \left[\frac{Y_D + jY_0\tan(\beta l)}{Y_0 + jY_D\tan(\beta l)} \right] = Y_0 \left[\frac{Y_D + jY_0\tan\theta}{Y_0 + jY_D\tan\theta} \right] \tag{3.65}$$

Applying the extended resonance technique [12], the length of the transmission line is selected such that real and imaginary part of the admittance Y_C is given by

$$\text{Re}[Y_C] = G_L - G_D \tag{3.66}$$

$$\text{Im}[Y_C] = -jB_D \tag{3.67}$$

From Equations (3.64) and (3.65),

$$\tan(\beta l) = \frac{2B_D Y_0}{B_D^2 - Y_0^2 + (G_L - G_D)^2} \tag{3.68}$$

During startup of the oscillation, the real parts of the admittances Y_C and Y_D are negative, and as the signal level increases, the device gain drops until the losses are compensated. Under the steady-state oscillation conditions, $G_L - G_D = 0$ and the electrical length θ of the transmission line is given from Equation (3.68) as

$$\theta = (\beta l) = \tan^{-1}\left[\frac{2B_D Y_0}{B_D^2 - Y_0^2}\right] \tag{3.69}$$

The [Y] parameter of the transmission line can be rewritten from Equation (3.63) as

$$[Y]_{transmissi\ on\ line} = \begin{bmatrix} -jY_0 \cot(\beta l) & jY_0 \cos ec(\beta l) \\ jY_0 \cos ec(\beta l) & -jY_0 \cot(\beta l) \end{bmatrix} = \begin{bmatrix} -j\dfrac{B_D^2 - Y_0^2}{2B_D} & j\dfrac{B_D^2 + Y_0^2}{2B_D} \\ j\dfrac{B_D^2 + Y_0^2}{2B_D} & -j\dfrac{B_D^2 - Y_0^2}{2B_D} \end{bmatrix} \tag{3.70}$$

From (3.63) and (3.70), the phase difference is given by

$$e^{\pm j(\varphi_2 - \varphi_1)} = \frac{[Y_D + Y_{11}]}{-[Y_{12}]} = \left[\frac{Y_D - j\dfrac{B_D^2 - Y_0^2}{2B_D}}{j\dfrac{B_D^2 + Y_0^2}{2B_D}}\right] = \left[\frac{jB_D - j\dfrac{B_D^2 - Y_0^2}{2B_D}}{j\dfrac{B_D^2 + Y_0^2}{2B_D}}\right] = -1 \Rightarrow \Delta\varphi = \varphi_2 - \varphi_1 = \pm 180^0 \tag{3.71}$$

Equation (3.71) gives the necessary phase condition for the mutually locked conditions of the coupled oscillator system, thus the outputs of the mutually synchronized coupled oscillator (Push-Push) are in antiphase ($\Delta\varphi = 180$ degree).

The following shows an example of mutually synchronized coupled oscillators for a frequency of 2000 MHz ($2f_0$) in which two individual oscillators oscillate at 1000 MHz (f_0). This is provided to give some insight into the phase relationship between the two identical mutually coupled oscillator circuit osc #1 and osc #2. Figure 3-4(b) shows the

circuit diagram of the mutually coupled oscillator. The circuit is fabricated on 32-mil thickness Roger substrate of dielectric constant 3.38 and loss tangent $2.7 \cdot 10^{-4}$. Figure 3-4(c) shows the simulated (Ansoft Designer) plot of the base current I_{b1} and I_{b2}, which is phase shifted by 180 degree in mutually synchronized condition. The transmission line MSL2, shown in Figure 3-4 (b), provides the phase shift for the mutually synchronized coupled oscillators (Equation 3.71).
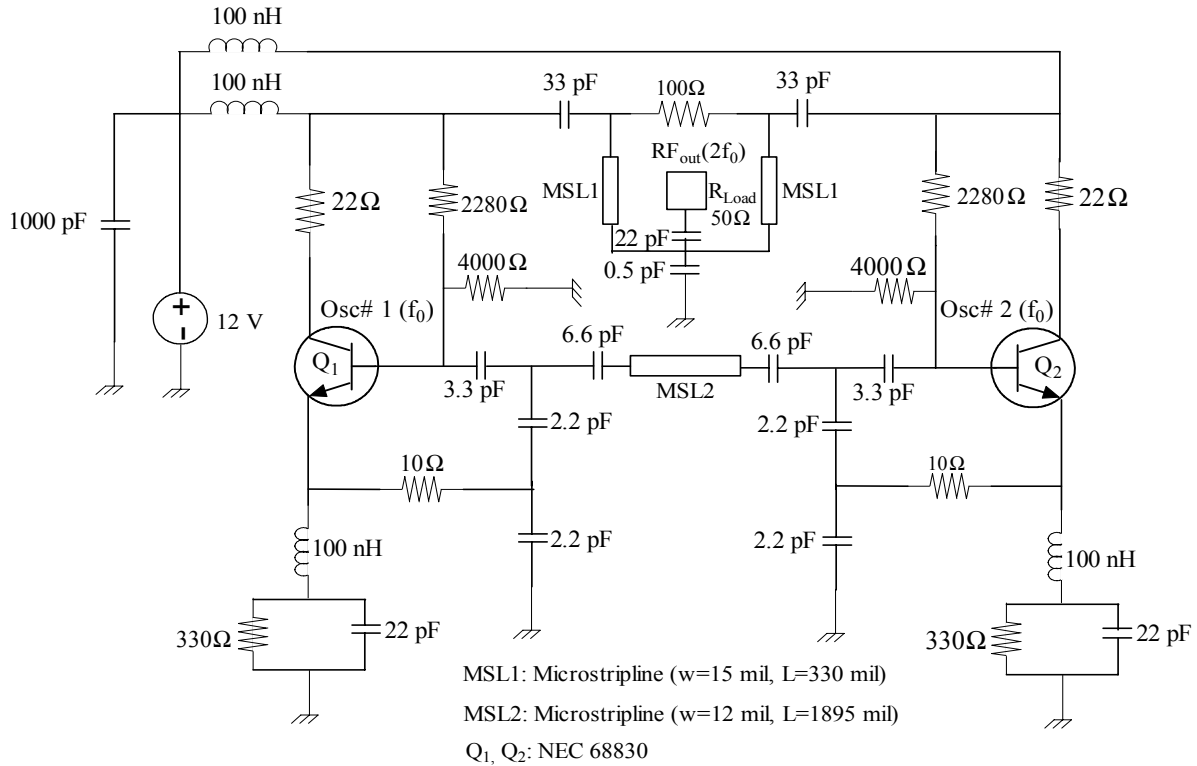
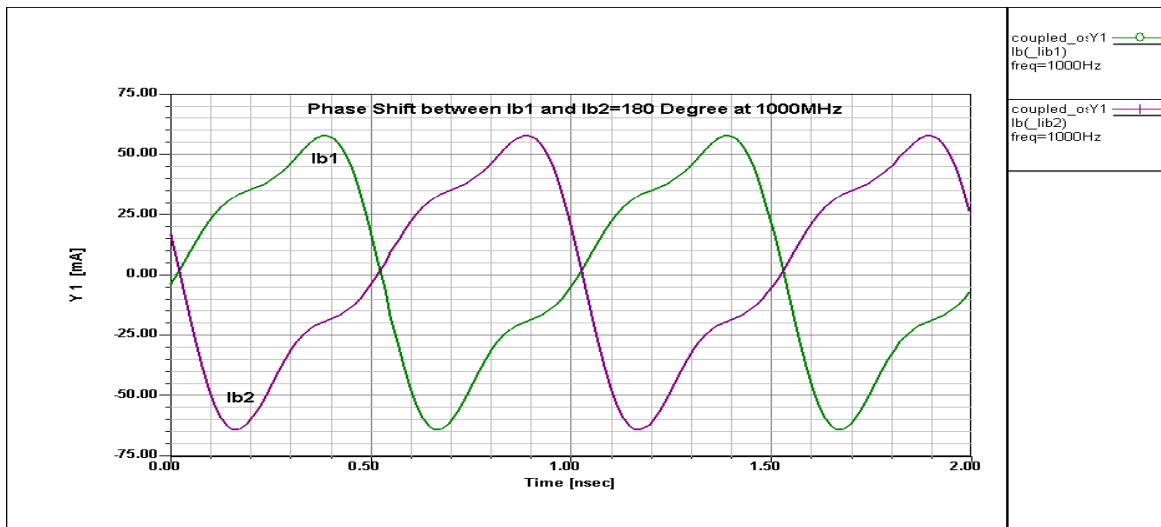Figure 3-4(b): Schematic of a 2000 MHz mutually coupled oscillators.

MSL1: Microstripline (w=15 mil, L=330 mil)

MSL2: Microstripline (w=12 mil, L=1895 mil)

Q_1, Q_2: NEC 68830

Figure 3-4(c): Plot of the RF base current of the mutually coupled oscillators.

30

3.3   Dynamics of Coupled Oscillators

The objective of this analysis is to develop time domain dynamics of the coupled oscillator systems based on Van der Pol (VDP) model [13]. The time dependent characteristic of the VDP model is the basis for using this model to our particular class of problem for the analysis of the system dynamics of the coupled oscillators.
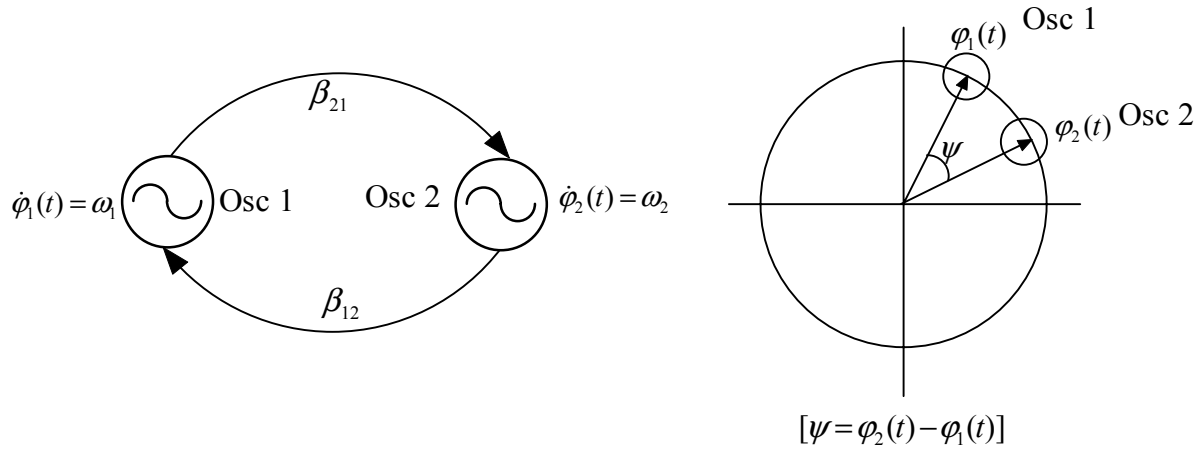

$$[\psi = \varphi_2(t) - \varphi_1(t)]$$

Figure 3-5: Simple model of the system of two-coupled oscillators

Figure 3-5 shows the simple model of the two identical coupled oscillators where β_{12} and β_{21} are coupling coefficients.
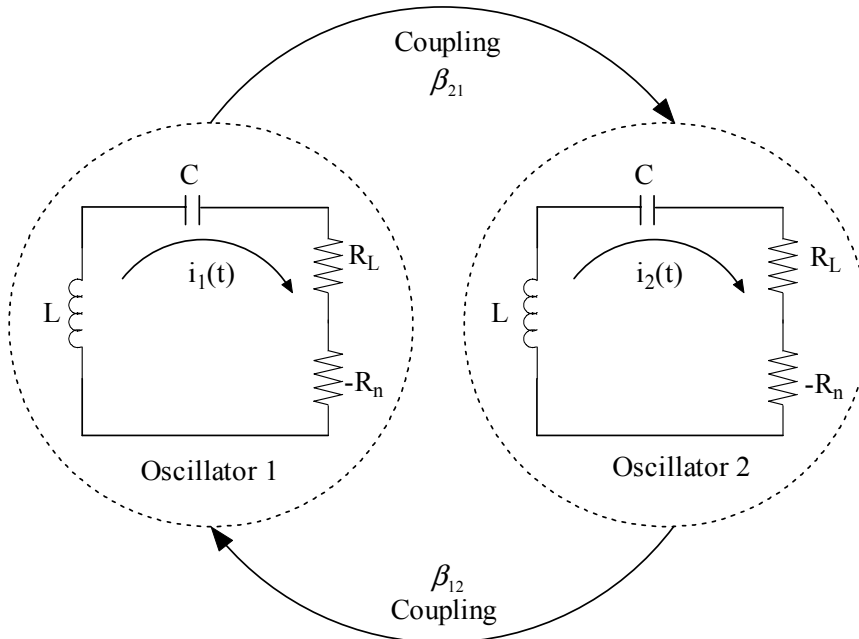

Figure 3-6: Equivalent circuit representation of the Figure 3-5

31

Figure 3-6 shows the equivalent circuit model of the Figure 3-5, where the series tuned resonator circuit models the single oscillator for the coupled oscillator system [68]. The equivalent model of the oscillator circuit can be given either by series tuned or parallel tuned configuration, and the condition for system dynamics is valid for both the cases.

Regardless of the topology, the system of coupled oscillators must synchronize to a common frequency and maintain a desired phase relationship in the steady state oscillating condition. For the analysis of the dynamics of the coupled oscillator system, a very simple equivalent circuit model is shown in Figure 3-6, where oscillator 1 in Figure 3-5 is replaced by the source $V_{inj}(t)$ that accounts for the interaction and coupling with the adjacent oscillator 2 [27, 68].
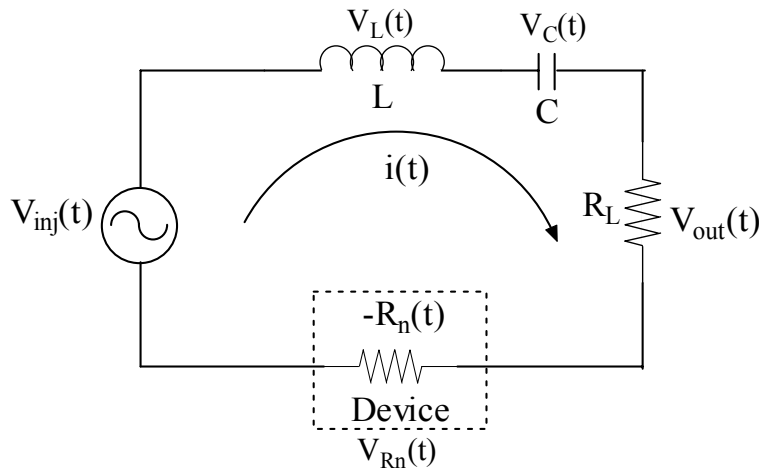

Figure 3-7: The simplified representation of the Figure 3-6, where $V_{inj}(t)$ accounts for the interaction and coupling.

The negative resistance of the device can be described as a time-averaged value and is given by [13] as

$$R_n(t) = \frac{1}{T}\int_0^T \frac{V_{Rn}(t)}{I_{Rn}(t)}\,dt = \frac{1}{T}\int_0^T \frac{V_{Rn}(t)}{i(t)}\,dt \qquad (3.72)$$

For a series tuned resonator circuit, we define

$$\omega_0 = \sqrt{\frac{1}{LC}}\,,\ Q = \frac{\omega_0 L}{R_L} = \frac{1}{\omega_0 C R_L}\,,\ R_n \approx R_n[|V_{out}(t)|]$$

R_n is a strong function of $V_{out}(t)$, ω_0 is the resonance frequency and Q is the quality factor of the embedded resonator circuit. The quality factor of the series tuned resonator is assumed to be greater than 10 so that the frequency of the output signal $V_{out}(t)$ is close to the natural resonance frequency of the oscillator circuit.

The circuit equations of Figure 3-7 are given from the Kirchoff voltage law (KVL) as

$$V_{inj}(t) = V_L(t) + V_C(t) + V_{Rn}(t) + V_{out}(t) = L\frac{\partial i(t)}{\partial t} + \frac{1}{C}\int i(t)dt - R_n(|V_{out}(t)|)i(t) + R_L i(t) \quad (3.73)$$

$$i(t) = \frac{V_{out}(t)}{R_L} \quad (3.74)$$

The output signal $V_{out}(t)$ can be expressed as

$$V_{out}(t) = A(t)\exp\{j[\omega_0 t + \varphi(t)]\} = A(t)\exp[j\theta(t)] \quad (3.75)$$

where $\theta(t)$ is the instantaneous phase, $A(t)$ and $\varphi(t)$ are amplitude and phase terms of the output signal which are having slow variation with respect to time in comparison to the output periodic oscillation.

For solving Equation (3-73), $\int V_{out}(t)dt$ and $\dfrac{\partial V_{out}(t)}{\partial t}$ are to be evaluated first and can be given by

$$\int V_{out}(t)dt = -\frac{j2A(t)\exp[j\theta(t)]}{\omega_o} + \frac{1}{\omega_o^2}\frac{\partial[A(t)\exp[j\theta(t)]]}{\partial t} + \dots \text{ (Higher order terms)} \quad (3.76)$$

$$\frac{\partial}{\partial t}[V_{out}(t)] = \left[\frac{\partial A(t)}{\partial t}\right][\exp j[\theta(t)]] + A(t)\left[\exp\{j[\theta(t)]\} \cdot j\left\{\omega_0 + \frac{\partial\varphi(t)}{\partial t}\right\}\right] \quad (3.77)$$

The higher order term in the Equation (3.76) can be neglected in comparison to the output periodic oscillation and can be rewritten as

$$\int V_{out}(t)dt = -\frac{j2V_{out}(t)}{\omega_o} + \frac{1}{\omega_o^2}\frac{\partial V_{out}(t)}{\partial t} \quad (3.78)$$

From (3.73) and (3.74)

$$V_{inj}(t) = \left[\frac{L}{R_L}\right]\frac{\partial V_{out}(t)}{\partial t} + \left[\frac{1}{CR_L}\right]\int V_{out}(t)dt + \left[1 - \frac{R_n(|V_{out}(t)|)}{R_L}\right]V_{out}(t) \quad (3.79)$$

By multiplying Equation (3.79) with $\dfrac{\omega_0}{Q}$

$$\left[\frac{\omega_0}{Q}\right]V_{inj}(t) = \frac{\partial V_{out}(t)}{\partial t} + \omega_0^2 \int V_{out}(t)dt + \left[1 - \frac{R_n(|V_{out}(t)|)}{R_L}\right]\left[\frac{\omega_0}{Q}\right]V_{out}(t) \qquad (3.80)$$

where

$$V_{inj}(t) = A_{inj}(t)\exp\{j[\omega_{inj}t + \psi_{inj}(t)]\} \Rightarrow A_{inj}(t)\exp\{j\theta_{inj}(t)\}$$

Following Van der Pol [13], the device saturation and amplitude dependence of the negative resistance is modeled by a quadratic function such that $\left[1 - \dfrac{R_n(|V_{out}(t)|)}{R_L}\right] \Rightarrow -\mu(\alpha_0^2 - |V_{out}(t)|^2)$, where α_0 is free-running amplitude of the oscillation and μ is an empirical nonlinear parameter describing the oscillator. For uncoupled free-running oscillator $[V_{inj}(t) = 0]$, and the value of $\left[1 - \dfrac{R_n(|V_{out}(t)|)}{R_L}\right]$ is being zero ($R_n \rightarrow R_L$), whereas, for the case of the coupled oscillator $[V_{inj}(t) \neq 0]$, and the value of $\left[1 - \dfrac{R_n(|V_{out}(t)|)}{R_L}\right]$ is nonzero to compensate the additional energy being supplied due to the injection mechanism from the other neighboring oscillator.

From Equations (3.78) and (3.80),

$$\frac{\partial V_{out}(t)}{\partial t} = V_{out}(t)\left[\frac{\mu\omega_0}{2Q}(\alpha_0^2 - |V_{out}(t)|^2) + j\omega_0\right] + \frac{\omega_o}{2Q}V_{inj}(t) \qquad (3.81)$$

From Equations (3.77) and (3.81),

$$\left\{V_{out}(t)\left[\frac{\mu\omega_0}{2Q}(\alpha_0^2 - |V_{out}(t)|^2) + j\omega_0\right] + \frac{\omega_o}{2Q}V_{inj}(t)\right\} =$$

$$\left\{\left[\frac{\partial A(t)}{\partial t}\right][\exp j[\theta(t)]] + A(t)\left[\exp j[\theta(t)]\cdot\left\{\omega_0 + \frac{\partial\varphi(t)}{\partial t}\right\}\right]\right\} \qquad (3.82)$$

Amplitude and Phase Dynamics of the Coupled Oscillator

By equating real and imaginary part of the Equation (3.82), the amplitude and phase dynamics of the coupled oscillator system can be given as [30]

$$\frac{\partial A(t)}{\partial t} = \mu \left[\frac{\omega_0}{2Q} \right] A(t)(\alpha_0^2 - |A(t)|^2) + \left[\frac{\omega_o}{2Q} \right] A(t) \operatorname{Re}\left[\frac{V_{inj}(t)}{V_{out}(t)} \right] \rightarrow \text{Amplitude Dynamics} \qquad (3.83)$$

$$\frac{\partial \theta(t)}{\partial t} = \omega_o + \left[\frac{\omega_o}{2Q} \right] \operatorname{Im}\left[\frac{V_{inj}(t)}{V_{out}(t)} \right] \rightarrow \text{Phase Dynamics} \qquad (3.84)$$

For $|V_{out}(t)| \gg |V_{inj}(t)|$, the oscillator amplitude remains close to its free-running value and the system dynamics of the coupled oscillator is predominantly determined by the phase dynamics given by Equation (3.84).

From Equation (3.84),

$$\frac{\partial \theta(t)}{\partial t} = \omega_o + \left[\frac{\omega_o}{2Q} \right] \operatorname{Im}\left[\frac{V_{inj}(t)}{V_{out}(t)} \right] = \omega_o + \left[\frac{\omega_o}{2Q} \right] \operatorname{Im}\left[\frac{A_{inj}(t)\exp[j\theta_{inj}(t)]}{A(t)\exp[j\theta(t)]} \right] \qquad (3.85)$$

$$\frac{\partial \theta(t)}{\partial t} = \omega_o + \left[\frac{\omega_o}{2Q} \right]\left[\frac{A_{inj}(t)}{A(t)} \right] \sin[\theta_{inj}(t) - \theta(t)] \qquad (3.86)$$

$$\frac{\partial \theta(t)}{\partial t} = \omega_o + \left[\frac{\omega_o}{2Q} \right]\left[\frac{A_{inj}(t)}{A(t)} \right] \sin\{[\omega_{inj}t + \psi_{inj}(t)] - [\omega_0 t + \varphi(t)]\} \qquad (3.87)$$

$$\frac{\partial \theta(t)}{\partial t} = \omega_o + \left[\frac{\omega_o}{2Q} \right]\left[\frac{A_{inj}(t)}{A(t)} \right] \sin[(\omega_{inj} - \omega_0)t + (\psi_{inj}(t) - \varphi(t))] \qquad (3.88)$$

where
$$\theta_{inj}(t) = [\omega_{inj}t + \psi_{inj}(t)]; \theta(t) = [\omega_0 t + \varphi(t)] \text{ and } V_{out}(t) = A(t)\exp[j\theta(t)]$$

Locking Bandwidth of the Coupled Oscillator

In presence of the injection signal from the neighboring oscillator, oscillator locks onto the injected signal as $\frac{\partial \theta(t)}{\partial t} \rightarrow \omega_{inj}$ and at steady state, the equation of the phase dynamics

is given from (3.88) as

$$\frac{\partial \theta(t)}{\partial t} \to \omega_{inj} \Rightarrow \omega_{inj} = \omega_o + \left[\frac{\omega_o}{2Q}\right]\left[\frac{A_{inj}(t)}{A(t)}\right]Sin[\theta_{inj}(t) - \theta(t)] \tag{3.89}$$

From (3.89),

$$\omega_{inj} - \omega_o = \left[\frac{\omega_o}{2Q}\right]\left[\frac{A_{inj}(t)}{A(t)}\right]Sin[\theta_{inj}(t) - \theta(t)] \tag{3.90}$$

$$\left|\omega_{inj} - \omega_o\right| = \left|(\Delta\omega_{lock})Sin(\Delta\theta)\right| \tag{3.91}$$

where

$$\left|\Delta\omega_{lock}\right| = \left[\frac{\omega_o}{2Q}\right]\left|\frac{A_{inj}(t)}{A(t)}\right| = \left[\frac{\omega_o}{2Q}\right]\left[\frac{A_{inj}}{A}\right] \to \text{Locking Bandwidth}$$

$\Delta\theta = \theta_{inj}(t) - \theta(t) \to$ Steady-state phase difference between the oscillator and injected signal

From (3.90) and (3.91)

$$\left[\Delta\omega_{lock}\right]_{Locking-Bandwidth} \propto \frac{1}{Q} \tag{3.92}$$

From Equation (3.92), low Q-factor is required for wide locking range, but it will degrade the noise performance of the coupled oscillator system, therefore there is tradeoff between the phase noise and locking bandwidth of the VCOs.

From (3.91)

$$sin(\Delta\theta) = \left[\frac{\omega_{inj} - \omega_o}{\Delta\omega_{lock}}\right] \Rightarrow \Delta\theta = sin^{-1}\left[\frac{\omega_{inj} - \omega_o}{\Delta\omega_{lock}}\right], \quad -\frac{\pi}{2} \le \Delta\theta \le \frac{\pi}{2} \tag{3.93}$$

$$\omega_{inj} = \omega_o \pm \Delta\omega_{lock}, \quad \text{For } \Delta\theta = \pm\frac{\pi}{2} \tag{3.94}$$

$$\omega_{inj} - \omega_o = \pm\Delta\omega_{lock} \Rightarrow \left|\omega_{inj} - \omega_o\right| = \Delta\omega_{lock}, \quad \text{For } \Delta\theta = \pm\frac{\pi}{2} \tag{3.95}$$

From (3.94), the injected signal frequency ω_{inj} is tuned over the locking range of the oscillator $(\omega_o \pm \Delta\omega_{lock})$ and the associated phase difference $\Delta\theta$ varies from $-\frac{\pi}{2}$ to $+\frac{\pi}{2}$.

To determine locking mechanism [14], Equation (3.95) can be expressed as

$$\Delta\omega_{lock} > \left|\omega_{inj} - \omega_o\right|, \text{ for } -\frac{\pi}{2} < \Delta\theta < \frac{\pi}{2} \tag{3.96}$$

The oscillator can synchronize to an injected signal as long as $\Delta\omega_{lock} > \left|\omega_{inj} - \omega_o\right|$, where $\Delta\omega_{lock}$ represents half the entire locking range whereas, if the frequency of the injected signal ω_{inj} is such that $\Delta\omega_{lock} \leq \omega_{inj} - \omega_o$, then the oscillator cannot lock onto the injected signal and the nonlinearity of the oscillator will then generate mixing products in the coupled oscillator system.

3.4 Dynamics of N-Coupled Oscillators

As discussed in the section 3.3, the amplitude and phase dynamics of the mutually coupled oscillators are given by the Equations (3.83) and (3.84), which are based on the coupled set of differential equations and are derived by first describing the behavior of the individual oscillator with injection locking and then allowing the injection signals to be provided by the neighboring oscillator. The objective of this analysis is to develop general system dynamics of the N-coupled oscillators for bilateral coupling through N port arbitrary coupling network. Figure 3-8 shows the chain of the N-coupled oscillator system with bilateral coupling between the neighboring oscillators.

For N-coupled oscillator system, the coupling between i^{th} and j^{th} oscillators can be described by a coupling coefficient β_{ij} as

$$\beta_{ij} = \lambda_{ij} \exp[-j\varphi_{ij}] \tag{3.97}$$

where λ_{ij} and φ_{ij} is magnitude and phase of the coupling coefficient for the coupling between i^{th} and j^{th} oscillators in the N bilateral coupled oscillator systems. For reciprocal system, coupling coefficient is defined as $\beta_{ij} = \beta_{ji}$ and it is unitless.
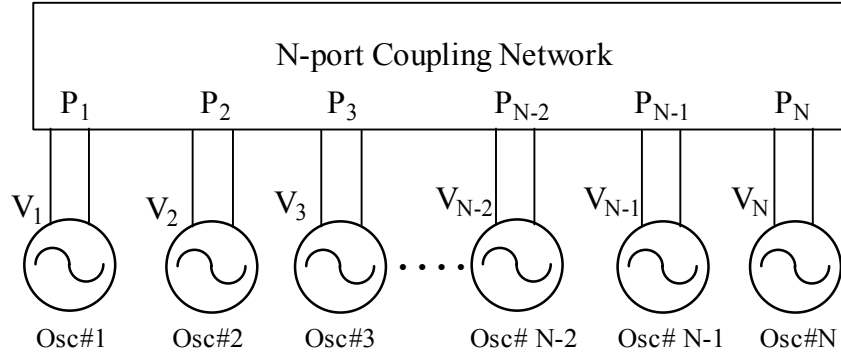
The injected signal $V_{inj}(t)$ seen by the ith oscillator for N-coupled oscillator system is given by

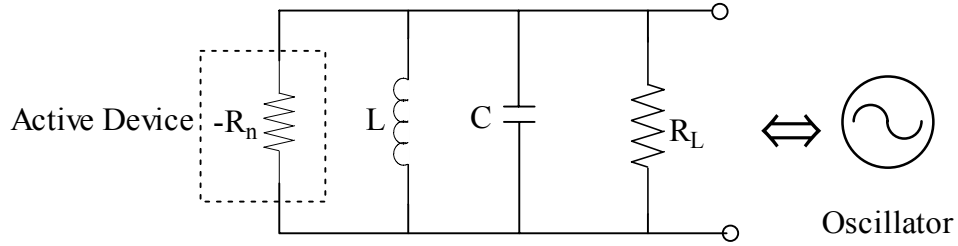$$V_{inj}(t) = \sum_{\substack{j=1 \\ j \neq i}}^{N} \beta_{ij} V_j(t) \tag{3.98}$$

where $V_j(t)$ is the output voltage of the jth oscillator.
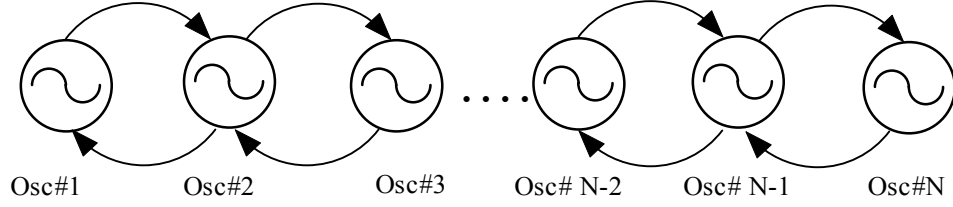
Figure 3-8: a) N-coupled oscillator with bilateral coupling b) N-coupled oscillator coupled through the N-port coupling network c) Equivalent parallel model of the free-running oscillator

Assuming all the N oscillators are having approximately same Q and μ factors, the coupled oscillator system dynamics can be given from (3-81) as

$$\frac{\partial V_i(t)}{\partial t} = V_i(t)\left[\frac{\mu\omega_i}{2Q}(\alpha_i^2 - |V_i(t)|^2) + j\omega_i\right] + \frac{\omega_i}{2Q}V_{inj}(t) \qquad (3.99)$$

After substituting the expression of $V_{inj}(t)$, Equation (3.99) can be rewritten as

$$\frac{\partial V_i(t)}{\partial t} = V_i(t)\left[\frac{\mu\omega_i}{2Q}(\alpha_i^2 - |V_i(t)|^2) + j\omega_i\right] + \frac{\omega_i}{2Q}\sum_{\substack{j=1 \\ j\neq i}}^{N}\beta_{ij}V_j(t) \qquad (3.100)$$

where $V_i(t)$ is the output voltage, α_i is the free-running amplitude and ω_i is the free-running frequency of the ith oscillator.

The output voltage $V_i(t)$ of the ith oscillator can be expressed as

$$V_i(t) = A_i(t)\exp\{j[\omega_i t + \varphi_i(t)]\} \Rightarrow A_i(t)\exp[j\theta_i(t)] \tag{3.101}$$

where $A_i(t)$ is the amplitude, and $\varphi_i(t)$ is the instantaneous phase of the ith oscillator.

From (3.101)

$$\frac{\partial V_i(t)}{\partial t} = j\left[\omega_i + \frac{\partial \varphi_i(t)}{\partial t} - j\frac{1}{A_i(t)}\frac{\partial A_i(t)}{\partial t}\right]V_i(t) \tag{3.102}$$

From Equations (3.100) and (3.102), the system dynamics of the N-coupled oscillator can be described in terms of amplitude and phase dynamics as

$$\frac{\partial A_i(t)}{\partial t} = A_i(t)\left[\frac{\mu\omega_i}{2Q}(\alpha_i^2 - |A_i(t)|^2)\right] + \frac{\omega_i}{2Q}\sum_{\substack{j=1\\j\neq i}}^{N}\lambda_{ij}A_j(t)\cos[\theta_i(t) - \theta_j(t) + \varphi_{ij}]; i = 1,2,3....N \tag{3.103}$$

$$\frac{\partial \theta_i(t)}{\partial t} = \omega_i - \left[\frac{\omega_i}{2Q}\right]\left\{\sum_{\substack{j=1\\j\neq i}}^{N}\lambda_{ij}\left[\frac{A_j(t)}{A_i(t)}\right]\sin[\theta_i(t) - \theta_j(t) + \varphi_{ij}]\right\} ; i = 1,2,3....N \tag{3.104}$$

Coupling Parameters

For $\lambda_{ij} \to 0$ (Zero coupling):

System dynamics of the N-coupled oscillators is reduced to dynamics of uncoupled free-running oscillators and can be given from Equations (3.103) and (3.104) as

$$\left[\frac{\partial A_i(t)}{\partial t}\right]_{\lambda_{ij}=0} = A_i(t)\left[\frac{\mu\omega_i}{2Q}(\alpha_i^2 - |A_i(t)|^2)\right]; i = 1,2,3....N \tag{3.105}$$

$$\left[\frac{\partial \theta_i(t)}{\partial t}\right]_{\lambda_{ij}=0} = \omega_i; i = 1,2,3....N \tag{3.106}$$

Equation (3.105) and (3.106) are the time dynamics of the set of individual oscillators with amplitudes $A_i(t)$ and frequencies ω_i and can be considered as a generalized version of the Adler's Equation [14], and the basis for the formulation of the system dynamics of the N-coupled oscillators.

For $1 \gg \lambda_{ij} > 0$ (Weak coupling):

The amplitude of the oscillators in the N-coupled oscillator system remains close to its free-running values $(A_i = \alpha_i, A_j = \alpha_j)$ and the system dynamics of the N-coupled oscillators essentially governed and influenced by the phase dynamics as given in Equation (3.104).

For $1 \gg \lambda_{ij} > 0$, Equation (3.104) can be rewritten as

$$\frac{\partial \theta_i(t)}{\partial t} = \omega_i - \left[\frac{\omega_i}{2Q}\right]\left\{\sum_{\substack{j=1 \\ j \neq i}}^{N} \lambda_{ij}\left[\frac{\alpha_j}{\alpha_i}\right]\sin[\theta_i(t) - \theta_j(t) + \varphi_{ij}]\right\}; i = 1,2,3....N \qquad (3.107)$$

Synchronized Coupled Oscillator Frequency

In this case $(1 \gg \lambda_{ij} > 0)$ the oscillators in the N-coupled oscillator system may lock to a single frequency ω_s.

For $(1 \gg \lambda_{ij} > 0)$, under the synchronization to a common frequency $\rightarrow \omega_s$, the value of $\frac{\partial \theta_i(t)}{\partial t}$ can be given by

$$\left[\frac{\partial \theta_i(t)}{\partial t}\right]_{i=1,2,3...N} \rightarrow \omega_s \qquad (3.108)$$

From Equation (3.107) and (3.108), the steady-state synchronized frequency ω_s is given by

$$\omega_s = \omega_i - \left[\frac{\omega_i}{2Q}\right]\left\{\sum_{\substack{j=1 \\ j \neq i}}^{N} \lambda_{ij}\left[\frac{\alpha_j}{\alpha_i}\right]\sin[\theta_i(t) - \theta_j(t) + \varphi_{ij}]\right\}; i = 1,2,3....N \qquad (3.109)$$

Chapter 4

Noise Analysis of the Oscillators

4.1   Oscillator Noise

Noise is associated with all the components of the oscillator circuit, however the major contribution of the noise in an oscillator is from the active device, which introduces AM (amplitude modulation) noise and PM (phase modulation) noise. The AM component of the noise is generally ignored because the gain limiting effects of the active device operating under saturation, allowing only little variation in the output amplitude due to the noise in comparison to PM noise component, which directly affects the frequency stability of the oscillator and creates noise sidebands. To have a better insight of the noise effects in the oscillator design, it is necessary to understand how the noise arises in a transistor. The designer has very limited control over the noise sources in a transistor, only being able to control the device selection and the operating bias point. However, using knowledge about how noise affects oscillator waveforms, the designer is able to substantially improve phase-noise performance by the optimization of the conduction angle and drive-level.

Source of Noise

There are mainly two types of noise sources in oscillator circuit: broadband noise sources due to thermal and shot noise effects and the low-frequency noise source due to $1/f$ (flicker noise effects) characteristics. The current flow in a transistor is not a continuous process but is made up of the diffusive flow of large number of discrete carriers and the motions of theses carriers are random and explains the noise phenomenon. The thermal fluctuation in the minority carrier flow and generation-recombination processes in the semiconductor device generates thermal noise, shot noise, partition-noise, burst noise and $1/f$ noise.

Figure 4-1(a) shows the equivalent schematic of the bipolar transistor in a grounded emitter configuration, and the high frequency noise of a silicon bipolar transistor in common emitter configuration can be modeled by using the three noise sources as shown in equivalent schematic (hybrid-π) in Figure 4-1(b).

The emitter junction in this case is conductive and this generates shot noise on the emitter. The emitter current is divided in to a base (I_b) and a collector current (I_c) and both these currents generate shot noise. There is the collector reverse current (I_{cob}), which also generates shot noise. The emitter, base and collector are made of semiconductor material and have finite value of resistance associated with them, which generates thermal noise.
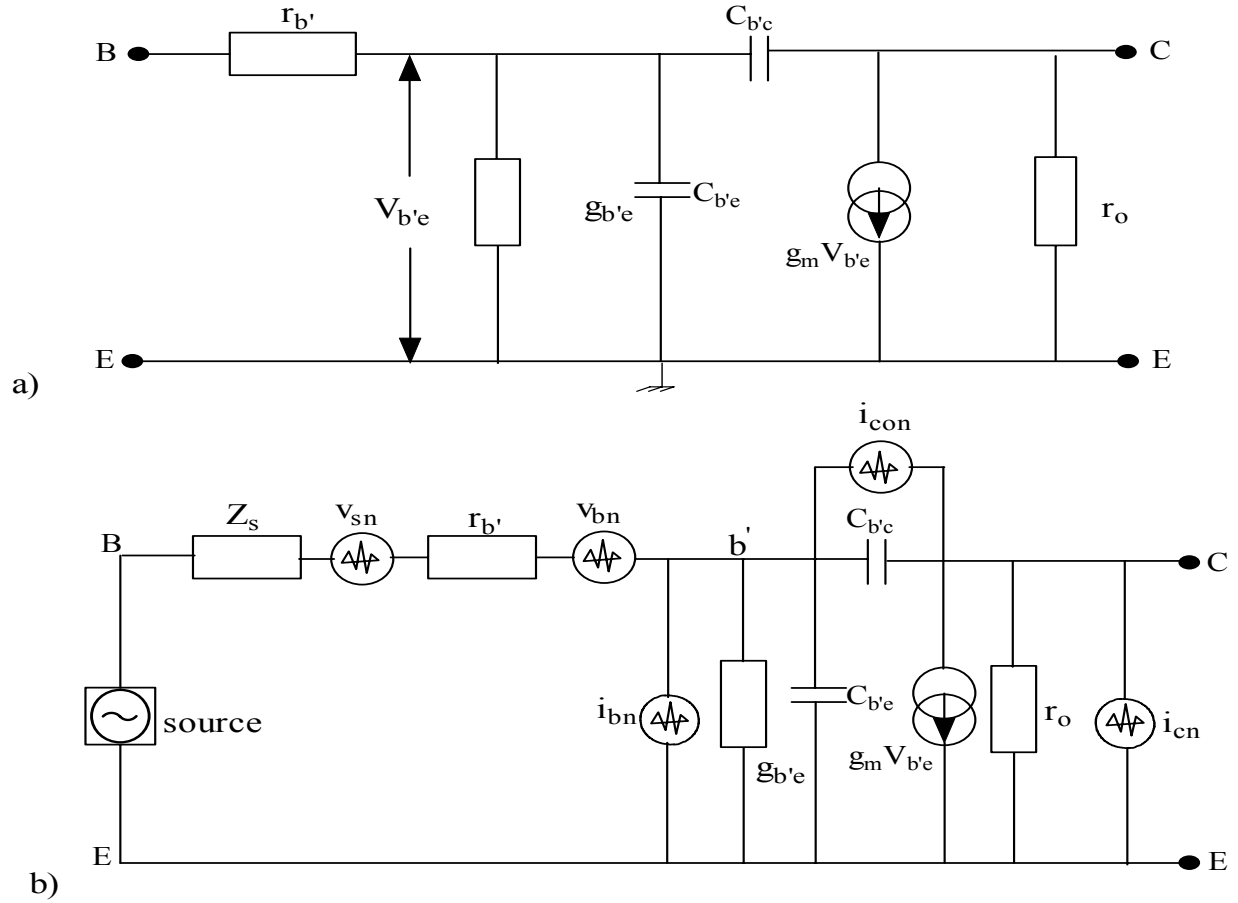
Figure 4-1: a) π- configuration of the GE-bipolar transistor and b) π- configuration of CE-bipolar transistor with noise sources.

The value of the base resistor is relatively high in comparison to resistance associated with emitter and collector, so the noise contribution of these resistors can be neglected. For noise analysis three sources are introduced in a noiseless transistor and these noise generators are due to fluctuation in DC bias current (i_{bn}), DC collector current (i_{cn}) and thermal noise of the base resistance (v_{bn}). In Silicon transistor the collector reverse current (I_{cob}) is very small and noise (i_{con}) generated due to this can be neglected.

For the evaluation of the noise performances, the signal-driving source should also be taken into consideration because its internal conductance generates noise and its susceptance affects the noise figure through noise tuning.

The mean square values of the noise generator in a narrow frequency interval Δf is given by

$$\overline{i_{bn}^2} = 2qI_b\Delta f \tag{4.1}$$

42

$$\overline{i_{cn}^2} = 2qI_c\Delta f \tag{4.2}$$

$$\overline{i_{con}^2} = 2qI_{cob}\Delta f \tag{4.3}$$

$$\overline{v_{bn}^2} = 4kTr_b'\Delta f \tag{4.4}$$

$$\overline{v_{sn}^2} = 4kTR_s\Delta f \tag{4.5}$$

I_b, I_c and I_{cob} are average DC current over Δf noise bandwidth. The noise power spectral densities due to noise sources is given as

$$S(i_{cn}) = \frac{\overline{i_{cn}^2}}{\Delta f} = 2qI_c = 2KTg_m \tag{4.6}$$

$$S(i_{bn}) = \frac{\overline{i_{bn}^2}}{\Delta f} = 2qI_b = \frac{2KTg_m}{\beta} \tag{4.7}$$

$$S(v_{bn}) = \frac{\overline{v_{bn}^2}}{\Delta f} = 4KTr_b' \tag{4.8}$$

$$S(v_{sn}) = \frac{\overline{v_{sn}^2}}{\Delta f} = 4KTR_s \tag{4.9}$$

r_b' and R_s are base and source resistance and Z_s is the complex source impedance.

Oscillator Noise Model Comments

The phenomenon of phase noise generation in oscillators/VCOs has been the main focus of important research efforts, and it is still an open issue despite significant gains in practical experience and modern CAD tools for design. In the design of VCOs, minimizing the phase noise is the prime task and these objectives have been accomplished using empirical rules or numerical optimizations, and to this end, are often held as trade secrets by many manufacturers. The ability to achieve optimum phase noise performance is paramount in most RF design and the continued improvement of phase noise in oscillators is required for the efficient use of frequency spectrum. The degree to which an oscillator generates constant frequency throughout a specified period of time is defined as the frequency stability of the oscillator and the cause of the frequency instability is due to the presence of noise in the oscillator circuit that effectively modulates the signal, causing a change in frequency spectrum commonly known as phase noise. Phase noise and timing jitter are both measures of uncertainty in the output of an oscillator. Phase noise defines the frequency domain uncertainty of an oscillator, whereas timing jitter is a measure of oscillator uncertainty in the time domain.

The Equation for ideal sinusoidal oscillator in time domain is given by

$$V_{out}(t) = A\cos(2\pi f_0 t + \varphi) \qquad (4.10)$$

where A, f_0 and φ are the amplitude, frequency and fixed phase of the oscillator.

The Equation of the real oscillator in time domain is given by

$$V_{out}(t) = A(t)\cos[2\pi f_0 t + \varphi(t)] \qquad (4.11)$$

where $A(t)$, f_0 and $\varphi(t)$ are the time variable-amplitude, frequency and time variable-phase of the oscillator.

Figure 4-2 (a) and (b) illustrate the frequency spectrum of ideal and real oscillators, and the frequency fluctuation corresponding to jitter in the time domain, which is random perturbation of the zero crossing of a periodic signal.

a) Ideal Oscillator (Time domain)   Frequency domain

b) Real oscillator (Time domain:Jitter)   Frequency domain
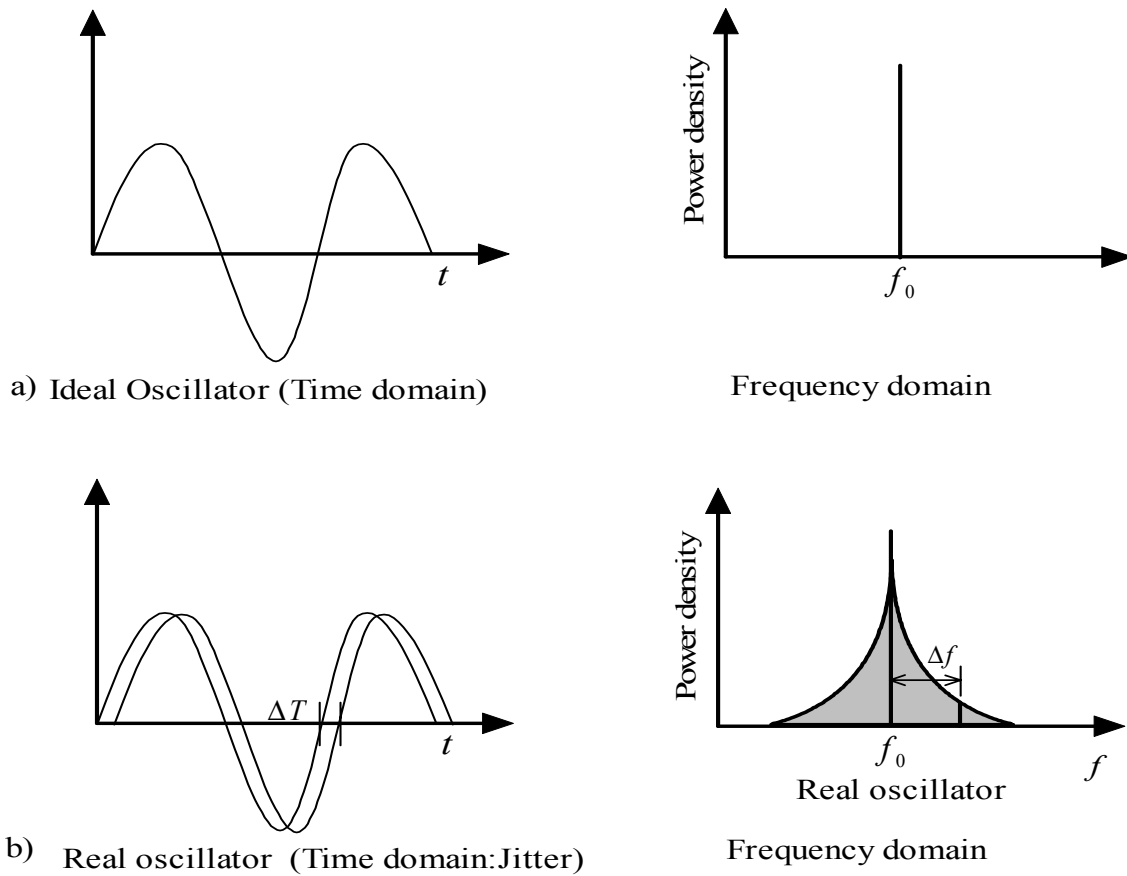
Fig 4-2: (a) Frequency spectrum of ideal and real oscillators and (b) Jitter in time domain relates to phase noise in the frequency domain.

From Equations (4.10) and (4.11), the fluctuation introduced by $A(t)$ and $\varphi(t)$ are functions of time and lead to sidebands around the center frequency f_0. In the frequency domain the spectrum of the oscillator consists of Dirac-impulses at $\pm f_0$

At present, three separate, but closely related, models of the oscillator phase noise exist. The first is proposed by Leeson [15], which is referred to as Leeson's model, and the noise prediction using Leeson's model is based on LTIV (Linear-time-invariant) properties of the oscillator, such as resonator Q, feedback gain, output power, and noise figure; the second is proposed by Lee and Hajimiri [16], based on time-varying properties of the oscillator RF current waveform; and the third is proposed by Rohde [11], based on the signal drive level and the conduction angle of the time-varying properties of the oscillator current waveform.

Leeson's Noise Model

Leeson's phase noise equation is given by

$$\pounds(f_m) = 10\log\left\{\left[1+\frac{f_0^2}{(2f_mQ_L)^2(1-\frac{Q_L}{Q_0})^2}\right]\left(1+\frac{f_c}{f_m}\right)\frac{FkT}{2P_o}+\frac{2kTRK_0^2}{f_m^2}\right\} \qquad (4.13)$$

$\pounds(f_m)$ = ratio of sideband power in a 1Hz bandwidth at f_m to total power in dB
f_m = frequency offset from the carrier
f_0 = center frequency
f_c = flicker frequency
Q_L = loaded Q of the tuned circuit
Q_0 = unloaded Q of the tuned circuit
F = noise factor
$kT = 4.1 \times 10^{-21}$ at 300 K (room temperature)
P_o = average power at oscillator output
R = equivalent noise resistance of tuning diode
K_0 = oscillator voltage gain

It is important to understand that the Leeson model is based on linear time invariant characteristics (LTIV) and is the best case since it assumes the tuned circuit filters out of all the harmonics. In all practical cases, it is hard to predict what the operating Q and noise figure will be. The predictive power of the Leeson model is limited due to the following which is not known prior to measurement: the output power, the noise figure under large signal conditions, and the loaded Q. This classic paper [15] is still an extraordinarily good design guide. The advantage of this approach is the fact that it is easy to understand and leads to a good approximation of the phase noise. The drawback

of this approach is the fact that the values for the flicker noise contribution, which is a necessary input to the equation; the RF output power, the loaded Q, and the noise factor of the amplifier under large signal condition, are not known.

Lee and Hajimiri's Noise Model

Lee and Hajimiri's noise model [16] is based on the nonlinear time varying [NLTV] properties of the oscillator current waveform, and the phase noise analysis is given based on the effect of noise impulse on a periodic signal. Figure 4-3 shows the noise signal in response of the injected impulse current at two different times, peak and zero crossing.
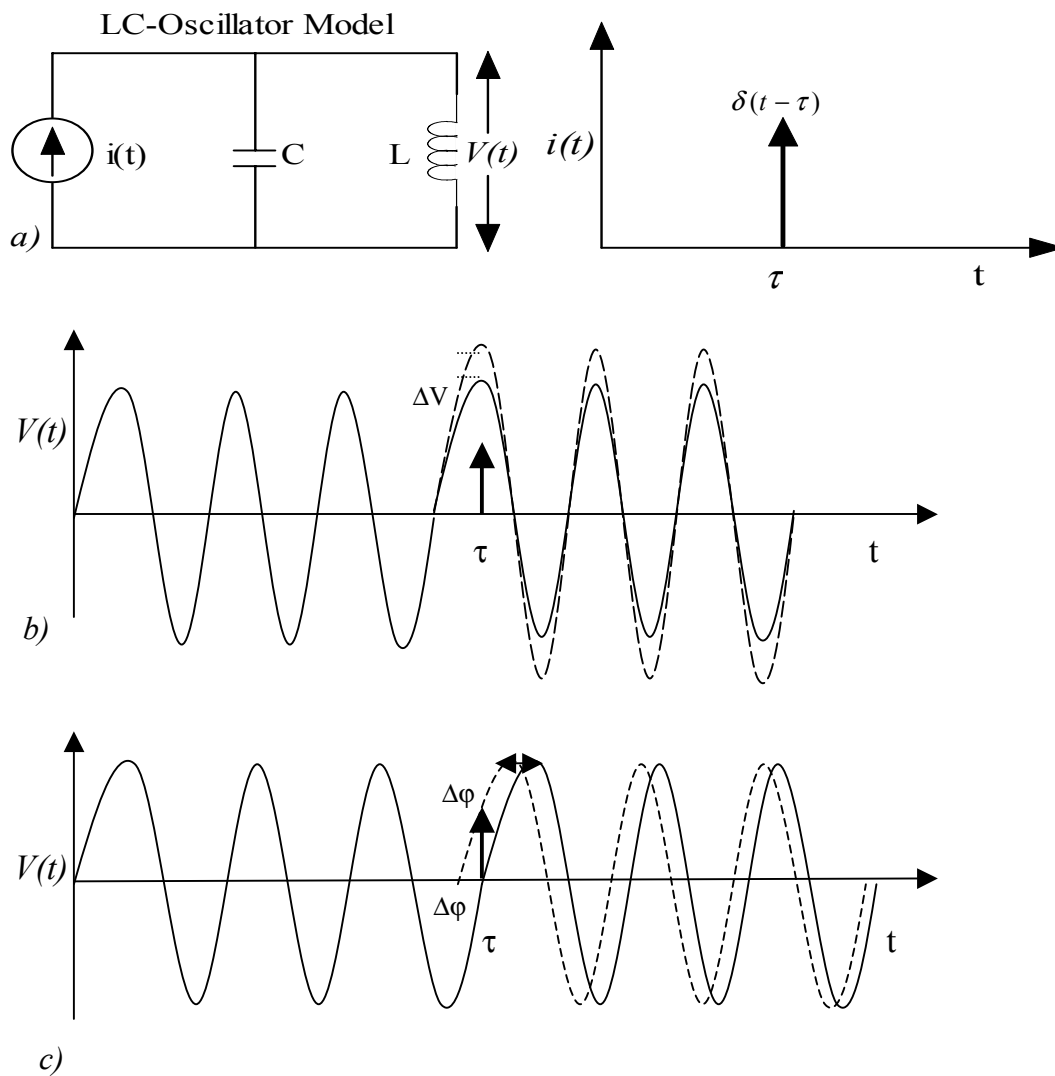
Figure 4-3: a) LC oscillator excited by current pulse b) Impulse injected at peak of the oscillation signal and c) Impulse injected at zero crossing of the oscillation signal.

46

As illustrated in Figure 4-3, if an impulse is injected into the tuned circuit at the peak of the signal, it will cause maximum amplitude modulation and no phase modulation whereas; if an impulse is injected at the zero crossing of the signal, there will be no amplitude modulation but maximum phase modulation. If noise impulses are injected between zero crossing and the peak, there will be components of both phase and amplitude modulation. Variations in amplitude are generally ignored because they are limited by the gain control mechanism of the oscillator. Therefore, according to this theory, to obtain the minimal phase noise, special techniques have to be adopted so that any noise impulse should coincide in time with the peaks of the output voltage signal rather than at the zero crossing or in between of zero-crossing and peak.

Lee and Hajimiri introduced an impulse sensitivity function (ISF) based on injected impulse, which is different for each topology of the oscillator. It has its largest value when the most phase modulation occurs and has the smallest value when only amplitude modulation occurs. The calculation of the ISF is tedious and depends upon the topology of the oscillator. Based on this theory, phase noise equation is expressed as [16]

$$\pounds(f_m) = \begin{cases} 10\log\left[\dfrac{C_0^{\,2}}{q_{max}^2} * \dfrac{i_n^{\,2}/\Delta f}{8f_m^2} * \dfrac{\omega_{1/f}}{f_m}\right] & \dfrac{1}{f^3} \rightarrow region \\[4ex] 10\log\left[10\log\left[\dfrac{\Gamma_{rms}^{\,2}}{q_{max}^2} * \dfrac{i_n^{\,2}/\Delta f}{4f_m^2}\right]\right] & \dfrac{1}{f^2} \rightarrow region \end{cases} \tag{4.14}$$

where

$i_n^{\,2}/\Delta f$ = Noise power spectral density

Δf = Noise bandwidth

$\Gamma_{rms}^2 = \dfrac{1}{\pi}\int_0^{2\pi}|\Gamma(x)|^2 dx = \sum_{n=0}^{\infty} C_n^2$ = Root mean square (RMS) value of $\Gamma(x)$

$\Gamma(x) = \dfrac{C_0}{2} + \sum_{n=1}^{\infty} C_n Cos(nx + \theta_n)$ = Impulse Sensitivity function (ISF)

C_n = Fourier series coefficient

C_0 = 0th order of the ISF (Fourier series coefficient)

θ_n = Phase of the nth harmonic

f_m = Offset frequency from the carrier

$\omega_{1/f}$ = Flicker corner frequency of the device

q_{max} = Maximum charge stored across the capacitor in the resonator.

Equation (4.14) gives good results once all the data is known, but does not lead to exact design rules.

Rohde's Noise Model

The implication of Lee and Hajimiri's theory is that the designer does not have much control in terms of the oscillator circuit component parameters over the timing of the noise impulse injected into the oscillator circuit. Rohde's [11] proposed noise model, is based on the signal drive level and the conduction angle of the time-varying properties of the oscillator current waveform and the phase noise equation, is explicitly expressed in terms of the oscillator circuit parameters. Since the signal drive voltage produces an output current consisting of a series of current pulses, it's shape and conduction angle depends upon the strength of the signal drive level. Figure 4-4 shows the typical noise current i_{noise} relative to the RF current i_c for a LC-Colpitts oscillator in presence of resonator signal voltage $v_{resonator}$.
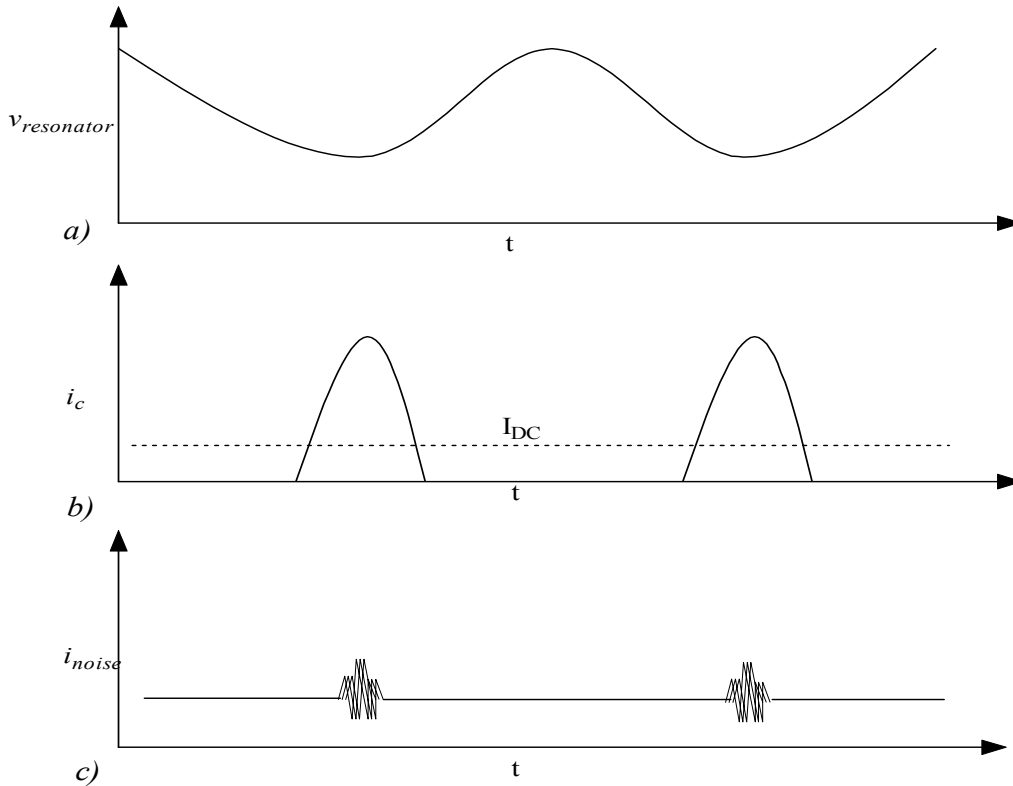
Figure 4-4: a) voltage across resonator b) oscillator RF current c) noise current.

The natural operation of the oscillator will cause the current pulses to be centered on the negative peaks of the resonator tank voltages and the associated noise components depend on the conduction angle (width of the RF current pulse). From Rohde's noise model, the conduction angle φ ($\varphi \propto \dfrac{1}{C_2}$) is inversely proportional to the feedback capacitor C_2, and directly proportional to the drive-level x ($x \propto C_2$). The following example given in the Figure 4-5 illustrates the circuit diagram of the 100 MHz LC

Colpitts oscillator for giving insight into the relationship between the drive level, the current pulse, and the phase noise. As shown in Figure 4-4, the majority of noise current exists only during collector current pulses and the oscillator output current will be negligible or zero during the time between output current pulses, and therefore, aside from thermal noise, the noise sources, which depend on current such as shot, partition, and 1/f, exist only during the conducting angle of output current pulses. If the signal drive level is increased, the oscillator output current pulse will be narrower, and consequently, noise pulse during conduction angle also becomes narrowed, and thereby, has less PM noise contribution than the wider pulse.
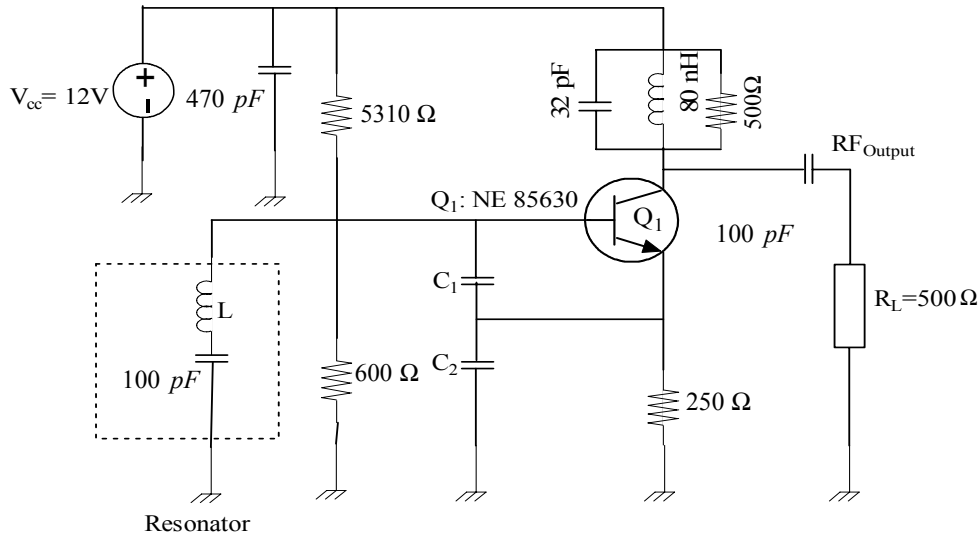
Figure 4-5: Schematic of 100 MHz LC Colpitts oscillator.

Table 4-1 shows the drive level for different values of C_2 for a 100 MHz oscillator.

Table 4-1 Drive level for different values of C_2 for a 100MHz Oscillator.

$x = \dfrac{qV_{base}}{kT}$	C_1	C_2	L	Phase Noise @10KHz offset	Frequency
3	500pF	50pF	80nH	-98dBc/Hz	100MHz
10	500pF	100pF	55nH	-113dBc/Hz	100MHz
15	500pF	150pF	47nH	-125dBc/Hz	100MHz
20	500pF	200pF	42nH	-125dBc/Hz	100MHz

The collector current of the circuit shown in the Figure 4-5 is plotted in Figure 4-6, becomes narrower as the drive level x increases, and the corresponding base voltage V_{base} swing increases as illustrated in Figure 4-7. The improvement in the phase noise, with respect to the drive level, is shown in Figure 4-8, and it is limited by the strong harmonic content due to the large signal drive level.
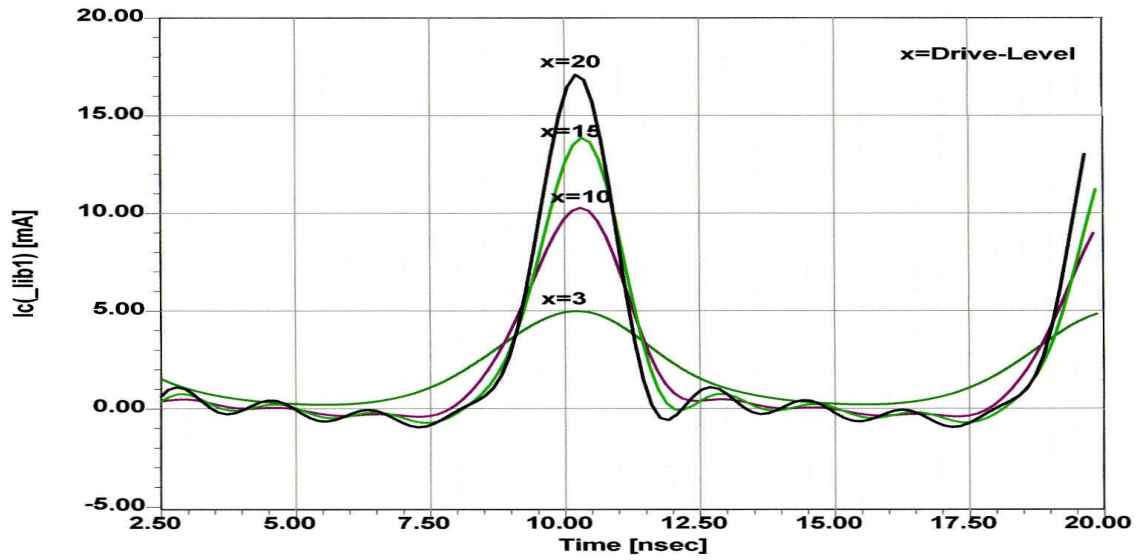
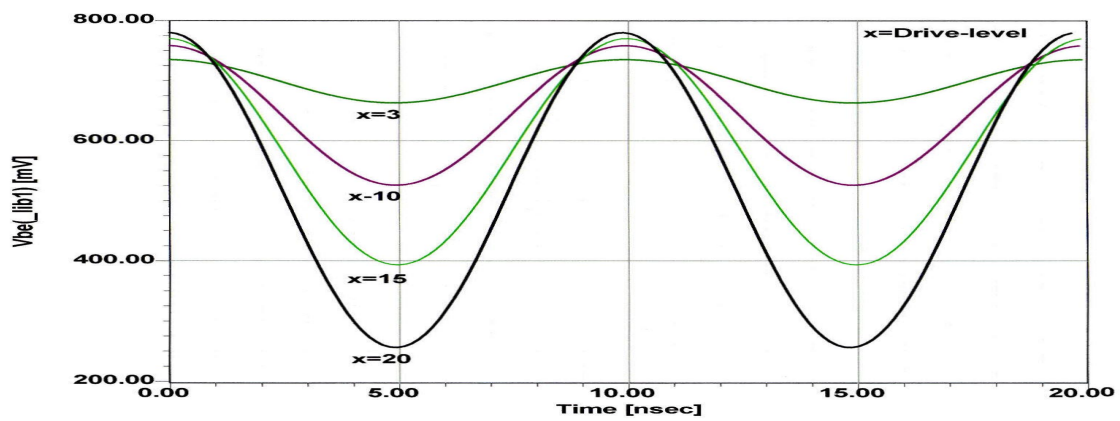Figure 4-6: RF current as a function of the normalized drive level x for the circuit in Figure 4-5.

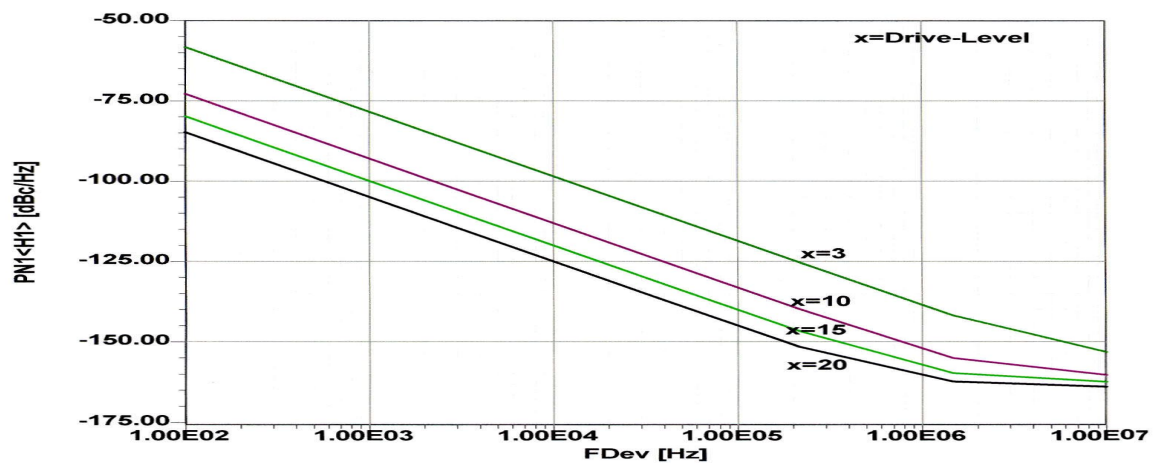Figure 4-7: RF voltage V_{be} across the base emitter as a function of the normalized drive level x.

Figure 4-8: Phase noise as a function of the normalized drive level x for the circuit in Figure 4-5.

50

Based on this theory, phase noise equation is expressed as (Appendix C),

$$\pounds(\omega) = 10 Log \left\{ \left[\left[4kTR + \left[\frac{4qI_c g_m^2 + \frac{K_f I_b^{AF}}{\omega} g_m^2}{\omega_0^2 C_1^2 (\omega_0^2 (\beta^+)^2 C_2^2 + g_m^2 \frac{C_2^2}{C_1^2})} \right] \right] \left[\frac{\omega_0^2}{4\omega^2 V_{cc}^2} \right] \left[\frac{1}{Q_L^2} + \frac{[C_1 + C_2]^2}{C_1^2 C_2^2 \omega_0^4 L^2} \right] \right\} 4.15) $$

where

$$\beta^+ = \left[\frac{Y_{21}^+}{Y_{11}^+} \right] \left[\frac{C_1}{C_2} \right]^p$$

$$g_m = \left[Y_{21}^+ \right] \left[\frac{C_1}{C_2} \right]^q \; ; \text{Values of p and q depends upon the drive level [11]}$$

Y_{21}^+, Y_{11}^+ = large signal [Y] parameter of the active device
K_f = flicker noise coefficient
AF = flicker noise exponent
$\pounds(\omega)$ = ratio of sideband power in a 1Hz BW at ω to total power in dB
ω = frequency offset from the carrier
ω_0 = center frequency
Q_L = loaded Q of the tuned circuit
kT = 4.1×10^{-21} at 300 K (room temperature)
R = equivalent loss resistance of the tuned resonator circuit
I_c = RF collector current
I_b = RF base current
V_{cc} = RF collector voltage
C_1, C_2 = feedback capacitor as shown in Figure 4-5.

Equation (4.15) gives better insight and apriori estimation of the phase noise in terms of the operating condition and circuit parameters. However, all three noise models discuss and point out about the free-running oscillator and do not explain the phase noise improvement characteristics in the mutually coupled oscillator systems; therefore, suggesting the need for noise analysis for coupled oscillators/VCOs.

4.2   Noise Analysis of Uncoupled Oscillators

The following noise analysis for the oscillator is based on the approach [24], is an attempt to introduce the concept of the reduction in the phase noise in the mutually coupled oscillator systems. The purpose of this section is to provide the basic noise equation for the uncoupled free-running oscillator/VCO and the same can be extended for the mutually coupled oscillator and N-coupled oscillator systems.

Figure 4-9 shows the negative resistance series tuned model of the oscillator; Z_d is the active device impedance plus loss resistance associated with the oscillator circuit; Z_r is the resonator impedance and $e_n(t)$ is the noise perturbation.
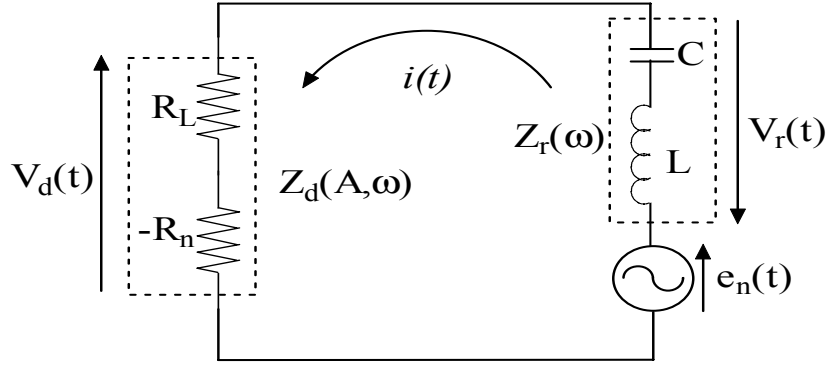

Figure 4-9: Negative resistance series tuned model of oscillator.

From the Kirchoff voltage law (KVL), the circuit equation of the Figure 4-9 is given by nonhomogeneous differential equation as

$$L\frac{\partial i(t)}{\partial t} + \frac{1}{C}\int i(t)dt + [R_L - R_n]i(t) = e_n(t) \tag{4.16}$$

defining $e(t)$ as

$$e(t) = e_n(t)e^{-j(\omega_0 t + \Delta\varphi)} \tag{4.17}$$

$$V_d(t) + V_r(t) = e_n(t) \Rightarrow e_n(t)e^{-j\omega_0 t} = e^{-j\omega_0 t}[V_d(t) + V_r(t)] \tag{4.18}$$

Equation (4.18) can be expressed in the frequency domain as

$$V_r(\omega) + V_d(\omega) = e(\omega) = Z(\omega, A)I(\omega) \tag{4.19}$$

The circuit impedance of the Figure 4-9 can be given by

$$Z(\omega, A) = Z_d(\omega, A) + Z_r(\omega) \tag{4.20}$$

Assuming the device impedance is a function of the amplitude of the RF current, but has less variation with frequency and is assumed to be frequency independent to the first order, Equation (4.20) can be rewritten as

$$Z(\omega, A) = Z_d(A) + Z_r(\omega) \tag{4.21}$$

defining,

$$\frac{\partial Z(\omega,A)}{\partial \omega}\bigg|_{\omega_0} = \frac{\partial Z_r(\omega)}{\partial \omega}\bigg|_{\omega_0} = \dot{Z}_{\omega_0} = \left|\dot{Z}_{\omega_0}\right|e^{j\alpha}; \text{ and } \frac{\partial Z(\omega,A)}{\partial A}\bigg|_{A_0} = \frac{\partial Z_d(A)}{\partial A}\bigg|_{A_0} = \dot{Z}_{A_0} = \left|\dot{Z}_{A_0}\right|e^{j\beta}$$

where α and β are defined as the phase associated with resonator and device circuit parameters.

In presence of the noise perturbation $e_n(t)$, the oscillator current $i(t)$ in Figure 4-9 can be expressed as

$$i(t) = A(t)e^{j\omega_0 t} \Rightarrow i(t)\big|_{e_n(t)=0} = A_0 e^{j\omega_0 t} \tag{4.22}$$

$A(t)$ is defined as, $A(t) = [A_0 + \Delta A(t)]e^{j\Delta\varphi(t)} = A_0\left[1 + \frac{\Delta A(t)}{A_0}\right]e^{j\Delta\varphi(t)}$ (4.23)

where ω_0 is free-running frequency, $\Delta A(t)$ and $\Delta\varphi(t)$ are the fluctuations in amplitude and phase of the oscillator.

The Fourier transform of $i(t)$ is given from time domain Equation (4.22) as

$$I(\omega) = \int_{-\infty}^{+\infty} i(t)e^{-j\omega t}dt = \int_{-\infty}^{+\infty} A(t)e^{j\omega_0 t}e^{-j\omega t}dt \tag{4.24}$$

The Fourier transform of $A(t)$ is given by

$$A(\omega) = \int_{-\infty}^{+\infty} A(t)e^{-j\omega t}dt \tag{4.25}$$

Voltage across Z_r is given by

$$V_r(t) = \int_{-\infty}^{+\infty} V_r(\omega)e^{j\omega t}d\omega = \int_{-\infty}^{+\infty} A(\omega)e^{j(\omega+\omega_0)t}Z_r(\omega+\omega_0)d\omega \tag{4.26}$$

Expanding Equation (4.26) around ω_0 [28],

$$V_r(t) = e^{j\omega_0 t}\left[Z_r(\omega_0)\int_{-\infty}^{+\infty} A(\omega)e^{j\omega t}d\omega + \frac{\partial Z_r}{\partial \omega}\bigg|_{\omega_0}\int_{-\infty}^{+\infty}\omega A(\omega)e^{j\omega t}d\omega + \frac{1}{2}\frac{\partial^2 Z_r}{\partial \omega^2}\bigg|_{\omega_0}\int_{-\infty}^{+\infty}\omega^2 A(\omega)e^{j\omega t}d\omega + ...\right] \tag{4.27}$$

From Equations (4.25) and (4.27),

$$V_r(t) = e^{j\omega_0 t}\left[Z_r(\omega_0)A(t) - j\left.\frac{\partial Z_r}{\partial\omega}\right|_{\omega_0}\frac{dA(t)}{dt} - \frac{1}{2}\left.\frac{\partial^2 Z_r}{\partial\omega^2}\right|_{\omega_0}\frac{d^2 A(t)}{dt^2} + \cdots \right] \qquad (4.28)$$

similarly,

$$V_d(t) = e^{j\omega_0 t}\left[Z_d(A_0)A(t) + A(t)\left.\frac{\partial Z_d}{\partial A}\right|_{A_0}\Delta A(t) + \cdots \right] \qquad (4.29)$$

From Equation (4.23),

$$\frac{dA(t)}{dt} = \left[\frac{d[\Delta A(t)]}{dt} + j[A_0 + \Delta A(t)]\frac{d[\Delta\varphi(t)]}{dt} \right]e^{j\Delta\varphi(t)} \qquad (4.30)$$

From Equations (4.16), (4.17), (4.28), (4.29) and (4.30),

$$e_n(t)e^{-j\omega_0 t} = e^{j\Delta\varphi(t)}\left[A_0 Z(A_0,\omega_0) - j\dot{Z}_{\omega_0}\left(\frac{d[\Delta A(t)]}{dt} + jA_0\frac{d[\Delta\varphi(t)]}{dt} \right) + \dot{Z}_{A_0}A_0[\Delta A(t)] \right]$$

$$\Rightarrow e(t) = e_n(t)e^{-j(\omega_0 t + \Delta\varphi)} = \left[A_0 Z(A_0,\omega_0) - j\dot{Z}_{\omega_0}\left(\frac{d[\Delta A(t)]}{dt} + jA_0\frac{d[\Delta\varphi(t)]}{dt} \right) + \dot{Z}_{A_0}A_0[\Delta A(t)] \right] \quad (4.31)$$

For the case of free-running noiseless oscillator $e_n(t) \to 0$, Equation (4.31) can be rewritten as

$$\left[A_0 Z(A_0,\omega_0) - j\dot{Z}_{\omega_0}\left(\frac{d[\Delta A(t)]}{dt} + jA_0\frac{d[\Delta\varphi(t)]}{dt} \right) + \dot{Z}_{A_0}A_0[\Delta A(t)] \right] = 0 \qquad (4.32)$$

At a stable point of operation the amplitude of the oscillator is constant and the phase difference does not change with the time i.e. $\frac{d[\Delta\varphi(t)]}{dt} = 0$ and $\Delta A(t) = 0$.

From (4.20), the condition for oscillation, the loss resistance is compensated by the negative resistance of the active device at resonance frequency $\omega = \omega_0$, $Z(\omega_0, A_0) \to 0$, and Equation (4.32) is reduced to

$$\left[\dot{Z}_{A_0}A_0[\Delta A(t)] - j\dot{Z}_{\omega_0}\left(\frac{d[\Delta A(t)]}{dt} + jA_0\frac{d[\Delta\varphi(t)]}{dt} \right) \right] = 0 \qquad (4.33)$$

From (4.17) and (4.31),

$$e(t) = e_n(t)e^{-j[\omega_0 + \Delta\varphi(t)]} = \left[A_0 Z(A_0, \omega_0) - j\dot{Z}_{\omega_0}\left(\frac{d[\Delta A(t)]}{dt} + jA_0\frac{d[\Delta\varphi(t)]}{dt} \right) + \dot{Z}_{A_0} A_0[\Delta A(t)] \right] \qquad (4.34)$$

At the oscillator resonance frequency, Equation (4.34) can be expressed as

$$e(t) = A_0 \frac{\partial Z(\omega, A)}{\partial A}[\Delta A(t)] - j\frac{\partial Z(\omega, A)}{\partial \omega}\left(\frac{d[\Delta A(t)]}{dt} + jA_0\frac{d[\Delta\varphi(t)]}{dt} \right) \qquad (4.35)$$

Now let us consider the noise perturbation $e(t)$ being a narrow-band noise signal and can be decomposed into quadrature components $e_{n1}(t)$ and $e_{n2}(t)$, and for simplification in analysis we assumed they are uncorrelated as shown in Figure 4-10.

$$e(t) = e_{n1}(t) + e_{n2}(t) \qquad (4\text{-}36)$$

We define $e_{n1}(t) = e_1(t)\sin[\omega_0 t + \varphi(t)]$ and $e_{n2}(t) = -e_2(t)\cos[\omega_0 t + \varphi(t)]$, where $e_{n1}(t)$ and $e_{n2}(t)$ are orthogonal functions, and $e_1(t)$ and $e_2(t)$ are slowly varying function of time.

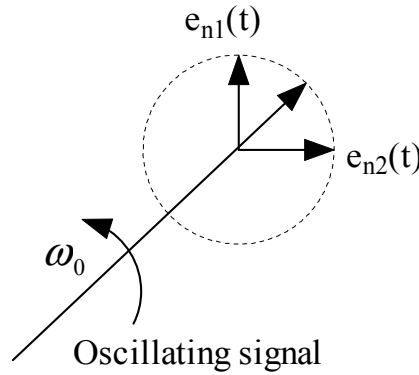Figure 4-10: Vector presentation of the oscillator signal and its modulation by the noise signal e_{n1} and e_{n2}.

From (4.36),

$$\overline{e^2(t)} = \overline{[e_{n1}^2(t) + e_{n2}^2(t) + 2(e_{n1}(t) * e_{n2}(t))]} \qquad (4.37)$$

$$\overline{(e_{n1}(t) * e_{n2}(t))]} = 0 \Rightarrow \overline{e^2(t)} = \overline{[e_{n1}^2(t) + e_{n2}^2(t)]} \qquad (4.38)$$

Considering, $\left|\overline{e_{n1}^2(t)}\right| = \left|\overline{e_{n2}^2(t)}\right|$ then

$$\overline{e_{n1}^2(t)} = \frac{\overline{e^2(t)}}{2} \tag{4.39}$$

$$\overline{e_{n2}^2(t)} = \frac{\overline{e^2(t)}}{2} \tag{4.40}$$

From (4.36), the orthogonal components of the noise perturbation can be given by

$$e_{n1}(t) = A_0\left|\dot{Z}_{A_0}\right|[\Delta A(t)]\cos\beta + \left|\dot{Z}_{\omega_0}\right|\left(\frac{d[\Delta A(t)]}{dt}\sin\alpha + A_0\frac{d[\Delta\varphi(t)]}{dt}\cos\alpha\right) \tag{4.41}$$

$$e_{n2}(t) = A_0\left|\dot{Z}_{A_0}\right|[\Delta A(t)]\sin\beta - \left|\dot{Z}_{\omega_0}\right|\left(\frac{d[\Delta A(t)]}{dt}\cos\alpha - A_0\frac{d[\Delta\varphi(t)]}{dt}\sin\alpha\right) \tag{4.42}$$

From (4.41) and (4.42)

$$\left|\dot{Z}_{\omega_0}\right|\frac{d[\Delta A(t)]}{dt} + A_0\left|\dot{Z}_{A_0}\right|[\Delta A(t)]\sin(\alpha-\beta) = [e_{n1}(t)\sin\alpha - e_{n2}(t)\cos\alpha] \tag{4.43}$$

$$A_0\left|\dot{Z}_{\omega_0}\right|\frac{d[\Delta\varphi(t)]}{dt} + \left|\dot{Z}_{A_0}\right|A_0[\Delta A(t)]\cos s(\alpha-\beta) = [e_{n1}(t)\cos\alpha + e_{n2}(t)\sin\alpha] \tag{4.44}$$

In frequency domain, operator $\dfrac{d}{dt} \to j\omega$ and noise spectral density due to amplitude and phase is obtained from Equations (4.43) and (4.44) as

$$|\Delta A(\omega)|^2 = \frac{|e|^2}{2\left|\dot{Z}_{\omega_0}\right|^2\omega^2 + 2\left|\dot{Z}_{A_0}\right|^2 A_0^2\sin^2(\alpha-\beta)} \tag{4.45}$$

$$|\Delta\varphi(\omega)|^2 = \left[\frac{|e|^2}{2A_0^2\omega^2}\right]\left[\frac{\left|\dot{Z}_{\omega_0}\right|^2\omega^2 + \left|\dot{Z}_{A_0}\right|^2 A_0^2}{\left|\dot{Z}_{\omega_0}\right|^4\omega^2 + \left|\dot{Z}_{\omega_0}\right|^2\left|\dot{Z}_{A_0}\right|^2 A_0^2\sin^2(\alpha-\beta)}\right] \tag{4.46}$$

At near carrier frequency ($\omega \to 0$), Equation (4.46) is reduced to

$$|\Delta\varphi(\omega)|^2 = \left[\frac{|e|^2}{2\omega^2 A_0^2\left|\dot{Z}_{\omega_0}\right|^2\sin^2(\alpha-\beta)}\right] \tag{4.47}$$

where ω is the spacing from the center frequency.

4.3   Noise Analysis of Mutually Coupled Oscillators

Now we want to show a simple oscillator model that can be used to give a good explanation for the relative noise reduction in the mutually coupled oscillator systems and to compare with the experimental results [Figure 8-12].

Figure 4-11 shows the two identical mutually coupled oscillators where β_{12} and β_{21} are the coupling coefficients.
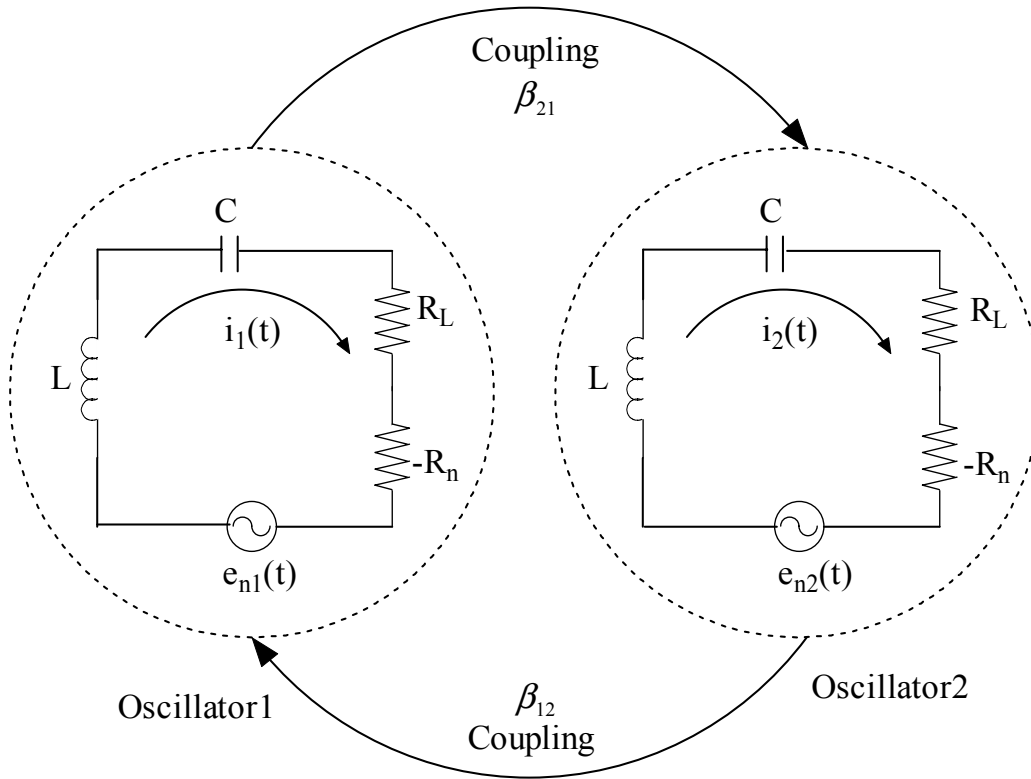

Figure 4-11: Two identical coupled oscillators coupled through arbitrary coupling network.

Although the effect of noise in coupled oscillator system has been discussed previously [18-28], it was not in a convenient form for explaining the improvement in the phase noise performance of the coupled oscillator system.

Figure 4-12 shows the equivalent representation of the Figure 4-11, where $e_{inj}(t)$ accounts for the mutual interaction and coupling with the adjacent oscillator.
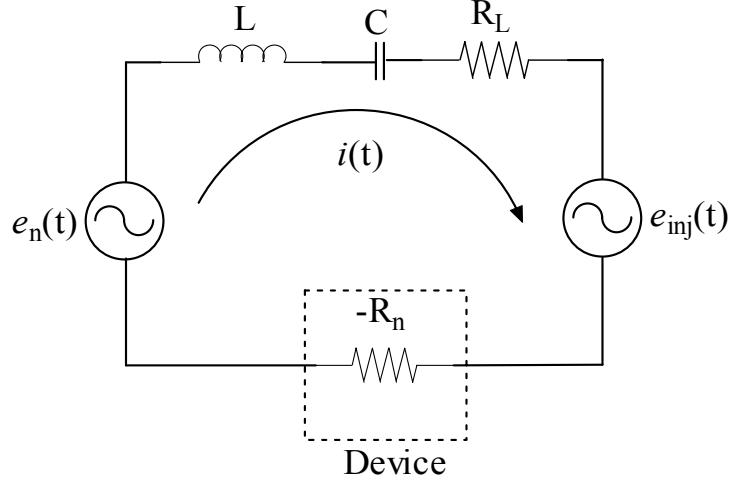
Figure 4-12: Equivalent representation of the Figure 4-11

The circuit equation of the Figure 4-12 is given by

$$L\frac{di(t)}{dt} + [R_L - R_n(t)]i(t) + \frac{1}{C}\int i(t)dt = e_{inj}(t) + e_n(t) \tag{4.48}$$

$$e_{n1}(t) = e_{n2}(t) = e_n(t) \tag{4.49}$$

The RF current $i(t)$ is

$$i(t) = \sum_n A_n(t)\cos[n\omega t + \varphi_n(t)] = A_1(t)\cos[\omega t + \varphi_1(t)] + A_2(t)\cos[2\omega t + \varphi_2(t)] + \cdots A_n(t)\cos[n\omega t + \varphi_n(t)] \tag{4.50}$$

Equation (4.49) is a nonhomogeneous differential equation. After substituting the values of $\frac{di(t)}{dt}$ and $\int i(t)dt$, and neglecting the higher order harmonic terms, it can be rewritten as

$$L\left[-A_1(t)(\omega + \frac{d\varphi_1(t)}{dt})\sin[\omega t + \varphi_1(t)] + \frac{dA_1(t)}{dt}\cos[\omega t + \varphi_1(t)]\right] + \left[(R_L - R_n(t))A_1(t)\right] +$$

$$\frac{1}{C}\left\{\left[\frac{A_1(t)}{\omega} - \frac{A_1(t)}{\omega^2}\left(\frac{d\varphi_1(t)}{dt}\right)\right]\sin[\omega t + \varphi_1(t)] + \frac{1}{\omega^2}\left(\frac{dA_1(t)}{dt}\right)\cos[\omega t + \varphi_1(t)]\right\} = e_{inj}(t) + e_n(t) \tag{4.51}$$

Defining

$$e(t) = e_{inj}(t) + e_n(t) \tag{4.52}$$

58

Following [24], the equations above are multiplied with $\sin[\omega t + \varphi_1(t)]$ or $\cos[\omega t + \varphi_1(t)]$ and integrated over one period of the oscillation cycle (from t-T_0 to t), which will give an approximate differential equation for phase $\varphi(t)$ and amplitude $A(t)$ as

$$-\frac{d\varphi(t)}{dt}\left[L+\frac{1}{\omega^2 C}\right]+\left[-\omega L+\frac{1}{\omega C}\right]=\left[\frac{2}{AT_0}\right]\left[\int_{t-T_0}^{t}[e_{inj}(t)+e_n(t)]\sin[\omega t+\varphi(t)]dt\right] \quad (4.53)$$

$$\frac{dA(t)}{dt}\left[L+\frac{1}{\omega^2 C}\right]+\left[R_L-\overline{R_n(t)}\right]A(t)=\left[\frac{2}{T_0}\right]\left[\int_{t-T_0}^{t}[e_{inj}(t)+e_n(t)]\cos[\omega t+\varphi(t)]dt\right] \quad (4.54)$$

From (4.54)

$$\frac{dA(t)}{dt}\left[L+\frac{1}{\omega^2 C}\right]+\gamma\Delta A A(t)=\left[\frac{2}{T_0}\right]\left[\int_{t-T_0}^{t}[e_{inj}(t)+e_n(t)]\cos[\omega t+\varphi(t)]dt\right] \quad (4.55)$$

where $\gamma=\frac{\Delta R}{\Delta I}=\frac{[R_L-\overline{R_n(t)}]}{\Delta A}$

$\overline{R_n(t)}$ is the average negative resistance over one cycle and is defined as

$$\overline{R_n(t)}=\left[\frac{2}{T_0 A}\right]\int_{t-T_0}^{t}R_n(t)A(t)\cos^2[\omega t+\varphi(t)]dt \quad (4.56)$$

Since magnitude of the higher harmonics is not significant, subscript of $\varphi(t)$ and $A(t)$ are dropped in the Equations (4.53), (4.54) and (4.55).

In Equation (4.54), $[R_L-\overline{R_n(t)}]I(t)\rightarrow 0$ gives the intersection of $[\overline{R_n(t)}]$ and R_L and this value is defined as A_0 which is the minimum value of the current needed for steady-state sustained oscillation condition. Figure 4-13 shows the plot of the nonlinear negative resistance as a function of the amplitude of the RF current.

From Figure 4-13, $\gamma\Delta I$ can be found from the intersection on vertical axis by drawing the tangential line on $[\overline{R_n(t)}]$ at $I=A_0$ and $|\Delta I|$ decreases exponentially with time for $\gamma>0$. Hence, A_0 represents the stable operating point and on the other hand, if $[\overline{R_n(t)}]$ intersects R_L from the other side for $\gamma<0$ then $|\Delta I|$ grows indefinitely with time. Such an operating point does not support stable operation [24].
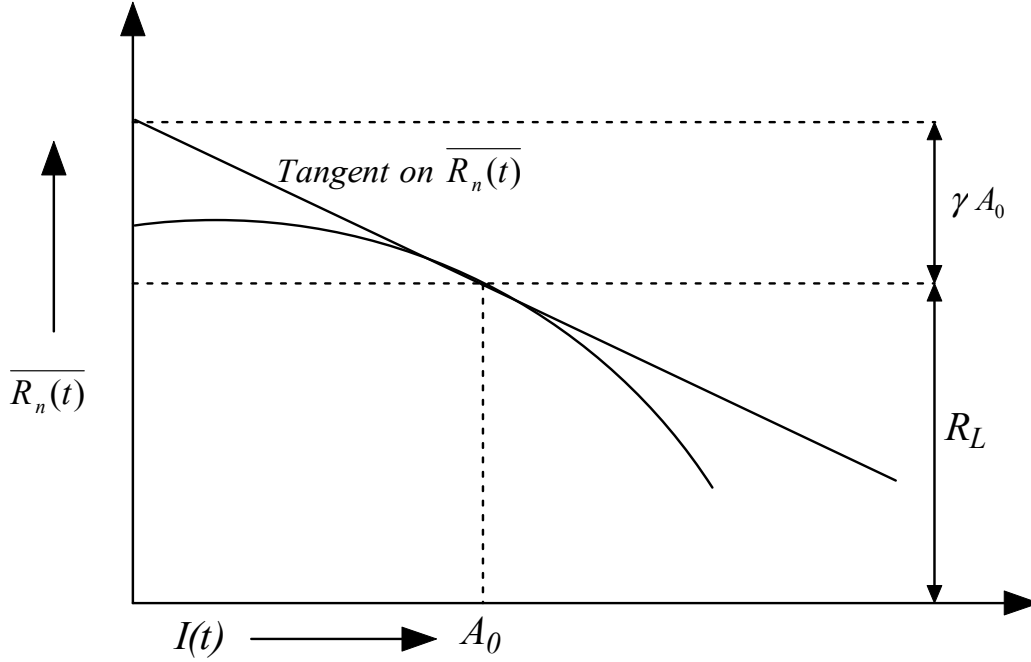
Figure 4-13: Plot of negative resistance of [$\overline{R_n(t)}$] versus amplitude of current *I(t)*.

Defining $n_1(t)$ and $n_2(t)$ for the uncoupled oscillator as

$$n_1(t) \rightarrow \frac{2}{T_0} \int_{t-T_0}^{t} e_n(t) \sin[\omega t + \varphi(t)]dt \tag{4.57}$$

$$n_2(t) \rightarrow \frac{2}{T_0} \int_{t-T_0}^{t} e_n(t) \cos[\omega t + \varphi(t)]dt \tag{4.58}$$

The time average of the square of the [n_1(t)] and [n_2(t)] are given from Equations (4.57) and (4.58) as

$$\overline{n_1^2(t)} = 2\overline{e_n^2(t)} \tag{4.59}$$

$$\overline{n_2^2(t)} = 2\overline{e_n^2(t)} \tag{4.60}$$

From (4.57) and (4.58), $n_1(t)$ and $n_2(t)$ are orthogonal functions and the correlation between $n_1(t)$ and $n_2(t)$ is defined as→ $\overline{n_1(t) * n_2(t)} = 0$

Defining, $\varphi(t) = \varphi_0 + \Delta\varphi(t)$ and $A(t) = A_0 + \Delta A(t)$; where $\Delta\varphi(t)$ and $\Delta A(t)$ are phase and amplitude fluctuations of the RF output current.

Assuming the phase and current fluctuations, $\Delta\varphi(t)$ and $\Delta A(t)$ are orthogonal functions, therefore the correlation is given by

$$\overline{\Delta\varphi(t) * \Delta A(t)} = 0 \qquad (4.61)$$

Uncoupled free-running oscillator:

For uncoupled free-running oscillator ($\omega \rightarrow \omega_0$), Equations (4.53) and (4.55) can be given as

$$-\frac{d[\Delta\varphi(t)]}{dt}\left[L + \frac{1}{\omega^2 C}\right]_{\omega=\omega_0} + \left[-\omega L + \frac{1}{\omega C}\right]_{\omega=\omega_0} = \left[\frac{2}{AT_0}\right]\left[\int_{t-T_0}^{t} e(t)\sin[\omega t + \varphi(t)]dt\right]_{e(t)\rightarrow e_n(t)} \qquad (4.62)$$

$$\frac{d[\Delta A(t)]}{dt}\left[L + \frac{1}{\omega^2 C}\right]_{\omega=\omega_0} + \gamma\Delta AA(t) = \left[\frac{2}{T_0}\right]\left[\int_{t-T_0}^{t} e(t)\cos[\omega t + \varphi(t)]dt\right]_{e(t)\rightarrow e_n(t)} \qquad (4.63)$$

At steady-state condition ($\omega \rightarrow \omega_0$), the phase dynamics is given from Equations (4.59) and (4.62) as

$$-2L\frac{d[\Delta\varphi(t)]}{dt} = \left[\frac{1}{A}\right]n_1(t) \qquad (4.64)$$

The PM noise spectral density can be expressed from (4.62) as

$$|\Delta\varphi(\omega)|^2 = \frac{1}{4\omega^2 L^2 A^2}|n_1(\omega)|^2 \approx \frac{|e_n(\omega)|^2}{2\omega^2 L^2 A_0^2} \qquad (4.65)$$

At steady-state condition ($\omega \rightarrow \omega_0$), the amplitude dynamics is given from (4.63) as,

$$\left[2L\frac{d[\Delta A(t)]}{dt} + \gamma\Delta AA(t)\right] = n_2(t) \qquad (4.66)$$

The amplitude of the RF current can be written as of Equation 4.22, where A_0 represents the stable operating point of the free-running oscillator; Equation (4.66) can be given by

$$\left[2L\frac{d[\Delta A(t)]}{dt} + \Delta A(t)A_0\gamma + \Delta A^2(t)\gamma\right] = n_2(t) \qquad (4.67)$$

$\Delta A^2(t)$ is negligible in comparison with A_0, its value can be assumed to be zero for simplification in the analysis and the Equation (4.67) can be rewritten as

$$2L\frac{d}{dt}[\Delta A(t)] + \Delta A(t)A_0\gamma = n_2(t) \tag{4.68}$$

The AM noise spectral density in the frequency domain can be expressed from (4.68) as

$$|\Delta A(\omega)|^2 = \frac{1}{[4L^2\omega^2 + (A_0\gamma)^2]}|n_2(\omega)|^2 \Rightarrow |\Delta A(\omega)|^2 = \frac{2|e_n(\omega)|^2}{[4L^2\omega^2 + (A_0\gamma)^2]} \tag{4.69}$$

Mutually Coupled Oscillator:

In the case of free-running oscillator phase φ could take almost any value whereas, under mutually coupled condition the oscillator is synchronized with the injected signal from the adjacent oscillator and phase φ should stay in the vicinity of φ_0 because of the restoring force due to the injected signal $e_{inj}(t)$ from the adjacent neighboring oscillator.

Defining
$$e_{inj}(t) = A_{inj}\cos(\omega_{inj}t), \ \varphi(t) = \varphi_0 + \Delta\varphi(t) \text{ and } A(t) = A_0 + \Delta A(t)$$

For $\omega \to \omega_0$, Equation (4.53) is reduced to

$$-2L\frac{d[\Delta\varphi(t)]}{dt} = \left[\frac{2}{AT_0}\right]\left[\int_{t-T_0}^{t} e_n(t)\sin[\omega t + \varphi(t)]dt + \int_{t-T_0}^{t} A_{inj}\cos(\omega_{inj}t)\sin[\omega t + \varphi(t)]dt\right] \tag{4.70}$$

$$-2L\frac{d[\Delta\varphi(t)]}{dt} \approx \frac{1}{A_0}n_1(t) + \frac{A_{inj}}{A_0}[\Delta\varphi(t)]\cos(\varphi_0) \tag{4.71}$$

where $A(t) \approx A_0$

For $\omega \to \omega_0$, Equation (4.55) is reduced to

$$2L\frac{d[\Delta A(t)]}{dt} + \gamma\Delta A A_0 = \left[\frac{2}{T_0}\right]\left[\int_{t-T_0}^{t} e_n(t)]\cos[\omega t + \varphi(t)]dt + \int_{t-T_0}^{t} A_{inj}\cos(\omega_{inj}t)\cos[\omega t + \varphi(t)]dt\right] \tag{4.72}$$

$$2L\frac{d[\Delta A(t)]}{dt} + \gamma[\Delta A(t)]A_0 = n_2(t) - A_{inj}[\Delta\varphi(t)]\sin(\varphi_0) \tag{4.73}$$

From (4.71) and (4.73), phase and amplitude noise spectral density is given by [68]

$$\left|\Delta\varphi(\omega)\right|^2 = \frac{2\left|n_1(\omega)\right|^2}{4\omega^2 L^2 A_0^2 + A_{inj}^2 \cos^2(\varphi_0)} \Rightarrow \left|\Delta\varphi(\omega)\right|^2 = \frac{2\left|e_n(\omega)\right|^2}{4\omega^2 L^2 A_0^2 + A_{inj}^2 \cos^2(\varphi_0)} \qquad (4.74)$$

$$\left|\Delta A(\omega)\right|^2 = \left[\frac{\left|n_2(\omega)\right|^2}{[4L^2\omega^2 + (A_0\gamma)^2]}\right] + \left[\frac{A_{inj}^2 \sin^2(\varphi_0)}{[4L^2\omega^2 + (A_0\gamma)^2]}\right]\left[\frac{\left|n_1(\omega)\right|^2}{[4L^2\omega^2 A_0^2 + (A_{inj}\cos\varphi_0)^2]}\right] \qquad (4.75)$$

From (4.75),

$$\left|\Delta A(\omega)\right|^2 = \left[\frac{2\left|e_n(\omega)\right|^2}{[4L^2\omega^2 + (A_0\gamma)^2]}\right]\left[\frac{4L^2\omega^2 A_0^2 + A_{inj}^2}{4L^2\omega^2 A_0^2 + (A_{inj}\cos\varphi_0)^2}\right] \qquad (4.76)$$

An attempt has been made to calculate the noise of the two identical mutually coupled oscillators (without considering the $1/f$ noise in the oscillator).

Equations (4.65) and (4.74) show the relative improvement of the phase noise when the oscillator is mutually coupled. It can be seen from Equations (4.69) and (4.76) that the AM noise of the coupled oscillator is considerably increased.

However, in practical applications, the increase of the envelope fluctuation associated with the amplitude is controlled with the gain-limiting active device. Thus, the effect of the AM noise is small in comparison to the effect of phase noise.


4.4   Noise Analysis of N-Coupled Oscillators

Equation (4.74) shows the relative phase noise improvement for the two identical mutually coupled oscillators. The purpose of this analysis is to show the relative noise improvement in the N-coupled oscillators system coupled through the arbitrary N port-coupling network. The analytical expression shows that the total phase noise of the coupled oscillator system is reduced compared to that of a single free-running oscillator in direct proportion to the number of arrays in the oscillators, provided that the coupling network is designed and optimized properly. The coupling configuration of the N-coupled oscillator system is shown in Figure 4-14 as a) nearest neighbor unilateral coupling b) nearest neighbor bilateral coupling and c) global coupling [68].

Figure 4-15 shows the parallel negative conductance oscillator model noise equivalent admittance Y_{noise} corresponding to the noise associated with the oscillator circuit. Noisy oscillator can be described either through the addition of equivalent noise admittance or an equivalent noise-current generator [18].
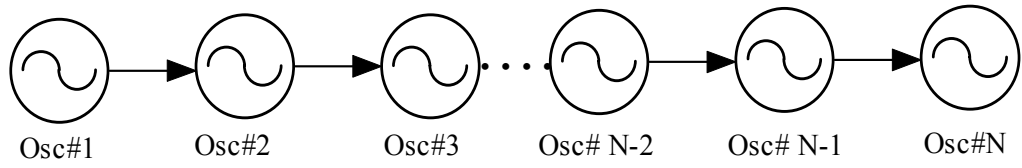
(a) Nearest neighbor unilateral coupling
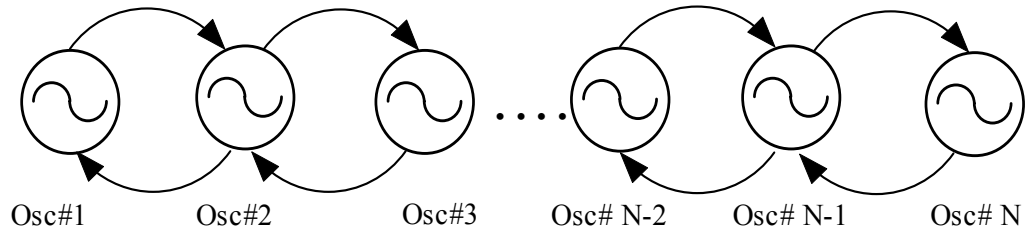
(b) Nearest neighbor bilateral coupling
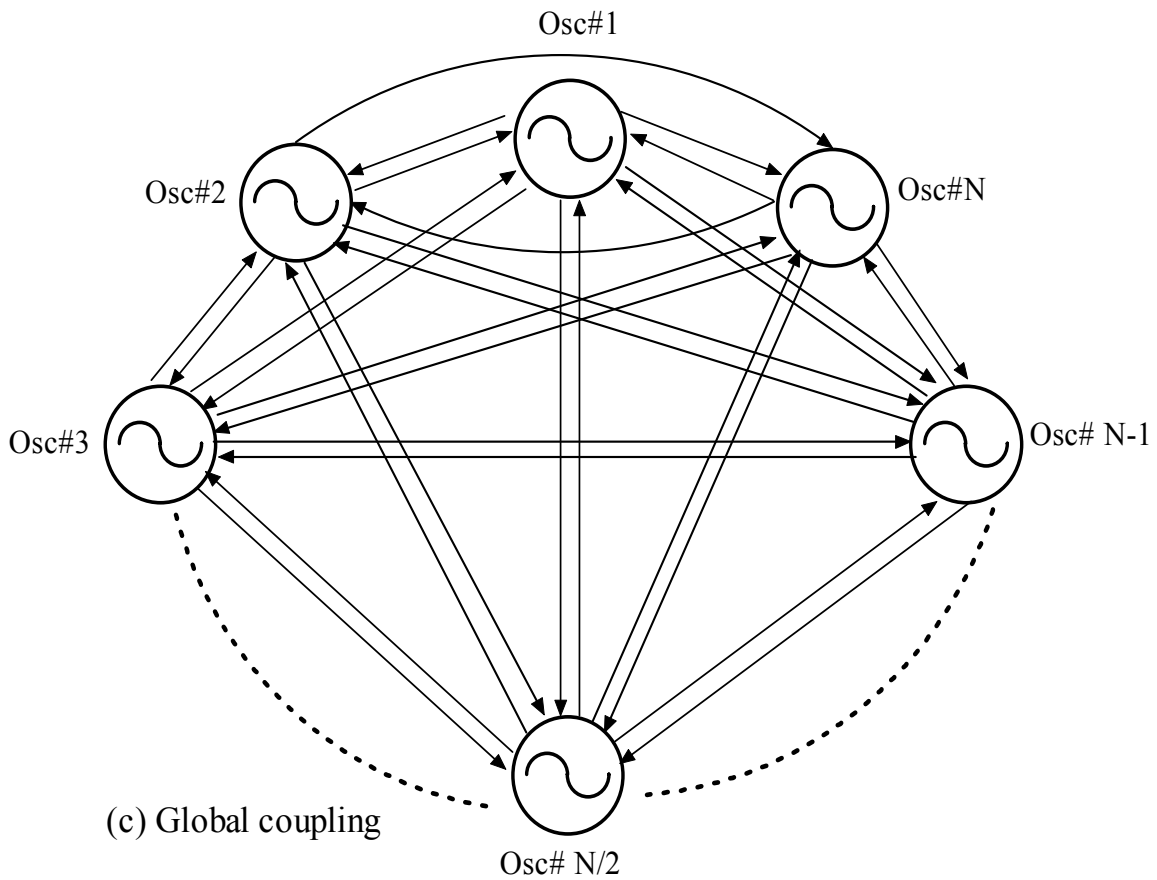
(c) Global coupling

Figure 4-14: a) Nearest neighbor unilateral coupling b) Nearest neighbor bilateral coupling and c) Global coupling.
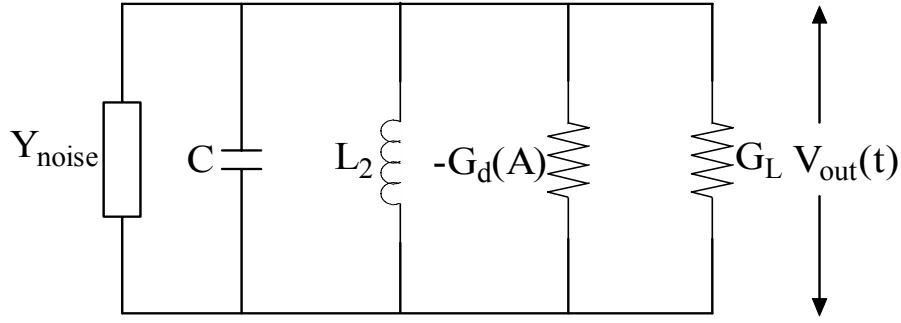
Figure 4-15: Oscillator model with noise admittance.

The normalized noise admittance Y_n with respect to load admittance G_L is given by

$$Y_n = \frac{Y_{noise}}{G_L} = \frac{G_{noise}}{G_L} + j\frac{B_{noise}}{G_L} = G_n + jB_n \qquad (4\text{-}77)$$

where $\qquad$ G_L : Oscillator load admittance in the free-running state
$\qquad\qquad$ G_n : In-phase component of noise source
$\qquad\qquad$ B_n : Quadrature component of noise source.

For an uncoupled free-running oscillator, G_n corresponds to the oscillator amplitude fluctuations and B_n corresponds to the phase fluctuations.

The amplitude and phase dynamics of each oscillator in the N-coupled oscillators system are given from Equations (3.103) and (3.104) as

$$\frac{\partial A_i(t)}{\partial t} = A_i(t)\left[\frac{\mu_i\omega_i}{2Q_i}(\alpha_i^2 - |A_i(t)|^2)\right] + \frac{\omega_i}{2Q_i}\left[\sum_{\substack{j=1 \\ j\neq i}}^{N} \beta_{ij} A_j(t)\cos[\theta_i(t) - \theta_j(t) + \varphi_{ij}]\right]$$

$$-\left[\frac{\omega_i}{2Q_i} A_i(t)G_{ni}(t)\right]; \quad i = 1,2,3....N \qquad (4.78)$$

$$\frac{\partial\theta_i(t)}{\partial t} = \omega_i - \left[\frac{\omega_i}{2Q_i}\right]\left[\sum_{\substack{j=1 \\ j\neq i}}^{N} \beta_{ij}\left(\frac{A_j(t)}{A_i(t)}\right)\sin[\theta_i(t) - \theta_j(t) + \varphi_{ij}]\right] - \left[\frac{\omega_i}{2Q_i} B_{ni}(t)\right]; i = 1,2,3....N \quad (4.79)$$

where $A_i(t), \theta_i(t), \omega_i$ and Q_i are the amplitude, phase, free-running frequency, and Q factor of the ith oscillator, respectively, and β_{ij} and φ_{ij} are the coupling parameters between the ith and j^{th} oscillators.

Defining

$$A_i(t) = \dot{A}_i + \Delta A_i(t) \text{ and } \theta_i(t) = \dot{\theta}_i + \Delta \theta_i(t) \tag{4.80}$$

where $[\dot{A}, \dot{\theta}]$ are the steady-state solutions of the N-coupled oscillators coupling and $[\Delta A_i(t), \Delta \theta_i(t)]$ are the amplitude and phase fluctuations of the ith oscillator. Assuming fluctuations $\rightarrow [\Delta A_i(t), \Delta \theta_i(t)]$ are small in comparisons to the steady state solutions $\rightarrow [\dot{A}, \dot{\theta}]$, for simplification of the noise analysis, Equations (4.78) and (4.79) are linearized around $(\dot{A}, \dot{\theta})$ and can be expressed as

$$\frac{\partial[\Delta A_i(t)]}{\partial t} = \mu_i \frac{\omega_i}{2Q_i}\left[[\alpha_i^2 - 3\dot{A}_i^2]\Delta A_i(t)\right] + \frac{\omega_i}{2Q_i}\left[\sum_{\substack{j=1 \\ j\neq i}}^{N}\beta_{ij}[\Delta A_j(t)]\cos[\dot{\theta}_i - \dot{\theta}_j + \varphi_{ij}]\right]$$

$$-\frac{\omega_i}{2Q_i}\left[\sum_{\substack{j=1 \\ j\neq i}}^{N}\beta_{ij}[\Delta\theta_i(t) - \Delta\theta_j(t)]\dot{A}_j\sin[\dot{\theta}_i - \dot{\theta}_j + \varphi_{ij}]\right] - \frac{\omega_i}{2Q_i}\left[\dot{A}_i G_{ni}(t)\right] \quad i = 1,2,3....N \tag{4.81}$$

$$\frac{\partial[\Delta\theta_i(t)]}{\partial t} = -\frac{\omega_i}{2Q_i}\sum_{\substack{j=1 \\ j\neq i}}^{N}\left[\beta_{ij}\left(\frac{\dot{A}_j}{\dot{A}_i}\right)\left(\frac{[\Delta A_j(t) - \Delta A_i(t)]}{\dot{A}_i}\right)\sin[\dot{\theta}_i - \dot{\theta}_j + \varphi_{ij}]\right]$$

$$-\frac{\omega_i}{2Q_i}\sum_{\substack{j=1 \\ j\neq i}}^{N}\beta_{ij}\left([\Delta\theta_i(t) - \Delta\theta_j(t)]\left(\frac{\dot{A}_j}{\dot{A}_i}\right)\cos[\dot{\theta}_i - \dot{\theta}_j + \varphi_{ij}]\right) - \frac{\omega_i}{2Q_i}[B_{ni}(t)] \quad i = 1,2,3....N \tag{4.82}$$

In the case of N identical oscillators coupled through the N port-coupling network of $\varphi_{ij} = 2\pi$, and transforming time dynamics to the frequency domain analysis by using Fourier transformation, Equations (4.81) and (4.82) can be given by

$$[\Delta A_i(\omega)] = \left[\frac{\mu\omega_i}{2Q\omega}\right][\alpha_i^2 - 3\dot{A}_i^2][\Delta A_i(\omega)] + \left[\frac{\omega_i}{2Q\omega}\right]\sum_{\substack{j=1 \\ j\neq i}}^{N}\beta_{ij}[\Delta A_j(\omega)]\cos[\dot{\theta}_i - \dot{\theta}_j]$$

$$-\left[\frac{\omega_i}{2Q\omega}\right]\sum_{\substack{j=1 \\ j\neq i}}^{N}\beta_{ij}[\Delta\theta_i(\omega) - \Delta\theta_j(\omega)\dot{A}_j\sin[\dot{\theta}_i - \dot{\theta}_j]] - \left[\frac{\omega_i}{2Q\omega}\right]\dot{A}_i G_{ni}(\omega) \; ; \; i = 1,2,3....N \tag{4.83}$$

$$[\Delta\theta_i(\omega)] = -\left[\frac{\omega_i}{2Q\omega}\right]\sum_{\substack{j=1 \\ j\neq i}}^{N}\left[\beta_{ij}\left(\frac{\dot{A}_j}{\dot{A}_i}\right)\left(\frac{[\Delta A_j(\omega) - \Delta A_i(\omega)]}{\dot{A}_i}\right)\sin[\dot{\theta}_i - \dot{\theta}_j]\right]$$

$$-\left[\frac{\omega_i}{2Q\omega}\right]\sum_{\substack{j=1 \\ j\neq i}}^{N}\beta_{ij}\left([\Delta\theta_i(\omega)] - [\Delta\theta_j(\omega)]\frac{\dot{A}_j}{\dot{A}_i}\cos[\dot{\theta}_i - \dot{\theta}_j]\right) - \left[\frac{\omega_i}{2Q\omega}\right]B_{ni}(\omega) \; ; \; i = 1,2,3....N \tag{4.84}$$

where ω is the noise offset frequency from the carrier, $\mu_I = \mu$ and $Q_i = Q$ for N identical coupled oscillator.

From Equation (4.83), the second term of the RHS represents AM noise transformed from all the $j \neq i$ oscillators to the AM noise of the ith oscillator as

$$\left[\frac{\omega_i}{2Q\omega}\right]\sum_{\substack{j=1\\j\neq i}}^{N}\beta_{ij}[\Delta A_j(\omega)]\cos[\dot{\theta}_i - \dot{\theta}_j] \Rightarrow AM \rightarrow AM$$

and the third term is the conversion of PM noise to AM noise as

$$\left[\frac{\omega_i}{2Q\omega}\right]\sum_{\substack{j=1\\j\neq i}}^{N}\beta_{ij}\left[[\Delta\theta_i(\omega) - \Delta\theta_j(\omega]\dot{A}_j\sin[\dot{\theta}_i - \dot{\theta}_j]\right] \Rightarrow PM \rightarrow AM$$

Similarly, from Equation (4.84), the first term of the RHS (right hand side) represents AM noise transformed to PM noise as

$$-\left[\frac{\omega_i}{2Q\omega}\right]\sum_{\substack{j=1\\j\neq i}}^{N}\left[\beta_{ij}\left(\frac{\dot{A}_j}{\dot{A}_i}\right)\left(\frac{[\Delta A_j(\omega) - \Delta A_i(\omega)]}{\dot{A}_i}\right)\sin[\dot{\theta}_i - \dot{\theta}_j]\right] \Rightarrow AM \rightarrow PM$$

and the second term is conversion of PM to PM noise as

$$\left[\frac{\omega_i}{2Q\omega}\right]\sum_{\substack{j=1\\j\neq i}}^{N}\beta_{ij}\left([\Delta\theta_i(\omega)] - [\Delta\theta_j(\omega)]\frac{\dot{A}_j}{\dot{A}_i}\cos[\dot{\theta}_i - \dot{\theta}_j]\right) \Rightarrow PM \rightarrow PM$$

Equations (4.83) and (4.84) can be expressed in the following concise matrix format [18]:

$$\begin{bmatrix} AM \rightarrow AM & PM \rightarrow AM \\ AM \rightarrow PM & PM \rightarrow PM \end{bmatrix}\begin{bmatrix} \overline{\Delta A(\omega}) \\ \overline{\Delta\theta(\omega)} \end{bmatrix} = \begin{bmatrix} \overline{\dot{A}G_n(\omega)} \\ \overline{B_n(\omega)} \end{bmatrix} \tag{4.85}$$

where $\overline{\dot{A}G_n(\omega)}$ and $\overline{B_n(\omega)}$ is the in-phase or AM and quadrature or PM noise source vector of the order N×1 respectively.

The influence of the PM-to-PM conversion is greater over the other terms. To simplify the analysis, contributions from the conversion of AM to AM, PM to AM and AM to PM noise conversion are considered negligible.

Assuming that all the steady-state amplitudes are identical ($\dot{A}_i = \dot{A}_j$), PM-to-PM noise conversion is considered for deriving the phase noise equation of the N-coupled oscillators. Therefore, Equation (4.84) is rewritten as

$$\left[\frac{\omega}{\omega_{3dB}}\right][\Delta\theta_i(\omega)] = -\left[\sum_{\substack{j=1 \\ j\neq i}}^{N}\beta_{ij}\left([\Delta\theta_i(\omega)]-[\Delta\theta_j(\omega)]\right)\left(\cos[\dot{\theta}_i-\dot{\theta}_j]\right)-B_{ni}(\omega)\right]; \quad i=1,2,3....N \quad (4.86)$$

where

$$\omega_{3dB} = \frac{\omega_i}{2Q}$$

Equation (4.86) can be expressed in matrix form as

$$[\overline{C}]\begin{bmatrix}[\Delta\theta_1(\omega)] \\ [\Delta\theta_2(\omega)] \\ \vdots \\ [[\Delta\theta_{N-1}(\omega)] \\ [\Delta\theta_N(\omega)]\end{bmatrix} = \begin{bmatrix}B_{n1}(\omega) \\ B_{n2}(\omega) \\ \vdots \\ B_{N-1}(\omega) \\ B_{nN}(\omega)\end{bmatrix} \Rightarrow [\overline{C}][\overline{\Delta\theta(\omega)}] = [\overline{B_n(\omega)}] \quad (4.87)$$

where

$$[\overline{\Delta\theta(\omega)}] = \begin{bmatrix}[\Delta\theta_1(\omega)] \\ [\Delta\theta_2(\omega)] \\ \vdots \\ [[\Delta\theta_{N-1}(\omega)] \\ [\Delta\theta_N(\omega)]\end{bmatrix}, \quad [\overline{B_n(\omega)}] = \begin{bmatrix}B_{n1}(\omega) \\ B_{n2}(\omega) \\ \vdots \\ B_{N-1}(\omega) \\ B_{nN}(\omega)\end{bmatrix}$$

The matrix $[\overline{C}]$ represents the arbitrary coupling topology of the N-coupled oscillators system.
The phase fluctuations of the individual oscillator can be given from Equation (4.87) as

$$[\overline{\Delta\theta(\omega)}] = [\overline{C}]^{-1}[\overline{B_n(\omega)}] = [\overline{P}][\overline{B_n(\omega)}] \quad (4.88)$$

where $[\overline{P}] = [\overline{C}]^{-1}$

Defining, $[\overline{P}] = \sum\limits_{j=1}^{N} p_{ij}$; where p_{ij} is the element of the matrix $[\overline{P}]$.

From Equation (4.88),

$$[\Delta\theta_i(\omega)] = \sum_{j=1}^{N} p_{ij} B_{nj}(\omega) \qquad (4.89)$$

Noise power spectral density of the ith oscillator is calculated by taking ensemble average of the phase fluctuation of the ith oscillator as

$$\left| [\Delta\theta_i(\omega)][\Delta\theta_i(\omega)]^* \right| = \left| \left[\sum_{j=1}^{N} p_{ij} B_{nj}(\omega) \right]\left[\sum_{j=1}^{N} p_{ij} B_{nj}(\omega) \right]^* \right| \qquad (4.90)$$

$$\left| [\Delta\theta_i(\omega)][\Delta\theta_i(\omega)]^* \right| = \sum_{j=1}^{N} \left| p_{ij} \right|^2 \left| B_{nj}(\omega) \right|^2 \qquad (4.91)$$

$$\left| \Delta\theta_i(\omega) \right|^2 = \left| B_n(\omega) \right|^2 \sum_{j=1}^{N} \left| p_{ij} \right|^2 \qquad (4.92)$$

where $\left| B_{ni}(\omega) \right|^2 = \left| B_{nj}(\omega) \right|^2 = \left| B_n(\omega) \right|^2$, assuming identical noise power spectral density from the N identical oscillator noise sources.

From Equation (4.92), the phase noise of the ith oscillator is expressed by the sum of the square magnitude of the elements in the ith row of the matrix $[\overline{P}]$.

The output of the N identical coupled oscillators system synchronized to a common frequency ω_0 can be expressed as

$$V(t) = A\sum_{j=1}^{N} \cos[\omega_0 t + \Delta\theta_j(t)] = A[\cos(\omega_0 + \Delta\theta_1(t)] + \cdots + A[\cos(\omega_0 + \Delta\theta_{N-1}(t)] + A[\cos(\omega_0 + \Delta\theta_N(t)] \qquad (4.93)$$

Assuming the small phase fluctuations, Equation (4.93) can be rewritten as

$$V(t) = NA[\cos(\omega_0 t + \Delta\theta_{total}(t)] \qquad (4.94)$$

where

$$[\Delta\theta_{total}(t)] = \frac{1}{N}\sum_{j=1}^{N}[\Delta\theta_j(t)] \qquad (4.95)$$

From Equations (4.89) and (4.95),

$$[\Delta\theta_{total}(\omega)] = \frac{1}{N}\sum_{j=1}^{N}\left(\sum_{i=1}^{N}p_{ij}\right)B_{nj}(\omega) \tag{4.95}$$

From (4.92) and (4.95), the total phase noise of the N-coupled oscillators is given by

$$\left|\Delta\theta_{total}(\omega)\right|^2 = \frac{\left|B_n(\omega)\right|^2}{N^2}\sum_{j=1}^{N}\left|\sum_{i=1}^{N}p_{ij}\right|^2 \tag{4.96}$$

where

$$\sum_{j=1}^{N}\left|\sum_{i=1}^{N}p_{ij}\right|^2 \rightarrow \text{ is the arbitrary coupling parameter and can be determined based on}$$

the coupling topology, which is discussed in Appendix A.

From Equations (4.92) and (4.96), the total phase noise of the N-coupled oscillators in terms of the single individual uncoupled free-running oscillator is given by [68]

$$\left|\Delta\theta_{total}(\omega)\right|^2 = \frac{1}{N}\left|\Delta\theta_i(\omega)\right|^2 \tag{4.97}$$

Equation (4.97) shows the relative phase noise improvement for N-coupled oscillators system, which becomes 1/N of that of the individual single uncoupled free-running oscillator.

The relative noise of the N identical coupled oscillators with respect to the free- running uncoupled oscillator has been calculated done (without considering the $1/f$ noise in the oscillator).

For better insight into the noise analysis for the N-coupled oscillator, refer to the coupling topology discussed in the Appendix A.

Chapter 5

Couple Mode Oscillator Topology

5.1   N-Push Coupled Mode Oscillator

The increasing demand for more bandwidth to support mobile communication applications has resulted in the demand for higher operating frequencies in the marketplace. A high frequency signal can be generated either based on an oscillator operating at a fundamental frequency or a harmonic oscillator. A typical oscillator operating at the fundamental frequency suffers from a low Q-factor, insufficient device gain, and higher phase noise at a high frequency of operation. The cascade structure and the parallel structure are the two configurations known for the harmonic oscillators. The cascade structure supports second-harmonic oscillation based on frequency doubling. On the other hand, the parallel structure supports the Nth harmonic frequency oscillation (N-push oscillator topology: 2-push/push-push, triple-push, quadruple-push…N-push) [31-36] based on the coupled oscillator approach. The frequency doubler and other means of up-conversion may provide a practical and quick solution to generate high frequency signals from the oscillators operating at a lower frequency, but it may also introduce distortions and have poor phase noise performances. The purpose of this chapter is to provide the insight and working principles of the oscillators/VCOs based on the N-push coupled mode topology.

The advantage of the N-push coupled mode topology is the extended frequency generation capabilities of the transistor and the reduction of the phase noise in comparison with the single oscillator by the factor of N, where N is the number of oscillator sub-circuits as given in Equation (4.97). A further advantage of N-Push design approach is that the load pulling is suppressed effectively due to the separation of internal and external frequency. The drawback of N-push/push-push oscillator is complicated design that requires large signal analysis to verify the odd-mode operation of the sub-circuits, and the bias network has to be properly designed with respect to two critical frequency associated with the even and odd mode of operations.

5.2   2-Push/Push-Push Oscillator

The push-push configuration is generally used for implementing a second-harmonic oscillator in which two identical oscillators are arranged anti-symmetrically. By combining the two out-of-phase oscillation signals, the fundamental frequency components are canceled out, and the second-harmonic components are enhanced and added constructively. As a push-push oscillator operates only at half the output frequency [1], a higher resonator Q level can be reached and low phase noise characteristic can be achieved.

Furthermore, the noise sources of the two individual oscillators are uncorrelated, while the carrier powers add in phase. Therefore, there is a noise reduction of the phase noise in a push-push oscillator of 9 dB compared with the fundamental frequency of the individual oscillator composing the push-push topologies. Figure 5-1 shows the block diagram of the push-push topology.
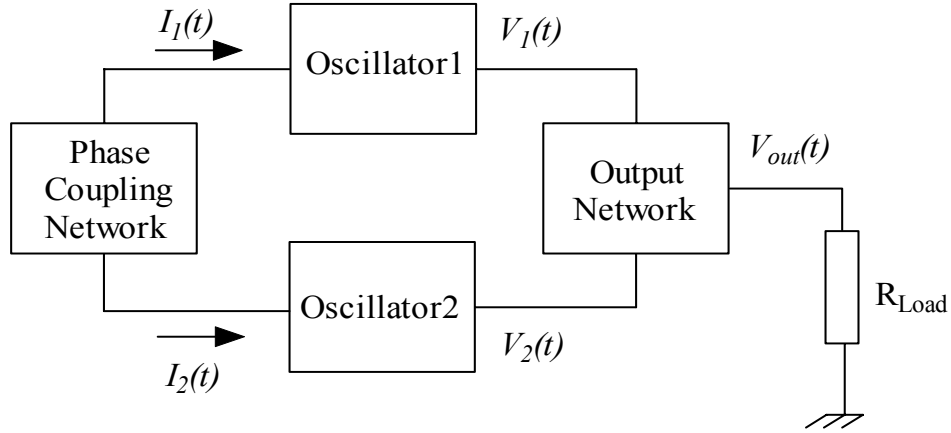

Figure 5-1: Block diagram of the push-push topology.

The time varying signals of the two individual oscillators are given by

$$V_1(t) = \sum_n A_n e^{jn(\omega_0 t)} = A_1 e^{j\omega_0 t} + A_2 e^{j2\omega_0 t} + A_3 e^{j3\omega_0 t} + A_4 e^{j4\omega_0 t} + \cdots A_n e^{jn\omega_0 t} \tag{5.1}$$

$$V_2(t) = \sum_n A_n e^{jn[\omega_0(t-\Delta t)]} = A_1 e^{j\omega_0(t-\Delta t)} + A_2 e^{j2\omega_0(t-\Delta t)} + A_3 e^{j3\omega_0(t-\Delta t)} + A_4 e^{j4\omega_0(t-\Delta t)} + \cdots A_n e^{jn\omega_0(t-\Delta t)} \tag{5.2}$$

$$V_{out}(t) = [V_1(t) + V_2(t)] = \left[\sum_n A_n e^{jn(\omega_0 t)} + \sum_n A_n e^{jn[\omega_0(t-\Delta t)]} \right] \tag{5.3}$$

$$V_{out}(t) = A_1 e^{j\omega_0 t}[1 + e^{-j\omega_0 \Delta t}] + A_2 e^{j2\omega_0 t}[1 + e^{-j2\omega_0 \Delta t}] + A_3 e^{j3\omega_0 t}[1 + e^{-j3\omega_0 \Delta t}] + \cdots \tag{5.4}$$

From Equation (3.71), the phase condition for a mutually locked coupled oscillator in push-push topology is $\omega_0 \Delta t = \pi$. Therefore, Equation (5.4) can be rewritten as

$$[V_{out}(t)]_{push-push} = \sum_{n=1}^{2} V_n(t) = 2A_2 e^{j2\omega_0 t} + 2A_4 e^{j4\omega_0} + 2A_6 e^{j6\omega_0 t} + \cdots \tag{5.5}$$

Equation (5.5) shows the cancellation of all the odd harmonics, especially the fundamental signal, where the even harmonics are added constructively. The higher order harmonics ($4\omega_0$, $6\omega_0$, $8\omega_0$...) are filtered out.

Noise Analysis

The following noise analysis is based on the pushing-factor [64, 68]. It is an attempt to introduce the concept of relative improvement in phase noise with respect to circuit configuration such as the fundamental oscillator and the push-push topologies. Figure 5-2 shows the Colpitts configuration of the oscillator circuit for the noise analysis.
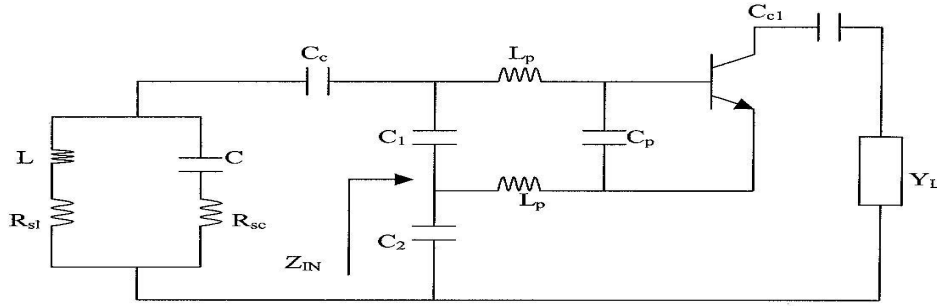

Figure 5-2: Colpitts oscillator with base-lead inductances (L_p) and package capacitance (C_p).

The expression of input impedance Z_{in} of the circuit shown in the Figure 5-2 is given as

$$Z_{IN}\big|_{pacakage} = -\left[\frac{Y_{21}}{\omega^2(C_1+C_p)C_2}\frac{1}{(1+\omega^2Y_{21}^2L_p^2)}\right] - j\left[\left\{\frac{(C_1+C_P+C_2)}{\omega(C_1+C_P)C_2}\right\} - \left\{\frac{\omega Y_{21}L_P}{(1+\omega^2Y_{21}^2L_p^2)}\right\}\left\{\frac{Y_{21}}{\omega(C_1+C_P)C_2}\right\}\right] \quad (5.6)$$

where L_p is the base lead-inductance, C_p is the package capacitance, and Y_{21} is the large signal Y-parameter of the device.

Figure 5-2 can be equivalently represented in terms of a negative conductance and capacitance, which is a nonlinear function of the oscillator RF signal amplitude V_0, and is shown in Figure 5-3.
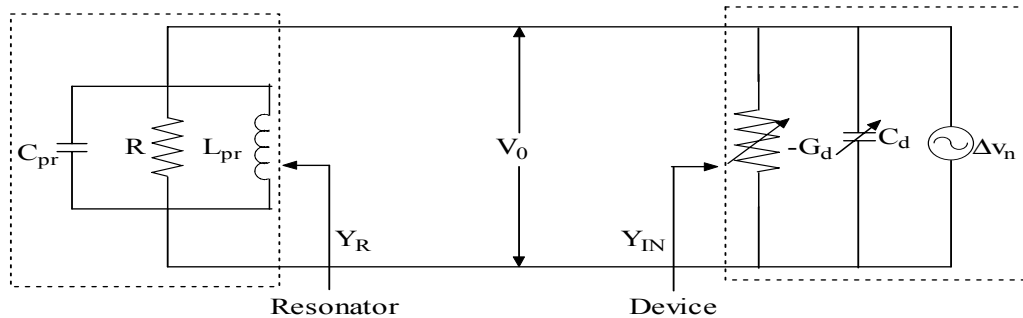

Figure 5-3: Equivalent model of the oscillator shown in Figure 5-2.

The input admittance of the circuit shown in Figure 5-3 is defined by

$$Y_{IN} = -G_d + j\omega C_d \quad (5.7)$$

where

$$G_d = \frac{\left(\dfrac{Y_{21}}{\omega^2(C_1+C_p)C_2}\dfrac{1}{(1+\omega^2 Y_{21}^2 L_p^2)}\right)}{\left(\dfrac{Y_{21}}{\omega^2(C_1+C_p)C_2}\dfrac{1}{(1+\omega^2 Y_{21}^2 L_p^2)}\right)^2 + \left(\dfrac{(C_1+C_P+C_2)}{\omega(C_1+C_P)C_2} - \dfrac{\omega Y_{21}L_P}{(1+\omega^2 Y_{21}^2 L_p^2)}\dfrac{Y_{21}}{\omega(C_1+C_P)C_2}\right)^2}$$ (5.8)

$$C_d = \frac{\left(\dfrac{(C_1+C_P+C_2)}{\omega^2(C_1+C_P)C_2} - \dfrac{\omega Y_{21}L_P}{(1+\omega^2 Y_{21}^2 L_p^2)}\dfrac{Y_{21}}{\omega^2(C_1+C_P)C_2}\right)}{\left(\dfrac{Y_{21}}{\omega^2(C_1+C_p)C_2}\dfrac{1}{(1+\omega^2 Y_{21}^2 L_p^2)}\right)^2 + \left(\dfrac{(C_1+C_P+C_2)}{\omega(C_1+C_P)C_2} - \dfrac{\omega Y_{21}L_P}{(1+\omega^2 Y_{21}^2 L_p^2)}\dfrac{Y_{21}}{\omega(C_1+C_P)C_2}\right)^2}$$ (5.9)

In this analysis, the effect of the active device LF (low-frequency) noise on the carrier frequency is calculated by considering the frequency sensitivity as a small-signal noise perturbation near the nonlinear operating point of the oscillator circuit. The pushing factor is defined as [64,68]

$$K_{PF} = \frac{\Delta f_n}{\Delta v_n} \quad \text{(Hz/V)}$$ (5.10)

where Δv_n is the input noise voltage perturbation (across the base-emitter junction of the bipolar transistor or gate-source junction of the FETs) and Δf_n is the oscillator noise frequency (square root of the frequency noise spectral density: $\Delta f_n = \sqrt{\overline{|\Delta f_n^2|}}$).

From Figure 5-3, the variation of the capacitance C_d due to the LF (low frequency) noise perturbation Δv_n gives rise to a frequency and phase deviation of the oscillator frequency.

From Equation (5.10), the pushing factor of the oscillator can be described as

$$[K_{PF}]_{f=f_0} = \frac{\Delta f_0}{\Delta v_n} = \frac{1}{2\pi}\left[\frac{\Delta \omega_0}{\Delta V_n}\right] = \frac{1}{2\pi}\left[\frac{\partial \omega_0}{\partial C_d}\right]\left[\frac{\partial C_d}{\partial V_n}\right]$$ (5.11)

where

$$\frac{\partial \omega_0}{\partial C_d} = \frac{R_p \omega_0 \omega_{reso}}{2(\omega_{reso} R_p C_p + \omega_{reso} R_p C_d)} = \frac{R_p \omega_0 \omega_{reso}}{2(Q_r + \omega_{reso} R_p C_d)}$$

$$Q_r = \omega_{reso} R_p C_p, \; \omega_{reso} = \frac{1}{\sqrt{L_p C_p}}, \; \omega_0 = \frac{1}{\sqrt{L_{reso}(C_d + C_r)}}$$

From (5.11), the pushing factor at fundamental frequency f_0 can be given by

$$[K_{PF}]_{f=f_0} = \left[\frac{1}{2\pi}\right]\left[\frac{R_p \omega_0 \omega_{reso}}{2(Q_r + \omega_{reso} R_p C_d)}\right]\left[\frac{\partial C_d}{\partial v_n}\right]$$ (5.12)

Considering the same quality factor of the resonator at half of the operating frequency, $f_0/2$, the pushing factor of the oscillator circuit at $f_0/2$ can be given by

$$[K_{PF}]_{f=\frac{f_0}{2}} = \left[\frac{1}{2\pi}\right]\left[\frac{R_p\omega_0\omega_{reso}}{4(2Q_r + \omega_{reso}R_pC_d)}\right]\left[\frac{\partial C_d}{\partial v_n}\right] \tag{5.13}$$

Assuming that the factor $\dfrac{\partial C_d}{\partial v_n}$ is independent of the operating frequency of the oscillator,

the ratio of the pushing factor at f_0 and $f_0/2$ is given from Equations (5.12) and (5.13) as

$$\frac{[K_{PF}]_{f=f_0}}{[K_{PF}]_{f=\frac{f_0}{2}}} = \frac{2(2Q_r + \omega_{reso}R_pC_d)}{(Q_r + \omega_{reso}R_pC_d)} \approx 4 \quad for \quad Q_r > \omega_{reso}R_pC_d \tag{5.14}$$

Equation (5.14) is valid under the assumption that the resonator has a reasonably high Q factor, and the imaginary parts of the active device admittance are negligible with respect to the resonator susceptance. Therefore, $C_p > C_d$ and $Q_{reso} > \omega_{reso}R_PC_d$.

The single sideband (SSB) phase noise can be given in terms of the pushing-factor as [68]

$$[\pounds(f_m)] = 20\log\left[\frac{\Delta f_n}{\sqrt{2}f_m}\right] = 20\log\left[\frac{K_{PF}\Delta V_n}{\sqrt{2}f_m}\right] \text{ (dBc/Hz)} \tag{5.15}$$

From (5.15),

$$\frac{[\pounds(f_m)]_{f=f_0}}{[\pounds(f_m)]_{f=\frac{f_0}{2}}} = \frac{20\log\left\{\dfrac{[K_{PF}]_{f=f_0}\Delta V_n}{\sqrt{2}f_m}\right\}}{20\log\left\{\dfrac{[K_{PF}]_{f=\frac{f_0}{2}}\Delta V_n}{\sqrt{2}f_m}\right\}} \Rightarrow [\pounds(f_m)]_{f=f_0} = 12dB + [\pounds(f_m)]_{f=\frac{f_0}{2}} \tag{5.16}$$

From Equation (5.16), phase noise is worsened by 12dB/octave. This figure could be even larger because the value is calculated based on the simplified oscillator model. For real applications, the resonator and the LF noise characteristics of the active device degrade and become worse when they operate at twice the frequency.

Push-Push Configuration

Figure 5-4 shows the two identical oscillator circuits coupled through the arbitrary coupling network in the push-push configuration. The evaluation of pushing factor in the push-push configuration is carried out by considering uncorrelated noise voltage perturbation, Δv_{n1} and Δv_{n2}, associated with the two identical oscillator circuits, as shown in Figure 5-4.

From [38-40], due to the symmetry of the push-push oscillator topology, two modes (common and differential) exist, and the corresponding pushing factor is calculated in terms of the common mode (CM) and differential mode (DM) pushing factors.
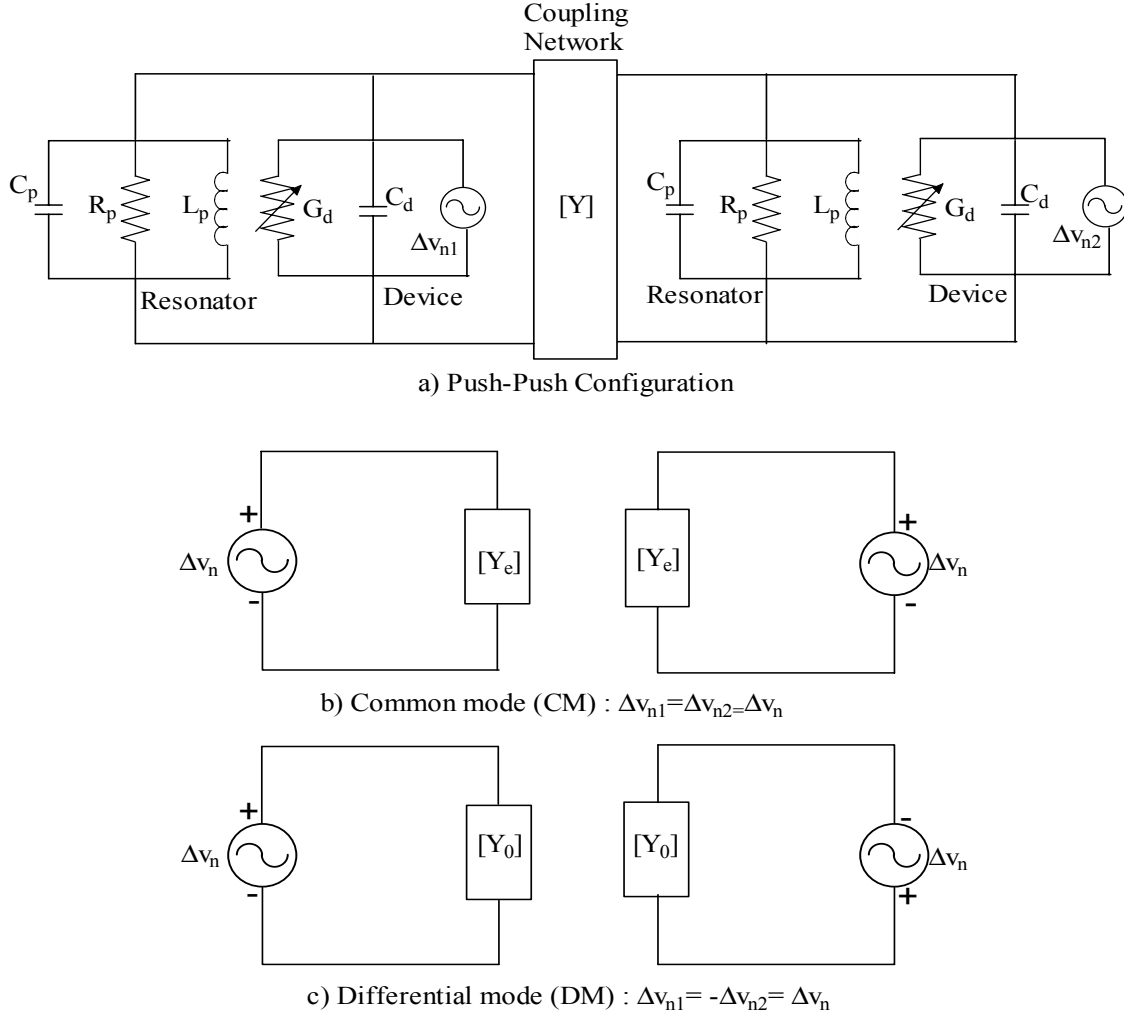

a) Push-Push Configuration

b) Common mode (CM) : $\Delta v_{n1} = \Delta v_{n2} = \Delta v_n$

c) Differential mode (DM) : $\Delta v_{n1} = -\Delta v_{n2} = \Delta v_n$

Figure 5-4: Two identical oscillator circuits coupled through the arbitrary coupling network in the push-push configuration. (a) Push-Push configuration; (b) common mode (CM); (c) differential mode (DM)

The frequency noise spectral density for the push-push topology can be given by

$$\left.\overline{\left|\Delta f_n^2\right|}\right|_{push-push} = \left([\Delta f_n]_{CM} + [\Delta f_n]_{DM}\right)^2 \tag{5.17}$$

$$\left.\overline{\left|\Delta f_n^2\right|}\right|_{push-push} = [K_{PF}]_{CM}^2 \overline{\left|\Delta v_n^2\right|}_{DM} + [K_{PF}]_{DM}^2 \overline{\left|\Delta v_n^2\right|}_{DM} + 2[K_{PF}]_{CM}[K_{PF}]_{DM}\left([\Delta v_n]_{CM} * [\Delta v_n]_{DM}\right) \tag{5.18}$$

where $[K_{PF}]_{CM}$ and $[K_{PF}]_{DM}$ are the common and differential mode pushing factors, and $[\Delta v_n]_{CM}$ and $[\Delta v_n]_{DM}$ are the common and differential mode noise perturbations.

The effect of the differential noise perturbation, due to the symmetry for the push-push topology, produces insignificant variation in the oscillating frequency, so $[K_{PF}]_{DM} \rightarrow 0$.

The common mode (CM) input noise perturbation of the circuit shown in Figure 5-4, can be given as

$$\overline{[\Delta v_n^2]}_{CM} = \overline{\left[\frac{\Delta v_{n1} + \Delta v_{n2}}{2}\right]^2} = \frac{1}{4}\left(\overline{[\Delta v_{n1}^2]} + \overline{[\Delta v_{n2}^2]} + \overline{[\Delta v_{n1} * \Delta v_{n2}]}\right) \qquad (5.19)$$

Since the input noise voltage perturbations Δv_{n1} and Δv_{n2} associated with the two identical active devices are uncorrelated, $\overline{[\Delta v_{n1} * \Delta v_{n2}]} = 0$.

Because the active devices (transistors) for the two identical oscillator circuits in push-push topology operate under the same working conditions, their input noise voltage perturbation can be described by the same statistic and is given as $\overline{[\Delta v_{n1}^2]} = \overline{[\Delta v_{n2}^2]}$.

From Equation (5.19),

$$\overline{[\Delta V_n^2]}_{CM} = \overline{\left[\frac{\Delta v_{n1} + \Delta v_{n2}}{2}\right]^2} = \left[\frac{\overline{[\Delta v_n^2]}}{2}\right] \qquad (5.20)$$

From Equation (5.18),

$$\overline{\left[\Delta f_n^2\right]}_{push-push} = [K_{PF}]_{CM}^2 \overline{[\Delta v_n^2]}_{CM} = [K_{PF}]_{CM}^2 \left[\frac{\overline{[\Delta v_n^2]}}{2}\right] \qquad (5.21$$

From Equations (5.10), (5.11) and (5.21),

$$[£(f_m)]_{push-push(f=f_0)} = 20\log\left\{\frac{[\Delta f_n]_{push-push}}{\sqrt{2}f_m}\right\} = -3dB + 20\log\left\{\frac{[K_{PF}]_{CM}\Delta v_n}{\sqrt{2}f_m}\right\} \qquad (5.22)$$

Equation (5.22) shows a 3dB improvement in phase noise with respect to the individual oscillator oscillating at half the frequency of the push-push frequency. The analysis agrees with the general equation of the N-coupled oscillator described by Equation (4.97).

The improvement in the phase noise of the push-push topology, referring to one individual oscillator, which oscillates at fundamental frequency f_0, can be expressed as

$$\frac{\left[\pounds(f_m)\right]_{push-push(f=f_0)}}{\left[\pounds(f_m)\right]_{fundamental(f=2\frac{f_0}{2})}} = \frac{20\log\left\{\dfrac{\left[\Delta f_n\right]_{push-push(f=f_0)}}{\sqrt{2}f_m}\right\}}{20\log\left\{\dfrac{\left[\Delta f_n\right]_{fundamental(f=2\frac{f_0}{2})}}{\sqrt{2}f_m}\right\}} \tag{5.23}$$

From Equations (5.10) and (5.15),

$$\left[\pounds(f_m)\right]_{push-push(f=f_0)} = -9dB + \left[\pounds(f_m)\right]_{fundamental(f=2\frac{f_0}{2})} \tag{5.24}$$

Since the noise sources of the two individual oscillators are uncorrelated, while the carrier powers add in phase, and therefore, a reduction of the phase noise in a push-push oscillator of 9 dB compared with the fundamental frequency of the individual oscillator composing push-push topologies.

From Equation (5.24), the push-push topology gives a 9 dB improvement in the phase noise compared to the fundamental frequency of the individual oscillator oscillating at f_0, twice the designed oscillating frequency of $f_0/2$.

Example

Figure 5-5 shows the schematic of the push-push oscillator with two identical oscillators. It consists of the two individual oscillator circuits, osc #1 and osc #2, which oscillates at half ($f_0/2$) of the push-push frequency (f_0). The individual oscillator circuit corresponding to the half-resonator oscillates at $f_0/2$ (1000 MHz) and is used as a starting point to verify the above noise analysis with respect to the push-push configuration.

The circuit shown in the Figure 5-5, is fabricated on 32 mil thickness Roger substrate of dielectric constant 3.38 and loss tangent $2.7 \cdot 10^{-4}$. As shown in Figure 5-5, the resonator is equivalently represented by the parallel RLC model (measured data at self-resonance frequency of 1000 MHz as R_P=12000Ω, L_P=5.2nH, C_P= 4.7pF), which acts as a resonator and also provides the required phase shift of 180 degree for the synchronization.

Figures 5-6, 5-7, and 5-8, show the simulated (Ansoft Designer) plot of the RF base current, phase noise, and output power for the push-push configuration (which is phase shifted by 180 degree in a mutually synchronized condition: f_0=2000MHz).
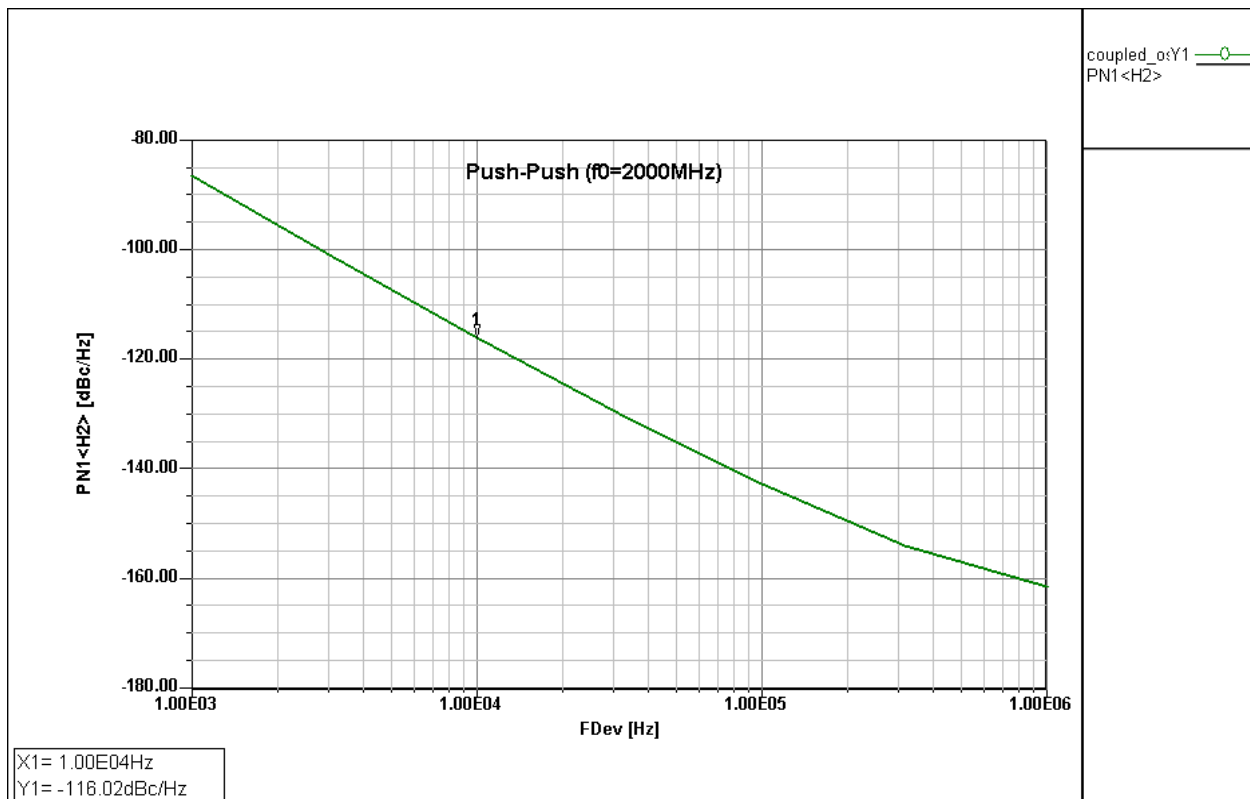
100 nH

100 nH

33 pF   100Ω   33 pF

Push-Push

(f_0)

1000 pF   22Ω   2280Ω   MSL R_{Load} MSL   2280Ω   22Ω

22 pF   50Ω

4000Ω   0.5 pF   4000Ω

12 V   Osc#1(f_0/2)   0.4 pF   0.4 pF   Osc#2(f_0/2)

Q_1 Resonator Q_2

3.3 pF   3.3 pF

2.2 pF $R_P = 12000\ \Omega$ 2.2 pF

$L_P = 5.2 nH$

10Ω $C_P = 4.7 pF$ 10Ω

$SRF = 1000 MHz$

100 nH   2.2 pF   2.2 pF   100 nH

330Ω   22 pF   330Ω   22 pF

MSL: Microstripline (w=15 mil, L=330 mil)

Q_1, Q_2: NEC 68830

Figure 5-5: Two identical oscillator circuits coupled through the resonator in the push-push configuration.

Osc#1

Ib1

Ib2

Osc#2

Y 1 [mA]

Time [nsec]

Figure 5-6: Simulated plot of the RF base current for the push-push configuration.

79

Figure 5-7: Simulated phase noise plot for the push-push configuration.
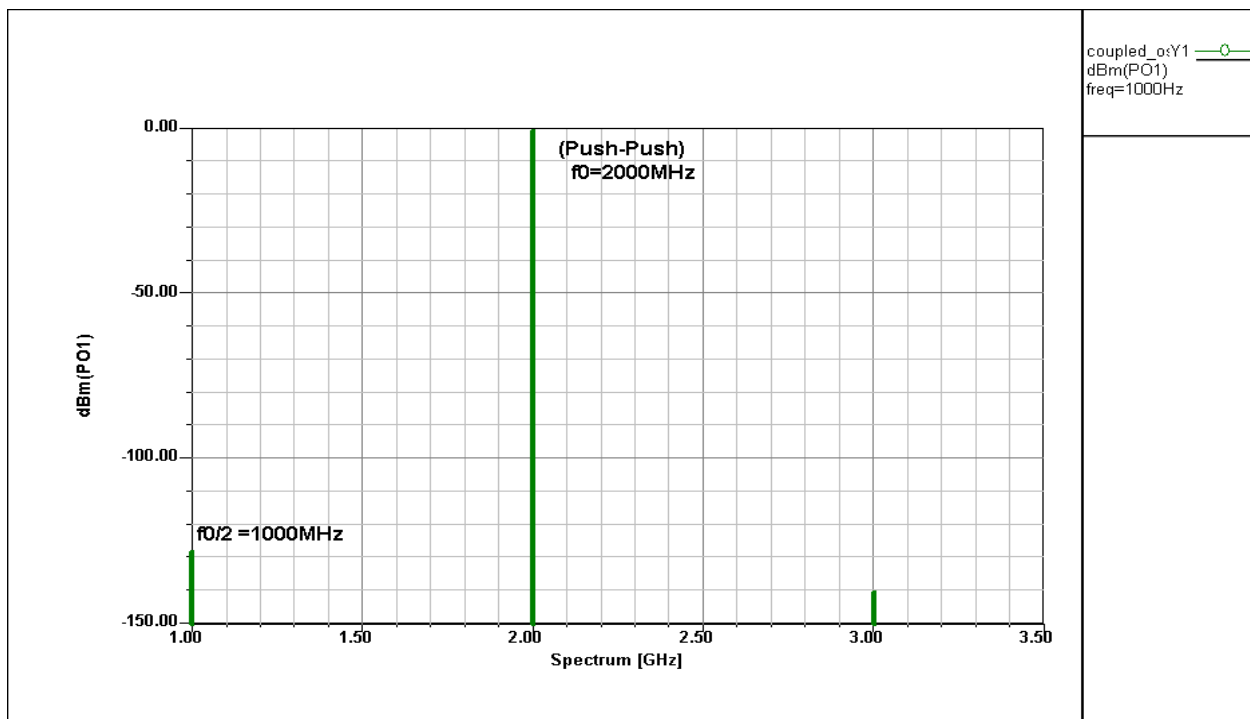
Figure 5-8: Simulated plot of the output power for the push-push configuration.

Figure 5-9 shows the schematic of the uncoupled individual oscillator circuit osc #1 for a comparative analysis of performance. The circuit is fabricated on 32 mil thickness Roger substrate of dielectric constant 3.38 and loss tangent $2.7 \cdot 10^{-4}$.

As shown in the Figure 5-9, the resonator is equivalently represented by a parallel RLC model (measured data at self-resonance frequency of 2000 MHz as $R_P = 12000$ Ω, $L_P = 1.24$ nH, $C_P = 4.7$ pF).

The oscillator circuit osc #1 as shown in the Figure 5-9, oscillates at f_0 (2000 MHz) and is used as a reference for the comparative noise analysis with respect to the push-push configuration.
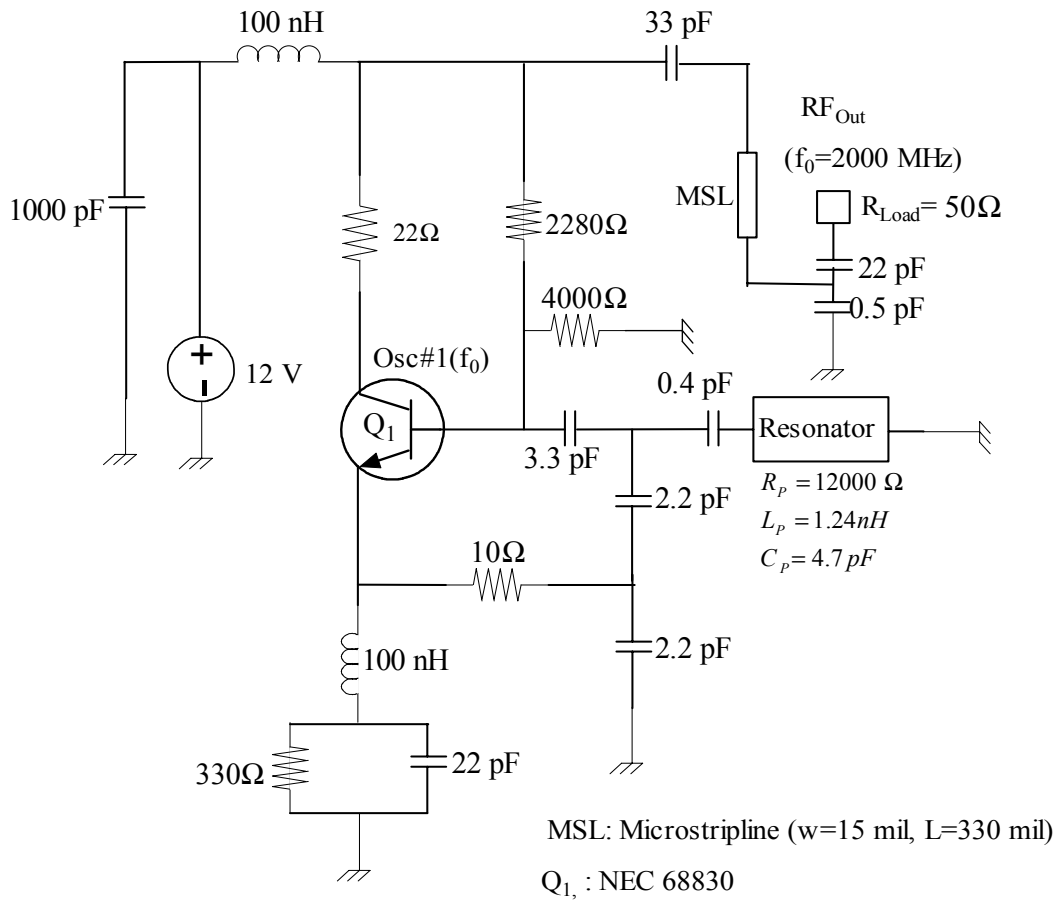
Figure 5-9: schematic of the uncoupled individual oscillator circuit Osc #1 (f_0= 2000MHz)

Figures 5-10 and 5-11 show the simulated (Ansoft Designer) plot of the phase noise and the output power for the individual uncoupled oscillator circuit shown in Figure 5-9.
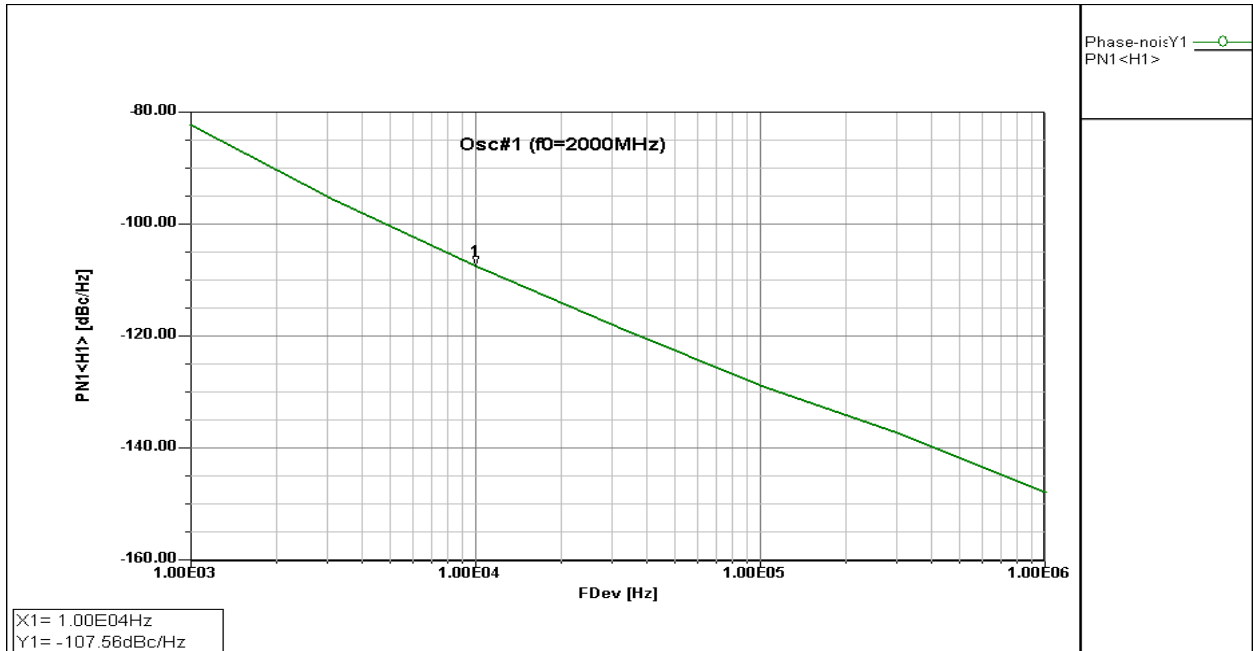
Figure 5-10: Simulated phase noise plot for the oscillator circuit shown in Figure 5-9.
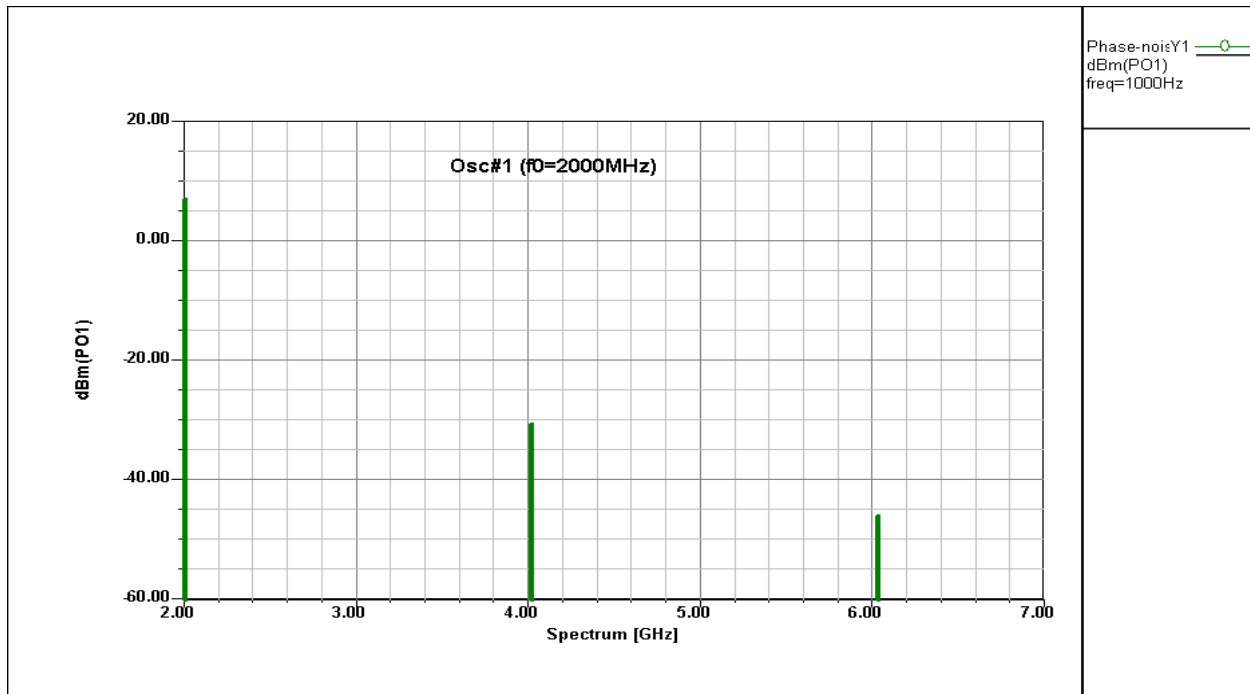
Figure 5-11: Simulated plot of the output power for the oscillator circuit shown in Figure 5-9.

From Figures 5-7 and 5-10, the improvement of the phase noise for the push-push topology at 10 KHz offset from the carrier is 8.46 dB, which agrees with the analytical expression given within 1 dB in Equation 5.24.

Figure 5-12 shows the measured phase noise plot for the push-push (f_0 = 2000 MHz) configuration and the uncoupled individual oscillator circuit (f_0 = 2000 MHz), shown in the Figures 5-5 and 5-9. The measured phase noise for the push-push configuration and the uncoupled individual oscillator at 10 kHz offset from the carrier is −113 dBc/Hz and −105 dBc/Hz, respectively.

The relative improvement in the measured phase noise of the push-push configuration, with respect to fundamental frequency of the oscillator in the push-push topology, is 8 dB, and agrees with the simulated (Ansoft Designer) and analytical values within 1 dB.

The discrepancy of 1 dB of the measured phase noise from the analytical value, Equation (5.23), can be attributed to the package parasitics, dynamic loaded Q, and tolerances of the component values of the two uncoupled individual oscillator circuits.
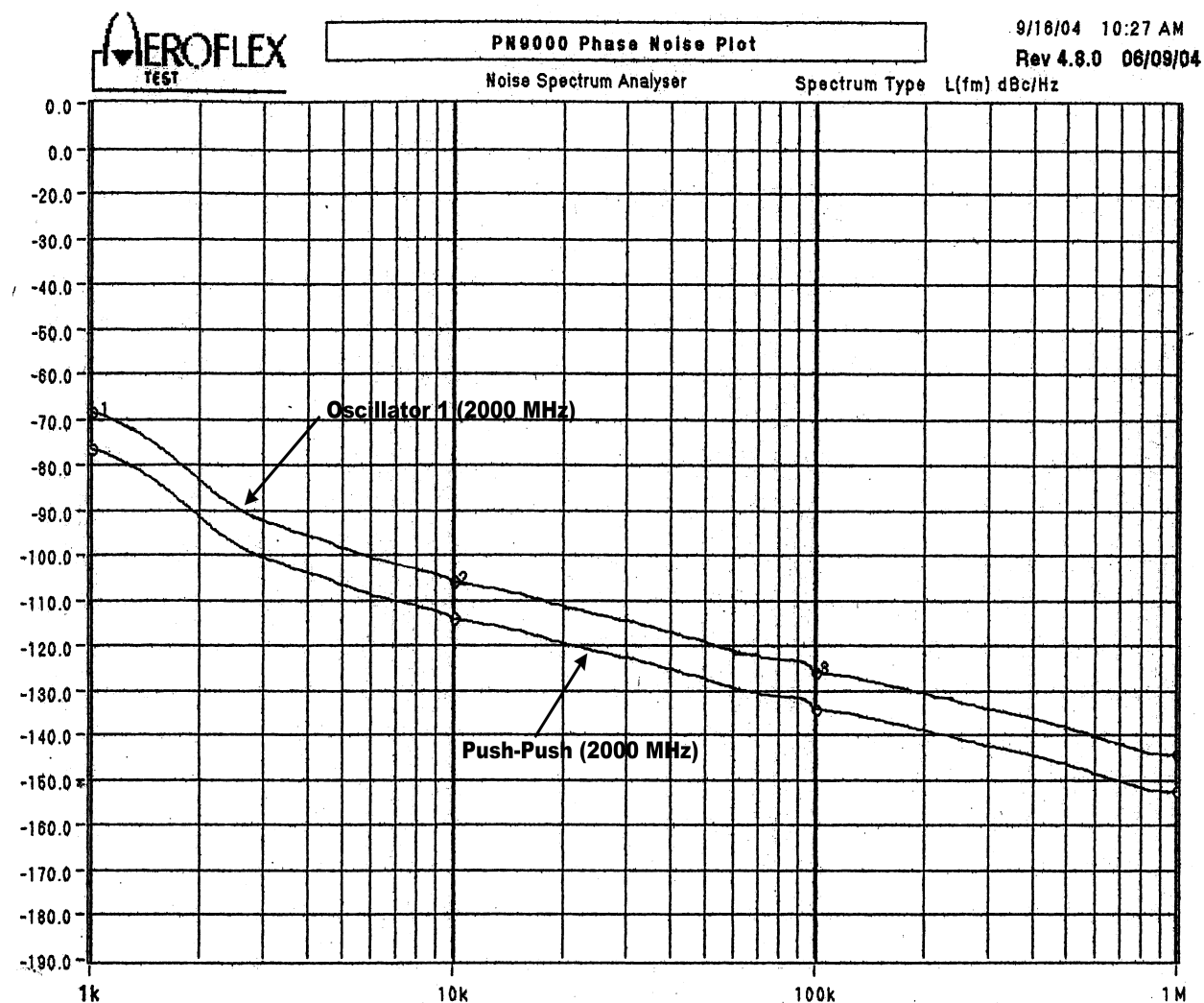
Figure 5-12:Measured phase noise plot for the push-push (f_0=2000 MHz) configuration and the uncoupled individual oscillator (f_0 =2000 MHz) circuit, as shown in Figures 5-5 and 5-9.

Chapter 6
Circuit and Device Characterization

6.1   Transistor Models

For the design of oscillators/VCOs, we are looking at members of active devices (bipolar and field-effect transistor), which are used to generate negative resistance in the oscillators/VCOs circuits. In the case of the bipolar transistor, conventional Si transistors are manufactured with an f_T up to 25 GHz, while SiGe transistors take over from this frequency range and are available up to 100 GHz if used as part of an RFIC. Their cousins, the heterojunction bipolar transistors (HBTs), based on GaAs technology, can achieve similar cut-off frequencies, but this technology is much more expensive for medium to large integrated circuits, and having higher flicker corner frequency noise. SiGe transistors have much lower flicker corner frequency noise and lower breakdown voltages (typically 2-3V). However, because of the losses of the transmission line in practical circuits, there is not much difference between HBT and SiGe oscillator noise as f_T is the same.

There is a similar competing situation between Bi-CMOS transistors implemented in a 0.12-micron technology and with GaAs FETs, specifically P-HEMTs. The GaAs FETs have a well-established performance with good models, and the Bi-CMOS transistors are currently being investigated as to what models are the best. Also, there is the *1/f* noise problem, specifically, with GaAs FETs more than with MOS transistors.

There are two types of models: 1) The models which describe DC and RF behavior are SPICE-type models, which means they can be incorporated in a frequency/time domain simulator and give a reasonable agreement with measured data, both in the DC as well as in the RF areas, and 2) linear RF microwave models based on equivalent circuits.

The use of linear models to predict oscillator behavior suffers from many limitations, which makes it difficult to accurately predict operating frequency and power. As attempts are made to improve oscillator performance by setting operating points further into nonlinear regimes, the ability to model these effects become critical since saturation can influence frequency of operation, power output, and efficiency. Therefore, designing oscillators/VCOs requires a more complete understanding of how the nonlinear aspects of the oscillator affect its operation. These models are used to describe the behavior of the transistors over a wide frequency, temperature and bias range, and their accuracy depends partially on the model. The most important factors are the input parameters used for the model. They are obtained from a process called parameter extraction. A successful path for generating model parameters has been the extraction of DC parameters and RF parameters such *S*-parameter sets under various bias and frequency conditions and curve fit them with analytic equations against this measured data [48-51].

Bipolar Transistors

For the purpose of this discussion, it should be assumed that the designers have the ability to do their own parameter extraction or receive this data from the transistor manufacturer, or in the case of a foundry, as part of the foundry service. Table 6-1 shows the measured data of BFP 520 provided from Infineon to further characterize the transistor.

SPICE parameters (Gummel- Poon Model, Berkley-Spice)

Parameters	BFP 520	Parameters	BFP 520	Package	BFP 520
IS	15E-18	MJC	0.236	C_{CB}	6.9fF
BF	235	XCJC	1	C_{CE}	134fF
NF	1	CJS	0E-15	C_{BE}	136fF
VAF	25	VJS	0.75	L_{BI}	0.47nH
IKF	0.4	MJS	0.333	L_{EI}	0.23nH
NE	2	TF	1.7E-12	L_{CI}	0.56nH
BR	1.5	XTF	10	L_{BO}	0.53nH
NR	1	VTF	5	L_{CO}	0.58nH
VAR	2	ITF	0.7	L_{EO}	0.05nH
IKR	0.01	PTF	50		
ISC	20E-15	TR	50E-9		
NC	2	EG	1.11		
RE	0.6	XTB	-0.25		
RB	11	XTI	0.035		
RBM	7.5	TNOM	298K		
FC	0.5	ISE	25E-15		
RC	7.6	VJE	0.958		
CJE	235E-15	MJE	0.335		
CJC	93E-15	VJC	0.661		

Table 6-1: SPICE parameters and package parameters of the Infineon transistor BFP520.

Large Signal Measurements

While the datasheets provided by the manufacturer are given under small signal conditions, small signal conditions mean power levels in the vicinity of –40 dBm. It is important to measure the device in the actual environments and bias conditions for the validation of the oscillators/VCOs circuits. The network analyzers used to measure these S-parameters, have bias tees built-in and have 90 dB dynamic ranges. Figure 6-1 shows the test fixture, which was generated to measure the large signal *S*-parameters for the device under test (DUT). The test fixture was calibrated to provide 50Ω to the transistor leads and a proper de-embedding has been done [50].
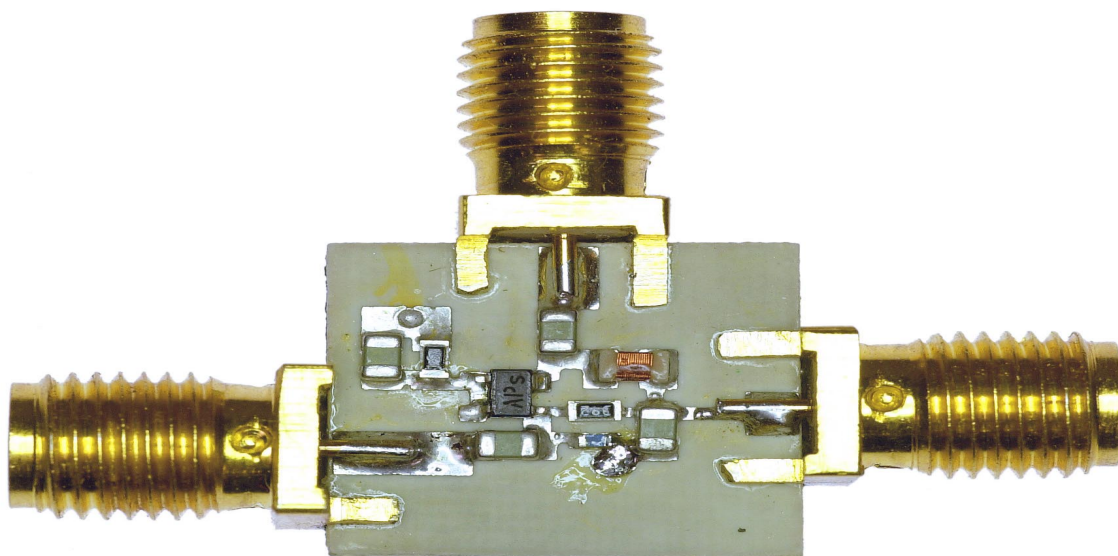
Figure 6-1   Test fixture to measure large signal *S*-parameters (A proper de-embedding has been done).

In the case of the oscillator, there is a large RF signal, voltage and current, imposed on the DC voltage/current. Assuming an RF output power from 0 dBm to 10 dBm, and assuming a 10-15 dB gain in the transistor, the RF power level driving the emitter/source or base/gate terminal is somewhere in the vicinity of –15 dBm. An RF drive of –15 dBm will change the input and output impedance of the transistor even if the transistor operates at fairly large DC currents.

Currents and voltages follow Kirchoff's law in a linear system. A linear system implies that there is a linear relationship between currents and voltages. All transistors, when driven at larger levels, show nonlinear characteristics. The FET shows a square law characteristic, while the bipolar transistor has an exponential transfer characteristic. It is important to note that the output impedances of FETs are much less RF voltage-dependent or power dependent than those of the bipolar transistor. The generation of large-signal S-parameters is, therefore, much more important for bipolar transistors than for FETs.

The definition of *S*-parameters in a large-signal environment is ambiguous compared to that of small-signal *S*-parameters. When an active device is driven with an increasingly higher level, the output current consists of a DC current and RF current, the fundamental frequency, and its harmonics. When the drive level is increased, the harmonic content rapidly increases. S_{12}, mostly defined by the feedback capacitance, now reflects harmonics back to the input. If these measurements are done in a 50 Ω system, which has no reactive components, then we have an ideal system for termination. In practical applications, however, the output is a tuned circuit or matching network, which is frequency selective. Depending on the type of circuit, it typically presents either a short-

circuit or an open-circuit for the harmonic. For example, suppose that the matching network has a resonant condition at the fundamental and second harmonic frequencies or at the fundamental and third harmonic frequencies (quarter-wave resonator). Then a high voltage occurs at the third harmonic, which affects the input impedance and, therefore, S_{11} (Miller effect).

This indicates that S-parameters measured under large-signal conditions in an ideal 50 Ω systems may not correctly predict device behavior when used in a non-50 Ω environment. A method called load pulling, which includes fundamental harmonics, has been developed to deal with this issue [52-56].

In the case of an oscillator, however, there is only one high Q resonator, which suppresses the harmonics of the fundamental frequency (short-circuit). In this limited case, the S-parameters stemming from a 50 Ω system are useful.

The following four plots, Figures 6-2 to 6-5, show S_{11}, S_{12}, S_{21}, and S_{22} measured from 50 MHz to 3000 MHz with driving levels from –20 dBm to 5 dBm. The DC operation conditions were 1.9 V and 20 mA, as shown in Figure 6-1.
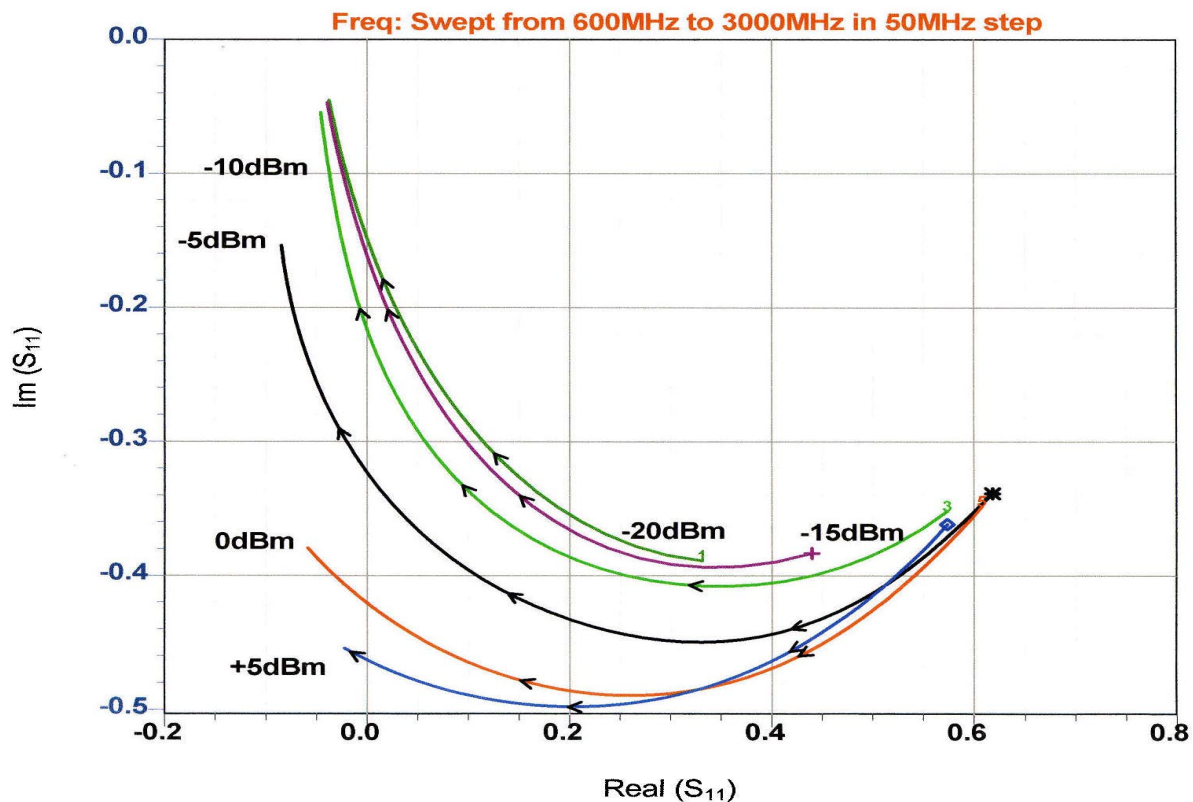
Figure 6-2: Measured large signals S_{11} of the BFP 520 (DC operating conditions were 1.9 V and 20 mA).

87
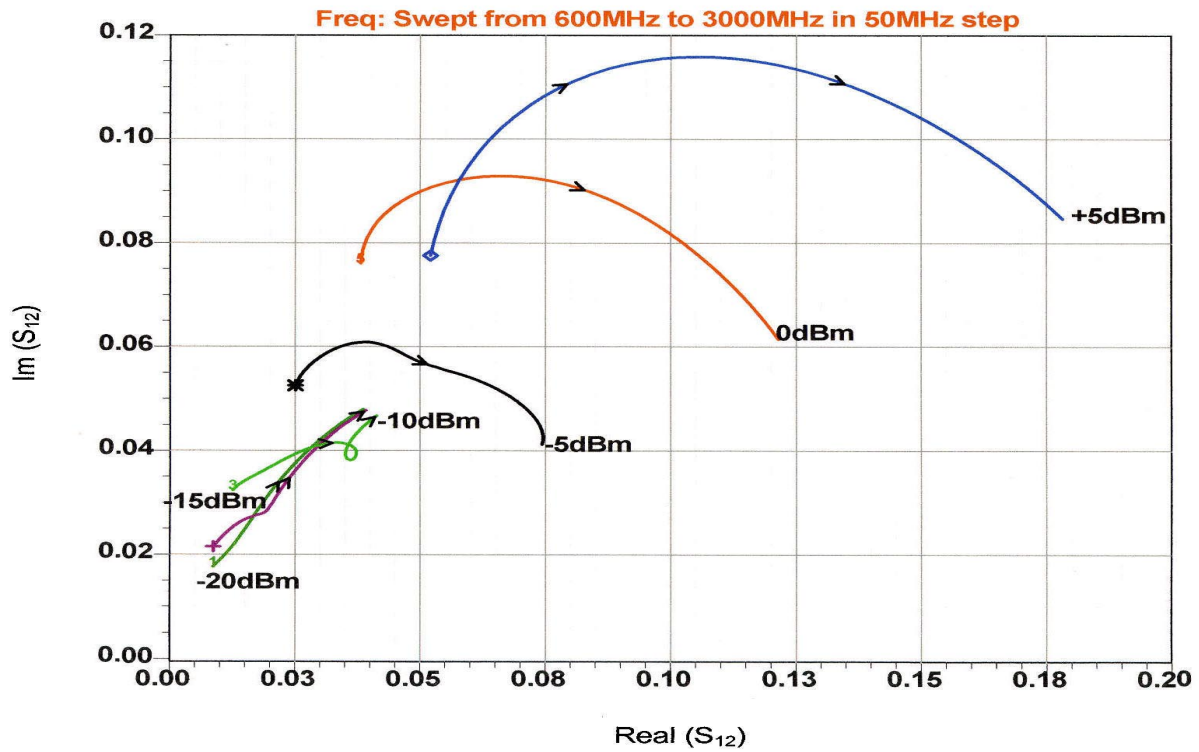
Figure 6-3: Measured large signal S_{12} of the BFP 520 (DC operating conditions were 1.9 V and 20 mA).
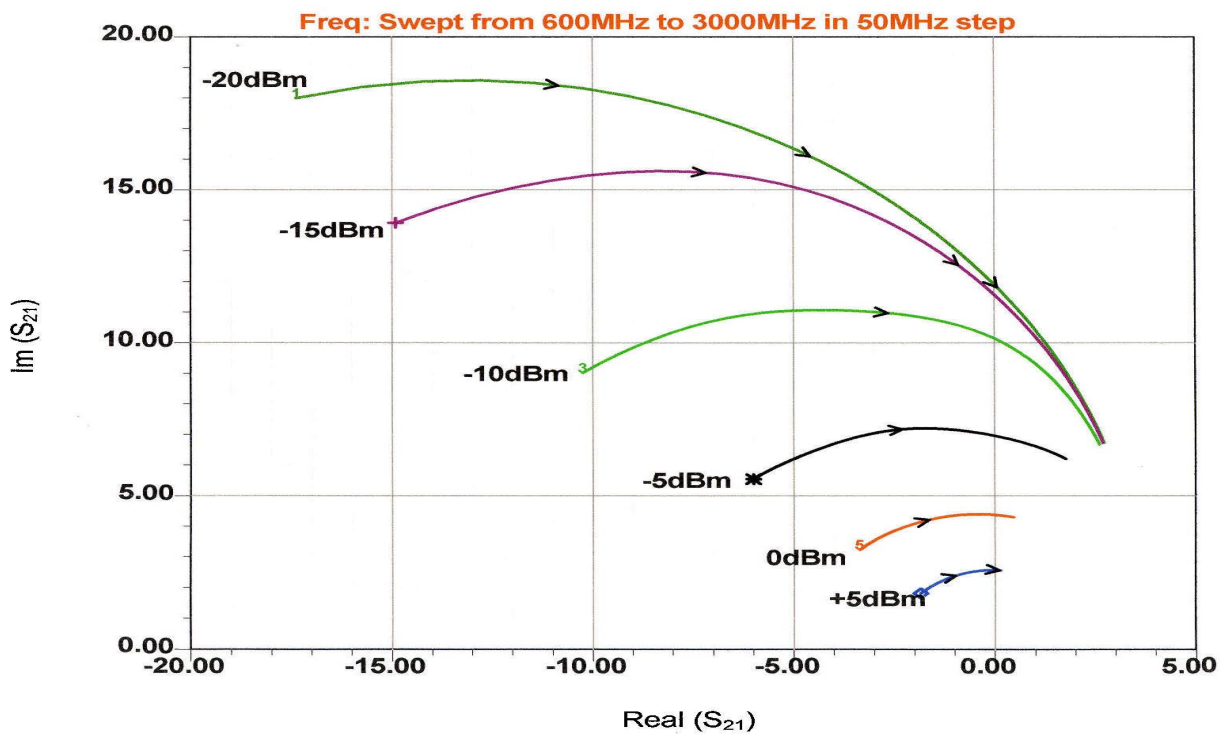
Figure 6-4: Measured large signals S_{21} of the BFP 520 (DC operating conditions were 1.9 V and 20 mA).

88
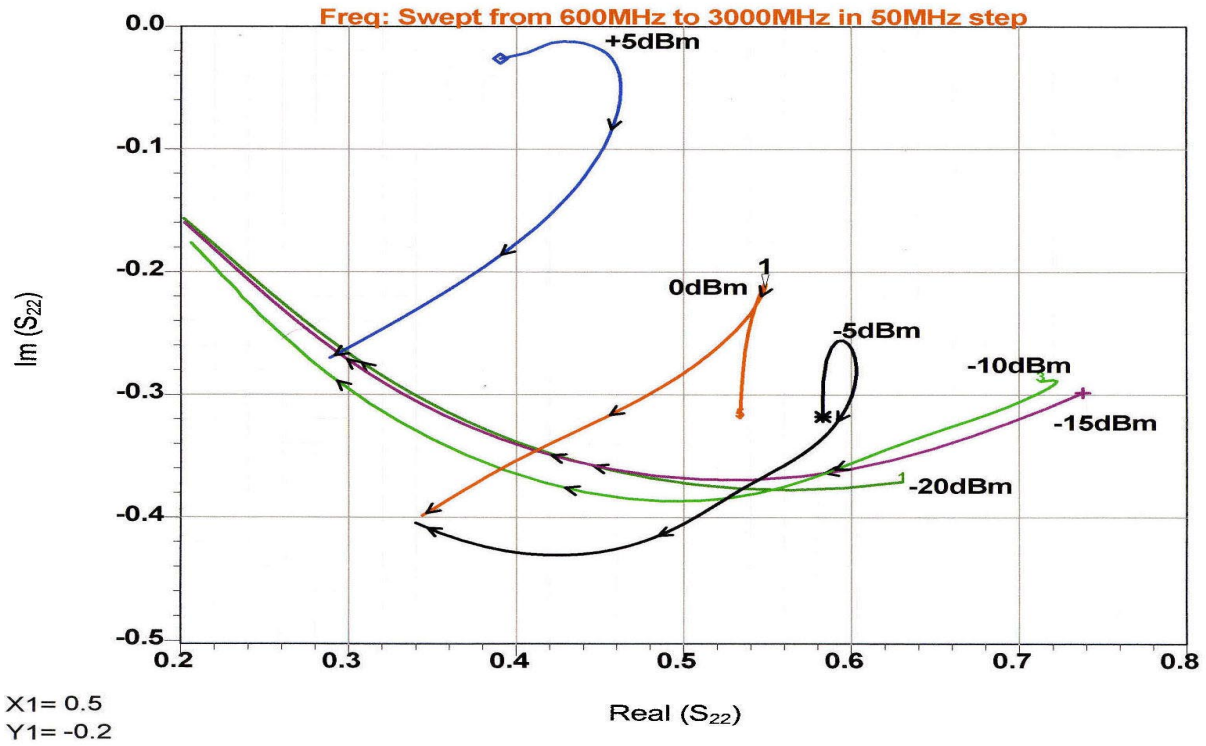
Figure 6-5: Measured large signal S_{22} of the BFP 520 (DC operating conditions were 1.9 V and 20 mA).

These large signals [S]-parameters are converted to [Z]-parameters as shown in the Figure 6-6 for determining the condition of oscillation.
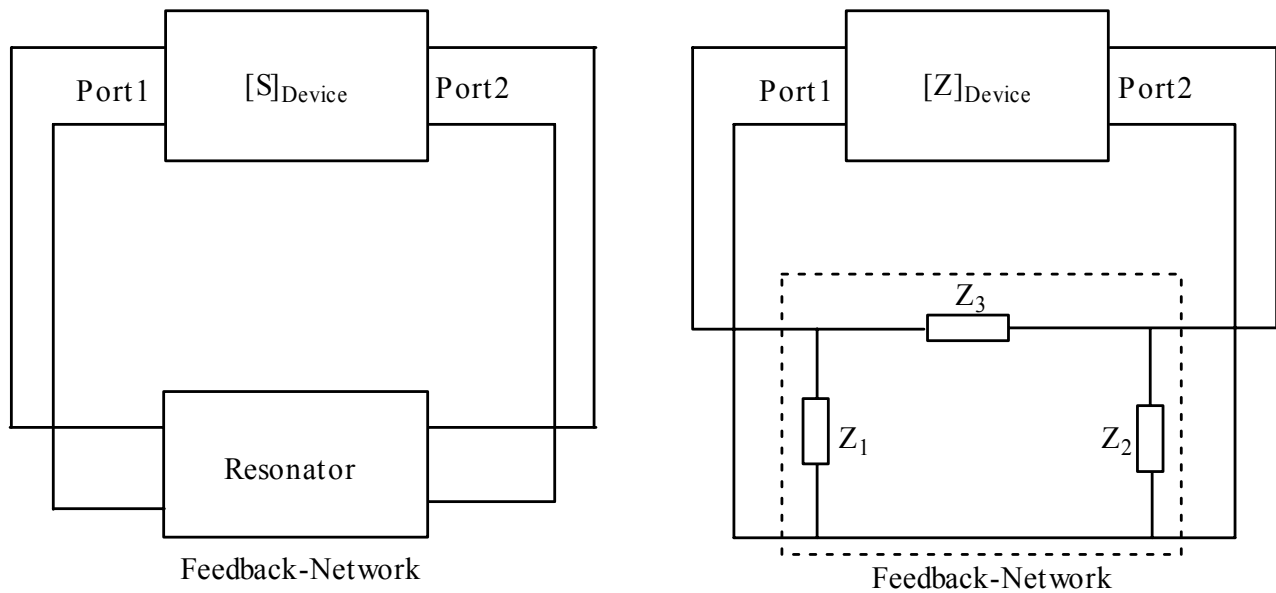

Figure 6-6: Two-port oscillator topology with large signal parameters.

From Figure 6-6, under steady state oscillation condition,

$$[Z_{in}]_{device}(Port1) + [Z_{in}]_{feedback}(Port1) = 0 \tag{6.1}$$

$$[Z_{out}]_{device}(Port2) + [Z_{out}]_{feedback}(Port2) = 0 \tag{6.2}$$

Figure 6-7 shows the equivalent model of the feedback oscillator for analysis of the insertion loss (G_{21}) and needed gain (G_{21}) with respect to the Q factor of the resonator.

The overall loading of the oscillator resonator is important, and the optimization of the loaded Q with respect to insertion loss (G_{21}) and needed gain (S_{21}) is dynamically done for ultra low noise performance over the tuning range.
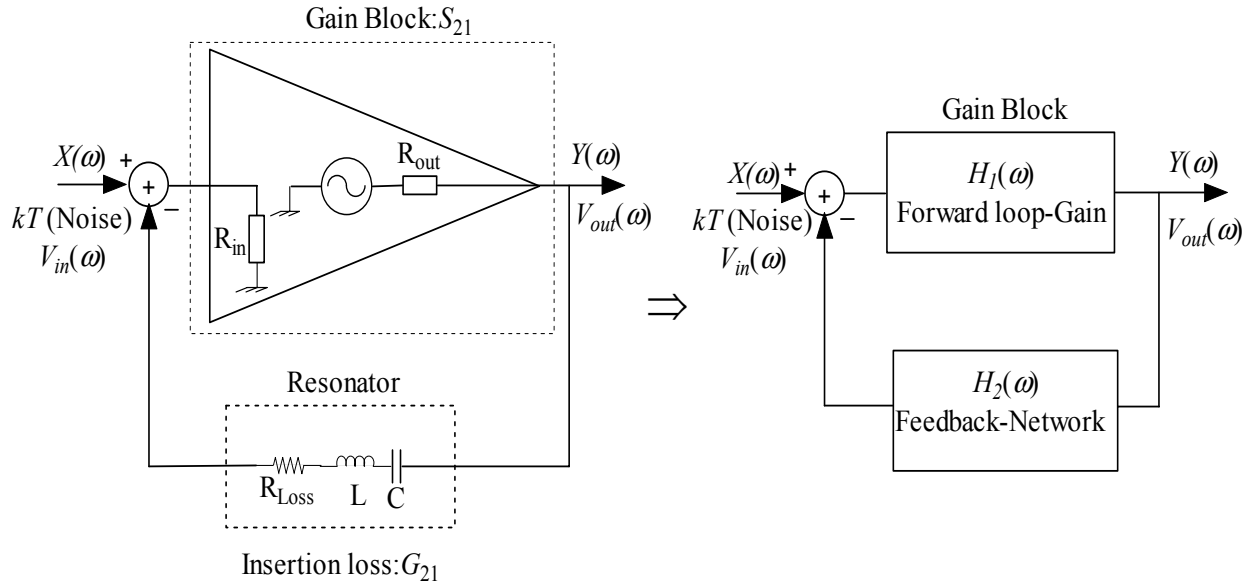
Figure 6-7:Equivalent model of the feedback oscillator.

The transfer function for Figure 6-7 is given by

$$[TF(j\omega)]_{closed-loop} = \frac{[Y(j\omega)]_{output}}{[X(j\omega)]_{input}} = \frac{V_o(\omega)}{V_{in}(\omega)} = \frac{H_1(j\omega)}{1 + H_1(j\omega)H_2(j\omega)} \tag{6.3}$$

The feedback coefficient between output and input can be expressed as

$$H_2(j\omega) = \frac{R_{in}}{(R_{Loss} + R_{in}) + j\left[\omega L - \dfrac{1}{\omega C}\right]} \tag{6.4}$$

The unloaded and loaded Q of the resonator are defined as

$$Q_0 = \frac{\omega_0 L}{R_{Loss}} \tag{6.5}$$

$$Q_L = \frac{\omega_0 L}{(R_{in} + R_{Loss} + R_{out})} \tag{6.6}$$

where ω_0 is the resonance frequency, Q_0 and Q_L are the unloaded and loaded Q of the oscillator.

From Equations (6.4) and (6.6),

$$H_2(j\omega) = \frac{R_{in}}{(R_{in} + R_{Loss}) + j\left[\omega L - \dfrac{1}{\omega C}\right]} \approx \frac{R_{in}}{(R_{in} + R_{Loss} + R_{out})\left[1 \pm j2Q_L \dfrac{\Delta\omega}{\omega_0}\right]} \tag{6.7}$$

defining

$$\omega L - \frac{1}{\omega C} = \pm 2\Delta\omega L$$

where $\Delta\omega$ is the offset frequency from the carrier frequency ω_0.

From Equations (6.5) and (6.6),

$$1 - \frac{Q_L}{Q_0} = \frac{(R_{in} + R_{out})}{(R_{in} + R_{Loss} + R_{out})} \tag{6.8}$$

From Equation (6.7), the feedback factor is given by

$$H_2(j\omega) = \frac{R_{in}}{(R_{in} + R_{Loss} + R_{out})\left[1 \pm j2Q_L \dfrac{\Delta\omega}{\omega_0}\right]} = \left[\frac{R_{in}}{(R_{in} + R_{out})}\right]\left[1 - \frac{Q_L}{Q_0}\right]\left[\frac{1}{1 \pm j2Q_L \dfrac{\Delta\omega}{\omega_0}}\right] \tag{6.9}$$

$$G_{21} \approx H_2(j\omega) = \frac{1}{2}\left[1 - \frac{Q_L}{Q_0}\right]\left[\frac{1}{1 \pm j2Q_L \dfrac{\Delta\omega}{\omega_0}}\right] \quad \text{for } R_{in} = R_{out} \tag{6.10}$$

Equation (6.10) describes the general equation for the variation of the insertion loss (G_{21}) of the resonator in the oscillator circuit in terms of the loaded and the unloaded Q. Figure 6-8 shows the plot of loaded Q versus insertion loss.
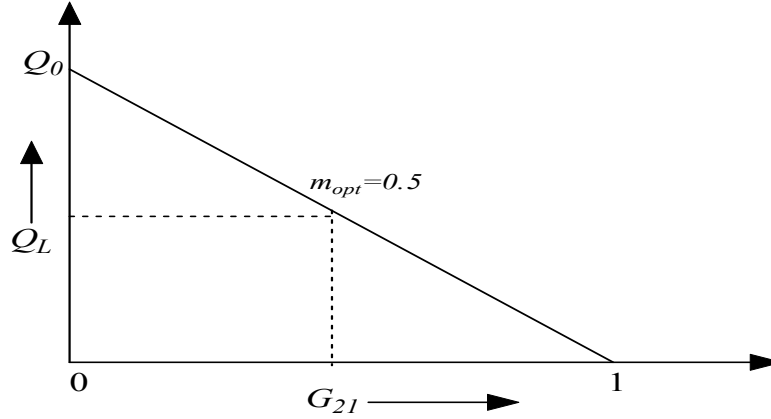
Figure 6-8: Loaded Q vs. insertion loss

For low phase noise performance, the insertion loss parameter (G_{21}) must be optimized dynamically over the tuning range for the application of the ultra low noise wideband VCOs, so that $m_{opt} = \dfrac{Q_L}{Q_0} = 0.5$, as given in Equation (6.48).

6.2 Tuning Diode Models

Varactors or voltage controlled capacitor are used as tuning elements (as variable capacitor) for the wideband voltage controlled oscillator (VCO) circuit and are mostly the Q factor limitation of the resonating network. Typically, the inductor is the second element that determines the Q. Tuning diodes are either abrupt or hyper abrupt. The abrupt junction is made with a linearly doped PN junction and typically has a capacitance change of 4:1 or less over the specified range of reverse bias, and are available with maximum reverse bias voltages between 5V and 60V. The higher voltages devices are advantageous as they lower the integration gain (MHz/V) of the oscillation, but require a large supply voltage. The hyper-abrupt junction has a nonlinear-doped PN junction that increases the capacitance change versus reverse bias in the order of 10:1 and more. The disadvantage of a hyper abrupt is its higher series resistance and its lower value of Q. Tuning diodes are manufactured in Si or GaAs technology. The GaAs process offers lower capacitance for the same resistance due to the higher electron mobility than Si. Hence, the Q of a GaAs varactor is better than that of silicon diode, but the flicker noise of a varactor made of GaAs is high, and therefore, the phase noise deteriorates.

For this work, Si-abrupt tuning diode, 1SV280 from Toshiba, is chosen. This diode has a very low series resistance, is low package parasitic and a tuning range of 1V to 15V. Table 6-2 shows the spice parameters of the 1SV280 for the purpose of further characterizing the tuning diode. Figure 6-9 (a) and (b) show the measured plots of series resistance R_S and the junction capacitance versus the reverse bias voltage. Figure 6-10 shows the plot of Q versus reverse voltage for frequencies of 2 GHz, 3.5 GHz, and 4.5GHz.

Spice parameters (Berkley-Spice parameters)

Parameters	1SV280	Parameters	1SV280	Package	1SV280
IS	5.381E-16	GC1	-1.669E-3	L_S	5E-10
N	1.037	GC2	1.303E4	L_P	1E-9
BV	15	GC3	-9.742E-6	C_P	8E-13
IBV	1E-6	V_J	3.272		
R_S	0.44	M	0.9812		
CJ0	6.89E-12	IMAX	10E-3		

Table 6-2: Spice and package parameters of the Toshiba 1SV280 varactor diode.
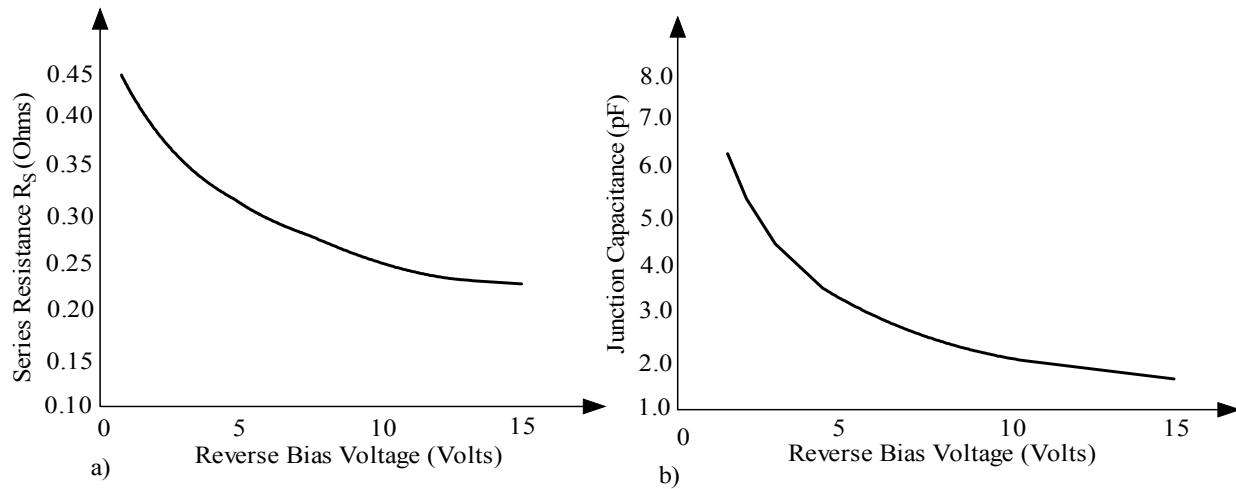
Figure 6-9: a) Measured series resistance and b) Measured capacitance vs. reverse bias voltage.
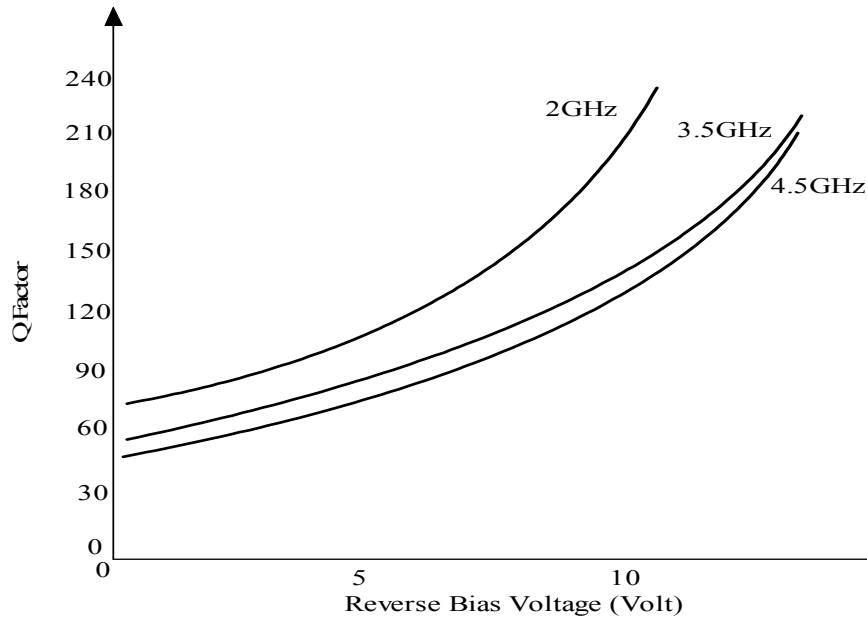
Figure 6-10: Measured Q factor vs. reverse voltage for Toshiba 1SV280 at 2 GHz, 3.5 GHz, and 4.5 GHz.

From Figures 6-9 and 6-10, it can be seen that the tuning diode shows a lower Q factor at low reverse bias voltages. The capacitance and the resistance are then at maximum values.

Tuning Characteristics and Loaded Q

For a fairly wide tuning range (more than octave band), hyper-abrupt tuning diodes are the best choice, but at the cost of a lower Q. Therefore, the phase noise performance is inferior to that provided by abrupt tuning diodes. In varactor-tuned VCOs, the tuning range is limited due to the resistive loading effect of the tuning diode. Figure 6-11 shows the equivalent circuit model of the varactor-tuned VCO, showing the varactor loading effect of the oscillator circuits.
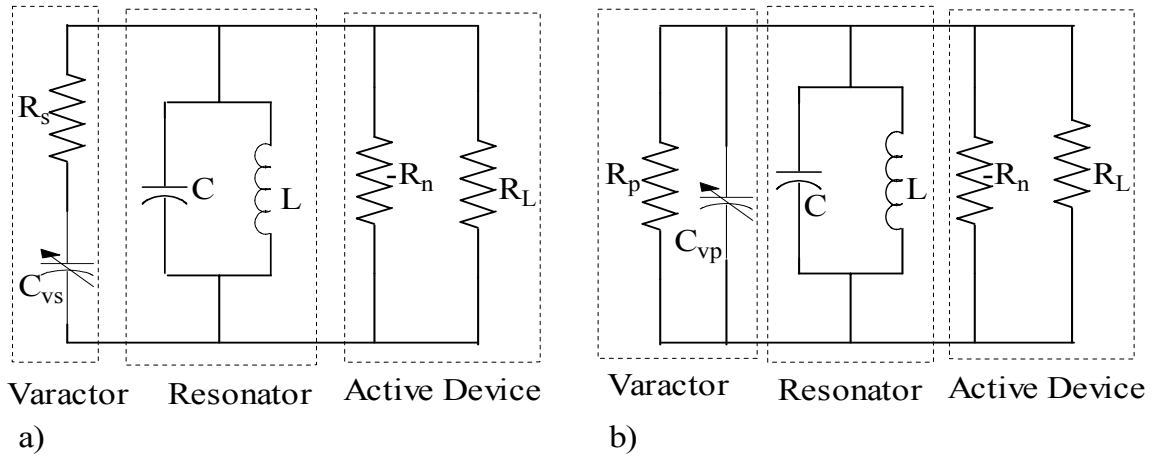
Figure 6-11: Equivalent circuit of the varactor-tuned negative resistance oscillator with the tuning diode represented by a) series RC (b) parallel RC.

The parasitics associated with the tuning diode are considered to be included in the equivalent resonator circuit of the oscillators/VCOs. The varactor capacitance C_v is a function of the tuning voltage, decreasing monotonically from C_{V0} at zero bias to C_{VB} at breakdown.

The capacitance ratio r is defined as

$$r = \frac{C_{V0}}{C_{VB}} > 1 \tag{6.11}$$

To simplify the analysis, the series resistance R_s given in Figure 6-11 (a) is assumed to be constant at all bias levels, and the equivalent parallel resistance R_P is given by

$$R_p = R_s\left[1 + Q_v^2\left(\frac{C_{v0}}{C_v}\right)^2\right] \cong R_s Q_v^2\left(\frac{C_{v0}}{C_v}\right)^2 \qquad \text{For } Q_v \gg 1 \tag{6.12}$$

where Q_v of the varactor is defined as

$$Q_v = \frac{1}{\omega R_s C_V} \tag{6.13}$$

The parallel equivalent capacitance of the tuning diode C_{vp} is given by

$$C_{vp} = \frac{C_{vs}}{\left[1 + \frac{1}{Q_v^2}\left(\frac{C_v}{C_{v0}}\right)^2 \right]} \cong C_{vs} \quad \text{for} \quad Q_v^2 \gg 1 \tag{6.14}$$

Without tuning diode, the resonant frequency and unloaded Q of the oscillator is given by

$$\omega_0 = \sqrt{\frac{1}{LC}} \tag{6.15}$$

$$Q_0 = \omega_0 CR \tag{6.16}$$

where $R = \left| -R_n \right| = R_L$

After the tuning diode is incorporated, the frequency of the oscillation can be tuned from ω_1 to ω_2 :

$$\omega_1 = \sqrt{\frac{1}{L(C + C_{v0})}} \tag{6.17}$$

$$\omega_2 = \sqrt{\frac{1}{L(C + C_{VB})}} \tag{6.18}$$

Practically, the difference between C_{v0} and C_{VB} is a small fraction of the total capacitance $(C + C_{V0})$. The fractional tuning range with respect to ω_1 can be expressed as a function of the capacitance ratio as

$$\frac{\Delta f}{f_1} = \frac{\omega_2 - \omega_1}{\omega_1} \cong \frac{1}{2}\left[\frac{C_{V0} - C_{VB}}{C + C_{V0}} \right] = \frac{1}{2}\left[\frac{1 - \frac{1}{r}}{1 + \frac{C}{C_{V0}}} \right] \tag{6.19}$$

The loaded Q of the oscillator at zero bias is defined as Q_L and can be given as

$$Q_L = \omega(C + C_{V0})\left[\frac{RR_sQ_v^2}{R + R_sQ_v^2}\right] = \left[\frac{Q_0Q_v^2}{\left(\dfrac{R}{R_s}\right) + Q_v^2} + \frac{Q_v}{1 + \left(\dfrac{R_s}{R}\right)Q_v^2}\right] \qquad (6.20)$$

$$\frac{Q_L}{Q_0} = \left[1 + \left(2r\frac{\Delta f}{f_1}\right)\frac{\left(\dfrac{Q_0}{Q_v} - 1\right)}{(r-1)}\right]^{-1} = \left[1 + (2rp)\frac{(q-1)}{(r-1)}\right]^{-1} \qquad (6.21)$$

where

$$p = \frac{\Delta f}{f_1} \ , q = \frac{Q_0}{Q_v}, \ Q_v\big|_{v=0} = \frac{1}{\omega R_s C_{V0}} \ \text{ and } \ Q_v\big|_{v=VB} = \frac{1}{\omega R_s C_{VB}}$$

The loaded Q of varactor-tuned VCOs reaches its lowest value at zero tuning voltage because varactor at zero bias introduces the greatest perturbation, and its own Q is lowest. For octave-band tunability, the ratio of the loaded Q to the unloaded Q is to be optimized for low noise performance as given in Equation (6.21).

6.3 Choice of the Resonator

The resonator acts as a frequency selective feedback network in the oscillator loop and has direct effect on the tunability and the phase noise performance. The resonator can be modeled as a series or parallel LCR equivalent circuit depending upon the topology of the oscillators/VCOs. A grounded base oscillator typically uses a parallel LCR resonator network, while a grounded emitter oscillator a series LCR representation. Figure 6-12 shows a resonator network consisting of a parallel *L-C* circuit having series loss resistances R_{sl} and R_{sc}.
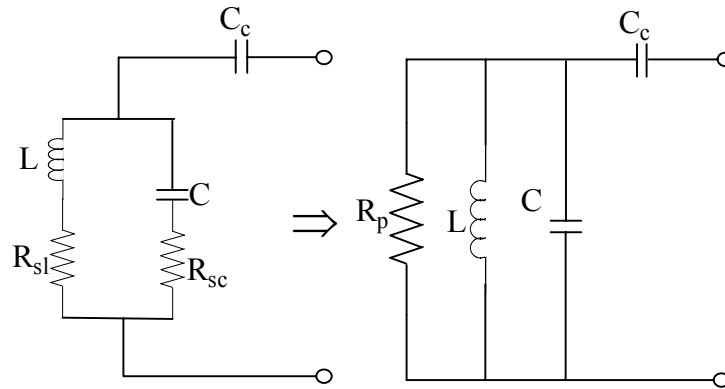

Figure 6-12: Equivalent representation of lumped resonator.

The quality factor of a resonator Q_R is defined as 2π times the energy stored in the circuit divided by the energy lost per cycle of oscillation.

$$Q_R = \left| \frac{2\pi(\frac{1}{2}CV_c^2)}{(\frac{2\pi}{\omega_0})(\frac{V_c^2}{2R_p})} \right| = \omega_0 C R_P \tag{6.22}$$

where V_c is the voltage across the capacitor and R_P is the parallel loss resistance associated with the resonator.

Similarly, Q_R can be expressed in terms of the inductor and parallel loss resistance as

$$Q_R = \left| \frac{2\pi(\frac{1}{2}LI^2)}{(\frac{2\pi}{\omega_0})(\frac{V_L^2}{2R_p})} \right| = \left| \frac{2\pi(\frac{1}{2}LI^2)}{(\frac{2\pi}{\omega_0})(\frac{\omega_0^2 L^2 I^2}{2R_p})} \right| = \frac{R_P}{\omega_0 L} \tag{6.23}$$

where $V_L == |jI\omega_0 L|$

Q_R in terms of inductor Q_L and capacitor Q_C can be given by

$$\frac{1}{Q_R} = \frac{1}{Q_L} + \frac{1}{Q_C} \Rightarrow Q_R = \left[Q_L^{-1} + Q_C^{-1} \right]^{-1} \tag{6.24}$$

where

$$Q_L = \frac{\omega_0 L}{R_{sl}} \text{ and } Q_C = \frac{1}{\omega_0 C R_{sc}} \tag{6.25}$$

where R_{sl} and R_{sc} are the series loss resistance associated with the inductor and capacitor.

The admittance of the inductance is given by

$$Y_L = \frac{1}{R_{sl} + j\omega L} = \left| \frac{\frac{\omega L}{Q_L} - j\omega L}{\frac{\omega^2 L^2}{Q_L^2} + \omega^2 L^2} \right| = \left[\frac{Q_L L}{\omega L^2 (1+Q_L^2)} - j\frac{LQ_L^2}{\omega L^2 (1+Q_L^2)} \right] \tag{6.26}$$

$$Y_L = \frac{1}{R_{PL}} - j\frac{1}{X_{PL}} \tag{6.27}$$

where

$$R_{PL} = \frac{\omega L(1+Q_L^2)}{Q_L} = R_{sl}(1+Q_L^2) \tag{6.28}$$

The equivalent representation of R_{sl} in terms of parallel resistance R_{PL} can be given as

$$R_{sl} = \frac{R_{PL}}{(1+Q_L^2)} \tag{6.29}$$

Similarly, R_{sc} in terms of parallel resistance R_{PC} can be expressed as

$$R_{sc} = \frac{R_{PC}}{(1+Q_C^2)} \tag{6.30}$$

For Q_L and $Q_C \gg 1$, $R_{PC} = R_{sc}Q_C^2$ and $R_{PL} = R_{sl}Q_L^2$

The equivalent parallel loss resistance R_P of the resonator tank will be a parallel configuration of R_{PC} and R_{PL} and can be given as

$$R_P = \frac{R_{PC}R_{PL}}{R_{PC}+R_{PL}} \tag{6.31}$$

The quality factor of the resonator circuit in terms of Q_L and Q_C is given as

$$Q_R = \left[\frac{1}{Q_L} + \frac{1}{Q_C} \right]^{-1} \tag{6.32}$$

$$Q_R = \frac{R_P}{\omega L} = \frac{\left[\frac{R_{PC}R_{PL}}{R_{PC}+R_{PL}} \right]}{\omega L} = \frac{R_{PC}R_{PL}}{[R_{PC}+R_{PL}]\omega L} \tag{6.33}$$

If the resistance value is fixed in the RLC resonator circuit, for a series resonant circuit, lower capacitance or higher inductance implies higher Q. For a parallel resonant circuit, lower capacitance or higher inductance means lower Q.

Coupled Resonators

The Q factor of the resonator can be increased by introducing coupling factor β, which is defined as the ratio of the series coupling capacitor to the resonator capacitor. Figure 6-13 shows two identical resonators with series coupling where Z_r and Z_c are the resonator and coupling network impedance, respectively.
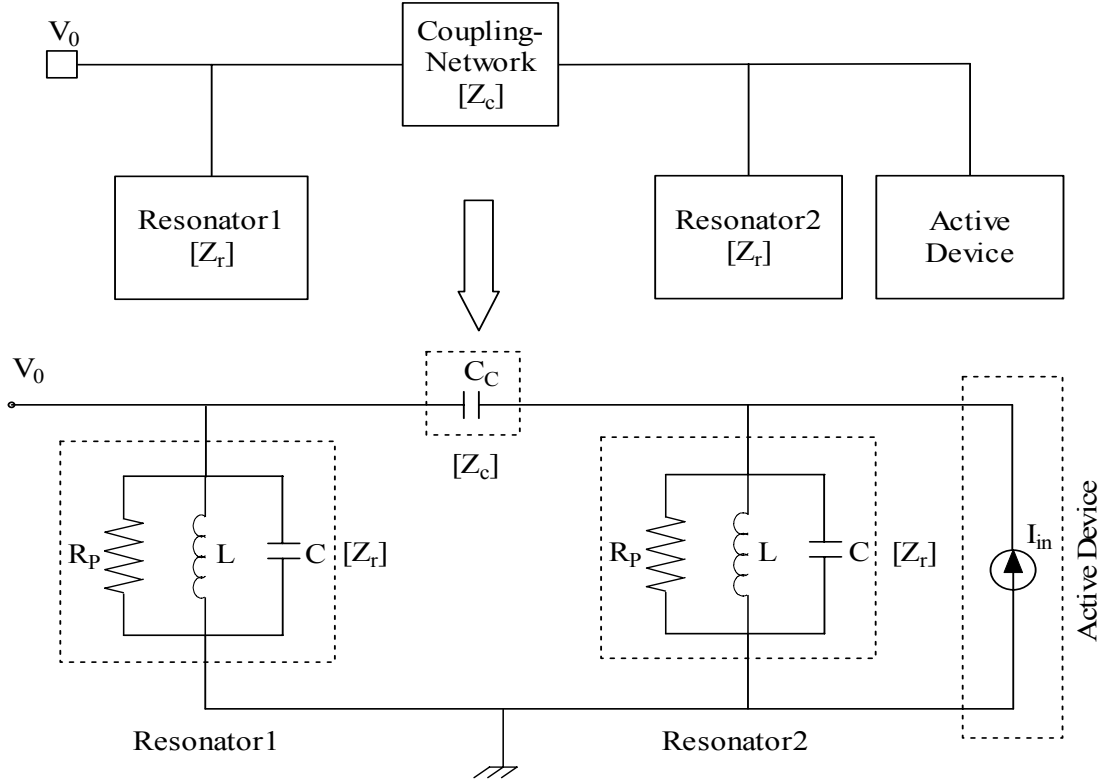
Figure 6-13: Series capacitive coupled resonator

The effective impedance of Figure 6-13 is given by

$$Z_{eff}(\omega) = \left[\frac{V_o}{I_{in}}\right] = \frac{Z_r(\omega)}{2 + \dfrac{Z_c(\omega)}{Z_r(\omega)}} = \frac{Z_r^2(\omega)}{Z_c(\omega) + 2Z_r(\omega)} \qquad (6.34)$$

where I_{in} is the large-signal current from active device.

$$Y_{eff}(\omega) = \frac{1}{Z_{eff}(\omega)} = \left[\frac{Z_c(\omega)}{Z_r^2(\omega)} + \frac{2}{Z_r(\omega)}\right] = \left[\frac{Y_r^2(\omega)}{Y_c(\omega)} + 2Y_r(\omega\right] \qquad (6.35)$$

For $Z_c(\omega) \gg Z_r(\omega)$, and assuming that the Q factor of $Z_r(\omega)$ is sufficiently large, the denominator of Equation (6.34) may be considered constant over the frequencies within the bandwidth of $Z_r(\omega)$. The coupling admittance is defined by $Y_c(\omega) = j\omega C_c$.

The resonator admittance is given by

$$Y_r(\omega) = \left[\frac{1}{R_P} + \frac{1}{j\omega L} + j\omega C\right] = \left[\frac{j\omega L R_P}{R_P(1 - \omega^2 LC) + j\omega L}\right]^{-1} \qquad (6.36)$$

From Equations (6.35) and (6.36) $Y_{eff}(\omega)$ can be rewritten as

$$Y_{eff}(\omega) = \left[\frac{2}{R_P} - \frac{2R_P(1-\omega^2 LC)}{\omega^2 LR_p^2 \beta C}\right] + j\left[\frac{[R_P^2(1-\omega^2 LC)^2 - \omega^2 L^2]}{\omega^3 R_P^2 L^2 \beta C} - \frac{2R_P(1-\omega^2 LC)}{R_P \omega L}\right] \quad (6.37)$$

From Equation (6.36), the phase shift of the coupled resonator is given as

$$\varphi = \tan^{-1}\left[\frac{\left(\dfrac{[R_P^2(1-\omega^2 LC)^2 - \omega^2 L^2]}{\omega^3 R_P^2 L^2 \beta C} - \dfrac{2R_P(1-\omega^2 LC)}{R_P \omega L}\right)}{\left(\dfrac{2}{R_P} - \dfrac{2R_P(1-\omega^2 LC)}{\omega^2 LR_p^2 \beta C}\right)}\right] \quad (6.38)$$

At resonance, the real part of $Y_{eff}(\omega)$ is reduced to zero, and the corresponding resonance frequency can be derived as

$$\text{Re}[Y_{eff}(\omega)]_{\omega=\omega_0} = \left[\frac{2}{R_P} - \frac{2R_P(1-\omega^2 LC)}{\omega^2 LR_p^2 \beta C}\right]_{\omega=\omega_0} = 0 \Rightarrow \omega_0^2 LC(1+\beta) = 1 \quad (6.39)$$

$$[\omega_0]_{\phi=90^0} = \frac{1}{\sqrt{LC(1+\beta)}} \quad (6.40)$$

$$[Y_{eff}(\omega)]_{\omega=\omega_0} = -j\left[\frac{R_P^2 \beta^2 C + (1+\beta)L}{\beta(1+\beta)\omega L R_P^2 C}\right] \quad (6.41)$$

$$Z_{eff}(\omega)]_{\omega=\omega_0} = j\left[\frac{\beta(1+\beta)\omega L R_P^2 C}{R_P^2 \beta^2 C + (1+\beta)L}\right] = j\left[\frac{\beta R_P^2 \omega C}{\dfrac{R_P^2 \beta^2 C}{(1+\beta)L} + 1}\right] \Rightarrow j\left[\frac{Q_0 \beta R_P}{1+Q^2 \beta^2}\right] \quad (6.42)$$

where $Q_0 = \omega CR_P = \dfrac{R_P}{\omega L}; \beta = \dfrac{C_c}{C}$

From Equation (6.38), the quality factor of the coupled resonator is given by [58-60]

$$[Q_{eff-coupled}(\omega)]_{\omega=\omega_0} = \frac{\omega_0}{2}\left[\frac{\partial \phi}{\partial \omega}\right] \Rightarrow \frac{2Q_0(1+\beta)}{(1+Q_0^2 \beta^2)} \quad (6.43)$$

$$[Q_{eff-coupled}(\omega_0)]_{\beta<<1} = \left[\frac{2Q_0(1+\beta)}{(1+Q_0^2\beta^2)} \right]_{\beta<<1} \approx 2Q_0 \qquad (6.44)$$

Weakly coupled resonators ($\beta<<1$) will produce high attenuation due to the large value of Z_c, so a trade-off between doubling the Q factor and the permissible attenuation is required for the best phase noise performance. For octave-band tunability, the coupling factor β is dynamically tuned and adjusted over the tuning range for low phase noise performance over the desired frequency range.

Example:

Figure 6-14 shows the schematic of a 1000 MHz parallel-coupled resonator based oscillator. This provides to some insight into the improvement of the phase noise of the coupled resonator based oscillator.
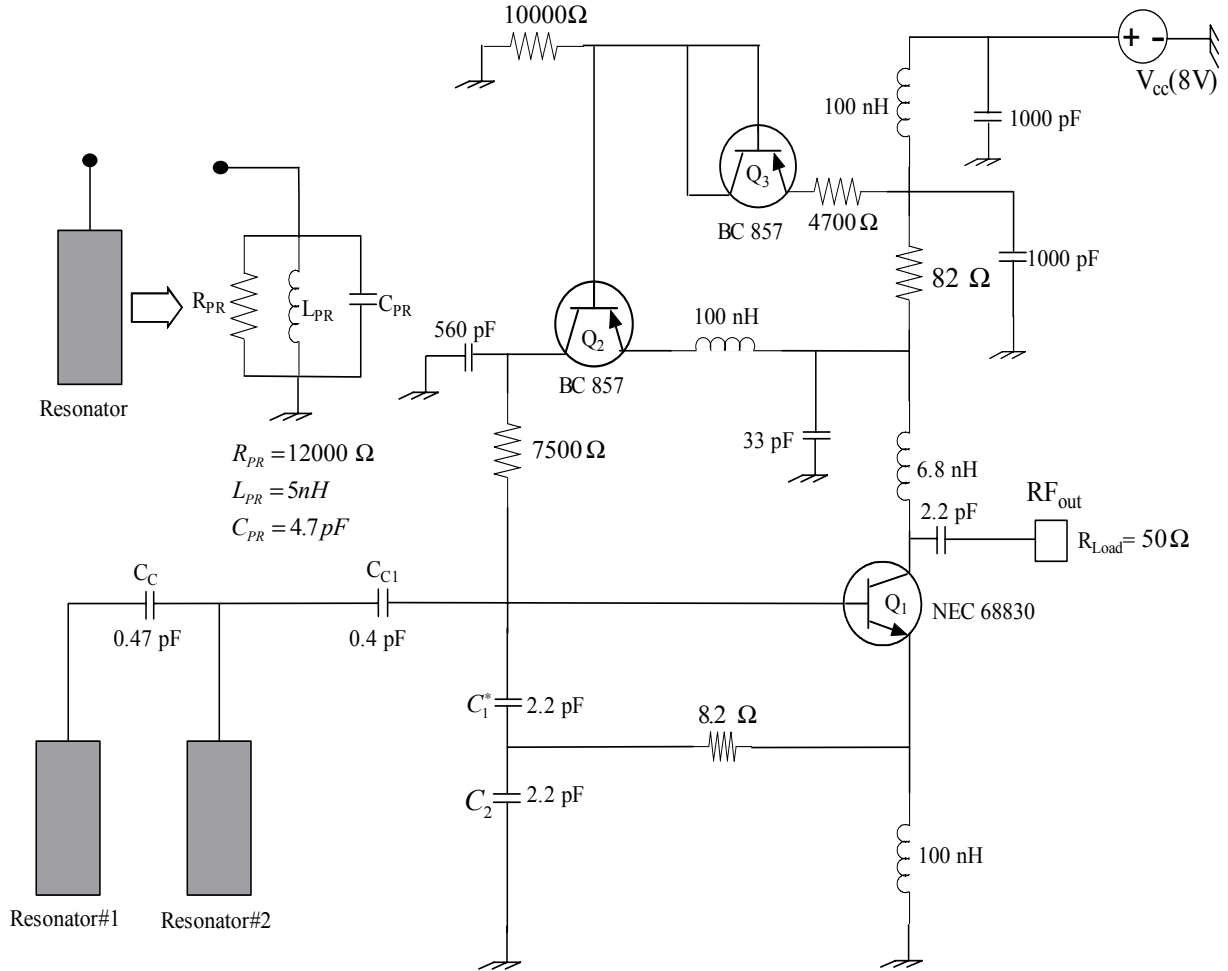
Figure 6-14: Schematic of the parallel-coupled resonator based oscillator.

Figure 6-15 shows the NE68830 transistor with the package parameters for the calculation of the oscillator frequency. Tables 6.2 shows SPICE and package parameters of NE68830 from data sheets.
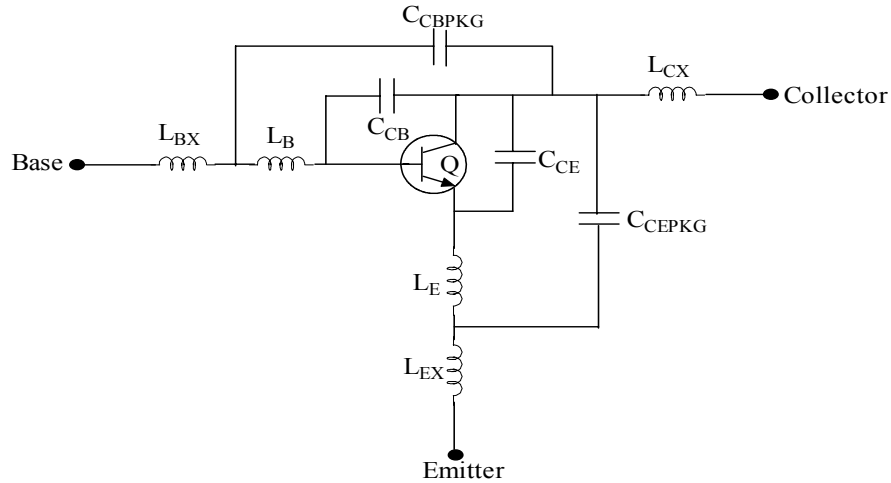

Figure 6-15: NE68830 with package parasitics (Q is the intrinsic bipolar transistor).

SPICE parameters (Gummel- Poon Model, Berkley-Spice)

Parameters	Q	Parameters	Q	Parameters	Package
IS	3.8E-16	MJC	0.48	C_{CB}	0.24E-12
BF	135.7	XCJC	0.56	C_{CE}	0.27E-12
NF	1	CJS	0	L_B	0.5E-9
VAF	28	VJS	0.75	L_E	0.86E-9
IKF	0.6	MJS	0	C_{CBPKG}	0.08E-12
NE	1.49	TF	11E-12	C_{CEPKG}	0.04E-12
BR	12.3	XTF	0.36	C_{BEPKG}	0.04E-12
NR	1.1	VTF	0.65	L_{BX}	0.2E-9
VAR	3.5	ITF	0.61	L_{CX}	0.1E-9
IKR	0.06	PTF	50	L_{EX}	0.2E-9
ISC	3.5E-16	TR	32E-12		
NC	1.62	EG	1.11		
RE	0.4	XTB	0		
RC	4.2	KF	0		
CJE	0.79E-12	AF	1		
CJC	0.549E-12	VJE	0.71		
XTI	3	RB	6.14		
RBM	3.5	RC	4.2		
IRB	0.001	CJE	0.79E-12		
CJC	0.549E-12	MJE	0.38		
VJC	0.65				

Table 6.2 SPICE parameters and package parameters of the NEC transistor NE68830.

The circuit shown in the Figure 6-14 is fabricated on 32 mil thickness Roger substrate of dielectric constant 3.38 and loss tangent $2.7 \cdot 10^{-4}$.

The frequency of the oscillation for the oscillator circuit given in Figure 6-14 is given by

$$\omega_0 = \sqrt{\left\{ \frac{\left(\frac{(C_1^* + C_P)C_2}{(C_1^* + C_P + C_2)} + C_{c1} \right)}{L_{PR}\left[\left(\frac{(C_1^* + C_P)C_2 C_{c1}}{(C_1^* + C_P + C_2)} \right) + C_{PR}\left(\frac{(C_1^* + C_P)C_2}{(C_1^* + C_P + C_2)} + C_{c1} \right) \right]} \right\}} \approx 1000 MHz \qquad (6.45)$$

with

$C_1^* = 2.2pF$, $C_1 = C_1^* + C_P$

$C_P = 1.1pF$ (C_{BEPKG} + Contribution from layout)

$C_1 = 2.2pF + 1.1pF(pacakage) = 3.3pF$; $C_2 = 2.2pF$, $C_{c1} = 0.4pF$

Resonator: $R_{PR} = 12000\Omega$, $C_{PR} = 4.7pF$, $L_{PR} = 5nH$

Figure 6-16 shows the simulated (Ansoft Designer) response of the single resonator (1-resonator) oscillator circuit having resonance at 999.8 MHz, or a less than 1% error. The little variation in resonant frequency may be due to the frequency dependent packaged parameters, but it is good starting value for the analysis of the coupled resonator based oscillator.
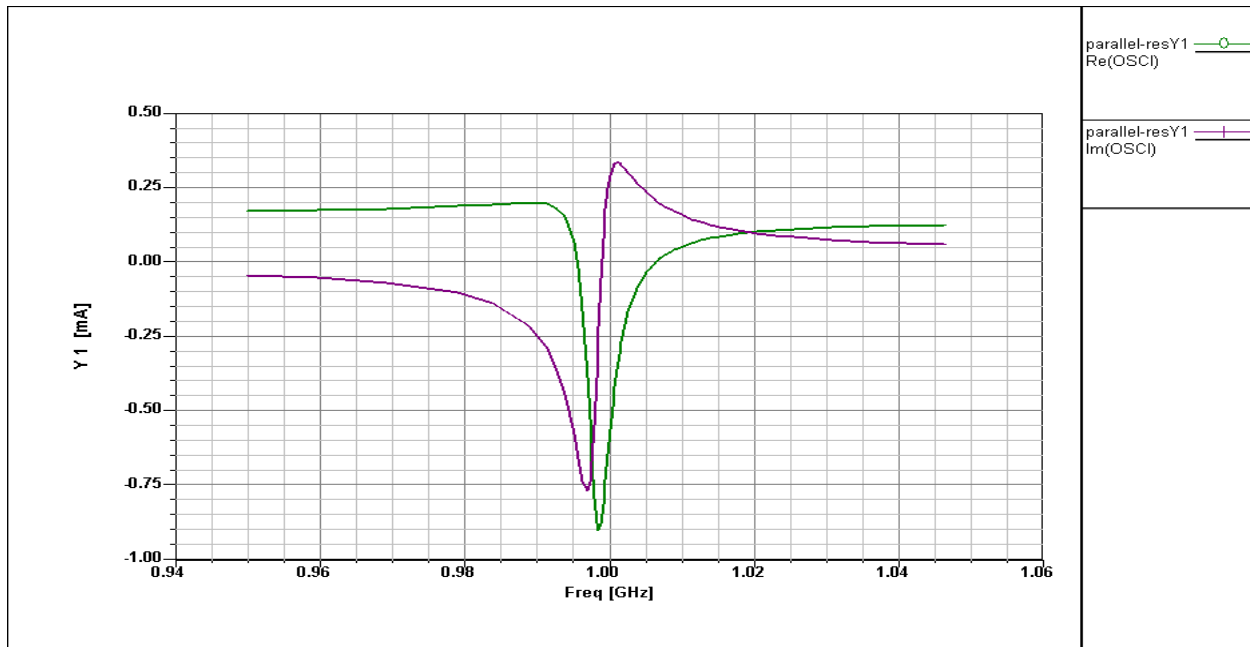

Figure 6-16: Simulated response of the real and imaginary current for oscillation.

Figures 6-17 (a) and 6-17 (b) show the simulated and measured phase noise plots for the single resonator (1-Resonator) and coupled resonator (2-resonator).
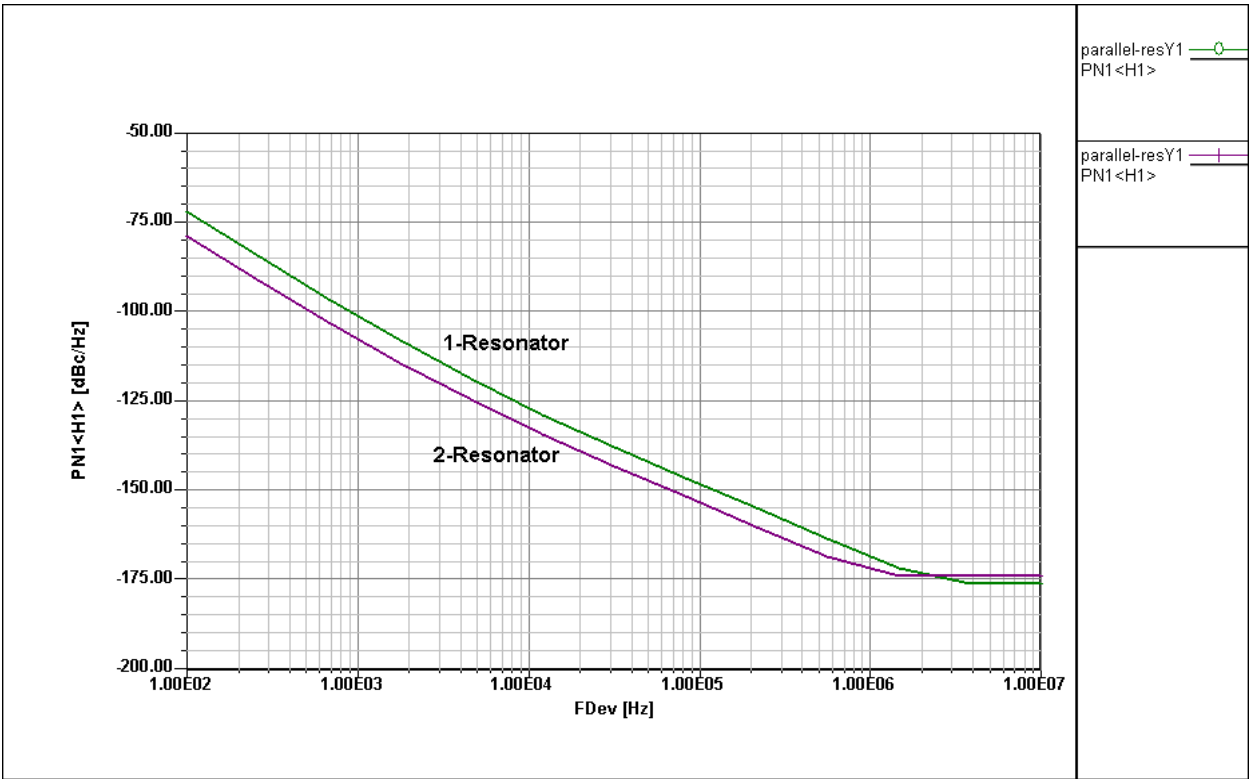

Figure 6-17 (a): Simulated phase noise plot for single resonator (1-Resonator) and coupled resonator (2-resonator).
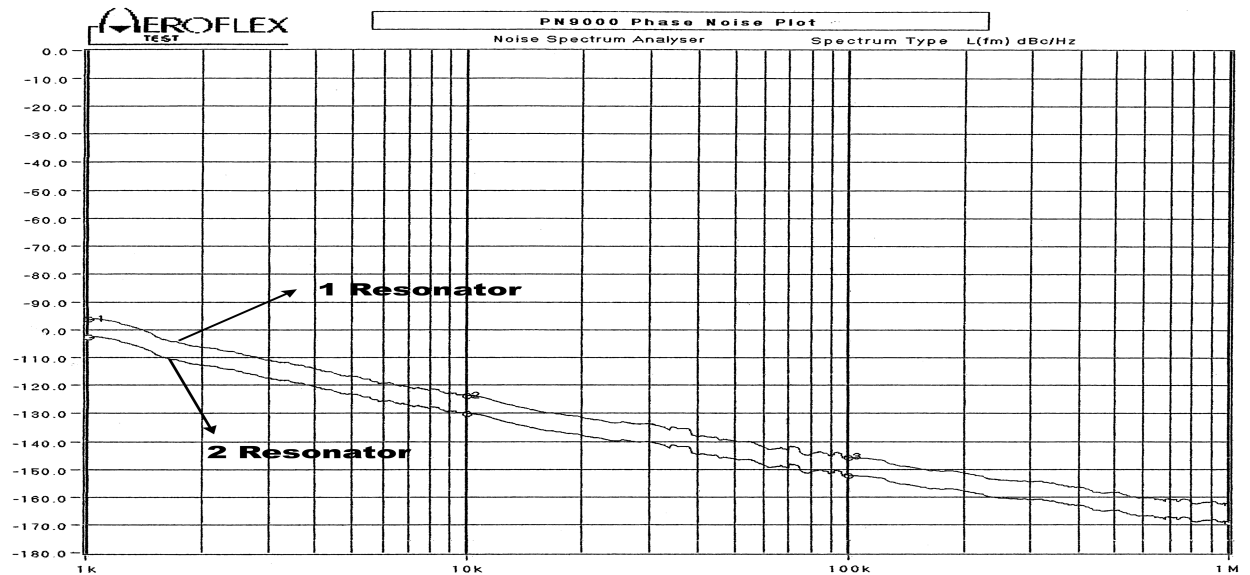

Figure 6-17 (b): Measured phase noise plot for single resonator (1-Resonator) and coupled resonator (2-resonator).

Optimum Phase Noise with Respect to the Loaded Q

The amount of the loading on a resonator is critical for optimum phase noise in VCOs. A very lightly loaded resonator will have a higher Q factor but will pass less power through it, whereas a heavily loaded resonator will have a very low Q factor but will pass more power through it. From Figure 6-18, the equivalent loading is R_{reso} in parallel with the series combination of $1/g_{ce}$ and R_L, and this represents the effective loading factor in the oscillator circuit for the grounded base configuration.
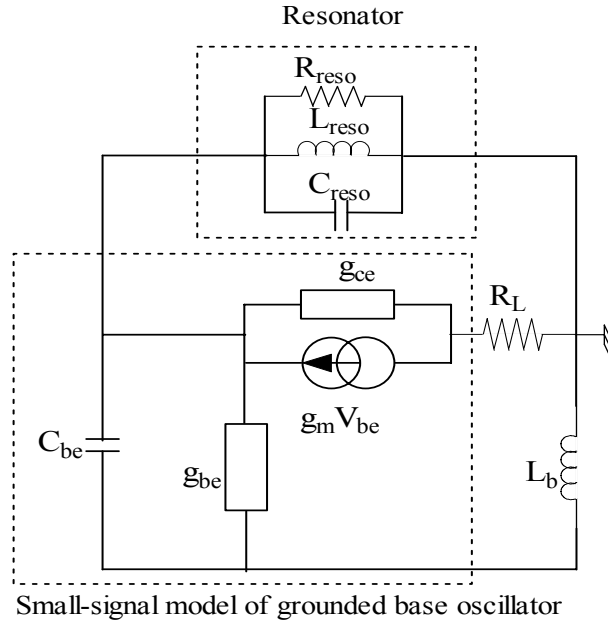
Figure 6-18: Small signal model of the grounded base oscillator.

From Equation (4.13), phase noise is given as

$$\pounds(f_m) = 10\log\left\{\left[1 + \frac{f_0^{\ 2}}{(2f_m Q_L)^2(1-m)^2}\right]\left(1 + \frac{f_c}{f_m}\right)\frac{FkT}{2P_0} + \frac{2kTRK_0^2}{f_m^2}\right\} \qquad (6.46)$$

$$\pounds(f_m) = 10\log\left\{\left[1 + \frac{f_0^{\ 2}}{(2f_m Q_0)^2 m^2(1-m)^2}\right]\left(1 + \frac{f_c}{f_m}\right)\frac{FkT}{2P_0} + \frac{2kTRK_0^2}{f_m^2}\right\} \qquad (6.47)$$

where $m = \dfrac{Loaded\ Q}{Unloaded\ Q} = \dfrac{Q_L}{Q_0}$

From Equation (6.47), the minimum phase noise can be found by differentiating the equation and equating to zero as $\dfrac{\partial}{\partial m}[\pounds(f_m)]_{m=m_{opt}} = 0$

$$\frac{d}{dm}\left[10\log\left\{\left[1+\frac{f_0^2}{(2f_mQ_0)^2m^2(1-m)^2}\right]\left(1+\frac{f_c}{f_m}\right)\frac{FkT}{2P_0}+\frac{2kTRK_0^2}{f_m^2}\right\}\right]=0 \Rightarrow m_{opt} \approx 0.5 \qquad (6.48)$$

Figure 6-19 shows the plot of relative phase noise versus the ratio of the loaded to the unloaded Q factor of the resonator. From Equation (6.48), typical phase noise plot with respect to m for the Figure 6-14, at 10 kHz offset from the carrier frequency is shown in the Figure 6-19. As illustrated in the Figure 6-19, for different values of the noise factor F ($F_1>F_2$), the phase noise plot is shifted symmetrically about the m_{opt}.

This implies that for low noise wideband application, the value of m should be dynamically controlled over the tuning range, and it should lie in the vicinity of m_{opt} for low noise performance over the frequency band [71, 74].
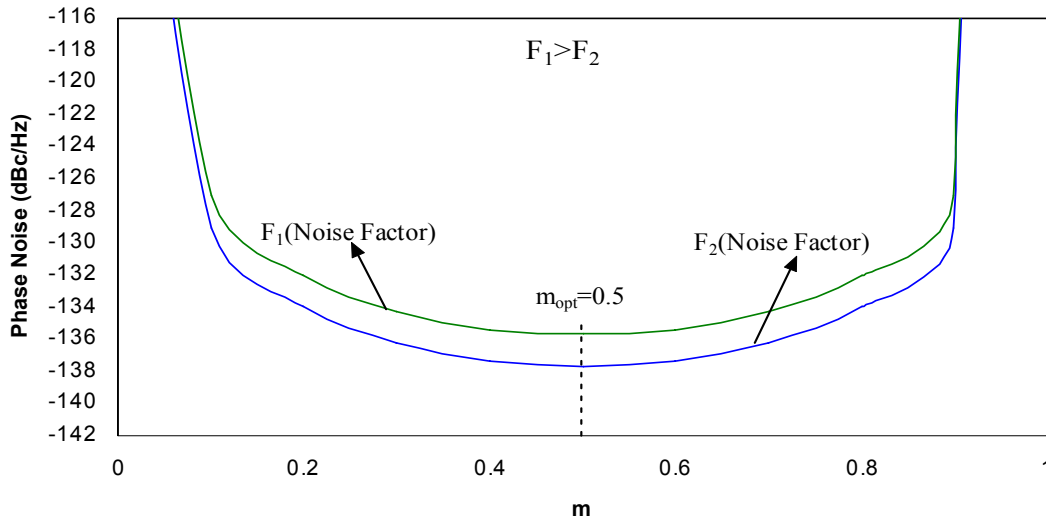

Figure 6-19: Typical phase noise versus the ratio of loaded to unloaded Q of the resonator.

Varactor Tuned Coupled Microstripline Resonator (Octave-Band)

The dynamic time average Q factor of the resonator, as well as the tuning diode noise contribution, sets the noise performance of the VCO, and in general, the dynamic loaded Q is inversely proportional to the frequency range of the VCO. The phase noise can vary dramatically over the tuning range of a wideband VCOs; therefore it is a major challenge to explore and find ways to realize uniform loaded Q over the tuning range (octave-band). The research described here explores a topology for the octave-band tunability. Figures 6-20 (a) and (b) depict the 2-D and 3-D view of the distributed coupled microstripline ($L \ll \lambda/4$: effectively parallel inductor for the operating frequency band) for the purpose of the evaluating the loaded Q of the resonator over the tuning range.
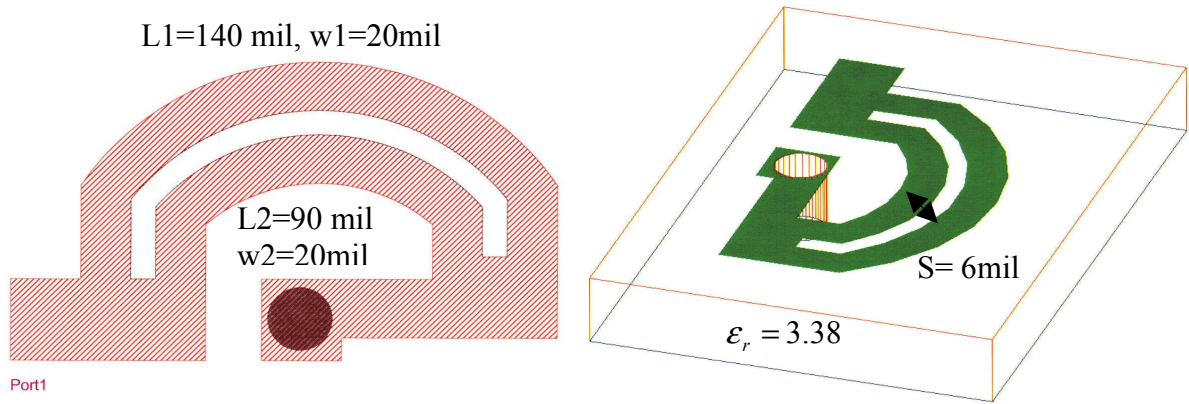
Figure 6-20: a) 2-D view of the coupled microstripline and b) 3-D view of the coupled microstripline (L<< λ/4; therefore Inductive for the desired frequency band).

As illustrated in the Figure 6-20, two-coupled branch of the half-circled distributed microstripline coupled lines are easily identifiable. One side of the coupled line is connected to the ground through a via-hole for the purpose of the DC return for the tuning diode network.

For wideband application, the length of the coupled microstripline is selected much shorter than the quarter wavelength, therefore, effectively it is inductive, and can be tuned over the desired frequency band by incorporating proper tuning diode network across the port 1 and via-hole. The frequency tuning range is determined by the usable capacitive tuning ratio of the tuning varactor and the parasitics associated with the tuning network because the parasitics deteriorate and limit the effective tuning capabilities of the varactors at high frequencies. For this work, the Si-abrupt tuning diode, 1SV280 from Toshiba, is chosen. This diode has a very low series resistance, low package parasitic and a tune range of 1V to 15V (section 6.2). Figure 6-21 shows the varactor tuned electrical equivalent circuit of the coupled microstripline structure as depicted in the Figure 6-20, where tuning diodes are mounted in anti-parallel arrangement for improved noise performance.
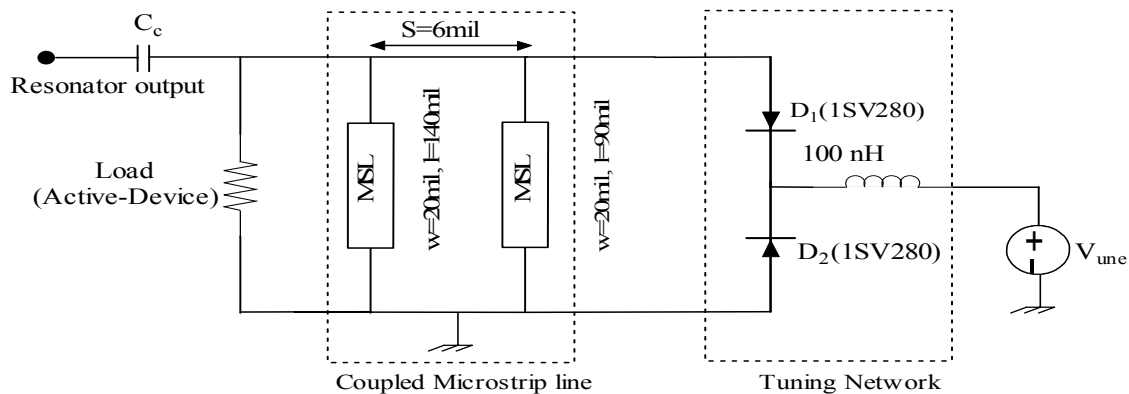

Figure 6-21: Varactor tuned coupled microstripline resonator circuit (MSL: microstrip transmission line).

The resonator circuit is fabricated on 32 mil thickness Roger substrate of dielectric constant 3.38 and loss tangent of $2.7 \cdot 10^{-4}$. The equivalent typical load of 212 Ω (Infineon BFP 520 transistor) across the emitter in the grounded base configuration (Vce =0.91V, Ic=12mA) for the frequency range (1500-4000 MHz) is connected across the resonator network for the purpose of the analysis of the loaded Q over the band.

The analysis of the coupled microstripline is done using 2.5D EM simulator (Ansoft Designer). Figure 6-22 (a) and (b) illustrate the plot of the loaded Q versus frequency for different values of spacing (s) and length (l/λ).
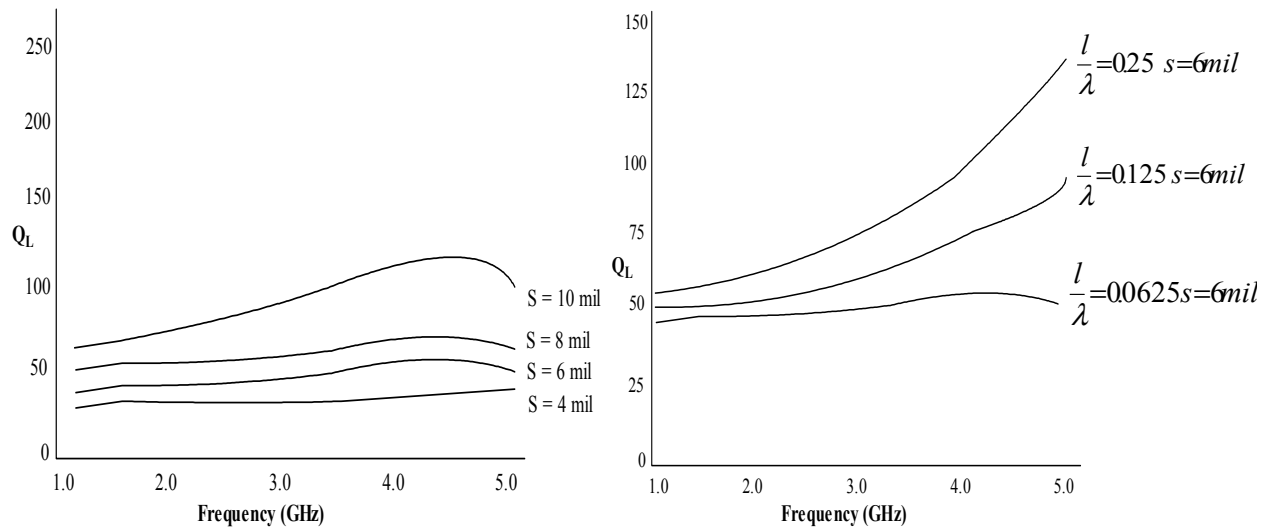

Figure 6-22: (a) Q_L vs. frequency for different values of 's' (b) Q_L vs. frequency for different values of 'l/λ'.

For wideband applications, the variation in the loaded Q over the tuning range should be kept minimum for uniform noise performance over the operating frequency band. The curve seen in Figure 6-22 shows the variation of the loaded Q with respect to spacing and length over the tuning range. As shown in the Figure 6-20, spacing between parallel microstripline is selected as s= 6 mil, which gives minimum variation in the loaded Q over the tuning range.

Figures 6-23 (a) and (b) show the simulated (Ansoft Designer) unloaded and loaded input impedance of the varactor tuned coupled resonator circuit, as shown in the Figure 6-21. From Figures 6-23 (a) and (b), for the simplification of the analysis, Q factor is evaluated graphically using 3dB bandwidth ($Q = \dfrac{f_0}{BW} = \dfrac{f_0}{f_H - f_L}$) of the varactor tuned coupled resonator circuit as shown in the Figure 6-21.
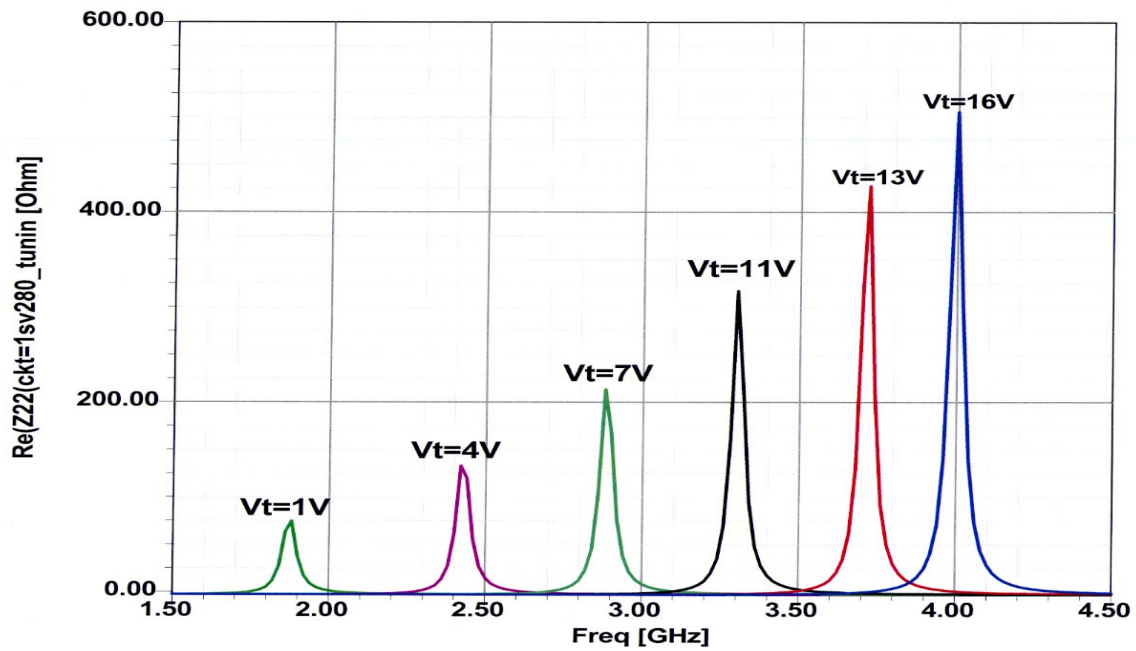
Figure 6-23 (a): Simulated unloaded input impedance of the varactor-tuned coupled resonator.
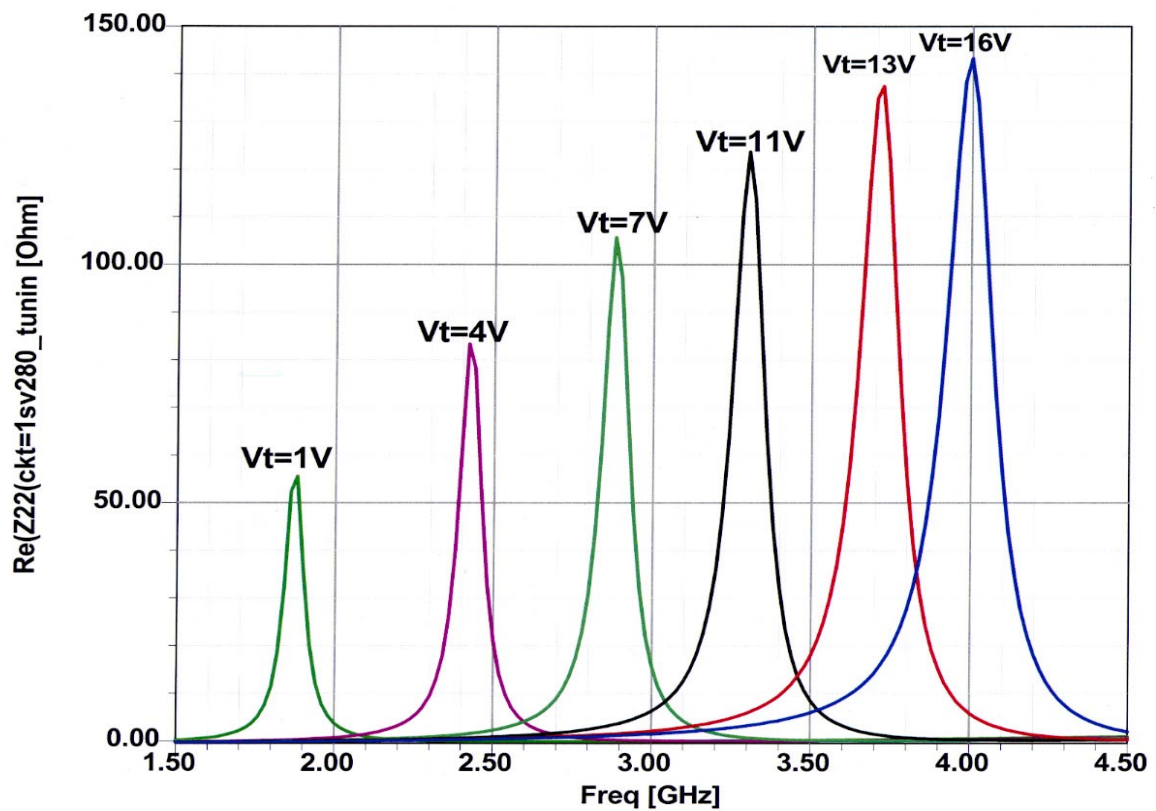

Figure 6-23 (b): Simulated loaded input impedance of the varactor-tuned coupled resonator.

Figure 6-24 shows the plot of the calculated loaded and unloaded Q factors, and the measured loaded Q factors versus frequency.
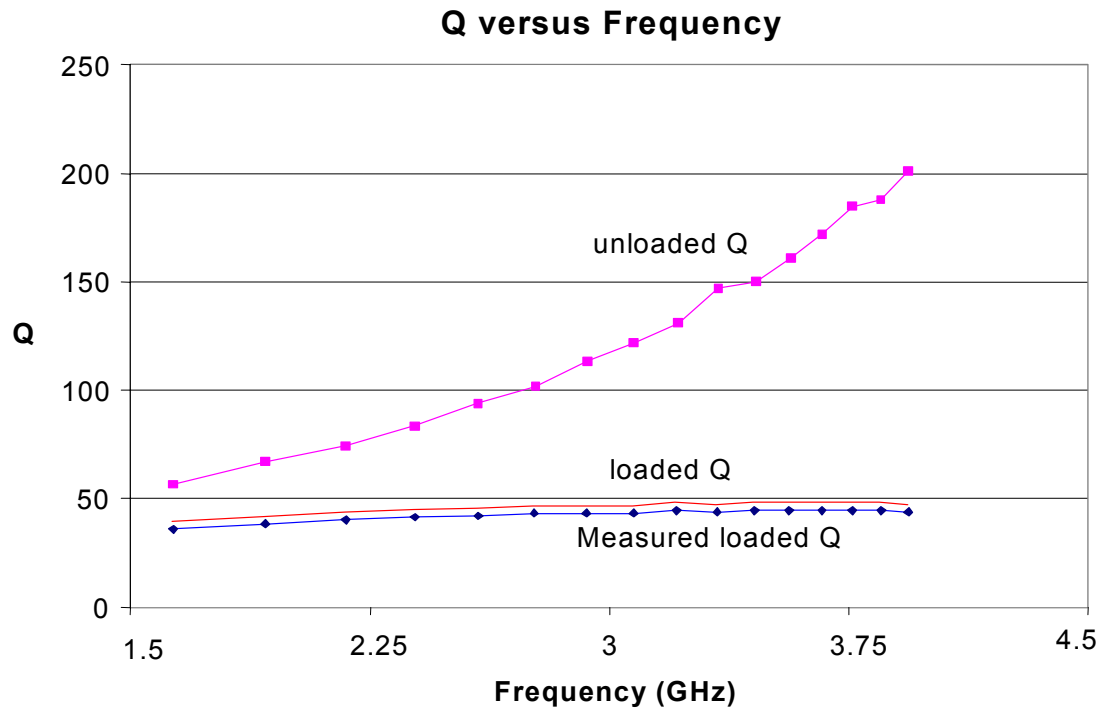

Figure 6-24: Q factor versus frequency.

From Figure 6-24, the unloaded Q of the tuned coupled resonator circuit is varying from 55 to 205, and the variation is about 1:4 ratio over the band, whereas the loaded Q of the tuned coupled resonator circuit is varying from 38 to 47, and the variation is about 1:1.2 over the band.

The measured loaded Q of the tuned coupled resonator circuit is varying from 37 to 45, and the variation is about 1:1.2 over the band, which closely agrees with the predicted values.

For optimum phase noise performance over the tuning range, variation of the loaded Q should be minimum over the desired tuning range. This type of the resonator plays major role in the design of low noise octave-band VCOs [74].

Figure 6-25 shows the actual circuit layout of a tuned coupled resonator oscillator for the purpose of depicting the coupled resonator, as it is built on a multi-layer printed circuit board.

As shown in the Figure 6-25, coupled resonator is symmetrically structured across the emitter of the transistor for wideband VCOs (1500-3000 MHz), and the analysis is given in the section 8.3 [74].
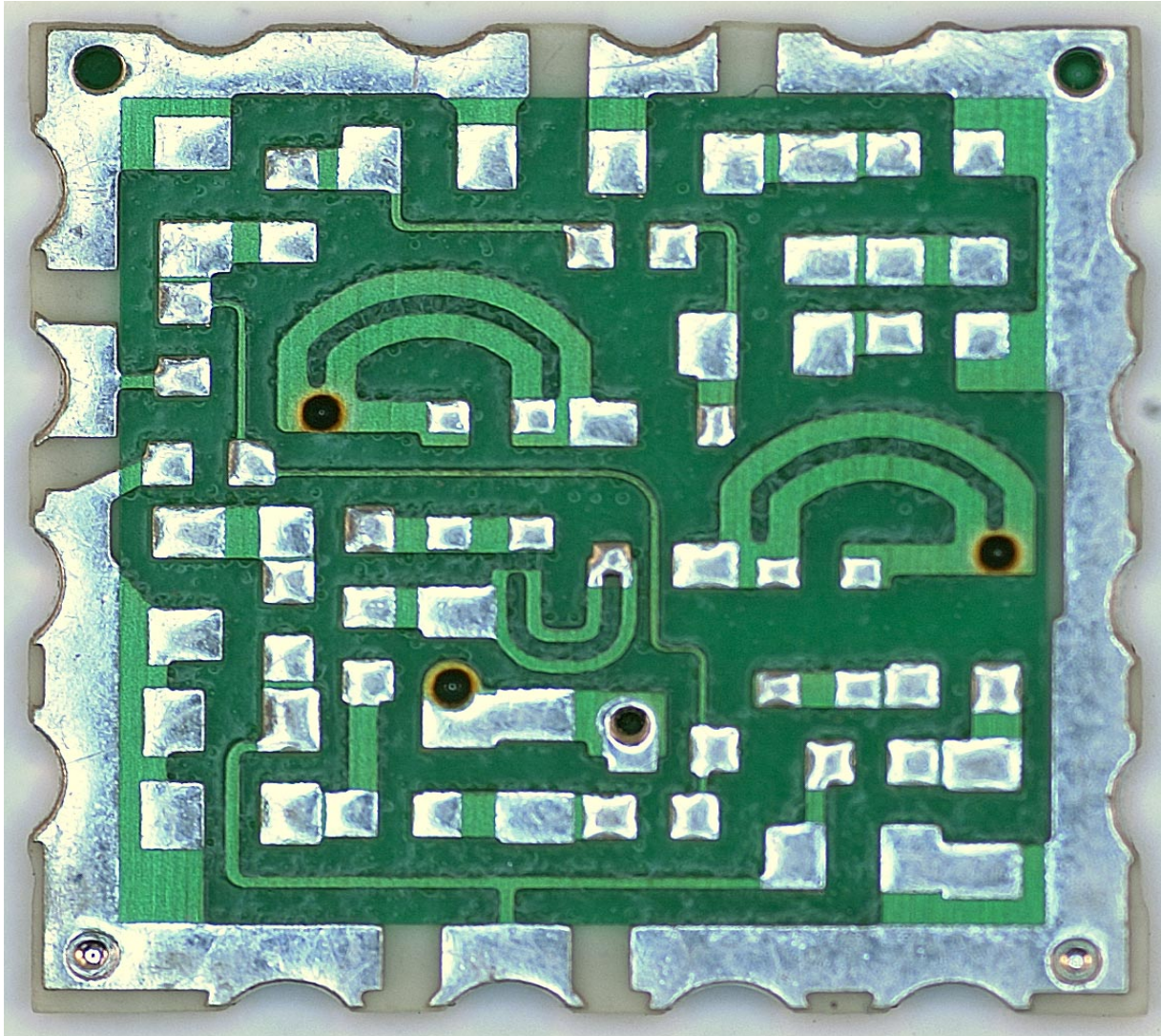

Figure 6-25: Layout of the wideband VCO (1500-3000 MHz) with coupled microstripline resonators.

6.4   Passive Device Models

Despite an ongoing trend towards higher integration levels, discrete RF components still have a place in contemporary wireless designs. Furthermore, discrete RF devices offer advantages such as superior performance, great design flexibility and versatility, faster time-to-market, low cost, and reduced risk. For low cost reasons, surface-mounted components are used in the VCOs circuits. In reality, these components possess parasitics resulting in a self-resonant frequency (SRF) comparable to the operating frequency and limit the operating frequency band.

An understanding of the parasitic and packaging effects of the passive surface-mounted devices (SMDs), including characterization of the pertinent interconnect is required for the large signal-analysis of the oscillator design. RF components packaging, pad footprint, PCB layout, and substrate interaction cause local parasitic effects such as resonant coupling, cross-talk, signal loss, signal distortion, and so on.

Extrinsic modeling of the devices is crucial for the large-signal analysis, which takes the above-mentioned parasitic effects into account. An incomplete specification of the passive components inevitably leads to inaccurate results and considerable tuning and testing after board fabrication. If the design analysis is based on the extrinsic circuit model, the increased accuracy attained by incorporating board parasitic can potentially reduce the number of design cycles. Furthermore, by using an accurate library base of equivalent-circuit models, it is feasible to accomplish most of the design on a circuit simulator instead of the trial and error at the bench.

Active devices are shrinking and are occupying less and less chip area, whereas passive devices remained large. While it was possible to fabricate small values of capacitance on chip, small inductors are virtually impossible due to the large physical area required to obtain sufficient inductance at a given frequency. This is compounded by the losses of the substrate, which makes it virtually impossible to fabricate high-quality devices. At a low frequency, this low loss design is possible as long as package parasitics are negligible in comparison with the external electrical characteristics of the device.

For instance, at 100MHz, a typical resonator inductance value is on the order of 100nH, whereas at 10GHz this value is around 1nH. To build a 1nH inductor is impossible in standard low-cost packaging since the bond wire inductance can exceed 1nH. Typical examples of passive devices include linear time-invariant resistors of finite resistance $R > 0$, which dissipate energy, and ideal linear time-invariant capacitors and inductors, which only store energy.

Quality of the Passive Devices

The complex power delivered to a one-port network at frequency ω is given by [57]

$$P = \frac{1}{2} \oint_S E \times H^* . dS = P_n + j2\omega(W_m - W_e) \tag{6.49}$$

where P_n represents the average power dissipated by the network, and W_m and W_e represent the time average of the stored magnetic and electrical energy. For $W_m > W_e$ the device acts inductively, and for $W_e > W_m$ it acts capactively.

The input impedance can be defined as

$$P = R + jX = \frac{V}{I} = \frac{VI^*}{|I|^2} = \frac{P}{\frac{1}{2}|I|^2} = \frac{P_n + j2\omega(W_m - W_e)}{\frac{1}{2}|I|^2} \qquad (6.50)$$

The quality factor Q of the passive device is defined as

$$Q = 2\pi \left[\frac{E_{stored}}{E_{dissipated}} \right] = 2\pi \left[\frac{(W_m + W_e)}{P_n \times T} \right] = \frac{\omega(W_m + W_e)}{P_n} \qquad (6.51)$$

where E_{stored} and $E_{dissipated}$ are the energy stored and dissipated per cycle.

$$Q_{inductor} = 2\pi \left[\frac{E_{stored}}{E_{dissipated}} \right]_{W_e=0} = 2\pi \left[\frac{W_m}{P_n \times T} \right] = \frac{\omega W_m}{P_n} = \omega \left[\frac{\frac{1}{2}(LI^2)}{\frac{1}{2}(I^2 R)} \right] = \frac{\omega L}{R} \qquad (6.52)$$

$$Q_{capacitor} = 2\pi \left[\frac{E_{stored}}{E_{dissipated}} \right]_{W_m=0} = 2\pi \left[\frac{W_e}{P_n \times T} \right] = \frac{\omega W_e}{P_n} = \omega \left[\frac{\frac{1}{2}(CV^2)}{\frac{1}{2}\left(\frac{V^2}{R}\right)} \right] = \frac{1}{\omega CR} \qquad (6.53)$$

where R is the series loss resistance in the inductor and capacitor.

Inductor Model

Figure 6-26 shows the equivalent circuit model for the inductor. The series resistance R accounts for the package losses, resistive effects of the winding, and pad or trace losses.
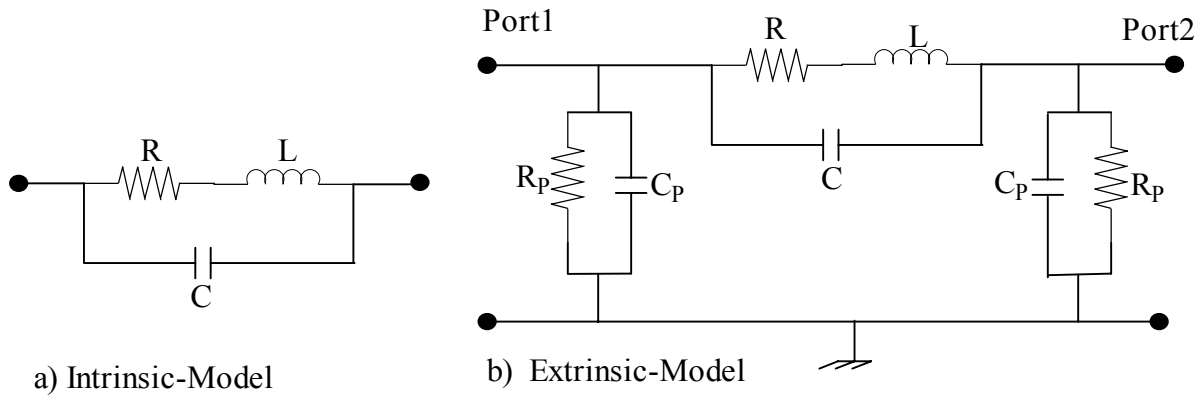

Figure 6-26: Model for SMD-inductor a) Intrinsic Model and b) Extrinsic Model.

The series capacitance C represents the self-capacitance of the inductor package and the capacitance between the pads. The pad is simply a step-in-width inductive transition and augments the series inductance of the intrinsic model. The total inductance is denoted as L. The dielectric losses in the substrate introduce a shunt conductance $G_P=1/R_P$, and the capacitance to ground of each pad introduces a shunt C_P, which is influenced by the substrate. The direct RF measurement of the model parameters L, R, and C of a SMD inductor is difficult because of their strong interaction with the board parasitic. Typically, any of theses parameters can be obtained indirectly from measurable parameters such as impedance, quality factor, and resonant frequency. Figure 6-27 shows the closed form of the inductor model in Figure 6-26.
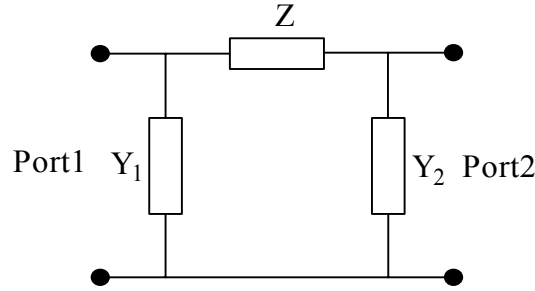

Figure 6-27: π-Model for an SMD inductor.

From Figures 6-26 (b) and 6-27,

$$Z = \frac{(R+j\omega L)\dfrac{1}{j\omega C}}{(R+j\omega L+\dfrac{1}{j\omega C})} = \frac{R+j\omega L}{(1-\omega^2 LC)+j\omega RC} \tag{6.54}$$

$$Y_P = G_P + j\omega C_P \tag{6.55}$$

The measured S-parameters on a vector network analyzer are transferred into the 2-port [Y] parameters using

$$[Y] = \begin{bmatrix} Y_{11} & Y_{12} \\ Y_{21} & Y_{22} \end{bmatrix} \tag{6.56}$$

where

$$Y_{11}= Y_0\left[\frac{(1-S_{11})(1+S_{22})+S_{12}S_{21}}{\Delta}\right], \quad Y_{12} = -Y_0\left[\frac{2S_{12}}{\Delta}\right]$$

$$Y_{22}= Y_0\left[\frac{(1+S_{11})(1-S_{22})+S_{12}S_{21}}{\Delta}\right], \quad Y_{21}= -Y_0\left[\frac{2S_{21}}{\Delta}\right]$$

$$\Delta = (1+S_{11})(1+S_{22})-S_{12}S_{21}, \quad Y_0 = \frac{1}{Z_0}$$

Z_0 is the characteristic impedance of the port. From reciprocity, $S_{12} = S_{21}$ and $Y_{12} = Y_{21}$.
From Figure 6-27,

$$Z = -\frac{1}{Y_{12}} \tag{6.57}$$

$$Y_1 = Y_{11} + Y_{12} \tag{6.58}$$

$$Y_2 = Y_{22} + Y_{21} \tag{6.59}$$

From symmetry,

$$Y_1 = Y_2 = Y_P \tag{6.60}$$

$$Y_P = G_P + j\omega C_P \tag{6.61}$$

$$G_P = \text{Re}[Y_P] \tag{6.62}$$

$$C_P = \frac{\text{Im}[Y_P]}{\omega} \tag{6.63}$$

The circuit variables for the SMD inductor are frequency dependent and can be expressed in terms of the resonant frequency, quality factor, and impedance at the resonance.

From Equation (6.54)

$$Z(\omega) = \frac{(R + j\omega L)(1 - \omega^2 LC - j\omega RC)}{(1 - \omega^2 LC)^2 + (\omega RC)^2} = \frac{R + j\omega L^2 C(\omega_0^2 - \omega^2)}{(1 - \omega^2 LC)^2 + (\omega RC)^2} \tag{6.64}$$

defining

$$\omega_0 = \frac{1}{\sqrt{L_0 C_0}} \left[\frac{Q^2}{1 + Q^2} \right]^{1/2} \tag{6.65}$$

$$Q = \left[\frac{\omega_0 L_0}{R_0} \right] = \left[\frac{\omega_0}{\Delta \omega} \right]_{3dB} \tag{6.66}$$

where L_0 and R_0 denote inductance and resistance at the resonant frequency.

Equation (6.64) can be expressed as

$$Z(\omega) = Z_{real}(\omega) + jZ_{imag}(\omega) \tag{6.67}$$

At resonance frequency $Z_{imag}(\omega)\big|_{\omega=\omega_0} = 0$ and $Z(\omega)$ is a real number at $\omega = \omega_0$.

$$Z(\omega)\big|_{\omega=\omega_0} = Z_0 = \frac{R}{(1-\omega_0^2\,LC)^2 + (\omega_0\,RC)^2} \qquad (6.68)$$

$$R_0 = \frac{Z_0}{1+Q^2} \qquad (6.69)$$

$$L_0 = Q\left[\frac{R_0}{\omega_0}\right] \qquad (6.70)$$

From Equation (6.54), admittance $Y(\omega)$ is given as

$$Y(\omega) = \frac{1}{Z(\omega)} = Y_{real}(\omega) + jY_{imag}(\omega) \qquad (6.71)$$

$$Y(\omega) = \left[\frac{R}{R^2 + \omega^2\,L^2}\right] + j\omega\left[C_0 - \frac{L}{R^2 + \omega^2\,L^2}\right] \qquad (6.72)$$

$$R = \frac{1 + \sqrt{1-(2Y_{real}\omega L)^2}}{2Y_{real}} \qquad (6.73)$$

$$Y_{imag} = \omega C_0 - Y_{real}\left[\frac{\omega L}{R}\right] \Rightarrow \frac{\omega C_0 - Y_{imag}}{Y_{real}} = \frac{\omega L}{R} \qquad (6.74)$$

From Equations (6.73) and (6.74), L can be expressed as a function of frequency $L(\omega)$ as

$$L = L(\omega) = \frac{R}{\omega}\left[\frac{\omega C_0 - Y_{imag}}{Y_{real}}\right] = \frac{1}{\omega\left[\omega C_0 + \dfrac{|Y|^2 - \omega C_0 Y_{imag}}{\omega C_0 - Y_{imag}}\right]} \qquad (6.75)$$

$$\omega L(\omega) = \left[\frac{Z_{imag}(\omega) + \omega C|Z(\omega)|^2}{[1 + \omega C Z_{imag}(\omega)]^2 + [\omega C Z_{real}(\omega)]^2}\right] \qquad (6.76)$$

where

$$|Y| = \frac{1}{|Z|}; \ Y_{real} = \frac{Z_{real}}{|Z|^2}; \ Y_{imag} = -\frac{Z_{imag}}{|Z|^2}$$

From Equation (6.74)

$$R(\omega) = \frac{Y_{real}}{(\omega C_0)^2 - 2\omega C_0 Y_{imag} + |Y|^2} = \frac{Z_{real}(\omega)}{[1 + \omega C Z_{imag}(\omega)]^2 + [\omega C Z_{real}(\omega)]^2} \qquad (6.77)$$

116

$$C(\omega_0) = C_0 = \left[\frac{1}{\omega_0^2 L_0} \right] \left[\frac{Q^2}{1+Q^2} \right] \tag{6.78}$$

$$\left[\frac{C_0}{C(\omega)} \right] \left[\frac{\omega_0}{\omega} \right]^2 = \left[1 - \left| \frac{Z_i(\omega)\omega_0}{\omega Q R_0} \right| \right] \tag{6.79}$$

From Equations (6.75) and (6.77), L and R are functions of the frequency, whereas self-capacitance C, as given in Equation (6.78), is practically independent of the frequency. Thus, apriori estimation of the resonant frequency, quality factor, and impedance at resonance frequency helps to determine the inductor-SMD component variables.

Capacitance Model

Figure 6-28 shows the equivalent circuit model for SMD capacitor. The measured S-parameters are transferred into the 2-Port [Y] parameters using Equation (6.56). The series impedance and shunt admittance of the π-equivalent representation of the capacitor, as shown in the Figure 6-29, are given from Equations (6.57), (6.58) and (6.59). For the capacitor, the equivalent circuit consists of a series connection of R, L, and C, as shown in the Figure 6-28, and by duality from the inductor model, the stray inductance L is invariant with frequency, just as self-capacitance is invariant with frequency in the inductor.
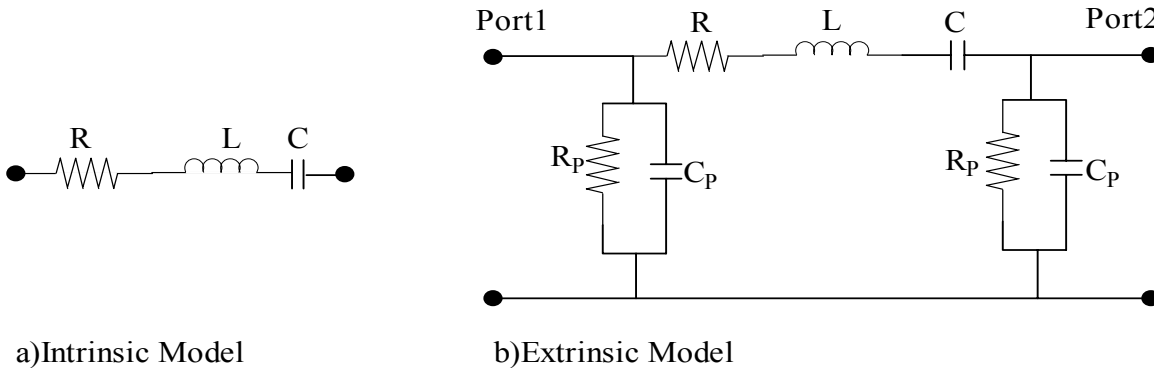

a)Intrinsic Model   b)Extrinsic Model

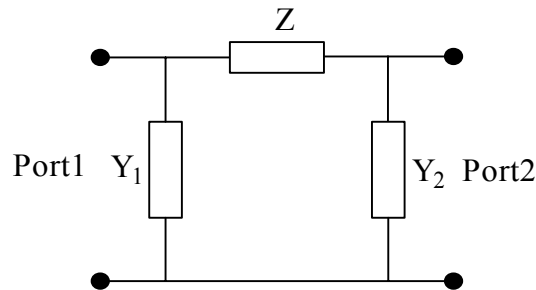Figure 6-28: Model for an SMD capacitor a) Intrinsic Model and b) Extrinsic Model

Figure 6-29: π-Model for an SMD capacitor

From Figures 6-28 and 6-29, impedance is given as

$$Z(\omega) = Z_{real}(\omega) + jZ_{imag}(\omega) = R(\omega) + jQ\left[\frac{\omega R_0}{\omega_0}\right]\left[1 - \left(\frac{\omega_0}{\omega}\right)^2 \frac{C_0}{C(\omega)}\right] \tag{6.80}$$

$$Z(\omega) = -\frac{1}{Y_{12}(\omega)} \tag{6.81}$$

$$R(\omega) = Z_{real}(\omega) \tag{6.82}$$

$$C(\omega) = \frac{1}{\omega(\omega L_0 - Z_{imag}(\omega))} \tag{6.83}$$

At resonance,

$$R_0 = R(\omega_0) = Z_{real}(\omega_0) \tag{6.84}$$

$$L_0 = Q\left[\frac{R_0}{\omega_0}\right] \tag{6.85}$$

$$C(\omega)\big|_{\omega=\omega_0} = C_0 = \frac{1}{\omega_0^2 L_0} \tag{6.86}$$

Thus, apriori estimation of the resonant frequency, quality factor, and impedance at resonance frequency helps to determine the SMD capacitor component variables.

Resistance Model

The resistor can be implemented in several ways. Figure 6-30 shows the two-port extrinsic equivalent circuit model for a resistor. The measured S-parameters are transferred into the 2-Port [Y] parameters using Equation (6.56).

The series impedance and shunt admittance of the π-equivalent representation of the resistor as shown in the Figure 6-31 are from Equations (6.57), (6.58), and (6.59).
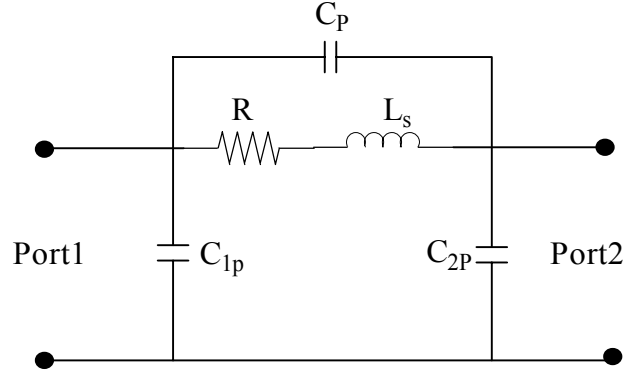
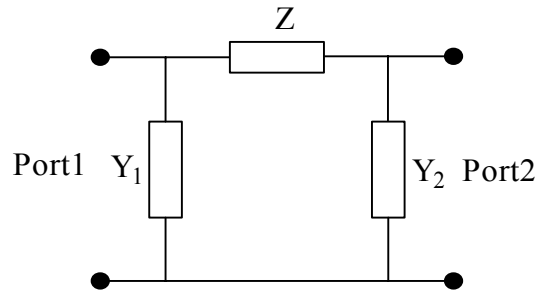Figure 6-30: Two- port extrinsic equivalent circuit model for a resistor

Figure 6-31: π-Model for an SMD Resistor

The two-port [Y] parameters of the resistor in Figure 6-30 are given by

$$[Y] = \begin{bmatrix} Y_{11} & Y_{12} \\ Y_{21} & Y_{22} \end{bmatrix} = \begin{bmatrix} \left(j\omega[C_{1P} + C_P] + \dfrac{1}{[R + j\omega L_s]} \right) & -\left(j\omega C_P + \dfrac{1}{[R + j\omega L_s]} \right) \\ -\left(j\omega C_P + \dfrac{1}{[R + j\omega L_s]} \right) & \left(j\omega[C_{1P} + C_P] + \dfrac{1}{[R + j\omega L_s]} \right) \end{bmatrix} \quad (6.87)$$

$$Z(\omega) = -\frac{1}{Y_{12}(\omega)} \quad (6.88)$$

$$Z(\omega) = Z_{real}(\omega) + jZ_{imag}(\omega) \quad (6.89)$$

$$R(\omega) = Z_{real}(\omega) \quad (6.90)$$

At resonance,

$$R_0 = R(\omega_0) = Z_{real}(\omega_0) \quad (6.91)$$

Thus, apriori estimation of the resonant frequency and impedance at resonance frequency facilitates unique determination of the SMD resistor variables.

Chapter 7

Low Noise Wideband VCOs

7.1   Wideband VCOs Approach

Voltage controlled oscillators (VCOs) with a wide tuning range (more than octave-band) and low phase noise are essential building blocks for next-generation wireless communication systems. The VCO is one of the most important blocks of the phase-locked loop (PLL) based frequency synthesizer because its performance is determined inside the loop bandwidth by the loop and outside the loop bandwidth by the phase noise of VCO. It is, therefore, of major importance to build a low-phase-noise integrated wideband oscillator that operates with low power consumption.

Typical oscillator designs for wideband VCOs use a grounded base or grounded emitter circuit for generating a negative resistance at one port, which is usually terminated with a parallel or series LC-resonant circuit. The main challenge in this design is to generate negative resistance over the wide tuning range, which cannot be easily extended to more than an octave band. For octave band tunability, the required negative resistance over the band is generated by the feedback base inductance (in the grounded base topology), but the polarity of the reactance may change over the frequency band and can lead to the disappearance of the negative resistance as the operating frequency exceeds its self-resonance frequency (SRF). Furthermore, the low Q of commercially available SMD inductors and tuning diodes degrade the phase noise performance over the band. Figure 7-1 shows the series and parallel configuration of the oscillator circuit.

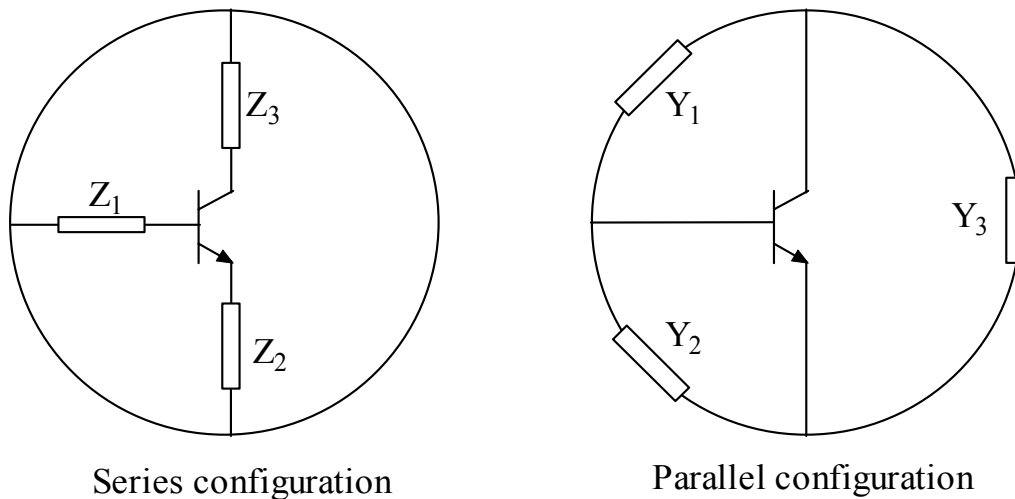Series configuration   Parallel configuration

Figure 7-1: Series and parallel configuration of the oscillator.

The detailed analysis of series and parallel feedback topology for optimum power is shown in Appendix B. Figure 7-2 shows the series feedback grounded base topology for analysis of the wideband VCOs. The negative resistance is created by an inductor in the base of the transistor instead of the capacitive feedback network as used in parallel feedback topology. The series feedback grounded base topology is best suited for wide tuning range applications because the loaded Q of the resonator is approximately same over the band and is not greatly affected by the large-signal nonlinear negative resistance-generating device.
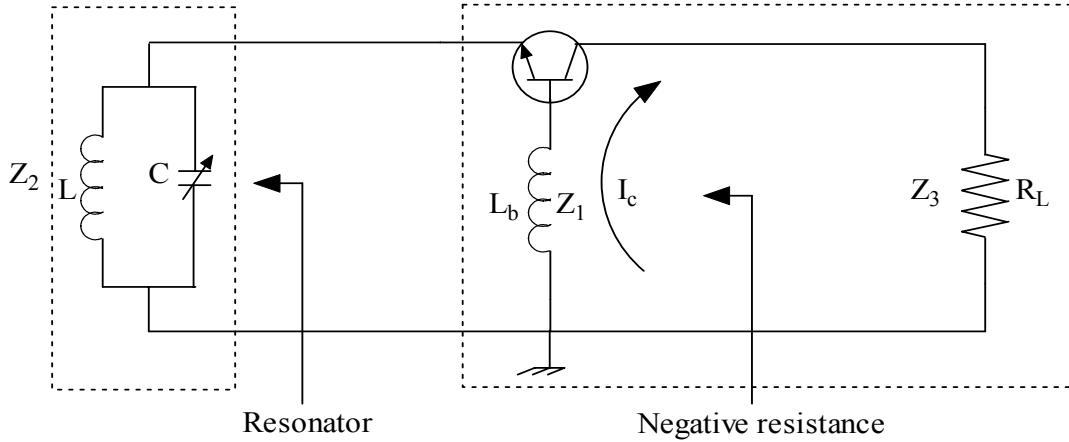

Figure 7-2: Series feedback grounded base topology.

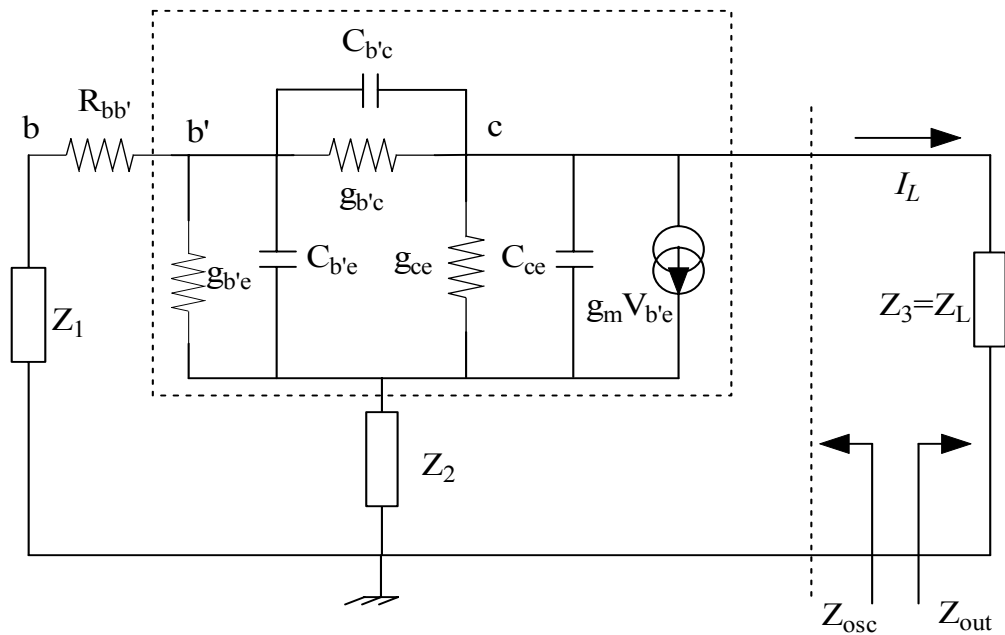Figure 7-3 shows the general topology of the series feedback oscillator.

Figure 7-3: Series feedback topology of the oscillator using bipolar transistor.

121

The steady-state oscillation condition for series feedback configuration shown in Figure 7-3 is given by

$$Z_{osc}(I_L,\omega) + Z_L(\omega) = 0 \tag{7.1}$$

where I_L is the load current amplitude and ω is the resonance frequency. Z_{osc} is the current and frequency-dependent output impedance, and Z_L is the function of frequency.

$$Z_{osc}(I_L,\omega) = R_{osc}(I_L,\omega) + jX_{osc}(I_L,\omega) \tag{7.2}$$

$R_{osc}(I_L,\omega) \rightarrow$ Negative resistance components generated by the device.

$$Z_L(\omega) = R_L(\omega) + jX_L(\omega) \tag{7.3}$$

$$Z_{osc} = [Z_{22} + Z_2] - \frac{[Z_{12} + Z_2][Z_{21} + Z_2]}{[Z_{11} + Z_1 + Z_2]} \tag{7.4}$$

where Z_{11}, Z_{22}, Z_{12} and Z_{21} are the [Z] parameters of the transistor.

The [Z] parameter of the transistor can be defined in terms of the [Y] parameter as

$$Z_{11} = \frac{Y_{22}}{Y_{11}Y_{22} - Y_{12}Y_{21}}; Z_{12} = \frac{-Y_{12}}{Y_{11}Y_{22} - Y_{12}Y_{21}}; Z_{21} = \frac{-Y_{21}}{Y_{11}Y_{22} - Y_{12}Y_{21}}; Z_{22} = \frac{Y_{11}}{Y_{11}Y_{22} - Y_{12}Y_{21}}$$

$$[Y] = \begin{bmatrix} (g_{b'c} + g_{b'e}) + j\omega(C_{b'c} + C_{b'e}) & -(g_{b'c} + j\omega C_{b'c}) \\ g_m - (g_{b'c} + j\omega C_{b'c}) & (g_{b'c} + g_{ce}) + j\omega(C_{b'c} + C_{ce}) \end{bmatrix} \tag{7.5}$$

$$Z_{11} = \frac{Y_{22}}{Y_{11}Y_{22} - Y_{12}Y_{21}}$$

$$= \frac{[(g_{b'c} + g_{ce}) + j\omega(C_{b'c} + C_{ce})]}{[(g_{b'c} + g_{b'e}) + j\omega(C_{b'c} + C_{b'e})][(g_{b'c} + g_{ce}) + j\omega(C_{b'c} + C_{ce})] + [(g_{b'c} + j\omega C_{b'c})][g_m - (g_{b'c} + j\omega C_{b'c})]} \tag{7.6}$$

$$Z_{12} = \frac{-Y_{12}}{Y_{11}Y_{22} - Y_{12}Y_{21}}$$

$$= \frac{[(g_{b'c} + j\omega C_{b'c})]}{[(g_{b'c} + g_{b'e}) + j\omega(C_{b'c} + C_{b'e})][(g_{b'c} + g_{ce}) + j\omega(C_{b'c} + C_{ce})] + [(g_{b'c} + j\omega C_{b'c})][g_m - (g_{b'c} + j\omega C_{b'c})]} \tag{7.7}$$

$$Z_{21} = \frac{-Y_{21}}{Y_{11}Y_{22} - Y_{12}Y_{21}}$$

$$= \frac{-[g_m - (g_{b'c} + j\omega C_{b'c})]}{[(g_{b'c} + g_{b'e}) + j\omega(C_{b'c} + C_{b'e})][(g_{b'c} + g_{ce}) + j\omega(C_{b'c} + C_{ce})] + [(g_{b'c} + j\omega C_{b'c})][g_m - (g_{b'c} + j\omega C_{b'c})]}$$

(7.8)

$$Z_{22} = \frac{Y_{11}}{Y_{11}Y_{22} - Y_{12}Y_{21}}$$

$$= \frac{[(g_{b'c} + g_{b'e}) + j\omega(C_{b'c} + C_{b'e})]}{[(g_{b'c} + g_{b'e}) + j\omega(C_{b'c} + C_{b'e})][(g_{b'c} + g_{ce}) + j\omega(C_{b'c} + C_{ce})] + [(g_{b'c} + j\omega C_{b'c})][g_m - (g_{b'c} + j\omega C_{b'c})]}$$

(7.9)

where

$$Z_1 = j\omega L_1, \; Z_2 = \frac{1}{j\omega C_2}$$

Assuming that $g_{b'c}, g_{b'e}, g_{ce}$ and $C_{b'c}$ have very little effect, the [Z] parameters of the transistor are

$$[Z] = \begin{bmatrix} \dfrac{1}{j\omega C_{b'e}} & 0 \\ \dfrac{g_m}{\omega^2 C_{b'e} C_{ce}} & \dfrac{1}{j\omega C_{ce}} \end{bmatrix}$$

(7.10)

where

$$Z_{11} = \frac{1}{j\omega C_{b'e}}, \; Z_{12} = 0, \; Z_{21} = \frac{g_m}{\omega^2 C_{b'e} C_{ce}}, \; Z_{22} = \frac{1}{j\omega C_{ce}}$$

From Equation (7.4), Z_{osc} is given by

$$Z_{osc} = \left[\frac{1}{j\omega C_{ce}} + \frac{1}{j\omega C_2}\right] - \frac{\left[\dfrac{1}{j\omega C_2}\right]\left[\dfrac{g_m}{\omega^2 C_{b'e} C_{ce}} + \dfrac{1}{j\omega C_2}\right]}{\left[j\omega L_1 + \dfrac{1}{j\omega C_{b'e}} + \dfrac{1}{j\omega C_2}\right]}$$

(7.11)

$$Z_{osc} = -\frac{g_m}{\omega^2 C_{ce}[C_{b'e} + C_2 - L_1 C_2 C_{b'e}\omega^2]} - j\left[\left(\frac{C_{ce} + C_2}{\omega C_{ce} C_2}\right) - \left(\frac{1}{\omega\left(\dfrac{C_2^2}{C_{b'e}}\right) + \omega C_2 - L_1 C_2^2 \omega^3}\right)\right]$$

(7.12)

$$Z_{osc} = [R_{osc} + jX_{osc}] \Rightarrow R_{osc} = R_n = -\left[\frac{g_m}{\omega^2 C_{ce}[C_{b'e} + C_2 - L_1 C_2 C_{b'e}\omega^2]}\right]$$

(7-13)

For sustained oscillation, $R_n < 0 \Rightarrow \left[L_1 C_2 C_{b'e} \omega^2\right] < \left[C_{b'e} + C_2\right] \rightarrow \omega < \sqrt{\dfrac{1}{L_1}\left[\dfrac{C_{b'e} + C_2}{C_{b'e} C_2}\right]}$

$$X_{osc} = -\left[\left(\frac{C_{ce} + C_2}{\omega C_{ce} C_2}\right) - \left(\frac{1}{\omega\left(\dfrac{C_2^2}{C_{b'e}}\right) + \omega C_2 - L_1 C_2^2 \omega^3}\right)\right] \tag{7.14}$$

where R_n is the negative resistance of the series feedback oscillator

From Equation (7.14), the frequency of the oscillation is given as

$$X_{osc} = 0 \Rightarrow \omega_0 = \sqrt{\frac{1}{L_1}\frac{[C_{b'e} + C_2 + C_{ce}]}{C_{b'e}[C_{ce} + C_2]}} \tag{7.15}$$

From Equation (7.13), for $C_{b'e} < C_2$

$$R_{osc} = -\left[\frac{g_m}{\omega^2 C_{ce} C_2 [1 - L_1 C_{b'e} \omega^2]}\right] \tag{7.16}$$

If $L_1 C_{b'e} \omega^2 < 1$, then

$$R_{osc} \rightarrow -\left[\frac{g_m}{\omega^2 C_{ce} C_2}\right] \tag{7.17}$$

If we now change from the small-signal transconductance g_m, to a large-signal time average transconductance, then the Equation (7.17) can be expressed as

$$R_{osc} = R_N(t) = -\left[\frac{g_m(t)}{\omega^2 C_{ce} C_2 [1 - L_1 C_{b'e} \omega^2]}\right] \tag{7.18}$$

where $g_m(t)$ is the large-signal transconductance and is defined as

$$g_m(t) = \sum_{n=-\infty}^{n=\infty} g_m^{(n)} \exp(jn\omega t) \text{ (n is number of harmonics)}$$

The total noise voltage power within 1 Hz bandwidth can be given as [11]:

$$\left|\overline{e_N^2(f)}\right|_{\omega=\omega_0} = \overline{e_R^2(f)} + \overline{e_{NR}^2(f)} \tag{7.19}$$

124

The first term in the Equation (7.19) is related to the thermal noise due to the loss resistance of the resonator tank. The second term is related to the shot noise and flicker noise in the transistor.

Following [11], and adding shot noise, flicker noise and the loss resistor, we obtain

$$\pounds(\omega) = \left[4kTR + \frac{\left|g_m^2(t)\right|\left[4qI_c + \dfrac{K_f I_b^{AF}}{\omega}\right]}{\omega_0^4 \beta^2 C_{ce}^2 (C_2 + C_{b'e} - L_1 C_2 C_{b'e}\omega_0^2)^2 + \left|g_m^2(t)\right|\omega_0^2 (C_2 + C_{b'e} - L_1 C_2 C_{b'e}\omega_0^2)^2} \right] *$$

$$\left[\frac{\omega_0^2}{4(\omega)^2 V_{cc}^2}\right]\left[\frac{1}{Q_L^2} + \left(1 - \left(\frac{1}{\omega_0^2 L_1}\right)\left(\frac{[(C_2 + C_{b'e} - L_1 C_2 C_{b'e}\omega_0^2) + C_{ce}]}{C_{ce}[(C_2 + C_{b'e} - L_1 C_2 C_{b'e}\omega_0^2)]}\right)\right)^2\right] \qquad (7.20)$$

The flicker noise contribution in the Equation (7.20) is introduced by adding term $\dfrac{K_f I_b^{AF}}{\omega}$ in RF collector current I_c, where K_f is the flicker noise coefficient, AF is the flicker noise exponent, and ω is the offset frequency from the carrier.

7.2   Low Noise Wideband VCO

Phase noise is the noise, which results from the modulations of the oscillation frequency or carrier frequency of an oscillator. Oscillator intended for fixed-frequency operation are relatively easy to optimize if only a parameter of particular concern is involved, but serious problems occur when they are tuned to operate over wideband frequencies. In contrast to single-frequency oscillators, wideband VCOs need to cover a range of up to 1 octave or more. For a varactor-tuned oscillator to tune continuously over a wide range, the tuning diode must exhibit a large change in capacitance in response to a small change in tuning voltage. However, the tuning diode's own capacitance is modulated by the random electronic noise signals generated internally by various oscillator circuit elements, including the tuning diode itself. The tuning range of the oscillator directly influences the phase noise, and there is a trade-off between the continuous tuning range of the VCO and the amount of phase noise generated by the varactor capacitance modulation. However, there are demanding requirements for low-noise performance over the complete frequency range. A wide tuning range with a small tuning voltage and good phase noise performance has always been needed, but it causes the problem of controlling the loop parameters and the dynamic loaded Q of the resonator over the wideband operation. Thus. There is a need for a method, which improves the phase noise performance over the wideband. This can be accomplished by using novel coupled oscillator topology integrated with a tuning diode or switched capacitor system. The N-push/push-push configuration is another attractive option to extend the frequency domain of operation of the transistor while keeping phase noise low.

7.2.1   Choice of the Active Device

The designer has no control over the noise sources in a transistor, being able to select only the device selection and the operating bias point. For example, the bulk resistance of a transistor, upon which thermal noise depends, is an unchangeable, intrinsic property of the device. However, knowing how the oscillator waveforms affect the noise, the designer can substantially improve phase noise performance by selecting the optimal bias point and signal drive level.

The transistor is used as a negative resistance-generating active device. Its choice should be based on the operating frequency, output power requirement, low *1/f* noise at desired frequency, and bias condition. Low *1/f* noise of the transistor is a critical parameter because it appears as the sideband noise around the carrier frequency and is directly related to the current density in the transistor. A bipolar transistor biased at low collector current will keep the flicker corner frequency to a minimum, typically around 2 to 10 kHz. A large transistor with high I_{cmax} used at low currents has the best *1/f* performance. Most active devices exhibit a broad U-shaped noise figure versus bias current curve. Based on this, the optimal operating bias current corresponding to minimum the noise factor for the device can be selected.

Noise Factor of the Oscillator:

Figure 7-4 shows the equivalent configuration of the oscillator circuit for the purpose of analyzing the noise factor with respect to the oscillator feedback components (C_1 and C_2) for better insight into the noise improvement. The objective of this section is to find the oscillator circuit parameters that influence the noise factor, thereby, influencing the phase noise of the oscillators/VCOs circuit, as given in Equation (4.13).

From [11,65,66], simplified and approximate noise factor F for the circuit shown in Figure 7-4 can be given by

$$F = 1 + \frac{Y_{21}^{+}C_2 C_c}{(C_1 + C_2)C_1}\left[r_b + \frac{1}{2r_e}\left(r_b + \frac{(C_1 + C_2)C_1}{Y_{21}^{+}C_2 C_c}\right)^2\left(\frac{1}{\beta} + \frac{f^2}{f_T^2}\right) + \frac{r_e}{2}\right] \tag{7.21}$$

The frequency of the oscillation for the oscillator circuit given in Figure 7-4 is given by

$$\omega_0 = \sqrt{\left\{\frac{\left(\dfrac{(C_1^{*} + C_P)C_2}{(C_1^{*} + C_P + C_2)} + C_c\right)}{L_{PR}\left[\left(\dfrac{(C_1^{*} + C_P)C_2 C_c}{(C_1^{*} + C_P + C_2)}\right) + C_{PR}\left(\dfrac{(C_1^{*} + C_P)C_2}{(C_1^{*} + C_P + C_2)} + C_c\right)\right]}\right\}} \approx 1000\,MHz \tag{7.22}$$

with

Transistor: NEC68830 (Table 6.2)

$C_1^* = 2.2pF$, $C_1 = C_1^* + C_P$, $C_P = 1.1pF$ (C_{BEPKG} + Contribution from layout)

$C_1 = 2.2pF + 1.1pF(pacakage) = 3.3pF$; $C_2 = 2.2pF$, $C_c = 0.4pF$

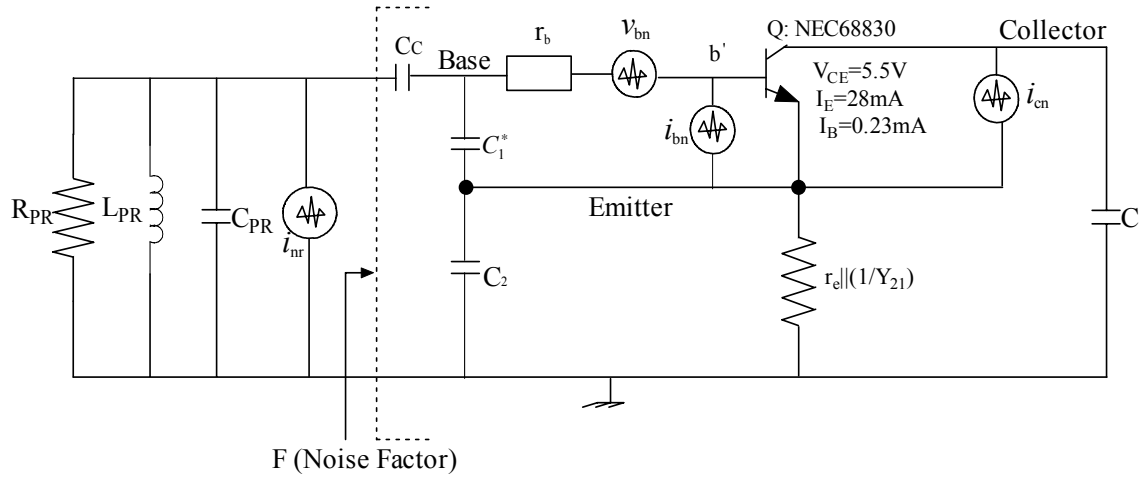Resonator: $R_{PR} = 18000$, $C_{PR} = 4.7pF$, $L_{PR} = 5nH$

F (Noise Factor)

Figure 7-4: Equivalent configuration of the oscillator circuit with the noise sources.

From Equation (7.21)

$$F = 1 + (9.7 \cdot 10^{-5})\left[6 + \frac{1}{2*0.9}\left(6 + \frac{500*5.5*3.3}{2.2*0.4}\right)^2 (0.02) + 0.45\right] = 104.47 \Rightarrow 20.18\,dB \qquad (7.23)$$

with,

$$Y_{21}^+ = \frac{1}{500} = 2.10^{-3}, \text{(large-signal Y-parameter for transistor NE68830)}$$

$r_b = 6\Omega$ $r_e = 0.9\Omega$ @ 28 mA, $\beta = 100$, $f = 1000$ MHz, $f_T = 10$ GHz

Figures (7-5) and (7-6) illustrate the dependency of the noise factor on the feedback capacitor C_1 and C_2. From Equation (4.13), the phase noise of the oscillator circuit can be optimized by optimizing the noise factor terms as given in Equation (7.21) with respect to the feedback capacitor C_1 and C_2.

For output power = 13 dBm, $C_1 = 3.3$ pF, $C_2 = 2.2$ pF, $Y_{21}^+ = 2$ mS, $Q_0 = 1000$, $Q_L = 380$, noise figure = 20 dB; the phase noise plot is given from Equation (4.15), and is shown in the Figure (7-7). The simulated (Ansoft Designer) phase noise plot is shown in Figure 7-8, which agrees with the calculated value within 2 dB.
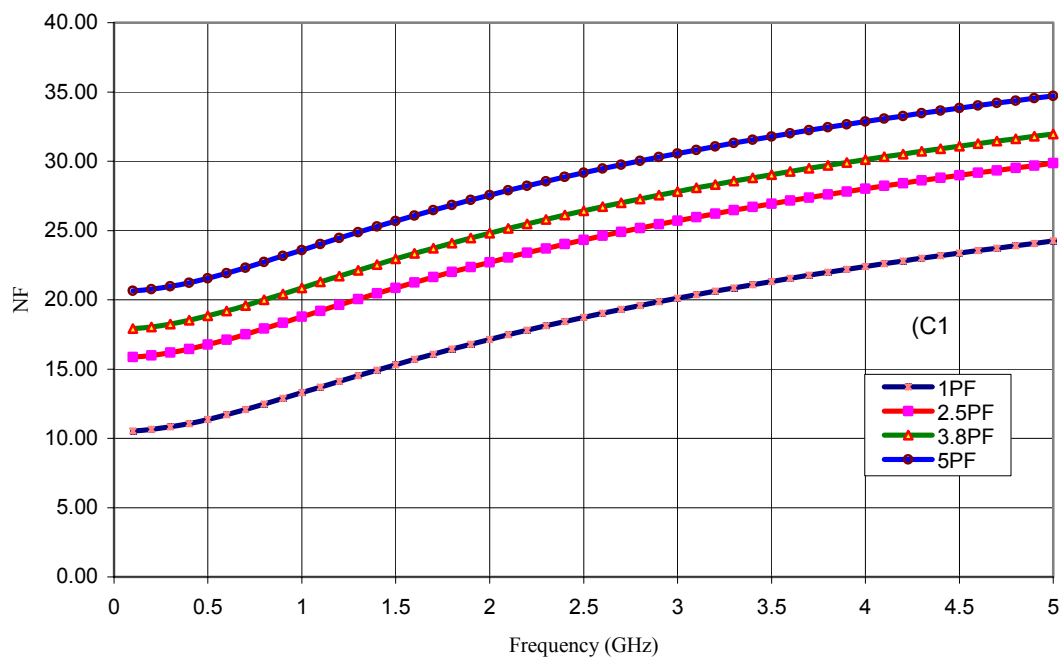
Noise factor for different values of C1 (C2=2.2pF)

Figure 7-5: Plot of the Noise figure versus frequency with respect to feedback capacitor C_1

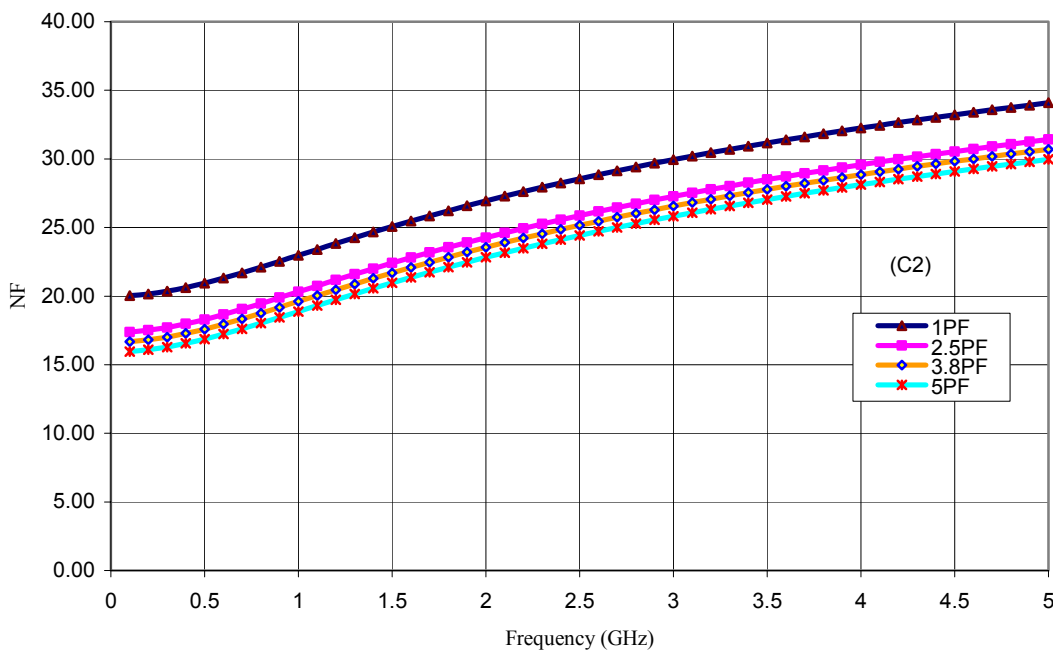Noise factor for different values of C2 (C1=3.3pF)

Figure 7-6: Plot of the Noise figure versus frequency with respect to feedback capacitor C_2

Phase Noise VCO:
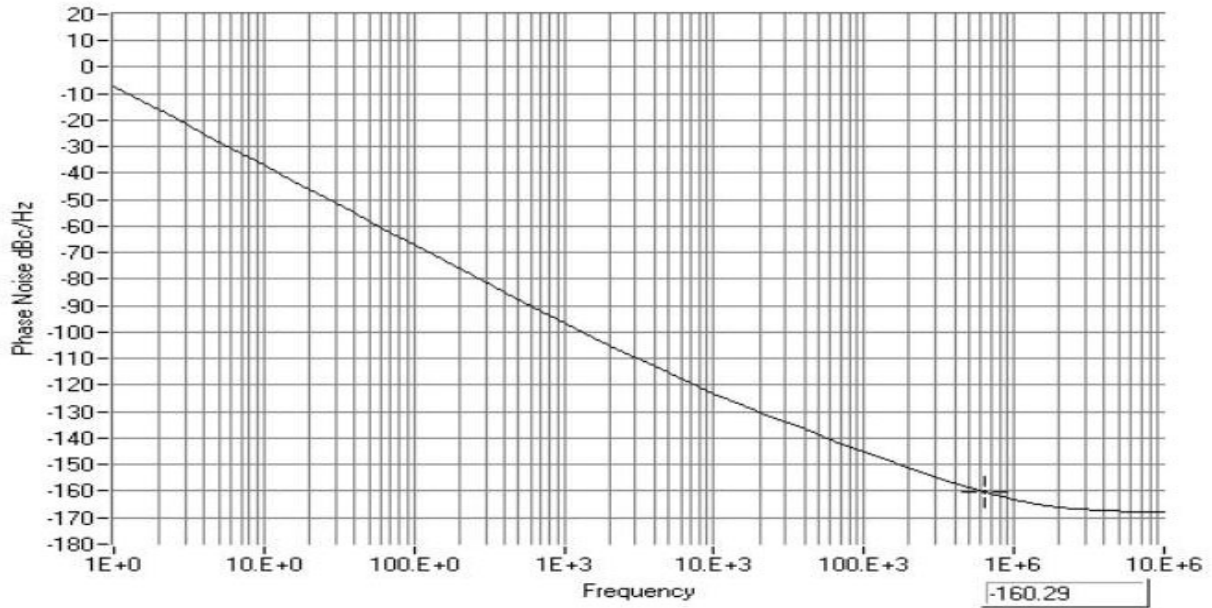
Figure 7-7: Calculated phase noise for an oscillator circuit shown in Figure 7-4.
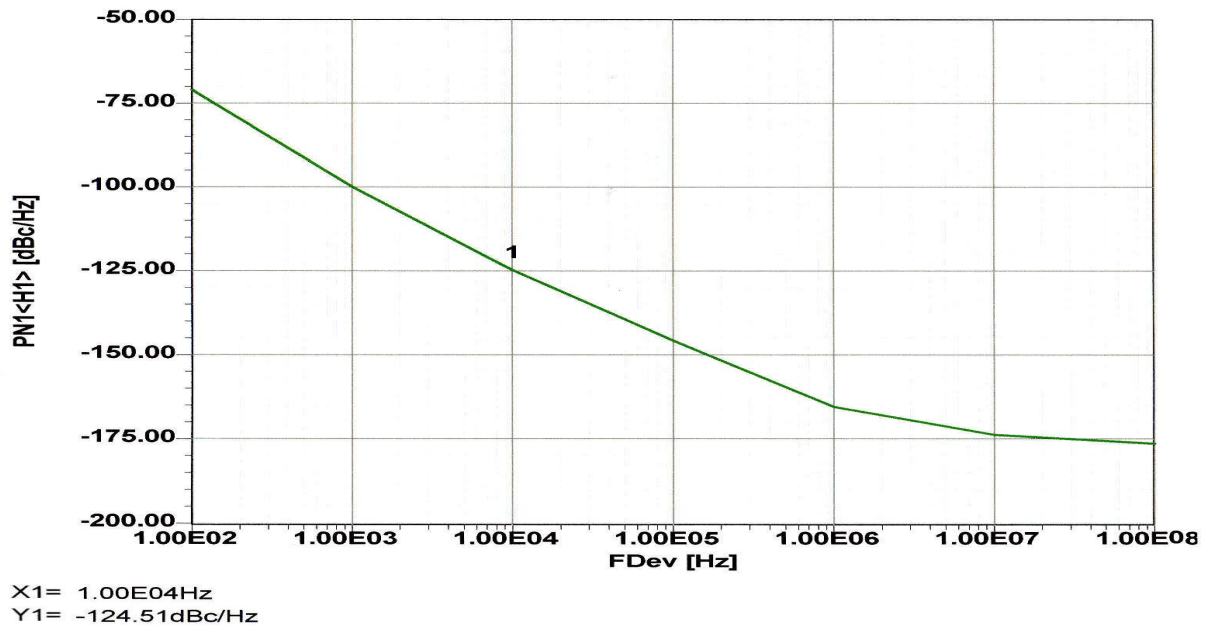

X1= 1.00E04Hz
Y1= −124.51dBc/Hz

Figure 7-8: Simulated phase noise plot for an oscillator circuit shown in Figure 7-4

For low noise and wideband tunability, the circuit topology and the layout of the resonator is selected in such a way that the feedback parameters (C_1 and C_2) are dynamically tuned for minimum noise factor over the tuning range.

129

Chapter 8
Validation Circuits

This dissertation demonstrates the state-of-the-art in designing ultra low noise wideband VCOs having a tuning bandwidth of more than octave-band, and amenable for integration in integrated chip form. This chapter deals with the design, fabrication, and testing of the wideband oscillator/VCOs, which can satisfy the needs for present demand for low-noise, low-cost, tuning-range, power-efficient, manufacturing-tolerance, and miniaturization.

The following circuits have been chosen for validation:

- wideband VCO (320-1120 MHz) based on coupled-resonator
- wideband VCO (1000-2000/2000-4000 MHz) based on push-push approach
- wideband VCO (1500-3000/3000-6000 MHz) based on dual coupled-resonator

8.1   Wideband VCO (300-1100MHz)

A number of operational parameters may be considered, depending on the oscillator's intended applications, but phase noise is the important figure for measurement and instruments applications. In view of the limitations of the wideband tunability, the circuit topology and the layout of the resonator are selected in such a way that they support uniform negative resistance over more than octave band [67,75]. Figure 8-1 illustrates the block diagram of the wideband VCO (320-1120 MHz).

The circuit topology as shown in Figure 8-2(a), is based on varactor-tuned coupled microstripline resonators. The VCO can be dynamically tuned to operate over a fairly wide range of frequencies while maintaining the low phase noise over the band. Replacing a simple distributed microstripline with a coupled microstripline optimizes the dynamic loaded Q of the tuned-resonator, and thereby increases the average loaded Q (Equation 6.43), which depends upon the coupling factor. In particular, by choosing appropriate spacing between the coupled microstripline structures, the coupling factor can be optimized, thus improving the phase noise. Further improvement is accomplished by incorporating noise filtering at the emitter of the bipolar transistor [71,75].

To support a uniform negative resistance over the tuning range, the varactor-tuned coupled microstripline resonator shown in Figure 8-2 (a) is connected across the base and collector of the active device. The negative resistance from the negative resistance-generating network compensates the loss resistance. It is dynamically adjusted as a change of oscillator frequency occurs dynamically, tuning the phase shift of the negative resistance-generating network to meet the phase shift criteria for the resonance over the operating frequency band. Furthermore, by incorporating a tracking filter at the output of the VCOs controls the harmonic level.
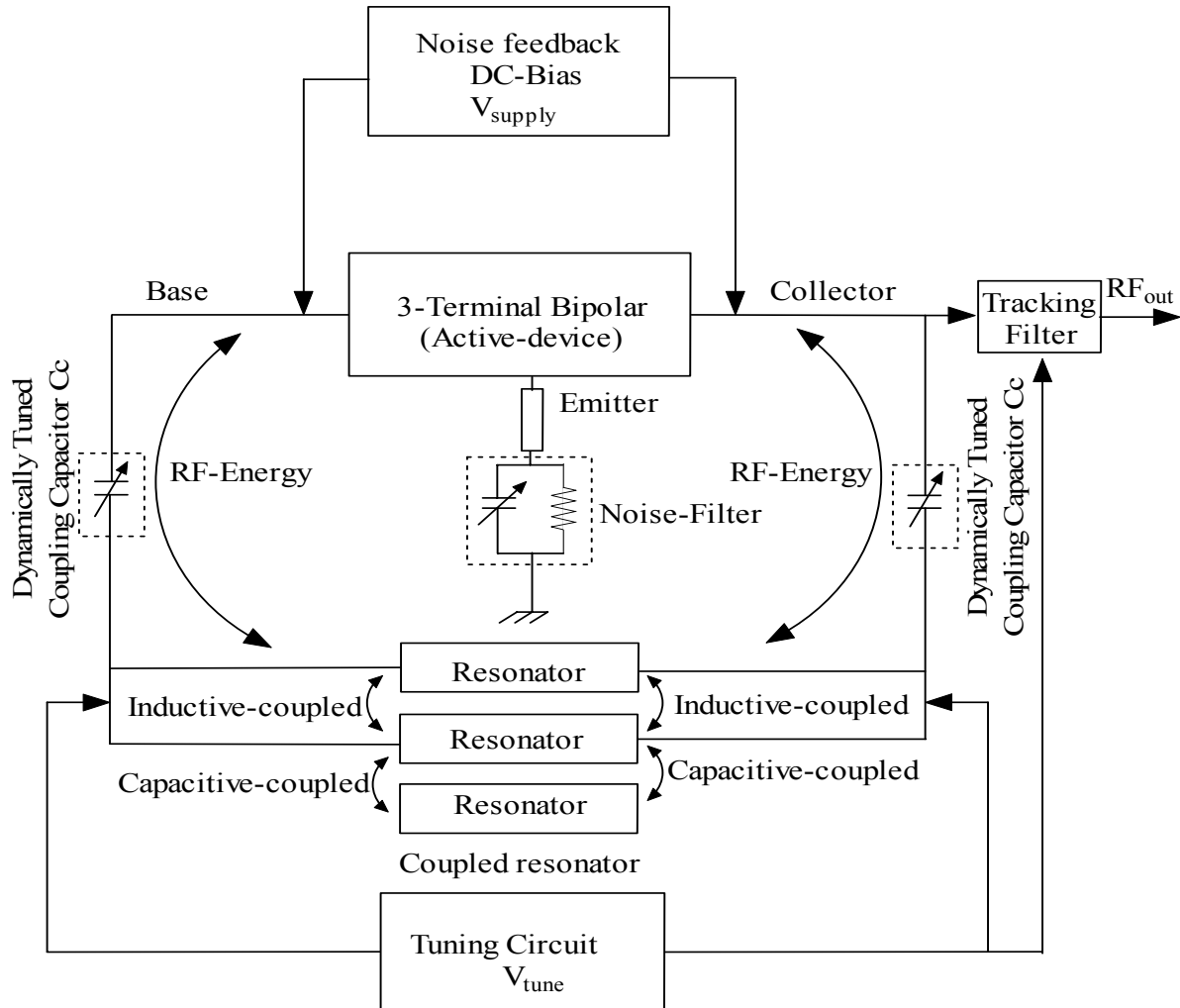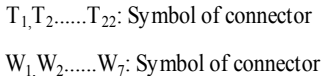
Figure 8-1: Block diagram of the wideband VCO (320-1120MHz).

The variable coupling capacitor Cc is designed for the optimum loading of the resonator network across the active device (the base and collector of the transistor), and is dynamically tuned for optimum performance. As shown in Figure 8-1, the coupled resonator is connected across the base and the collector of the three-terminal device through the coupling capacitor, which is electronically tuned by applying the tuning voltage to the tuning network integrated with the coupled microstripline resonator. The values of the coupling capacitor Cc are derived from the input stability circle. It should be within the input stability circle so that the circuit will oscillate at a particular frequency for the given lowest possible value of the Cc. The additional feature of this topology is that the user-defined frequency band is obtained by adjusting the length and spacing of the coupled microstripline resonator.

Figure 8-2(a) and 8-2(b) depict the corresponding circuit and layout diagram, which allows for a miniaturization and is amenable to integrated chip form. This structure and application is covered by U.S. patent application no. 60/564173.

Figure 8-2 (a): Circuit diagram of the wideband VCO (320-1120MHz).
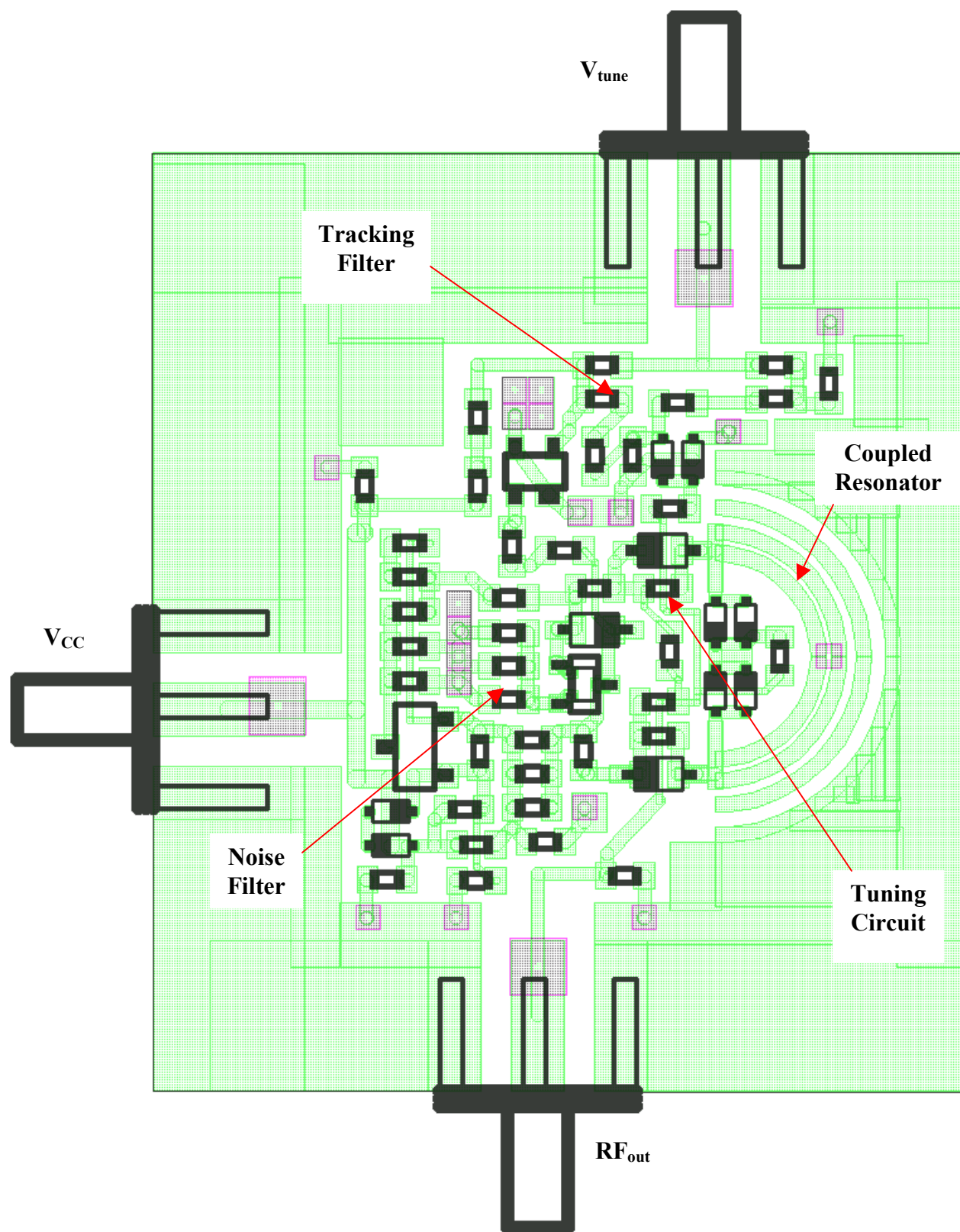
Figure 8-2(b): Layout diagram of the wideband VCO (320-1120MHz).

The layout shown in the Figure 8-2(b) is fabricated on 32 mil thickness Roger substrate of dielectric constant 3.38 and loss tangent $2.7 \cdot 10^{-4}$. As depicted in the Figure 8-2 (b), the coupled microstripline consisting TL1, TL2, TL3, TL4, TL5, and TL6, are symmetrically structured to minimize the stray reactance that would otherwise limit or reduce the circuit tuning range. Layout symmetry is important part of the design, which is implemented by incorporating grounding at the center of the half-circled coupled distributed resonator.

For optimum loading over the band, the variable coupling capacitor C_c as shown in the Figure 8-1, is realized by using D_3, C_2 and D_2, C_3, which are depicted in the Figure 8-2 (a). Table 8.1 shows the components for the circuit shown in the Figure 8-2 (a).

Components for the circuit shown in the Figure 8-2 (a) and (b)

Transistor	Diode	Resistor	Inductor	Capacitor	Microstrip Line	Gain Block
Q_1(BC 857) Philips	D_1(BB689) Infineon	R_1(8 Ω)	L_1(100 nH)	C_1(0.5 pF)	TL1 (w=3mm,l=15mm)	G_1(BGA 612) Infineon
Q_2(BC 857) Philips	D_2(BB555) Infineon	R_2(120 Ω)	L_2(220 nH)	C_2(22 pF)	TL2 (w=3mm,l=17mm)	
Q_3(NE68830) NEC/ Q_3(BFR380) Infineon	D_3(BB555) Infineon	R_3(4.2KΩ)	L_3(220 nH)	C_3(27 pF)	TL3 (w=3mm,l=20mm)	
	D_4(BB659) Infineon	R_4(0.5 Ω)	L_4(220 nH)	C_4(.2 pF)	TL4 (w=3mm,l=15mm)	
	D_5(BB659) Infineon	R_5(10 KΩ)	L_5(220 nH)	C_5(.2 pF)	TL5 (w=3mm,l=17mm)	
	D_6(BB659) Infineon	R_6(3.9KΩ)	L_6(12 nH)	C_6(330Pf)	TL6 (w=3mm,l=20mm)	
	D_7(BB659) Infineon	R_7(10KΩ)	L_7(12 nH)	C_7(10 Pf)	S_1=0.25mm	
	D_8(BB555) Infineon	R_8(220 Ω)	L_8(220nH)	C_8(100 pF)	S_2=0.5mm	
	D_9(BB555) Infineon	R_9(100 Ω)	L_9(100nH)	C_9(100 pF)		
			L_{10}(100nH)	C_{10}(0.1 uF)		
			L_{11}(100nH)	C_{11}(330 pF)		
				C_{12}(330 pF)		
				C_{13}(270 pF)		
				C_{14}(560 pF)		

Table 8.1: Components for the circuit shown in the Figure 8-2 (a).

The additional feature of this topology is user defined frequency band by adjusting the length and spacing of the layout of the distributed coupled microstripline structure. In order to achieve broadband tunability, tuning diodes (D_4, D_5, D_6, and D_7) are connected symmetrically across the coupled resonator to provide uniform time average loaded Q of the varactor-tuned resonator over the band. Figures 8-3 (a) and (b) show the simulated (Ansoft Designer) and measured phase noise plot for the wideband VCO.

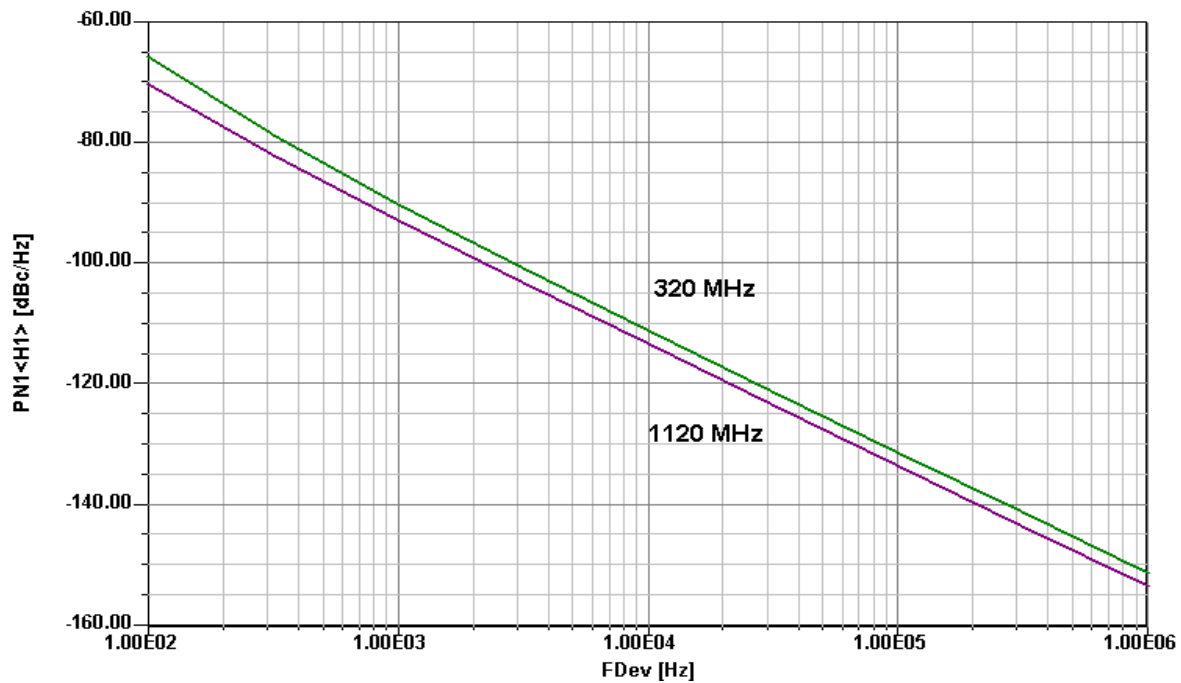Figure 8-3 (a): Simulated phase noise plot for the wideband VCO (320-1120 MHz).
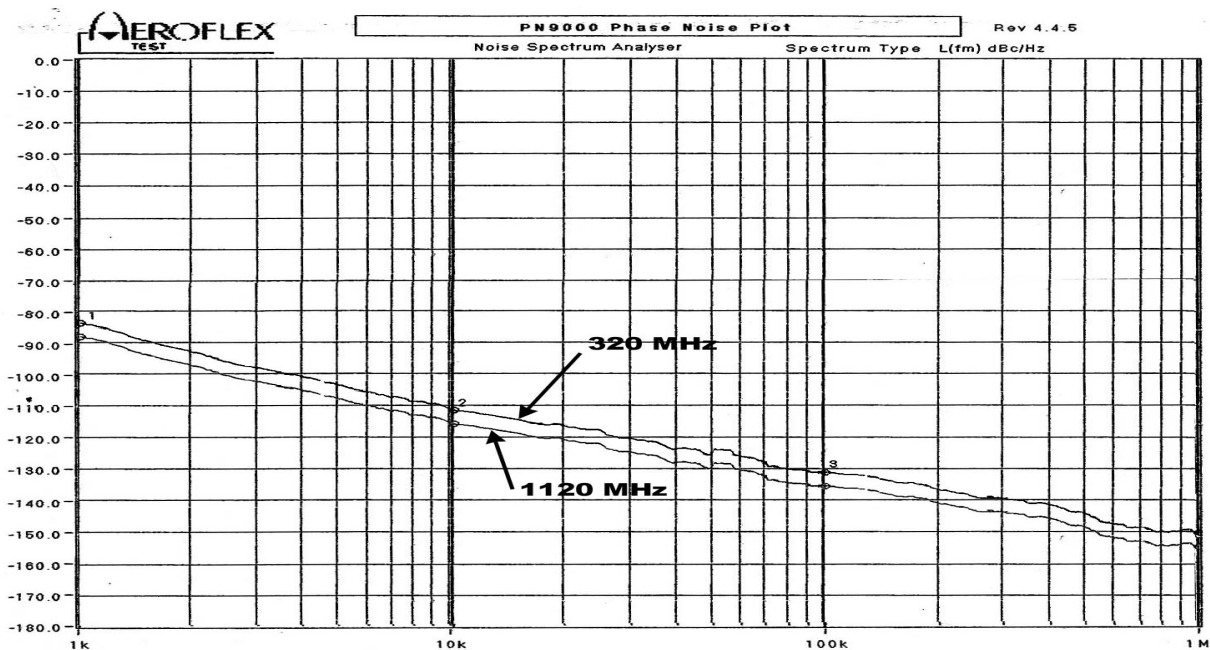
Figure 8-3 (b): Measured phase noise for the wideband VCO (320-1120 MHz).

The simulated (Ansoft Designer) plot of the phase noise agrees with the measured phase noise plot. The measured phase noise is better than –112 dBc/Hz @ 10 kHz for the tuning range of 300-1120 MHz (V_{tune} = 0.5V to 25V). The difference of 2 dB in the

phase noise is observed over the band, is due to the change in the component characteristics over the tuning range.

Figures 8-4, 8-5 and 8-6 show the measured tuning sensitivity, output power, and harmonic suppression plot for the wideband VCOs.

Figure 8-4: Measured frequency versus tuning voltage.

Figure 8-5: Measured output power versus frequency.
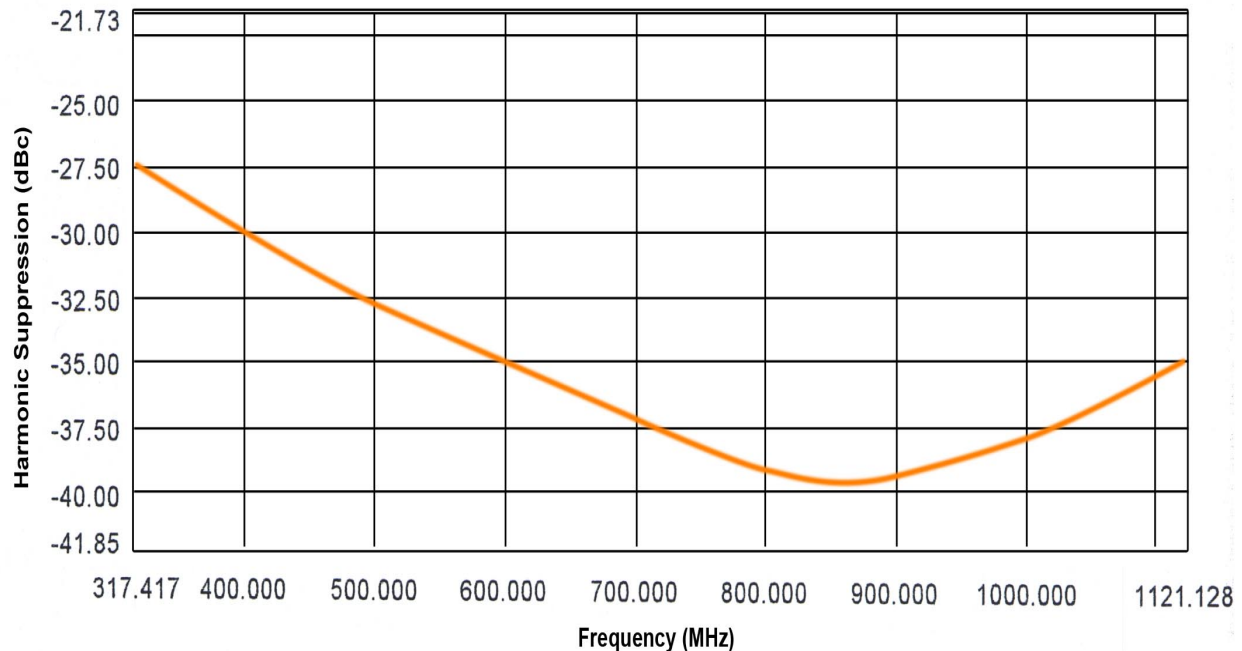
Figure 8-6: Measured second order harmonic versus frequency.
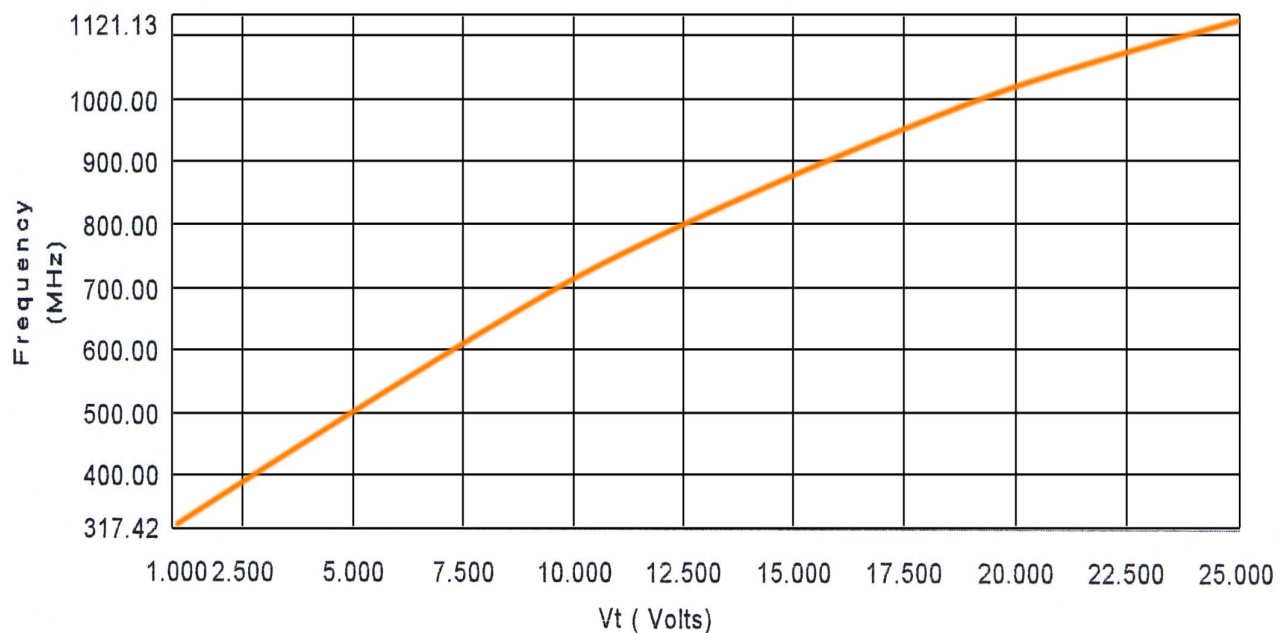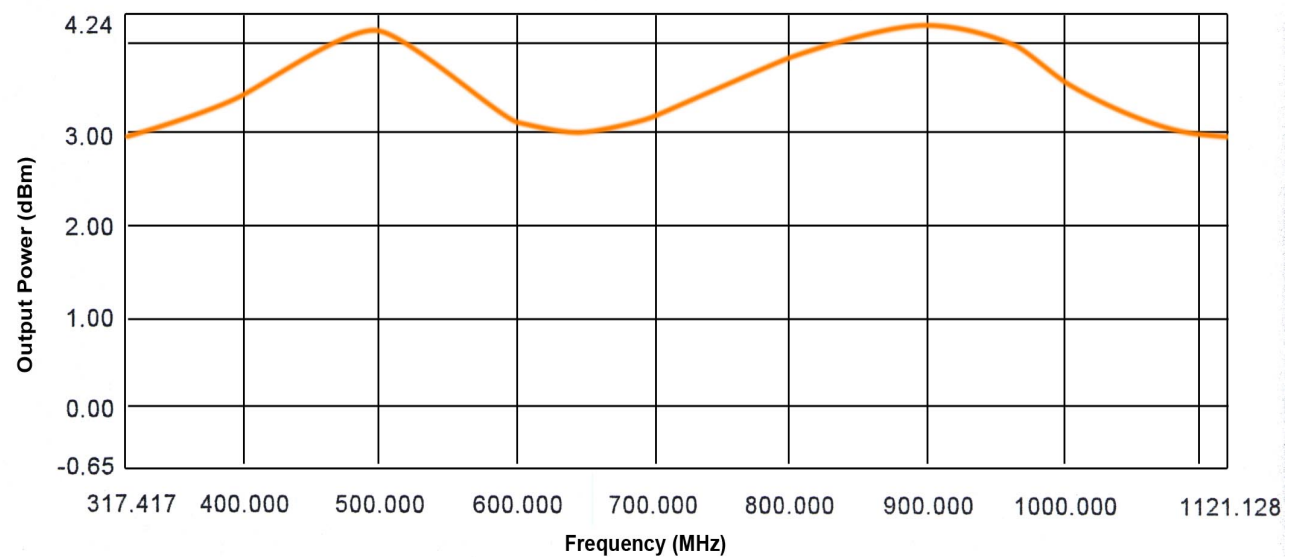
This work offers a cost-effective and power-efficient solution (BFR 380: 5V, 28 mA /NE68830: 8V, 25mA), and further efficiency can be improved by replacing the buffer amplifier with a matching network. The VCOs will then operate at 5V, 18 mA and is best suited for an application where power efficiency and phase noise are criteria for a selection of wideband VCOs.

Wideband VCO (320-1120MHz) Features

Oscillator Frequency:	320-1120 MHz
Tuning Voltage:	1 to 25 VDC (Nom)
Tuning Sensitivity:	24 to 48 MHz/Volt
Bias Voltage:	+5 VDC @ 30mA(Nom)
Output Power:	+2 dBm (Min)
Harmonic Suppression:	25 dBc (Min)
VSWR:	1.5:1
Phase Noise:	-112 dBc/Hz @10KHz offset (Typ)
Phase Noise:	-132 dBc/Hz @100KHz offset (Typ)
Frequency Pulling:	3 MHz (Max) @ 1.75:VSWR
Frequency Pushing:	2 MHz/V (Max)
Output Impedance:	50 Ohm
Operating Temp:	-40°C to 85°C
Size:	0.9 in $\times$0.9 in

8.2 Wideband VCO (1000-2000/2000-4000 MHz) based on Push-Push Approach

This work demonstrates the state-of-the-art of an ultra low phase noise wideband VCOs using Push-Push topology [72]. Figure 8-7 depicts the block diagram of wideband VCOs (1000-2000/2000-4000 MHz), in which all the modules are self-explanatory. In push-push topology, two sub-circuits of a symmetrical topology operate in opposite phase at the fundamental frequency, and the output of the two signals are combined through the dynamically-tuned combiner network so that the fundamental cancels out, while the first harmonics interfere constructively, and available over the tuning range (section 5.2).
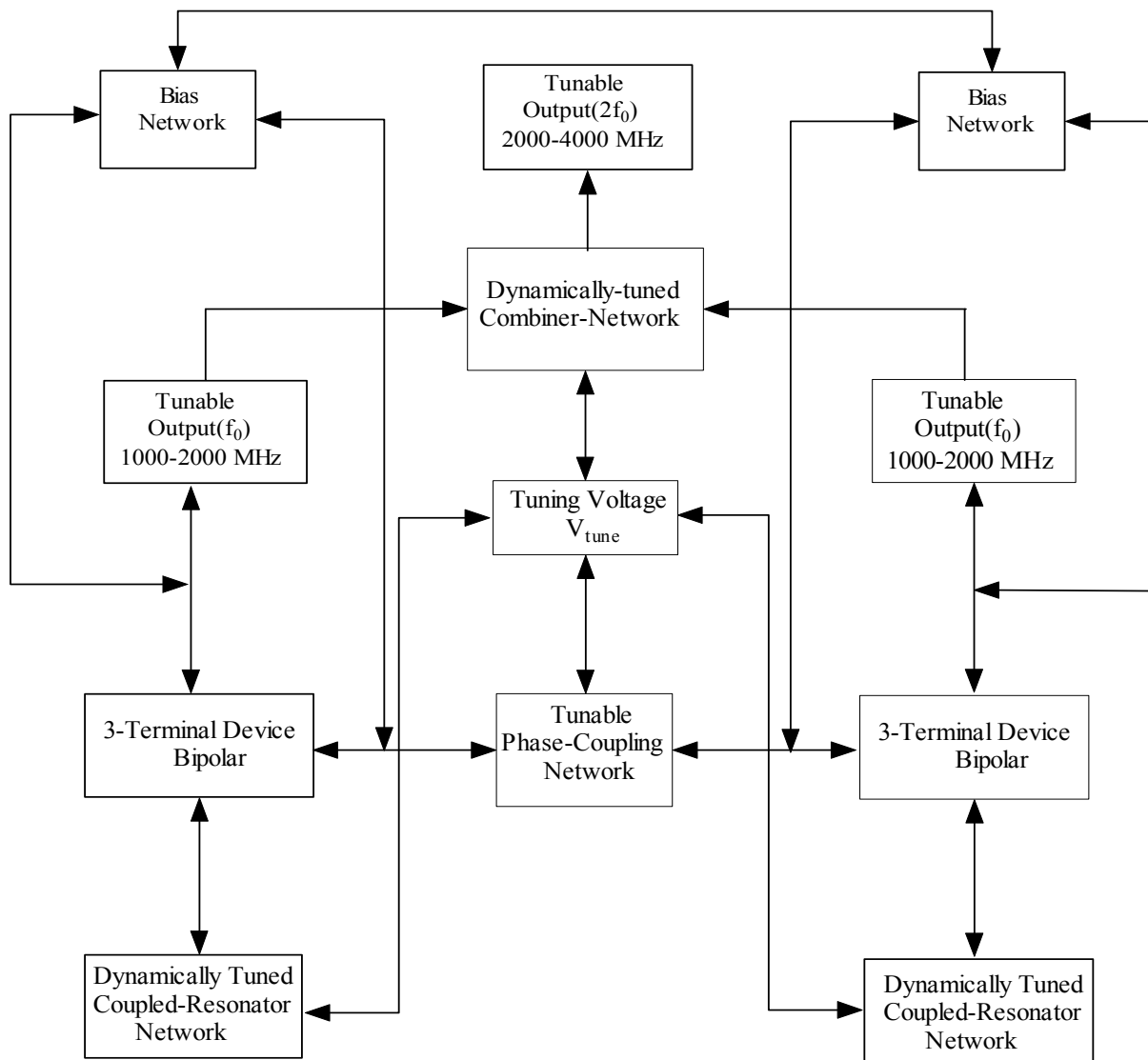
Figure 8-7: Block diagram of wideband VCO using Push-Push topology.

Figure 8-8 shows the schematic of the wideband VCO (1000-2000/2000-4000 MHz) in push-push configuration. The various modules as depicted in the Figure 8-7 are implemented in a way that allows miniaturization, and is amenable for integrated chip design. The structure and application is covered by U.S. patent application nos. 60/501371 and 60/501790.

Figure 8-8: Schematic diagram of wideband VCO using Push-Push topology.

As shown in Figure 8-8, each sub-circuit is runs at one-half of the desired output frequency (f_0), and thereby the second harmonic ($2f_0$) is constructively combined with the help of the dynamically tuned combiner network. Thus, separation of the two harmonics is accomplished using symmetry, which avoids space-consuming filter elements. The wideband tunability is achieved by incorporating a dynamically tuned phase coupling network so that the 180° phase difference, (mutually locked condition: Equation 3.71) is maintained over the tuning range for push-push operation.

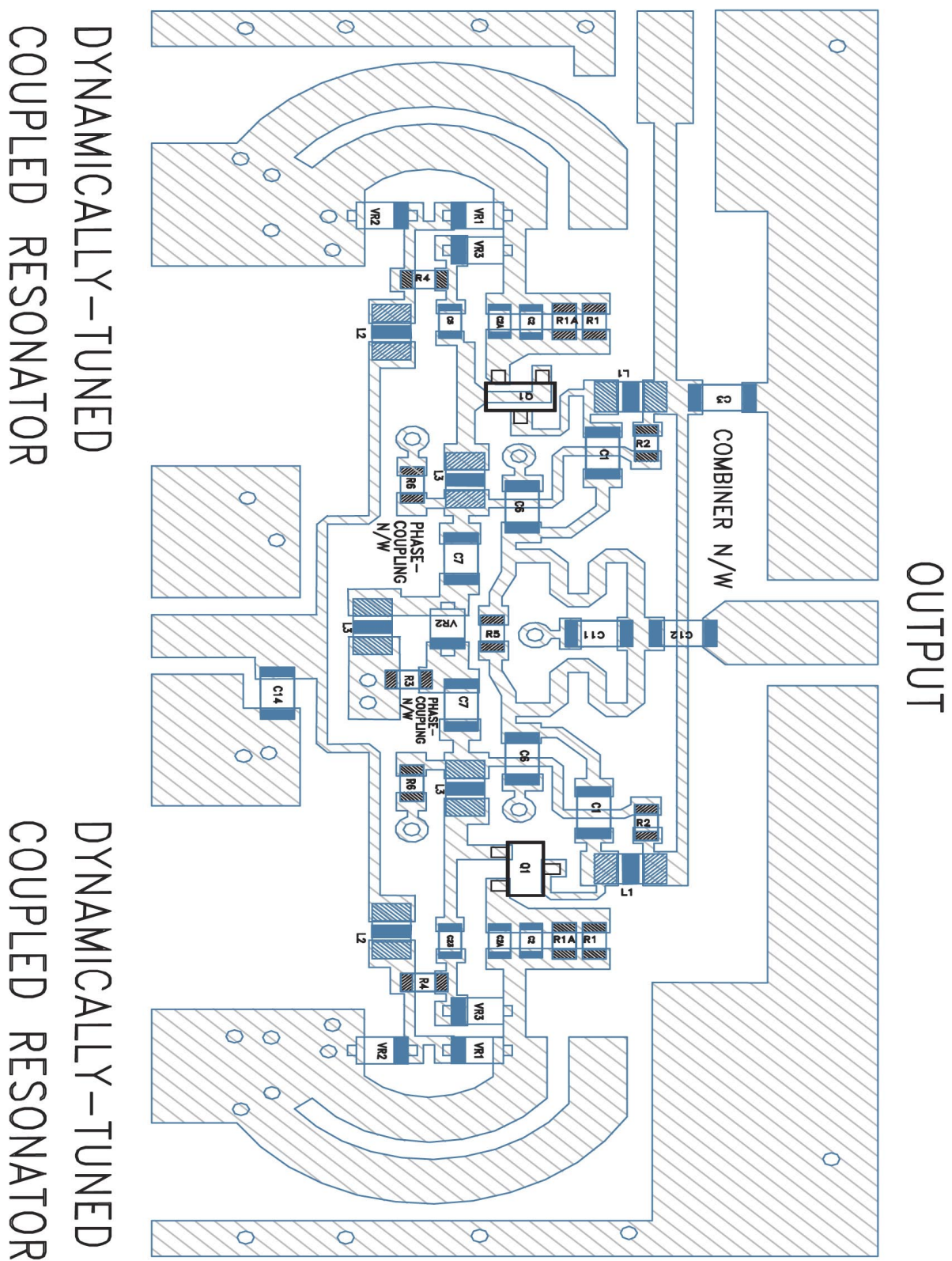Figure 8-9: Layout of wideband VCO using push-push topology (US Copyright Reg.: Vau-603-982).

The push-push topology has several advantages over single-ended versions other than improvement in phase noise. The usable frequency range of the transistors can be extended, and this can be exploited, for instance, using transistors that are larger than usual and have lower $1/f$ noise due to reduced current density. Figure 8-9 shows the layout of the Figure 8-8. The layout shown in the Figure 8-9 is fabricated on 32 mil thickness Roger substrate of dielectric constant 3.38 and loss tangent $2.7 \cdot 10^{-4}$. As shown in the Figure 8-8, dynamically tuned coupled resonator is connected with the emitter of the transistor (NE68830) to provide a uniform loaded Q over the tuning range. Experimental results have shown that a poor mismatch at the fundamental results in discontinuous tuning due to the non-uniform phase shift over the tuning range. This mismatch in phase-shift between the two sub-circuits is due to possible component tolerances, package parameters, and the phase associated with the path difference over the tuning range. Therefore, the system goes out of the locking range. Figure 8-10 shows the compact layout of Figure 8-9 so that the phase-shift between the two sub-circuits can be minimized. The effective phase shift is reduced in comparison to the layout in Figure 8-9.
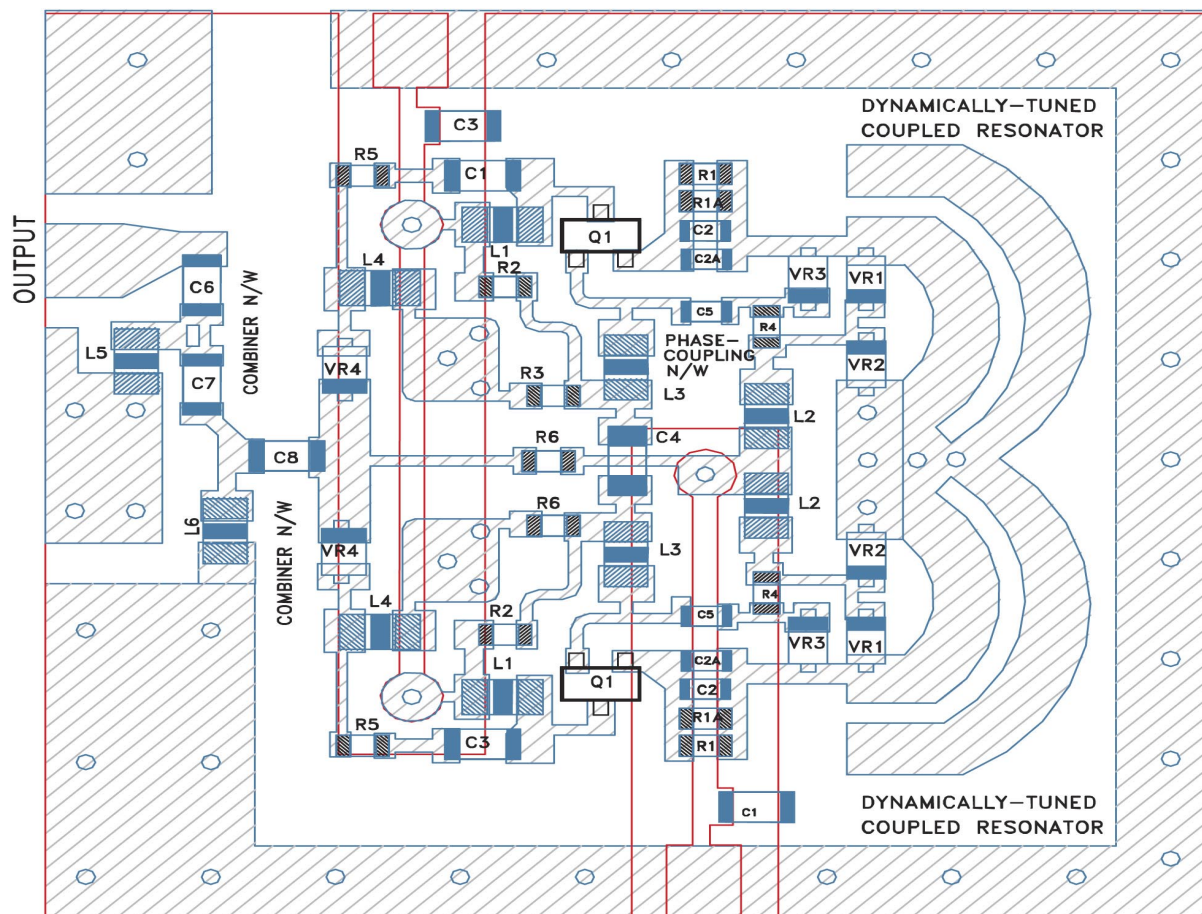

Figure 8-10: Compact layout of a wideband VCO using push-push topology
(US Copyright Registration No: Vau-603-982).

The layout shown in Figure 8-10 minimizes the phase-shift due to the path difference between the two sub-circuits over the tuning range, but still shows discontinuous tuning at some point over the band due to the package parasitics and component tolerances associated with the discrete components of the circuit. The problem of discontinuous tuning can be overcome by incorporating a phase detector (U.S. application patent no: 60/563481). Then the tuning range can be extended to a multi-octave band. Figure 8-11 shows the plot of the RF current of the sub-circuit 1 and sub-circuit 2, which are out of phase in a mutually synchronized condition, as given by Equation (3.71).
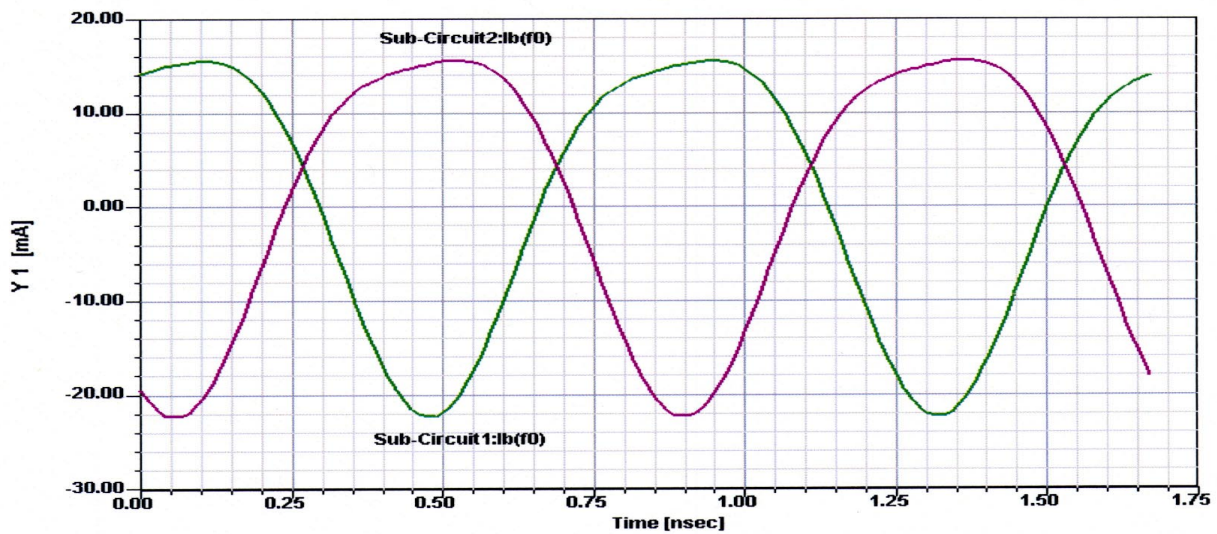
Figure 8-11: Plot of the RF-collector currents of the push-push topology.
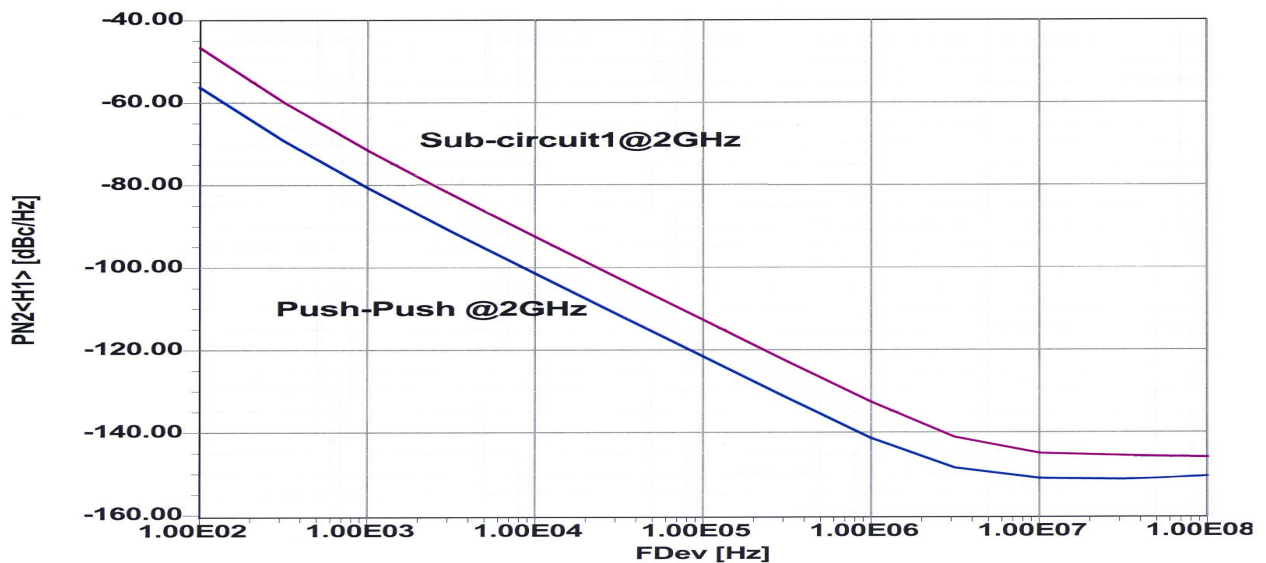
Figure 8-12(a): Simulated phase noise plot for push-push VCO (2000-4000 MHz) for the frequency of 2GHz.

142

Figures 8-12 (a) and (b) show the simulated phase noise plot for a wideband push-push VCO at a frequency of 2 GHz and 4 GHz.
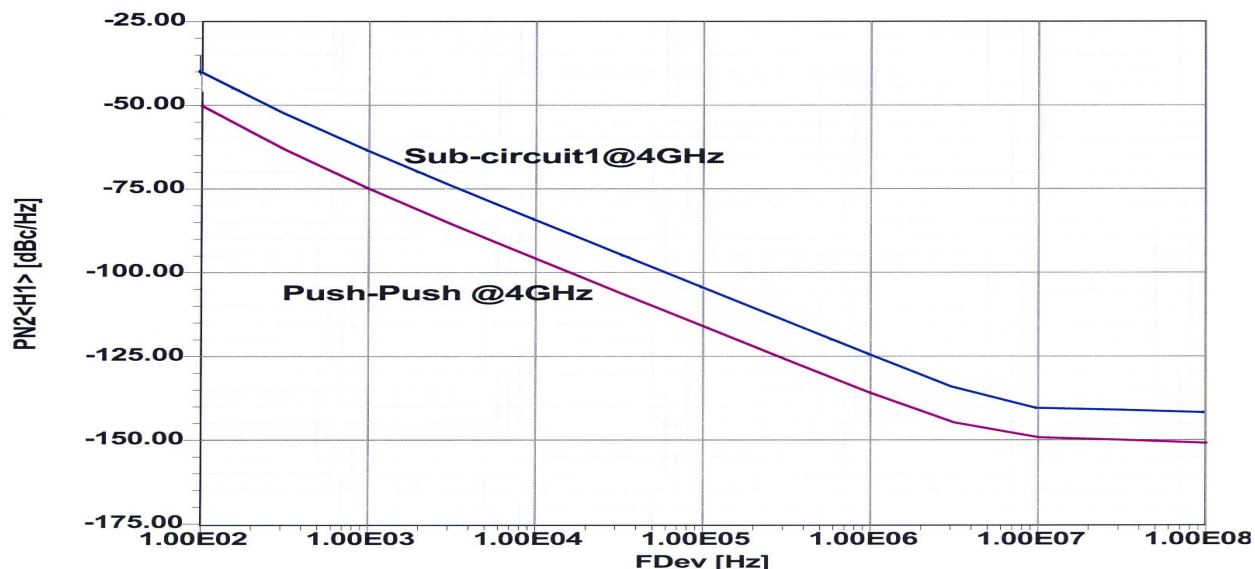
Figure 8-12(b): Simulated phase noise plot for push-push VCO (2000-4000MHz) for the frequency 4 GHz.

Figures 8-12 (a) and (b), show a simulated phase noise with an 8-9 dB improvement over the frequency band (2000-4000 MHz). Figures 8-12 (c), (d), (e) and (f) show the measured phase noise plot for the sub-circuit 1 and the push-push VCO at a frequency of 2000 MHz and 4000 MHz.

Figure 8-12(c): Measured phase noise plot for push-push VCO (2000-4000MHz) of sub-circuit 1 for the oscillation frequency 2000 MHz.

The measured phase noise show 5-7 dB improvement with respect to the fundamental oscillator sub-circuit and is better than −112 dBc/Hz at 100 kHz offset from the carrier for the tuning range of 2000-4000 MHz in the push-push configuration. From Equation (4.97), the phase noise relative to the carrier decreases by a factor of N, where N is the number of coupled oscillator circuits. For a bilateral coupled oscillator (push-push), the improvement of the simulated phase noise is 9 dB with respect to fundamental oscillator, as discussed in the Section 5.2.

Figure 8-12(d): Measured phase noise plot for the wideband push-push VCO (2000-4000 MHz) of combiner output for the oscillation frequency 2000 MHz.
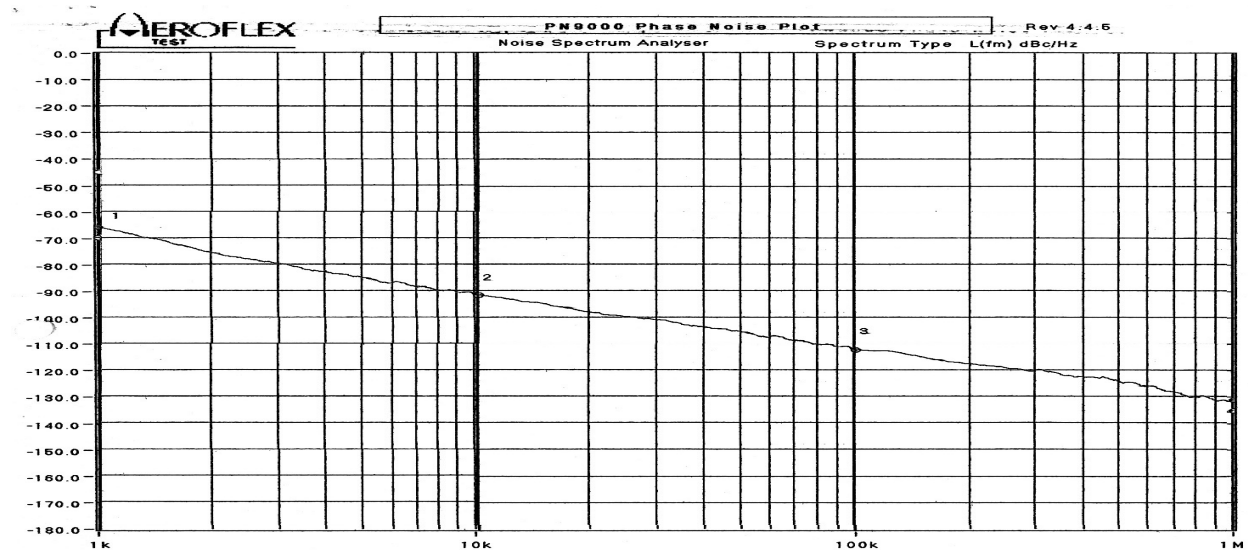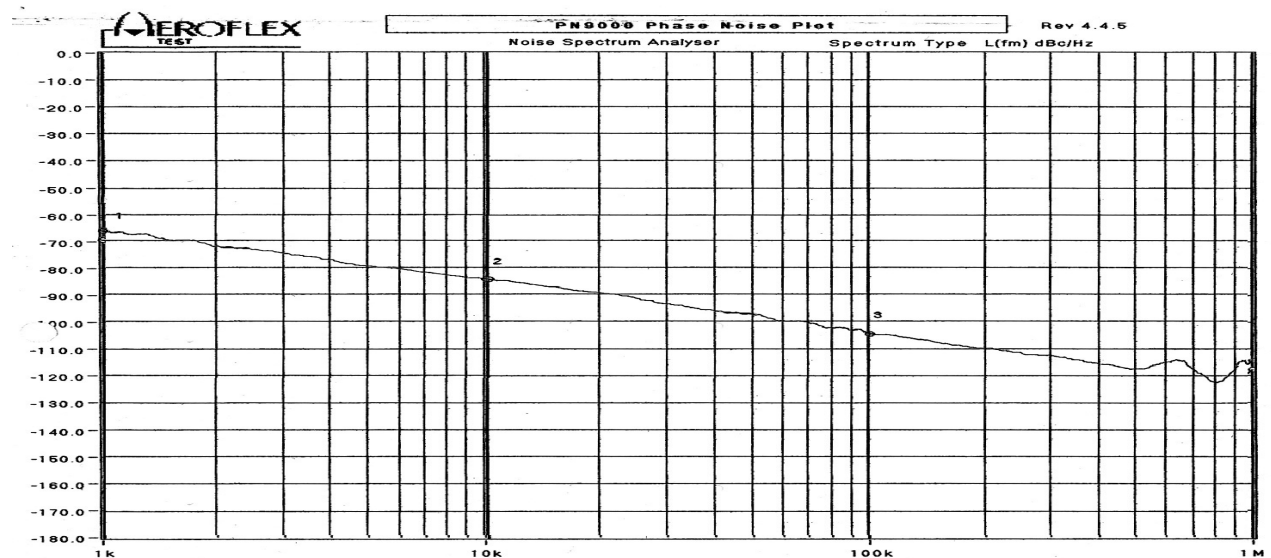

Figure 8-12(e): Measured phase noise plot for the wideband push-push VCO (2000-4000 MHz) of sub-circuit1 for the oscillation frequency 4000 MHz.
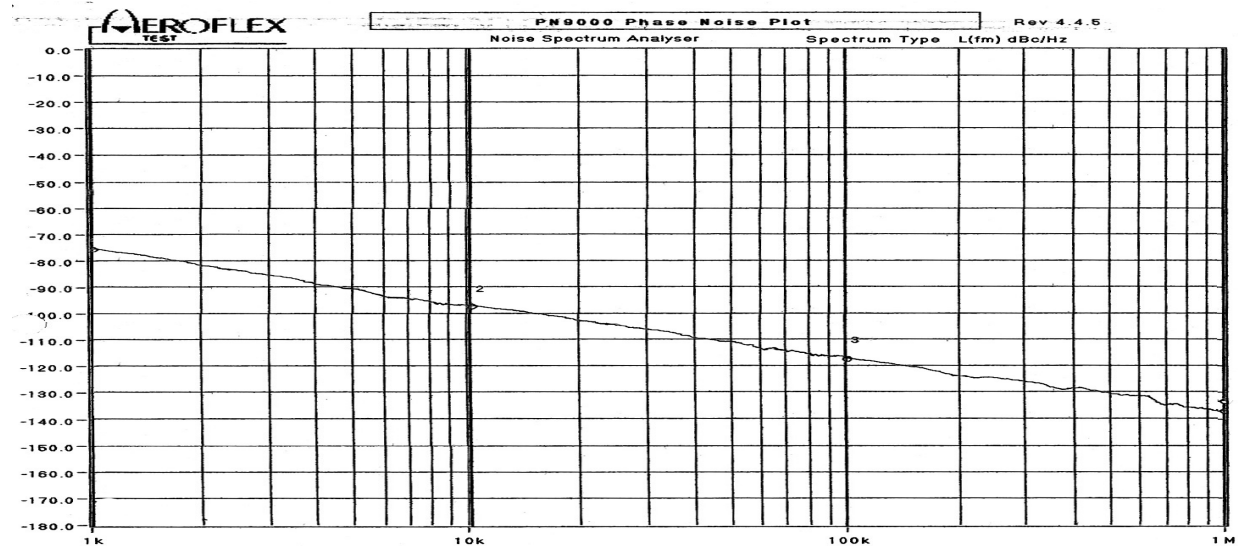
144
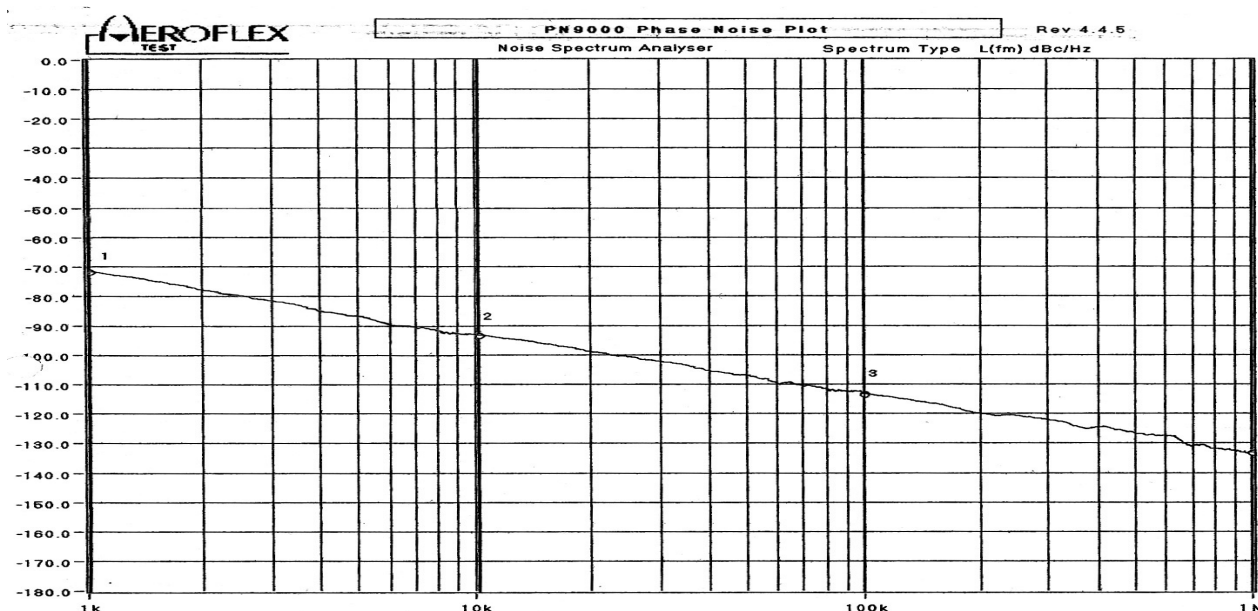
Figure 8-12(f): Measured phase noise plot for the wideband push-push VCO (2000-4000 MHz) of combiner output for the oscillation frequency 4000 MHz.

Measured result show a 5-7 dB improvement of the phase noise over the band. The discrepancy of 2-4 dB can be attributed to the package parasitics, dynamic loaded Q, and tolerances of the components values of the two sub-circuits over the tuning range. Further improvement in the phase noise can be achieved by implementing N-push approach with an integrated phase detector for minimizing and correcting the phase shift over the tuning range; this is a further extension of this research work for the purpose of covering the millimeter frequency range [68].

Wideband Push-Push VCO (1000-2000/2000-4000 MHz) Features

Oscillator Frequency:	1000-2000/2000-4000 MHz
Tuning Voltage:	0 to 25 VDC (Nom)
Tuning Sensitivity:	40-100MHz/Volt
Bias Voltage:	+12 VDC @ 30mA(Nom)
Output Power:	+0 dBm (Typ)
Harmonic Suppression:	20 dBc (Typ)
VSWR:	1.5:1
Phase Noise (2000 MHz):	-98 dBc/Hz @10 kHz offset (Typ)
Phase Noise (4000 MHz):	-93 dBc/Hz @10 kHz offset (Typ)
Frequency Pulling:	6 MHz (Max) @ 1.75:VSWR
Frequency Pushing:	4 MHz/V (Max)
Output Impedance:	50 Ohm
Operating Temp:	-40°C to 85°C
Size:	0.9 in ×0.9 in

145

8.3 Wideband VCO (1500-3000/3000-6000 MHz) Based on the Dual-Coupled Resonator

Figure 8-13 shows the schematic diagram of the wideband VCO (1500-3000/3000-6000 MHz) based on a dual-coupled resonator [74].
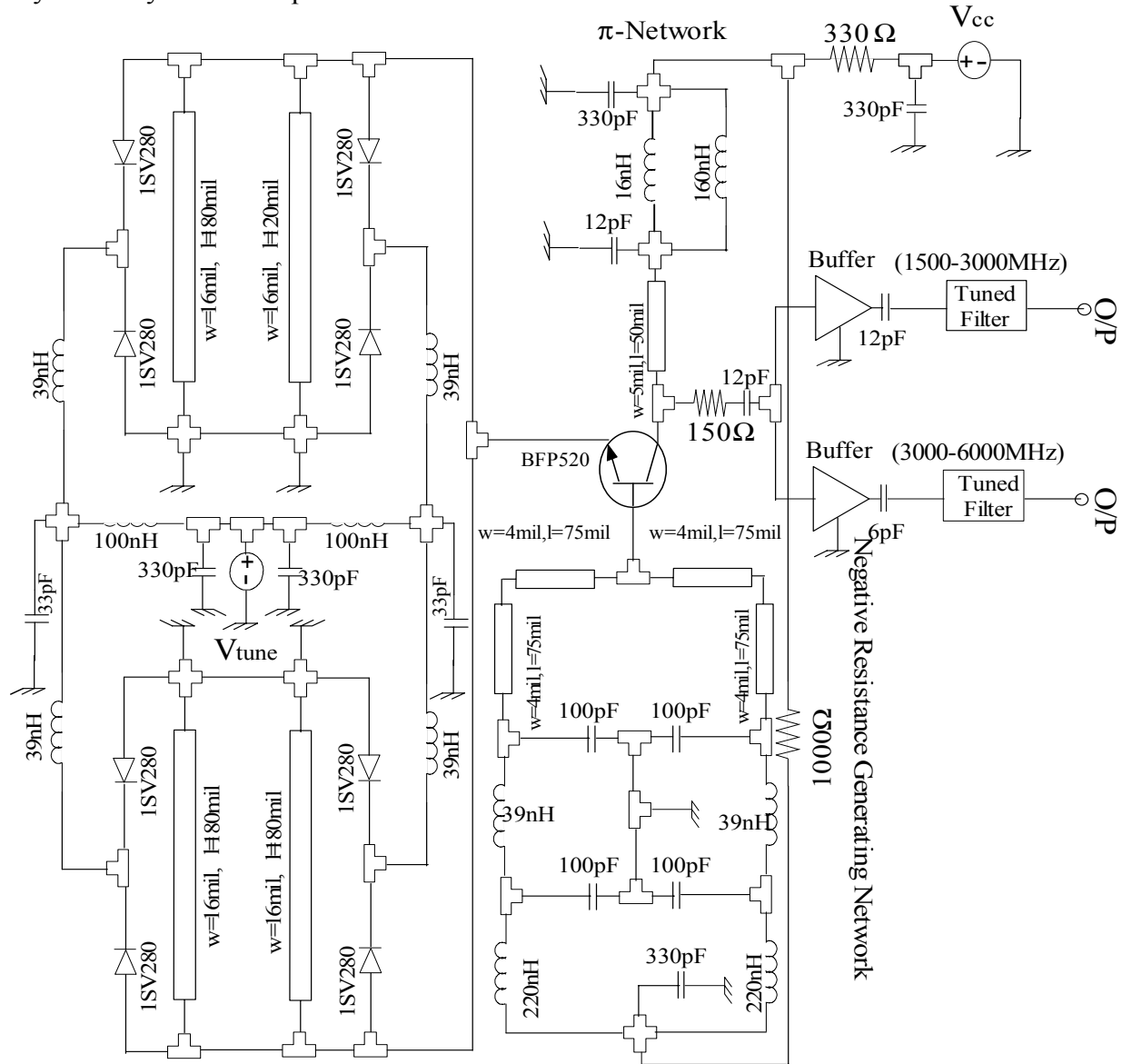
Figure 8-13: Schematic of the wideband VCO (1500-3000/3000-6000 MHz).

For wideband application such as the octave band, the grounded base topology is

preferred due to the broadband tunability factor. For wideband tunability, the required negative resistance over the band is generated by the feedback base-inductance, but the polarity of the reactance may change over the frequency band and can lead to the disappearance of the negative resistance as the operating frequency exceeds its SRF (self resonance frequency).

This problem is overcome by incorporating a coupled line topology instead of the lumped inductance used as a feedback element for generating the negative resistance over the tuning range, as shown in Figure 8-13.

Designing wideband VCOs at high frequency is challenging due to the change in the characteristics of the RF components over the tuning range. Biasing is critical and can have a negative effect on the overall performance if implemented poorly because the oscillator/VCO circuits are highly sensitive to voltage fluctuations and up-convert any noise on the bias points.

Biasing with a resistor provides a resonant free-solution for wideband applications, but it may unnecessarily load the output of the oscillator, thereby lowering the gain and degrading the phase noise performance. A normal biasing scheme such as a voltage divider or a current divider technique, using resistor is good for amplifier design, may significantly contribute to noise in the oscillator circuit. Biasing with the potential divider with the resistors effectively increase the noise, which may be up-converted into the fundamental frequency of oscillation as additional phase noise.

For VCOs circuits, the collector is generally biased using an inductor with an SRF as high as possible above the oscillation frequency so that it will not affect the fundamental frequency of oscillation. The value of the inductor must be high enough to resemble a broadband RF open circuit for a desired tuning range.

This can be achieved by incorporating two parallel inductor series with a transmission line to create the broadband open-circuit as shown in Figure 8-13. Similarly, multiple capacitors are used in parallel to create a broadband RF short-circuit with respect to the SRF for the lower and higher end of the tuning range.

Biasing for tuning network is also critical for overall phase noise performances. The tuning diode exhibits a change in capacitor as a function of tuning voltage. A resistor provides a resonant-free biasing, but it introduces noise to the oscillator due to the voltage gain (integration gain) K_0 (MHz/V) of the oscillator. Therefore, a π-network is incorporated to reduce the noise in the tuning network, as shown in Figure 8-13, which minimizes the noise at tuning port. Figure 8-14 shows the layout diagram of the wideband VCO (1500-3000/3000-6000 MHz) frequency band, and is fabricated on 32mil thickness Roger substrate of dielectric constant 3.38 and loss tangent $2.7 \cdot 10^{-4}$.

OUTPUT
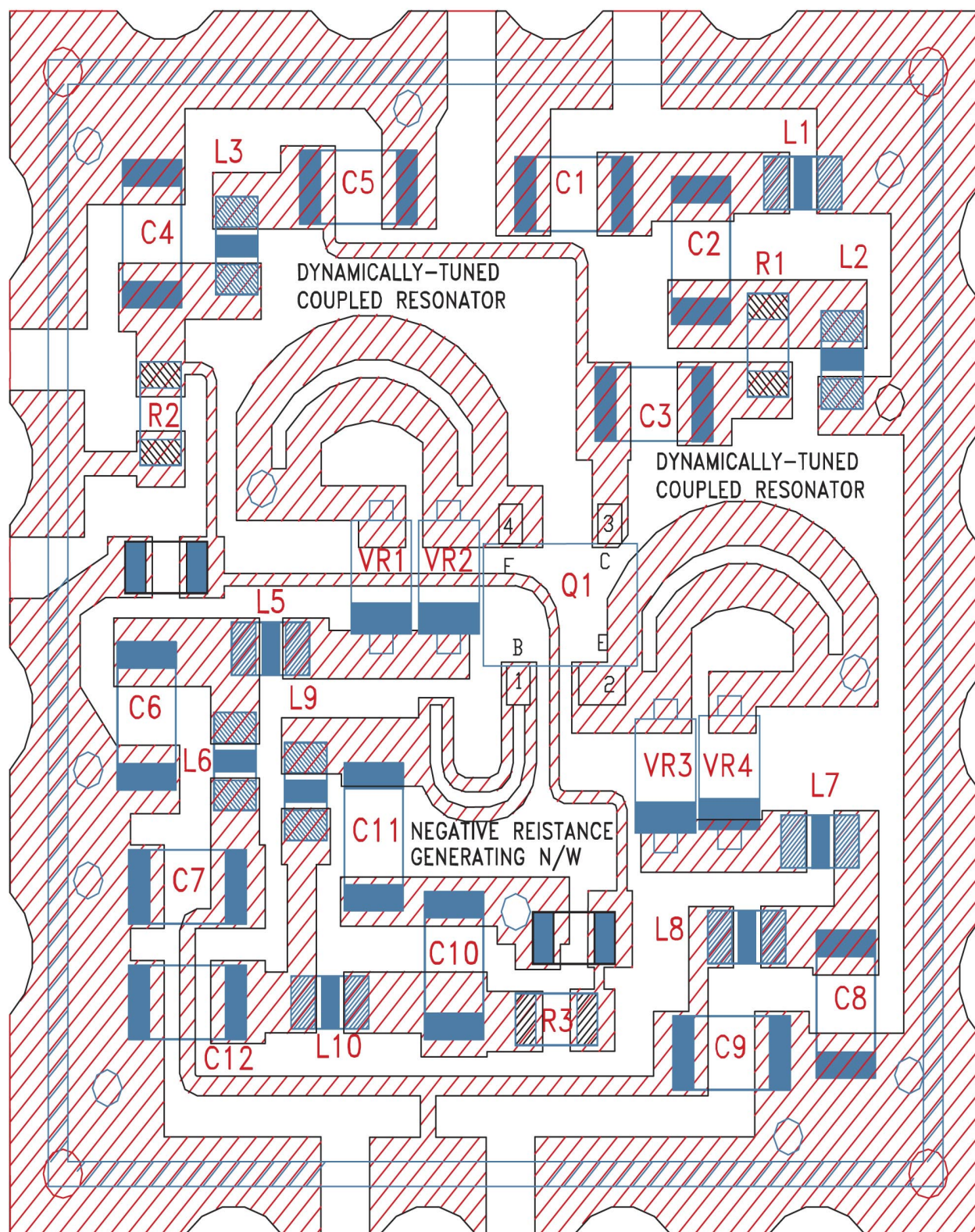
Figure 8-14: Layout of the wideband VCO (1500-3000 MHz/3000-6000 MHz)
(Copyright Registration No.: Vau-603-984).

As shown in the Figure 8-14, the symmetrical coupled resonator is connected across the two emitters of the transistor (Infineon BFP520) to provide a uniform loaded Q over the tuning range, thereby providing a uniform phase noise over the frequency band. Figures 8-15 and 8-16 show the simulated and measured phase noise plot of the wideband VCO (1500-3000 MHz), which closely agrees within 2.5 dB.
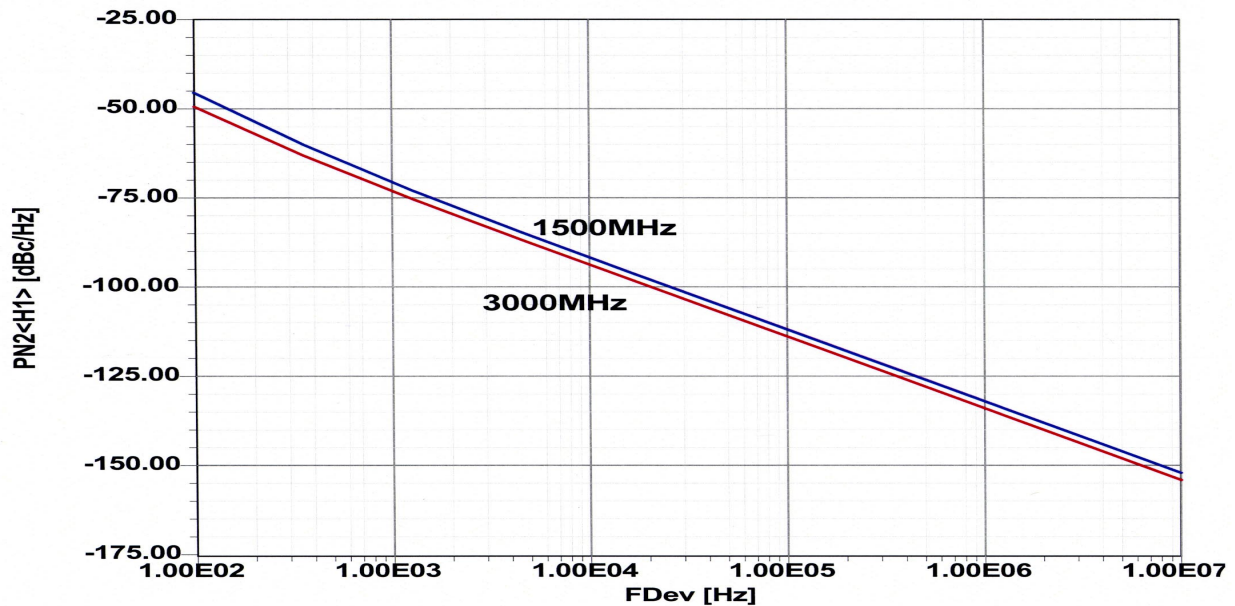
Figure 8-15: Simulated phase noise plot of the VCO (1500-3000 MHz).
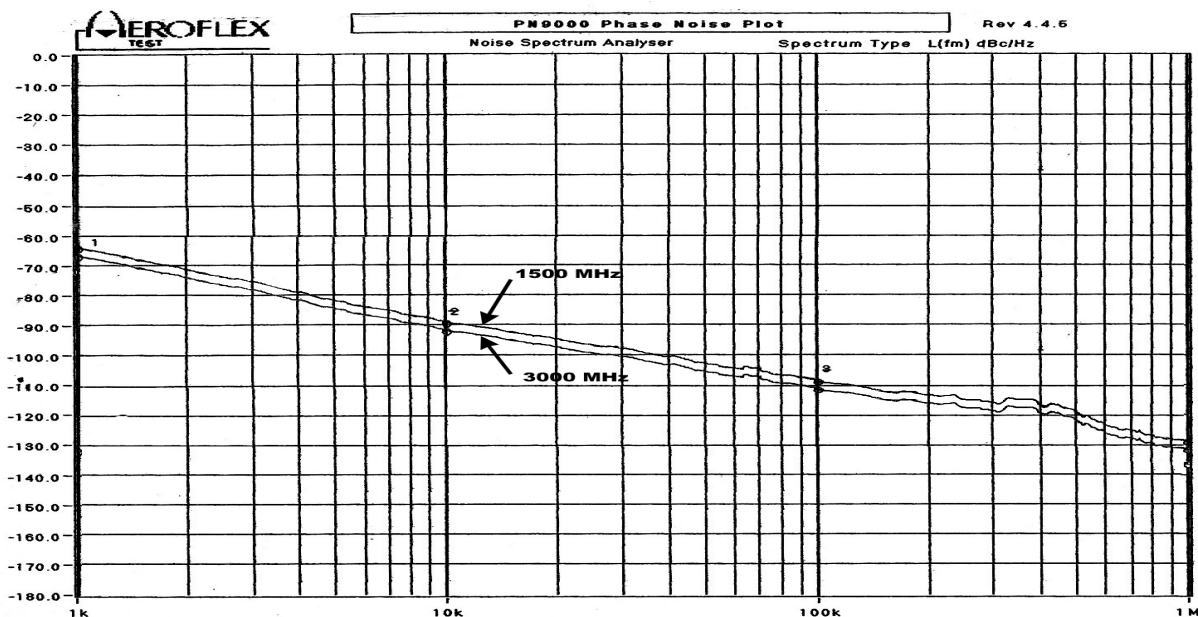
Figure 8-16: Measured phase noise plot for the VCO (1500-3000 MHz).

The circuit shown in the Figure 8-13, is rich of the second harmonic under large signal drive level, and the second harmonic (3000-6000 MHz) can be filtered out by as an extension of the fundamental frequency band without an external multiplier module.

Figures 8-17 and 8-18 show the simulated and measured phase noise plot of the wideband VCO (3000-6000 MHz), which closely agrees within 3 dB.
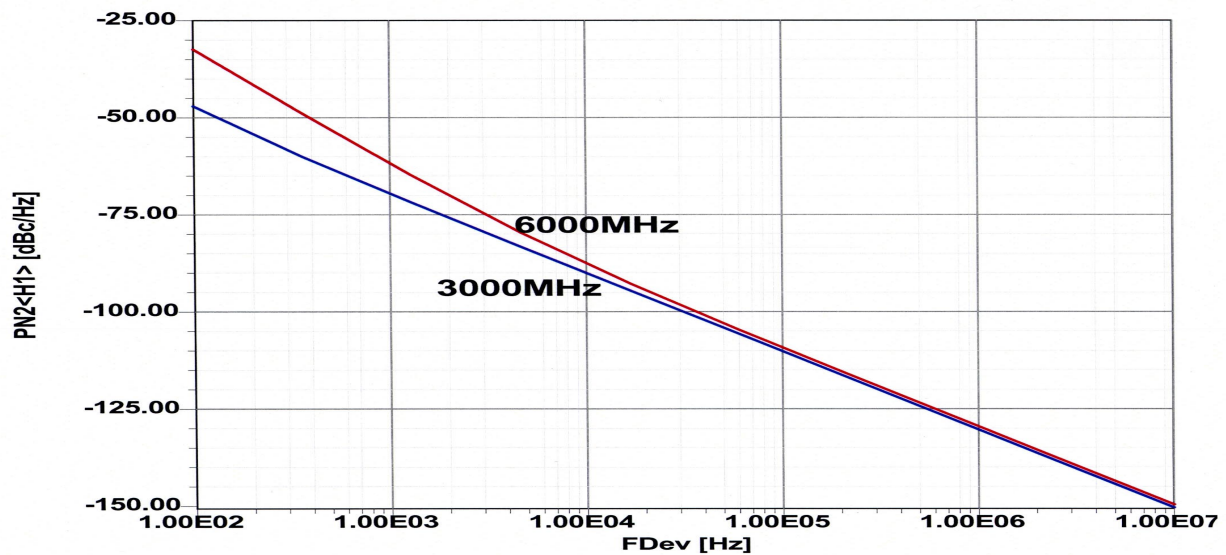
Figure 8-17: Phase noise plot of the wideband VCO (3000-6000 MHz).
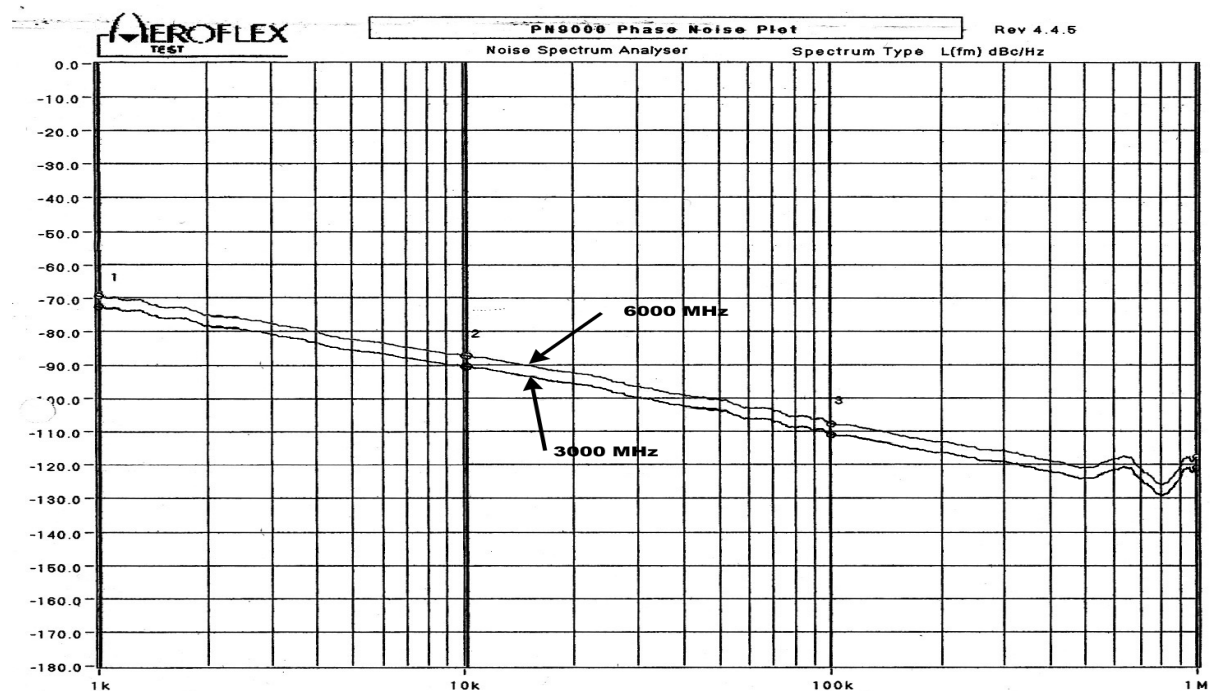
Figure 8-18: Measured phase noise plot of the wideband VCO (3000-6000 MHz).

Wideband VCO (1500-3000/3000-6000 MHz) Features

Oscillator Frequency:	1500-3000/3000-6000 MHz
Tuning Voltage:	0 to 20 VDC (Nom)
Tuning Sensitivity:	75 to 150 MHz/Volt
Bias Voltage:	+5 VDC @ 30mA(Nom)
Output Power:	+5 dBm (Typ)
Harmonic Suppression:	20 dBc (Typ)
VSWR:	1.5:1
Phase Noise (1500-3000 MHz):	-90 dBc/Hz @10 kHz offset (Typ)
Phase Noise: (3000-6000 MHz):	-88 dBc/Hz @10 kHz offset (Typ)
Frequency Puling:	2 MHz (Max) @ 1.75:VSWR
Frequency Pushing:	3 MHz/V (Max)
Output Impedance:	50 Ohm
Operating Temp:	-40°C to 85°C
Size:	0.5 in $\times$0.5 in

Chapter 9

Discussion and Conclusions

9.1 Accomplishments

The objective of this dissertation was to design a wideband (octave-band and more) voltage controlled oscillator that can satisfy the present demand for low-cost, low-noise, power-efficient, wide-band, compact-size, and are amenable for integration in integrated chip form. Furthermore, the freedom of selection of the frequency-band, compact size, low cost, low power consumption, and stability over temperature range will make this technology attractive for mobile communication applications. As a result of this work, a set of design guides and coupled-oscillator noise equations were found. All the important circuits were built, measured, and analyzed in Ansoft Designer.

There are a number of functional parameters that are important depending on the oscillator's intended applications, but phase noise is the most fundamental and important figure of merit. Wideband tunability and good phase noise performances are the most opposing requirements due to the problem of controlling the oscillator loop parameters and optimization of the time average loaded Q of the resonator over the tuning band, simultaneously. A low cost, small, long-battery-life solution has been the dream for decades. Many efforts have been devoted to the integration of such circuits in low-cost technology in order to reach the goal. The proposed topology under this work offers a cost-effective and power-efficient solution that maintains the noise performance over the tuning range. This objective is accomplished by dynamically tuning the transistor stability factor, phase coupling network, noise filtering network, tracking filter and maintaining the time average loaded Q of the coupled resonator over the desire band.

YIG resonator-based VCOs have wideband tunability with the external DC magnetic field, but at a high price and they are not amenable for integration in chip form. Thus, the work described here explores the different topology for the wideband oscillator (octave-band tunability) and offers a cost-effective alternative to the YIG resonator-based wideband VCO in the frequency range of L, S, and C band. This work demonstrates the feasibility of ultra low noise VCOs covering a frequency band from 320 MHz to 6000 MHz, and all the three circuits (320-1120 MHz, 1000-2000/2000-4000 MHz and 1500-3000/3000-6000 MHz) are the basis for the N-push approach for extending the frequency in the millimeter frequency band.

These VCOs represent the first octave band coupled/push-push designs being attempted, which give comparable phase noise performances of the existing narrowband VCOs, and thereby this research work may be useful for replacement of number of narrowband VCOs by single wideband VCOs and opens the door for many possible future works.

Wideband Integrated VCO

The increasing demand for the portable communications equipment has driven researchers to produce transreceivers at a lower cost, and this has led to an intense interest in integrating as many components as possible. One high-speed component that has been particularly hard to integrate is the VCO, due to the poor quality of on-chip passive components in silicon integrated circuit technologies, namely the low quality factor Q of on-chip inductors and the poor linearity of on-chip varactors. Larger inductors require long metal traces, hence they are susceptible to noise pick-up through electromagnetic coupling. Integrating the VCO on a single die is a challenging goal because with the VCO being an extremely sensitive, the analog part has to operate in an overly noisy environment where numerous digital sub-circuits share the same substrate. In order to reach the goal, special concepts have to be applied by trying a different topology such as the coupled oscillator/N-push approach with noise cancellation techniques. Despite the ongoing trend toward higher integration levels, discrete VCOs still have their place in contemporary wireless designs because discrete VCOs offers advantages such as superior performance, tremendous design flexibility, faster time-to-market, low cost, and reduce risk.

9.2   Conclusions and Future Possibilities

The improvement of the FM noise of the coupled oscillator system is discussed. The degradation of the phase noise due to the flicker frequency effects is more concern and this will be an important research area. Since on-chip resonators elements provide low Q factors, transistors with low $1/f$-noise and special concepts have to be applied in order to meet the present phase noise requirements.

One obvious extension of the present work is to tackle a multi-octave band voltage controlled oscillator, and one of the methods used to reach this goal is the N-push approach with the integrated phase detector. This approach is particularly useful if the frequency is high enough that a fundamental oscillator is beyond the capabilities of the given MMIC process. This work has concentrated on dynamically tuned coupled resonators, tuning networks, and phase shift networks. As an extension of this work, an effort is currently being undertaken to control the phase shift due to the tolerance of the RF components through the phase detector circuit, thereby the topology can be extended for ultra low noise integrated multi-octave-band VCOs.

An even smaller and more cost-effective VCO technology will emerge in the future by employing an N-push/push-push approach in Monolithic IC and MEMS [69] technology, but presently, this technology is not suitable or compatible with commercial applications due to the problems with the large current and size requirements. More attention and research work is needed to meet these challenges. Figure 9-1 shows the layout of the integrated VCO for multi-octave-band VCOs, which is based on N-Push coupled

topology integrated with the phase detector network; thereby, the non-uniform phase shift is dynamically corrected for N-Push operation over the band. This is a further extension of this research work, and can be implemented in MEMS technology for the purpose of the covering wide frequency range in the millimeter frequency band [72].
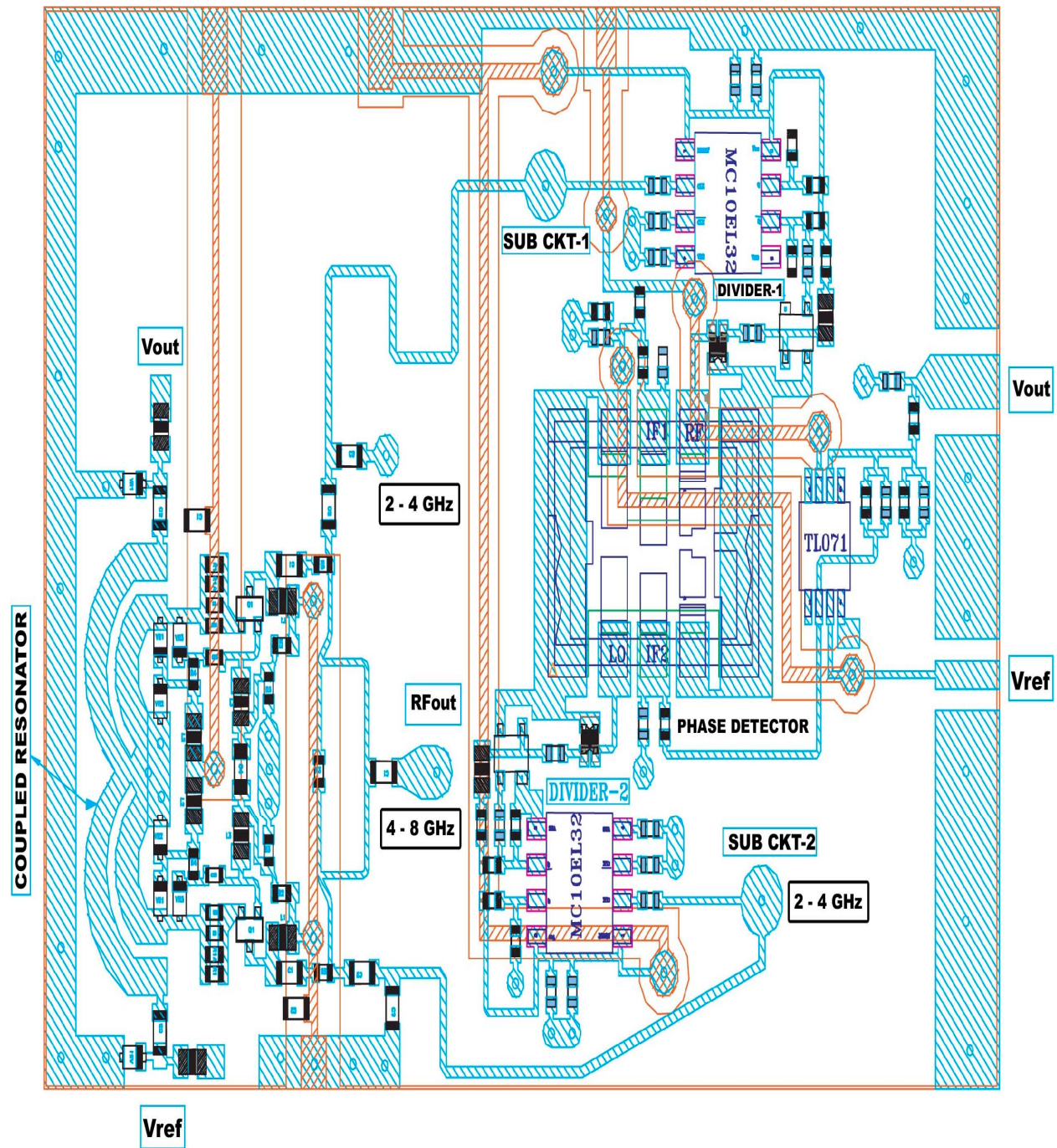
Figure 9-1:Layout of the integrated VCO for multi-octave-band tunability (2-8 GHz/8-16 GHz).

Chapter 10

Abbreviations and Symbols

Symbol	Description
$\Delta A(t)$	Amplitude fluctuation
$\Delta\varphi(t)$	Phase fluctuation
Δf	Noise bandwidth
$\Delta\theta$	Steady state phase difference
DUT	Device under test
LTV	Linear time variant
LTIV	Linear time invariant
NLTV	Nonlinear time variant
$I_c(t)$	Collector current
I_{cob}	Collector reverse current
Y_n	Normalized noise admittance
Y_e	Even mode admittance
Y_0	Odd mode admittance
λ_e	Even mode eigen value
λ_0	Odd mode eigen value
G_n	In-phase component of noise source
B_n	Quadrature component of noise source
R_P	Parallel loss resistance
m	Ratio of loaded and unloaded Q
m_{opt}	Optimum value of m for minimum phase noise
Q_L	Loaded quality factor
Q_0	Unloaded quality factor
β_{ij}	Coupling parameter
α_i	Free-running amplitude of the ith oscillator
$A_i(t)$	Instantaneous amplitude of the ith oscillator
$\varphi_i(t)$	Instantaneous phase of the ith oscillator
ω_i	Free-running frequency of the ith oscillator
g_m	Small signal transconductance
$g_m(t)$	Large signal transconductance
f_0	Center frequency
f_c	Flicker corner frequency
f_m	Frequency offset
P_0	Average power at oscillator output
K_0	Oscillator voltage gain
R_P	Parallel loss resistance associate with the resonator
NF	Noise Figure

MEMS	Micro-electro-mechanical-system
SMD	Surface mounted device
SRF	Self resonance frequency
MSL	Microstripline
$\pounds(f_m)$	Ratio of sideband power in a 1 Hz bandwidth at f_m
$e_n(t)$	Noise signal voltage
$e_{inj}(t)$	Injected signal voltage
$\Delta\omega_{lock}$	Locking bandwidth
ω_{inj}	Injected signal frequency
λ_{ij}	Magnitude of the coupling coefficient
φ_{ij}	Phase of the coupling coefficient
r	Capacitance ratio of the tuning diode
C_{V0}	Capacitance of tuning diode at zero bias voltage
C_{VB}	Capacitance of tuning diode at breakdown bias voltage
P_n	Average power dissipated by the network
μ	Empirical nonlinear parameter
$R_n(t)$	Time variant negative resistance
K	Boltzman's constant (1.38E-23 J/K)
$\Gamma(x)$	Impulse sensitivity function
C_n	Fourier series coefficient
$[\overline{C}]$	Matrix representation of arbitrary coupling topology
C	Coefficient of correlation
θ_n	Phase of the nth harmonic
W_e	Average stored electrical energy
W_e	Average stored magnetic energy
ω_{diff}	Modulation frequency
VNA	Vector network analyzer
VDP	Van der Pol
kT	4.1×10^{-21} at $300K$ (room temperature)
$\overline{i_{bn}^2} = 2qI_b\Delta f$	Mean square value of noise due to base current
$\overline{i_{cn}^2} = 2qI_c\Delta f$	Mean square value of noise due to collector current
$\overline{i_{con}^2} = 2qI_{cob}\Delta f$	Mean square of noise due to reverse collector current
$\overline{v_{bn}^2} = 4kTR_b\Delta f$	Mean square of noise voltage due to base resistance
$\overline{v_{sn}^2} = 4kTR_b\Delta f$	Mean square of noise voltage due to base resistance
$S(i_{cn}) = 2KTg_m$	Noise power spectral densities due to collector current
$S(i_{bn}) = \dfrac{2KTg_m}{\beta}$	Noise power spectral densities due to base current
$S(v_{bn}) = 4KTR_b$	Noise power spectral densities due to base resistance
$S(v_{sn}) = 4KTR_s$	Noise power spectral densities due to source resistance

Chapter 11
Bibliography

1. Franz X. Sinnesbichler, " Hybrid Millimeter-Wave Push-Push Oscillators Using Silicon- Germanium HBTs, "IEEE MTT-S, Vol. 51, February 2003.
2. S. Kudszus, W. H. Haydl, A. Tessmann, W. Bronner, and M. Schlechtweg, " Push-Push Oscillators for 94 and 140 GHz Applications Using Standard Pseudomorphic GaAs HEMTs, " IEEE MTT-S, Microwave Symp. Digest, 2001, pp. 1571-1574.
3. Y. Baeyens et al., " Compact InP-based HBT VCOs with a Wide Tuning Range at W-Band, " IEEE Trans. MTT, Vol. 48, pp. 2403-2408, Dec. 2001.
4. Y. Sun, T. Tieman, H. Pflung, and W. Velthius, " A Fully Integrated Dual-Frequency Push-Push VCO for 5.2 and 5.8GHz Wireless Applications, " Microwave Journal., pp. 64-74, April 2001.
5. M. Schott, H. Kuhnert, J. Hilsenbeck, J. Wurlf, and H. Heinrich, "38 GHz Push-Push GaAs-HBT MMIC Oscillator, " IEEE MTT-S, Digest, 2002, pp. 839-842.
6. F. X. Sinnesbichler and G. R. Olbrich, "SiGe HBT Push-Push Oscillators for V-Band Operation, "" IEEE MTT-S silicon Monolithic Integrated Circuits in RF Systems Symp., Garmisch, Germany, Apr. 26-28, 2000, pp. 55-59.
7. F. X. Sinnesbichler, H. Geltinger, and G. R. Olbrich, " A 38 GHz Push-Push Oscillator Based on 25 GHz-f_T BJTs, "" IEEE Microwave Guided Wave Lett. Vol. 9 pp. 151-153, Apr. 1999.
8. K. W. Kobayashi et al., " A 108-GHz InP-based HBT Monolithic Push-Push VCO with Low Phase Noise and Wide Tuning Bandwidth, " IEEE J. Solid-State Circuits, Vol. 34, pp. 1225-1232, Sept. 1999.
9. L. Dussopt, D. Guillois, and G. Rebeiz, " A Low Phase Noise Silicon 9 GHz VCO and an 18 GHz Push-Push Oscillator, " IEEE MTT-S. Digest, 2002, pp. 695-698.
10. F. X. Sinnesbichler, B Hauntz and G. R. Olbrich, " A Si/SiGe HBT Dielectric Resonator Push-Push Oscillators at 58 GHz, " IEEE Microwave Guided Wave Lett. Vol. 10, pp. 145-147, Apr. 2000.
11. U. L. Rohde, " A New and Efficient Method of Designing Low Noise Oscillators, " Ph.D. Dissertation, Technical University of Berlin, 12 February 2004.
12. Mortazawi A and B. C. De Loach, Jr., "Multiple Element Oscillators Utilizing a New Power Combining Technique, " in IEEE MTT-S Int. Microwave Symp. Dig., 1992, pp. 1093-1096.
13. B. Van der Pol, "The Nonlinear Theory of Electrical Oscillators, " Proc. IRE, Vol. 22 No.9, pp. 1051-1086, Sept 1934.
14. R. Adler, " A Study of Locking Phenomena in Oscillators, " Proc. IEEE, Vol. 61, pp. 180-1385, Oct 1973.
15. D. B. Leeson, A Simple Model of Feedback Oscillator Noise Spectrum, " Proc. IEEE, pp. 329-332, 1966.
16. M. Odyniec, Editor, *RF and Microwave Oscillator Design*, Chapter 3: Linearity, Time Variation, and Oscillator Phase Noise, by T. Lee and A. Hajimiri, Artech House, 2002

17. M. Ahdjoudj," Conception de VCO a Faible Bruit de Phase en Technologie Monolithique PHEMT dans les Bandes K et Ka," Ph.D. Thesis, Doctorat De L' Universite Pierre Et Marie Curie Paris VI, December 1997.
18. Heng-Chia Chang, Xudong Cao, Umesh K. Mishra, and R. York, " Phase Noise in Coupled Oscillators: Theory and experiment," IEEE Trans. MTT, Vol. 45, pp. 604-615, May 1997.
19. Heng-Chia Chang, Xudong Cao, Mark J. Vaughan, Umesh K. Mishra, and R. York, " Phase Noise in Externally Injection-Locked Oscillator Arrays," IEEE Trans. MTT, Vol. 45, pp. 2035-2042, Nov 1997
20. Andrea Borgioli, Pochi Yeh, and Robert A. York, " Analysis of Oscillators with External Feedback Loop for Improved Locking Range and Noise Reduction," IEEE Trans. MTT, Vol. 47, pp. 1535-1543, August 1999.
21. Jonathan J. Lynch and Robert A. York, "Synchronization of Oscillators Coupled through Narrow-Band Networks," IEEE Trans. MTT, pp. 238-249, Feb 2001.
22. Klaus F. Schunemann and Karl Behm, "Nonlinear Noise Theory for Synchronized Oscillators," IEEE Trans. MTT, Vol. 27, pp. 452-458, May 1979.
23. Kaneyuki Kurokawa, "The Single Cavity Multiple Device Oscillator," IEEE Trans. MTT, Vol. 19, pp. 793-801, October 1971.
24. Kaneyuki Kurokawa, "Noise in Synchronized Oscillators," IEEE Trans. MTT, Vol. 16, pp. 234-240, April 1968.
25. Byeong-Ha Park, "A Low-Voltage, Low Power, CMOS 900 MHz Frequency Synthesizer," Ph.D. Dissertation, Georgia Institute of Technology, December 1997.
26. W. O. Schlosser, " Noise in Mutually Synchronized Oscillators," IEEE Trans. Microwave Theory Tech., Vol. MTT-16, pp. 732-737, Sept 1968.
27. Heng-Chia Chang, "Analysis of Coupled Phase-Locked Loops With Independent Oscillators for Beam Control Active Phased," IEEE Trans. MTT, Vol. 52, pp. 1059-1065, March 2004.
28. Reidar L. Kuvas, "Noise in Single Frequency Oscillators and Amplifiers," IEEE Trans. Microwave Theory Tech., Vol. MTT-21, pp. 127-134, March 1973
29. H. Stark, and J. W. Woods, Probability, Random Processes, and Estimation Theory for Engineers. New York: Prentice-Hall, 1986.
30. R. A. York, P. Liao, and J. J. Lynch, "Oscillator Array Dynamics with Broad-Band N-Port Coupling Networks, " IEEE Trans. Microwave Theory Tech., Vol. 42, pp. 2040-2045, Nov.1994.
31. R. A. York, "Nonlinear Analysis of Phase Relationship in Quasi-Optical Oscillator Arrays, " IEEE Trans. Microwave Theory Tech., Vol. 41, pp. 1799-1809, oct.1993
32. Shih-Chieh Yen and Tah-Hsiung Chu," An Nth-Harmonic Oscillator Using an N-Push Coupled Oscillator Array with Voltage-Clamping Circuits", IEEE, MTT-S Digest, pp. 545-548, 1992.
33. J. R. Bender, C. Wong, " Push-Push Design Extends Bipolar Frequency Range, Microwave & RF, pp. 91-98, Oct. 1983.
34. Franco Ramirez, Jose Lius Garcia H., Tomas Fernandez and Almudena Suarez," Nonlinear Simulation Techniques for the Optimized Design of Push-Push Oscillators", IEEE, MTT-S Digest, pp. 2157-2160, 2003.

35. Jeong-Geun Kim, Dong-Hyun Baek, Sang-Hoon Jeon, Jae-Woo Park and Songcheol Hong," A 60 GHz InGaP/GaAs HBT Push-Push MMIC VCO, IEEE, MTT-S Digest, pp. 885-888, 2003.
36. F. X. Sinnesbichler, B. HAUTZ, G. R. Olbrich," A Low Phase Noise 58 GHz SiGe HBT Push-Push, Oscillator with Simultaneous 29 GHz Output", IEEE, MTT-S Digest, pp. 35-38, 2000.
37. Hai Xiao, Takayuki Tanka and Masayoshi Aikawa, "A Ka-Band Quadruple-Push Oscillator", IEEE, MTT-S Digest, pp. 889-892, 2003.
38. R. G. Freitag, S.H. Lee, D.M. Krafcsik, D.E. Dawson and J. E. Degenford," Stability and Improved Circuit Modeling Considerations for High Power MMIC Amplifiers", IEEE, MM-Wave Monolithic Circuits Symposium, pp. 2169-2172, 2003.
39. J. Heinbockel and A. Mortazawi," A Periodic Spatial Power Combining MESFET Oscillator", IEEE, MTT-S Digest, pp. 545-548, 1992.
40. M. Kuramitsu and F. Takasi, "Analytical method for Multimode Oscillators Using the Averaged Potential, " Elec. Communication Japan, Vol. 66-A, pp. 10-19, 1983.
41. Ronald G. Freitag, "A Unified Analysis of MMIC Power Amplifier Stability, "IEEE, MTT-S Digest, pp. 297-300, 1992.
42. Shigeji Nogi, Jenshan Lin and Tatsuo Itoh., " Mode Analysis and Stabilization of a Spatial Power Combining Array with Strongly Coupled oscillators, IEEE, MTT, Vol.41, pp. 1827-1837, October 1993.
43. Amir Mortazawi, Heinrich D. Foltz, and Tatsuo Itoh, " A Periodic Second Harmonic Spatial Power Combining Oscillator", IEEE, MTT, Vol.40, pp. 851-856, May 1992.
44. Jonathan J. Lynch and Robert A. York," An Analysis of Mode-Locked Arrays of Automatic Level Control Oscillators," IEEE Trans. on Circuits and Systems-I, Vol.41, pp.859-865, December 1994.
45. R. A. York and R.C. Compton," Mode-Locked Oscillator Arrays", IEEE Microwave and Guided Letter, Vol. 1, pp.215-218, Aug 1991.
46. Yu-Lung Tang and Huei Wang, " Triple-Push Oscillator Approach: Theory and Experiments," IEEE- JSS, Vol.36, pp. 1472-1479, October 2001.
47. J. Everard, *Fundamentals of RF Circuit Design with Low Noise Oscillators, John Wiley & Sons. Ltd, 2001*
48. U.L. Rohde, "New Nonlinear Noise Model for MESFETS Including MM-Wave Application," First International Workshop of the West German IEEE MTT/AP Joint Chapter on Integrated Nonlinear Microwave and Millimeter wave Circuits (INMMC'90) Digest, October 3-5, 1990, Duisburg University, Germany.
49. U.L. Rohde, "Improved Noise Modeling of GaAs FETS: Using an Enhanced Equivalent Circuit Technique," Microwave Journal, pp. 87-101 - November 1991.
50. R.A. Pucel, W. Struble, R Hallgren, U.L. Rohde, "A General Noise De-embedding Procedure for Packaged Two-Port Linear Active Devices," IEEE Transactions on MTT, Vol. 40, No. 11, pp. 2013-2024, November 1992.
51. U.L. Rohde, "Parameter Extraction for Large Signal Noise Models and Simulation of Noise in Large Signal Circuits Like Mixers and Oscillators," 23rd European Microwave Conference, Madrid, Spain, September 6-9, 1993.
52. C. Arnaud, D. Basataud, J. Nebus, J. Teyssier, J. Villotte, D. Floriot, "An Active Pulsed RF and Pulsed DC Load-Pull System for the Characterization of HBT Power

Amplifiers Used in Coherent Radar and Communication Systems," IEEE Transactions on MTT, Vol. 48, No.12, pp. 2625 –2629, December 2000.

53. F.M. Ghannouchi, R. Larose, R.G. Bosisio, "A New Multi-harmonic Loading Method for Large-Signal Microwave and Millimeter-Wave Transistor Characterization," IEEE Transactions on MTT, Vol.39, No. 6, pp. 986 –992, June 1991.

54. H. Abe, Y. Aono, "11 GHz GaAs Power MESFET Load-Pull Measurements Utilizing a New Method of Determining Tuner *Y*-Parameters, IEEE Transactions on Microwave Theory and Techniques, Vol. 27, No. 5, pp. 394 –399, May 1979.

55. Q. Cai, J. Gerber, S. Peng, "A Systematic Scheme for Power Amplifier Design Using a Multi-Harmonic Load-Pull Simulation Technique," 1998 IEEE MTT-S Symposium Digest, Vol. 1, pp. 161 -165, June 7-12, 1998.

56. P. Berini, M. Desgagne, F.M. Ghannouchi, R.G. Bosisio, "An Experimental Study of the Effects of Harmonic Loading on Microwave MESFET Oscillators and Amplifiers," IEEE Transactions on MTT, Vol. 42, No. 6, pp. 943 –950, June 1994.

57. D. M. Pozar, Microwave Engineering, John Wiley & Sons, 2nd Edition, 1998.

58. A. M. Elsayed and M. I. Elmasry," Low-Phase-Noise LC Quadrature VCO using Coupled Tank Resonators in Ring, " IEEE, JSSC, Vol. 36, pp. 701-705, April 2001.

59. M. Ticbout," Low power, Low Phase Noise, Differentially Tuned Quadrature VCO Design in Standard CMOS, " IEEE- JSSS, Vol. 36, pp. 1018-1024, July 2001.

60. K.O," Estimation Methods for Quality Factors of Inductors Fabricated in Silicon Integrated Circuit Process Technologies, " IEEE, JSSS, pp.1565-1567, Sept 1997.

61. A.V. Grebennikov, "Microwave Transistor Oscillators: an Analytic Approach to Simplify Computer-Aided Design", Microwave Journal, pp. 294-299, May1999.

62. Andrew V. Grebennikov, "Microwave FET Oscillators: an Analytic Approach to Simplify Computer-Aided Design", Microwave journal, pp. 102-111, Jan 2000.

63. Jwo-Shiun Sun, "Design Analysis of Microwave Varactor-Tuned Oscillators", Microwave journal, pp.302-308, May 1999.

64. M. Regis, O. Llopis, and J. Graffeuil, " Nonlinear Modeling and Design of Bipolar Transistor Ultra Low Phase-Noise Dielectric-Resonator Oscillators", IEEE transaction on MTT, Vol. 46, No. 10, pp. 1589-1593, Oct.1998,

65. R. J. Hawkins, "Limitations of Nielsen's and Related Noise Equations Applied to Microwave Bipolar Transistors and a New Expression for the Frequency and Current Dependent Noise Figure," Solid-State Electron., Vol.20 pp.191-196, 1977.

66. T. H. Hsu and C.P. Snapp, "Low-Noise Microwave Bipolar Transistor with Sub-Half-Micrometer Emitter Width," IEEE Trans. Electron Devices, Vol. ED-25, pp. 723-730, June 1978.

67. U. L. Rohde, K. Juergen Schoepf, A.K. Poddar, "Low Noise VCOs Conquer Wideband," Microwaves & RF, pp. 98-106, June 2004.

68. U. L. Rohde and A. K. Poddar, " Noise Analysis of Systems of Coupled Oscillators", (INMMIC) workshop, Italy, November 15-16, 2004.

69. A. K. Poddar and K. N. Pandey, "Microwave Switch using MEMS technology,"8th IEEE International Symposium, EDMO-2000, pp.134-139, Nov. 2000, UK.

70. A. Ward and B. Ward, " A Comparison of various Bipolar Transistor Biasing Circuits," Applied Microwave & Wireless, Vol. 13, pp. 30-52, 2001.

71. U. L. Rohde and A. K. Poddar, " Ultra Low Noise Low Cost Multi Octave Band VCO", IEEE Sarnoff Symposium, Princeton, NJ, USA, April 2005.

72. U. L. Rohde, A. K. Poddar, Juergen Schoepf, Reimund Rebel, and Parimal Patel, "Low Noise Low Cost Wideband N-Push VCO," IEEE, IMS Symposium, MTT-2005, USA.

73. U. L. Rohde, A. K. Poddar, and Juergen Schoepf, " A Unifying Theory and Characterization of Microwave Oscillators/VCOs," 18th IEEE CCECE05, May 2005, Canada.

74. U. L. Rohde and A. K. Poddar, " Configurable Ultra Low Ultra Wideband Power Efficient VCOs", 11th European Wireless, April 2005.

75. U. L. Rohde, A. K. Poddar, and Reimund Rebel, " Ultra Low Noise Low Cost Octave-Band Hybrid-Tuned VCO," 18th IEEE CCECE05, May 2005, Canada.

Chapter 12
Appendices

Appendix A

Noise Analysis of the N-Coupled Oscillator Coupled Through the Different Coupling Topology:

The objective of this Appendix to find the analytical expression of the phase noise of the N-coupled oscillators relative to a single free running uncoupled oscillator for different coupling configurations. Three types of coupling topology (global, bilateral and unilateral) are described for the noise analysis of the N-coupled oscillator systems.

For uncoupled oscillator coupling coefficient $\beta_{ij} \to 0$ and Equations (4.83) and (4.84) can be expressed as

$$[\Delta A_i(\omega)]_{uncoupled} = \left[\frac{\mu \omega_i}{2Q\omega}\right][\alpha_i^2 - 3\dot{A}_i^2][\Delta A_i(\omega)]_{uncoupled} - \left[\frac{\omega_i}{2Q\omega}\right]\dot{A}_i G_{ni}(\omega) \quad ; i = 1,2,3...N \quad (A.1)$$

$$[\Delta \theta_i(\omega)]_{uncoupled} = -\left[\frac{\omega_i}{2Q\omega}\right]B_{ni}(\omega) \quad ; i = 1,2,3...N \quad (A.2)$$

From (A.1),

$$[\Delta A_i(\omega)]_{uncoupled} = \frac{-\dot{A}_i G_{ni}(\omega)}{\left[\dfrac{2\omega Q}{\omega_i}\right] + \mu[3\dot{A}_i^2 - \alpha_i^2]} \quad (A.3)$$

The noise spectral density due to the amplitude fluctuation is given by

$$\left|\Delta A_i(\omega)\right|^2_{uncoupled} = \frac{\dot{A}_i^2 \left|G_{ni}(\omega)\right|^2}{\left[\dfrac{2\omega Q}{\omega_i}\right]^2 + \mu^2[3\dot{A}_i^2 - \alpha_i^2]^2} \quad (A.4)$$

The noise spectral density due to the phase fluctuation for single uncoupled free running oscillator is given from Equation (A.2) as

$$\left|\Delta \theta_i(\omega)\right|^2_{uncoupled} = \frac{\left|B_{ni}(\omega)\right|^2}{\left[\dfrac{2Q\omega}{\omega_i}\right]^2} \quad (A.5)$$

For series tuned free running oscillator, Equations (A.4) and (A.5) can be rewritten as

$$\left| \Delta A_i(\omega) \right|^2_{uncoupled} = \frac{\dot{A}_i^2 \left| G_{ni}(\omega) \right|^2 R^2}{4L^2\omega^2 + (\mu R)^2 [3\dot{A}_i^2 - \alpha_i^2]^2} \approx \frac{2|e|^2}{4L^2\omega^2 + (\gamma A_0)^2} \tag{A.6}$$

$$\left| \Delta \theta_i(\omega) \right|^2_{uncoupled} = \frac{\left| B_{ni}(\omega) \right|^2}{\left[\dfrac{\omega}{\omega_{3dB}} \right]^2} = \frac{\left| B_{ni}(\omega) \right|^2 \omega_i^2}{4\omega^2 Q^2} \approx \frac{2|e|^2}{4\omega^2 L^2 A_0^2} \tag{A.7}$$

Where

$$Q = \frac{\omega L}{R}, \quad \gamma A_0 \approx (\mu R)[3\dot{A}_i^2 - \alpha_i^2], \quad |e|^2 \approx \dot{A}_i^2 \left| G_{ni}(\omega) \right|^2 R^2$$

Equation (A.6) and (A.7) represents the AM and PM noise for the uncoupled free-running series tuned oscillator and this has same form as given in Equations (4.65) and (4.69).

Globally N-Coupled Oscillator Systems

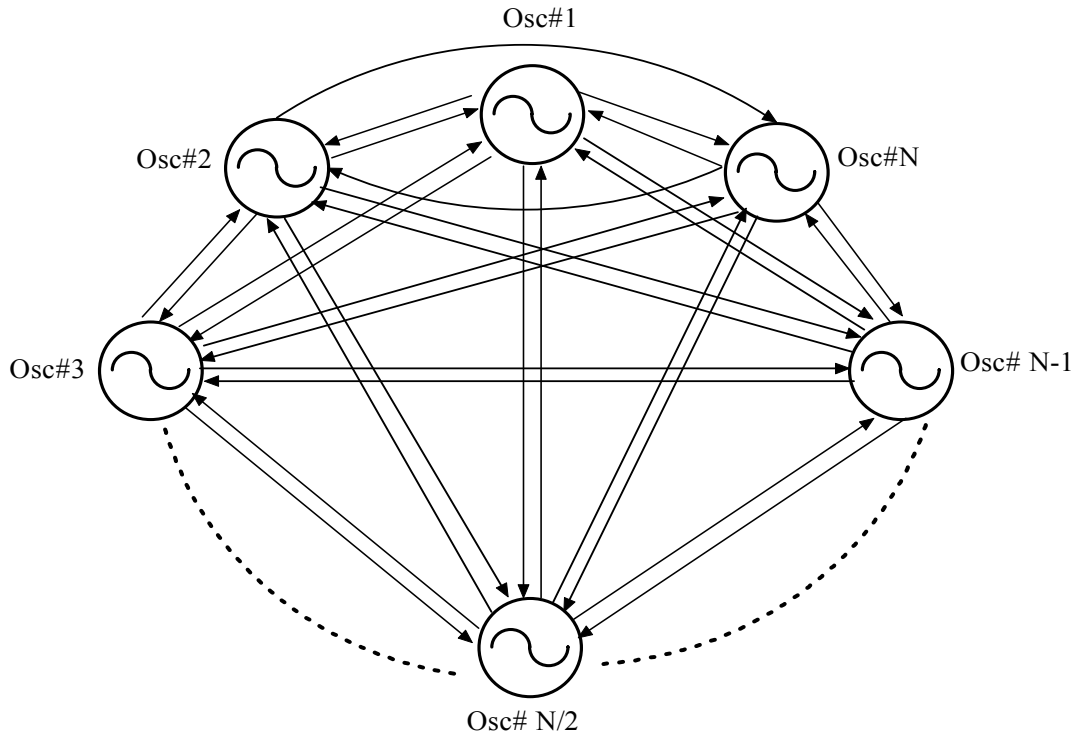Figure A-1 shows the globally N-coupled oscillator system.

Figure A-1: Globally N-coupled oscillator system

From Equation (4.86),

$$\left[\frac{2Q\omega}{\omega_i}\right][\Delta\theta_i(\omega)] = -\sum_{\substack{j=1\\j\neq i}}^{N}\beta_{ij}\big([\Delta\theta_i(\omega)]-[\Delta\theta_j(\omega)]\big)\cos[\dot{\theta}_i-\dot{\theta}_j] - B_{ni}(\omega); \qquad i=1,2,3..N \quad (A.8)$$

For globally coupled topology, considering coupling coefficient $\beta_{ij}=\beta$ for any i^{th} and j^{th} oscillators and all the oscillators are in phase, Equation (A.8) can be rewritten as

$$\left[\frac{2\omega Q}{\omega_i}\right][\Delta\theta_i(\omega)] = -\beta\sum_{\substack{j=1\\j\neq i}}^{N}\big([\Delta\theta_i(\omega)]-[\Delta\theta_j(\omega)]\big) - B_{ni}(\omega) \qquad i=1,2,3..N \quad (A.9)$$

Expanding the series of the Equation (A.9) as

$$\left[\frac{2\omega Q}{\beta\omega_i}\right][\Delta\theta_i(\omega)] = \{(N-1)[\Delta\theta_i(\omega)]\} + \{[\Delta\theta_1(\omega)]+[\Delta\theta_2(\omega)+...[\Delta\theta_N(\omega)]\} - \frac{B_{ni}(\omega)}{\beta} \quad (A.10)$$

$$x[\Delta\theta_i(\omega)] = \left[\{(N-1)[\Delta\theta_i(\omega)]\} + \{[\Delta\theta_1(\omega)]+[\Delta\theta_2(\omega)+...[\Delta\theta_N(\omega)]\} - \frac{B_{ni}(\omega)}{\beta}\right] \quad (A.11)$$

Where
$$x = \frac{2\omega Q}{\beta\omega_i}$$

Following [18]; from (4.87) and (A.11), $[\overline{C}]$ for global coupling can be described as

$$[\overline{C}] = \beta\begin{bmatrix} 1-N-x & 1 & 1 & ... & 1 \\ 1 & 1-N-x & 1 & ... & 1 \\ 1 & 1 & 1-N-x & \ddots & \vdots \\ \vdots & \vdots & \ddots & \ddots & 1 \\ 1 & 1 & ... & 1 & 1-N-x \end{bmatrix} \quad (A.12)$$

From (4.88)

$$[\overline{P}] = [\overline{C}]^{-1} = \frac{1}{-x\beta(N+x)}\begin{bmatrix} 1+x & 1 & 1 & ... & 1 \\ 1 & 1+x & 1 & ... & 1 \\ 1 & 1 & 1+x & \ddots & \vdots \\ \vdots & \vdots & \ddots & \ddots & 1 \\ 1 & 1 & ... & ... & 1+x \end{bmatrix} \quad (A.13)$$

From (4.89)

$$\sum_{j=1}^{N} p_{ij} = \frac{(N+x)}{-x\beta(N+x)} = \frac{-1}{x\beta} \quad ; \qquad \text{For all } i \qquad (A.14)$$

From Equation (4.96), the total output phase noise is given by

$$\left|\Delta\theta_{total}(\omega)\right|^2 = \frac{\left|B_n(\omega)\right|^2}{N^2} \sum_{j=1}^{N}\left|\sum_{i=1}^{N} p_{ij}\right|^2 = \frac{1}{N}\frac{\left|B_n(\omega)\right|^2}{\beta^2 x^2} = \frac{1}{N}\frac{\left|B_n(\omega)\right|^2}{\left[\dfrac{2\omega Q}{\omega_i}\right]^2} \qquad (A.15)$$

Comparing Equation (A.15) with the single oscillator phase noise Equation (A.5), we find

$$\left|\Delta\theta_{total}(\omega)\right|^2 = \frac{1}{N}\left|\Delta\theta_i(\omega)\right|^2_{uncoupled} \qquad (A.16)$$

From Equation (A.16) the total PM noise for N globally oscillators is reduced by the factor N of that of a single oscillator.

Bilateral N-Coupled Oscillator Systems

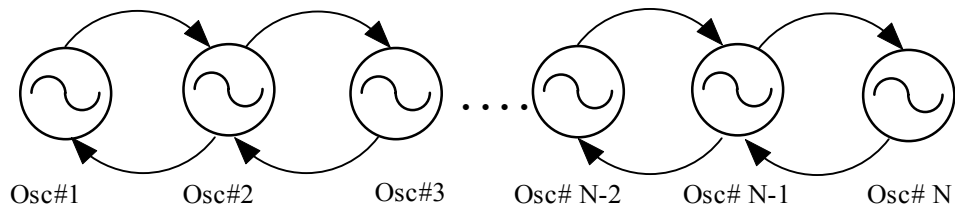Figure A-2 shows the nearest neighbor bilateral N-coupled oscillator system.

Figure A-2: Nearest neighbor bilateral N-coupled oscillator system

The coupling parameter β_{ij} for the Figure A-2 is defined as [29]

$$\beta_{ij} = \begin{cases} \beta, & \left|i-j\right| = 1 \\ 0, & otherwise \end{cases} \qquad (A.17)$$

Assuming constant phase progression along the array of the N-coupled oscillator system as

$$\dot{\theta}_i - \dot{\theta}_{i+1} = \Delta\dot{\theta} \tag{A.18}$$

From (4.87), $[\overline{C}]$ for bilateral coupling can be described as

$$[\overline{C}] = \beta \cos(\Delta\dot{\theta}) \begin{bmatrix} -1-y & 1 & 0 & 0 & \cdots & 0 \\ 1 & -2-y & 1 & 0 & \cdots & 0 \\ 0 & 1 & -2-y & 1 & \cdots & \vdots \\ \vdots & \ddots & \ddots & \ddots & \ddots & 0 \\ 0 & \cdots & \ddots & 1 & -2-y & 1 \\ 0 & 0 & \cdots & 0 & 1 & -1-y \end{bmatrix} \tag{A.19}$$

Where

$$y = \frac{\omega}{\left[\dfrac{\beta\omega_i}{2Q}\right]\cos(\Delta\dot{\theta})} \tag{A.20}$$

From (4.89)

$$\sum_{j=1}^{N} P_{ij} = \frac{-1}{\left[\dfrac{2Q\omega}{\omega_i}\right]}; \qquad \text{For all } i \tag{A.21}$$

From Equation (4.96), the total output phase noise is given by

$$\left|\Delta\theta_{total}(\omega)\right|^2 = \frac{\left|B_n(\omega)\right|^2}{N^2}\sum_{j=1}^{N}\left|\sum_{i=1}^{N}P_{ij}\right|^2 = \frac{1}{N}\frac{\left|B_n(\omega)\right|^2}{\left[\dfrac{2\omega Q}{\omega_i}\right]^2} \tag{A.22}$$

Comparing Equation (A.22) with the single oscillator phase noise Equation (A.5) we find

$$\left|\Delta\theta_{total}(\omega)\right|^2 = \frac{1}{N}\left|\Delta\theta_i(\omega)\right|^2_{uncoupled} \tag{A.23}$$

Unilateral N-Coupled Oscillator Systems

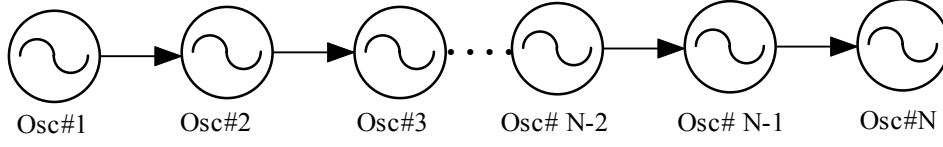Figure A-3 shows the nearest neighbor unilateral N-coupled oscillator system.

Figure A-3: Nearest neighbor unilateral N-coupled oscillator system

In this topology, each successive oscillator in the array of N-coupled oscillator system is slaved to the previous oscillator and the first oscillator in the array is considered as master oscillator.

The coupling parameter β_{ij} for the Figure B-3 is defined as [18]

$$\beta_{ij} = \begin{cases} \beta, & i - j = +1 \\ 0, & otherwise \end{cases} \tag{A.24}$$

From (4.87), $[\overline{C}]$ for unilateral coupling can be described as

$$[\overline{C}] = \beta \begin{bmatrix} -z & 0 & 0 & \cdots & 0 & 0 \\ 1 & -1-z & 0 & \cdots & \vdots & \vdots \\ 0 & 1 & -1-z & \cdots & \vdots & \vdots \\ \vdots & \ddots & \ddots & \ddots & 0 & \vdots \\ 0 & \cdots & \ddots & \ddots & -1-z & 0 \\ 0 & 0 & \cdots & 0 & 1 & -1-z \end{bmatrix} \tag{A.25}$$

$$[\overline{P}] = [\overline{C}]^{-1} = \frac{1}{\beta} \begin{bmatrix} \dfrac{-1}{z} & 0 & 0 & \cdots & 0 & 0 \\[2mm] \dfrac{-1}{z(1+z)} & \dfrac{-1}{(1+z)} & 0 & \cdots & 0 & 0 \\[2mm] \dfrac{-1}{z(1+z)^2} & \dfrac{-1}{(1+z)^2} & \dfrac{-1}{(1+z)} & \cdots & \vdots & 0 \\[2mm] \vdots & \vdots & \vdots & \ddots & 0 & \vdots \\[2mm] \dfrac{-1}{z(1+z)^{N-2}} & \dfrac{-1}{(1+z)^{N-2}} & \dfrac{-1}{(1+z)^{N-3}} & \ddots & \dfrac{-1}{(1+z)} & 0 \\[2mm] \dfrac{-1}{z(1+z)^{N-1}} & \dfrac{-1}{(1+z)^{N-1}} & \dfrac{-1}{(1+z)^{N-2}} & \cdots & \dfrac{-1}{(1+z)^2} & \dfrac{-1}{(1+z)} \end{bmatrix} \tag{A.26}$$

Where

$$z = \frac{2\omega Q}{\beta \omega_i}$$

The rows and columns of the Equation (A.26) form geometric series; the expression of $\sum_{j=1}^{N} p_{ij}$ can be calculated analytically.

For small value of z, expression of $\sum_{j=1}^{N} p_{ij}$ can be given as

$$\sum_{j=1}^{N} p_{ij} = \begin{cases} \dfrac{-N}{\beta z}, & i = 1 \\ -\dfrac{N+1-i}{\beta}, & 2 \le i \le N \end{cases} \tag{A.27}$$

From Equation (4.96), the total output phase noise is approximately given as

$$\left| \Delta \theta_{total}(\omega) \right|^2 = \frac{\left| B_n(\omega) \right|^2}{N^2} \sum_{j=1}^{N} \left| \sum_{i=1}^{N} p_{ij} \right|^2 = \left[1 + z^2 \left(\frac{N}{3} - \frac{1}{2} + \frac{1}{6N} \right) \left| \Delta \theta_i(\omega) \right|^2_{uncoupled} \right] \tag{A.28}$$

$$\left| \Delta \theta_{total}(\omega) \right|^2 = \left[1 + \left(\frac{2\omega Q}{\beta \omega_i} \right)^2 \left(\frac{N}{3} - \frac{1}{2} + \frac{1}{6N} \right) \left| \Delta \theta_i(\omega) \right|^2_{uncoupled} \right] \tag{A.29}$$

From Equation (A.29), there is noise degradation with respect to the single uncoupled free running oscillator and the noise of the unilateral coupled oscillator increases quadratically away from the carrier, and linearly with increasing number of the oscillator of the array of the N-coupled oscillator systems.

In general $z \ll 1$ and near the carrier frequency the noise is just that of the first-stage oscillator, thereby the total noise could be significantly reduced by making the first-stage oscillator as a master oscillator having low noise performance.

Appendix B

Analytical Approach For Designing Wideband Oscillators/VCOs (Optimum Power)

Figure B-1 shows the series and parallel feedback topology of the oscillator, and depending on application and ease of analysis, one model may be preferred over another. However, the designer has the freedom to convert *Y*-parameter to *Z*-parameter and vice-versa for designing oscillators/VCOs, based on the topology above.

a) Series feedback configuration
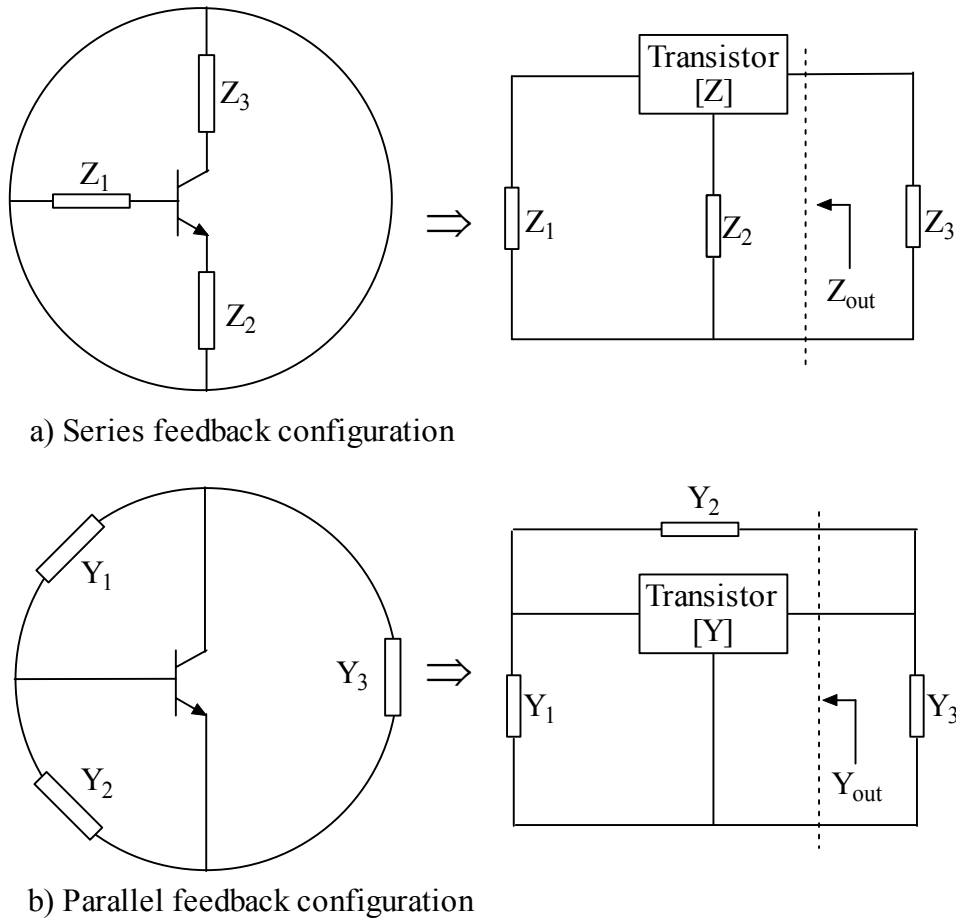

b) Parallel feedback configuration

Figure B-1: a) Series topology b) Parallel topology

The general transformation matrix from [*Y*] to [*Z*] can be expressed as

$$Y_{11} = \frac{Z_{22}}{Z_{11}.Z_{22} - Z_{12}Z_{21}} \; ; Y_{12} = \frac{-Z_{12}}{Z_{11}.Z_{22} - Z_{12}Z_{21}} \; ; Y_{21} = \frac{-Z_{21}}{Z_{11}.Z_{22} - Z_{12}Z_{21}} \; ; Y_{22} = \frac{Z_{11}}{Z_{11}.Z_{22} - Z_{12}Z_{21}}$$

and from $[Z]$ to $[Y]$ is given as

$$Z_{11} = \frac{Y_{22}}{Y_{11}.Y_{22} - Y_{12}Y_{21}} ; Z_{12} = \frac{-Y_{12}}{Y_{11}.Y_{22} - Y_{12}Y_{21}} ; Z_{21} = \frac{-Y_{21}}{Y_{11}.Y_{22} - Y_{12}Y_{21}} ; Z_{22} = \frac{Y_{11}}{Y_{11}.Y_{22} - Y_{12}Y_{21}}$$

Series Feedback Oscillators/VCOs

The analysis uses the large signal *Y*-parameters derived from the large signal *S*-parameters (measured or simulated). The steady-state oscillation condition for series feedback topology can be expressed as

$$Z_{out}(I,\omega) + Z_L(\omega) = 0 \Rightarrow [R_{out}(I,\omega) + jX_{out}(I,\omega)] + [R_L(\omega) + jX_L(\omega)] = 0 \qquad \text{(B.1)}$$

$$Z_L(\omega) \rightarrow Z_3(\omega) \qquad \text{(B.2)}$$

where *I* is the load current amplitude and ω is the resonance frequency. Z_{out} is function of the amplitude of the current and frequency whereas Z_L is function of frequency only.

The expression of output impedance, Z_{out} can be written as

$$Z_{out} = -Z_3 \Rightarrow [Z_{22} + Z_2] - \frac{[Z_{12} + Z_2][Z_{21} + Z_2]}{[Z_{11} + Z_1 + Z_2]} \qquad \text{(B.3)}$$

where Z_{ij} (*i,j*=1,2) is *Z*-parameters of hybrid transistor model and can be defined as

$$Z_{i,j} = [R_{ij} + jX_{ij}]_{i,j=1,2} \qquad \text{(B.4)}$$

According to optimum criterion, the negative real part of the output impedance Z_{out} has to be maximized and the possible optimal values of feedback reactance under which the negative value R_{out} is maximized by setting [61,62,63]

$$\frac{\partial \operatorname{Re}[Z_{out}]}{\partial X_1} = 0 \ and \ \frac{\partial \operatorname{Re}[Z_{out}]}{\partial X_2} = 0 \Rightarrow \frac{\partial [R_{out}]}{\partial X_1} = 0 \ and \ \frac{\partial [R_{out}]}{\partial X_2} = 0 \qquad \text{(B.5)}$$

The optimal values X_1^* and X_2^*, based on above condition, can be expressed in terms of

the impedance parameter of the 2-port network of the active device (BJT/FET) as and can be given as

$$X_1^* = -X_{11} + \left[\frac{X_{12} + X_{21}}{2}\right] + \left[\frac{R_{21} - R_{12}}{X_{21} - X_{12}}\right]\left[\frac{R_{12} + R_{21}}{2} - R_{11} - R_1\right] \tag{B.6}$$

$$X_2^* = -\left[\frac{X_{12} + X_{21}}{2}\right] - \left[\frac{(R_{21} - R_{12})(2R_2 + R_{12} + R_{21})}{2(X_{21} - X_{12})}\right] \tag{B.7}$$

By substituting values of X_1^* and X_2^* into above equation, the optimal real and imaginary parts of the output impedance Z_{out}^* can be expressed as

$$Z_{out}^* = R_{out}^* + X_{out}^* \tag{B.8}$$

$$R_{out}^* = R_2 + R_{22} - \left[\frac{(2R_2 + R_{21} + R_{12})^2 + (X_{21} - X_{12})^2}{4(R_{11} + R_2 + R_1)}\right] \tag{B.9}$$

$$X_{out}^* = X_2^* + X_{22} - \left[\frac{R_{21} - R_{12}}{X_{21} - X_{12}}\right]\left[R_{out}^* - R_2 - R_{22}\right] \tag{B.10}$$

Thus, in the steady-state operation mode of the oscillator, amplitude and phase balance conditions can be defined as $R_{out}^* + R_L = 0$ and $X_{out}^* + X_L^* = 0$.

The output power of the oscillator/VCO can be expressed in terms of load current and load impedance as

$$P_{out} = \frac{1}{2}I^2 \operatorname{Re}[Z_L] \tag{B.11}$$

$$I = \left[\frac{Z_{11} + Z_1 + Z_2}{Z_{22}(Z_{11} + Z_1 + Z_2) - Z_{21}(Z_{12} + Z_2)}\right]V \tag{B.12}$$

where I and V is the corresponding load current and voltage across the output.

Parallel Feedback Oscillators/VCOs

The analysis uses the large signal *Y*-parameters derived from the large signal *S*-parameters (measured or simulated). The steady state oscillation condition for the parallel feedback oscillators given in Figure B-1 (b) is shown as

$$Y_{out} + Y_3 \Rightarrow 0 \tag{B.13}$$

The steady-state stationary condition can be expressed as

$$Det\begin{bmatrix} Y_{11} + Y_1 + Y_2 & Y_{12} - Y_2 \\ Y_{21} - Y_2 & Y_{22} + Y_2 + Y_3 \end{bmatrix} = \begin{vmatrix} Y_{11} + Y_1 + Y_2 & Y_{12} - Y_2 \\ Y_{21} - Y_2 & Y_{22} + Y_2 + Y_3 \end{vmatrix} = 0 \tag{B.14}$$

From (B.14),

$$Y_3 = -[Y_{22} + Y_2] + \frac{[Y_{12} - Y_2][Y_{21} - Y_2]}{[Y_{11} + Y_1 + Y_2]} \tag{B.15}$$

where Y_{ij} (i,j=1,2) are Y-parameters of the hybrid bipolar/FET-transistor model.

As shown in Figure B-1(b), the active 2-port network, together with the feedback elements Y_1 and Y_2, is considered as a one-port negative resistance oscillator circuit. The output admittance Y_{out} can be given as

$$Y_{out} = -Y_3 \Rightarrow [Y_{22} + Y_2] - \frac{[Y_{12} - Y_2][Y_{21} - Y_2]}{[Y_{11} + Y_1 + Y_2]} \tag{B.16}$$

According to optimum criterion, the optimum values of feedback susceptance B_1 and B_2, at which the negative value of Re $[Y_{out}]$ is maximum, are determined by solving the following differential condition [61,62,63]:

$$\frac{\partial \text{Re}[Y_{out}]}{\partial B_1} = 0 \ and \ \frac{\partial \text{Re}[Y_{out}]}{\partial B_2} = 0 \tag{B.17}$$

and the solution of the above differential condition will give the optimum values of output admittance Y_{out}^* and feedback susceptance B_1^* and B_2^*, which can be expressed in terms of the two-port Y-parameters of the active device (BJT/FET) as

$$B_1^* = -\left\{ B_{11} + \left[\frac{B_{12} + B_{21}}{2} \right] + \left[\frac{G_{21} - G_{12}}{B_{21} - B_{12}} \right]\left[\frac{G_{12} + G_{21}}{2} + G_{11} \right] \right\} \tag{B.18}$$

$$B_2^* = \left[\frac{B_{12} + B_{21}}{2} \right] + \left[\frac{(G_{12} + G_{21})(G_{21} - G_{12})}{2(B_{21} - B_{12})} \right] \tag{B.19}$$

The optimum values of the real and imaginary part of the output admittance are

$$Y_{out}^* = [G_{out}^* + jB_{out}^*] \tag{B.20}$$

where G_{out}^{*} and B_{out}^{*} is given as

$$G_{out}^{*}= G_{22} - \left[\frac{(G_{12} + G_{21})^2 (B_{21} - B_{12})^2}{4G_{11}} \right] \tag{B.21}$$

$$B_{out}^{*}= B_{22} + \left[\frac{G_{21} - G_{12}}{B_{21} - B_{12}} \right] - \left[\frac{(G_{12} + G_{21})}{2} + G_{22} - G_{out}^{*} \right] + \left[\frac{B_{21} + B_{12}}{2} \right] \tag{B.22}$$

Thus, in the steady-state stationary oscillation mode, general condition for oscillation is given as

$$Y_{out}^{*} + Y_3 = 0 \Rightarrow [G_{out}^{*} + G_L] + [B_{out}^{*} + B_3^{*}] = 0 \; and \; we \; get \; G_{out}^{*} + G_L = 0 \; and \; B_{out}^{*} + B_3^{*} = 0 \tag{B.23}$$

Where $Y_3 = [G_L + jB_3]$, $G_L = 1/R_L$, R_L is the load resistance.

The output power for the given load $Y_3 = [G_L + jB_3]$ is given as $P_{out} = \frac{1}{2} V_{out}^2 G_L$, where V_{out} is the voltage across the load.

Example:

A tunable 3000 MHz oscillator is designed based on the above shown analytical series feedback approach and is also validated with the simulated results. Figure B-2 shows the series feedback oscillator.

Large signal Z-parameters measured data (Infineon BFP 520, I_c=20mA, V_{ce}=2V) @3000 MHz are given as

$Z_{11} = [R_{11} + jX_{11}] = [22.96 + j27.30]\Omega$; $Z_{21} = [R_{21} + jX_{21}] = [140 + j670]\Omega$
$Z_{12} = [R_{12} + jX_{12}] = [2.72 + j4.99]\Omega$; $Z_{22} = [R_{22} + jX_{22}] = [46.04 + j21.45]\Omega$

From (B-6) and (B.7),

$$X_1^{*} = -X_{11} + \left[\frac{X_{12} + X_{21}}{2} \right] + \left[\frac{R_{21} - R_{12}}{X_{21} - X_{12}} \right] \left[\frac{R_{12} + R_{21}}{2} - R_{11} - R_1 \right] \tag{B.13}$$

$$X_1^{*} = 319.9654\Omega \Rightarrow L_1 = 16.9nH \tag{B.14}$$

$$X_2^{*} = -\left[\frac{X_{12} + X_{21}}{2} \right] - \left[\frac{(R_{21} - R_{12})(2R_2 + R_{12} + R_{21})}{2(X_{21} - X_{12})} \right] \tag{B.15}$$

$$X_2^{*} = -311.67084 \Rightarrow C_2 = 0.17pF \tag{B.16}$$

$$X_{out}^* = X_2^* + X_{22} - \left[\frac{R_{21} - R_{12}}{X_{21} - X_{12}} \right] \left[R_{out}^* - R_2 - R_{22} \right] \tag{B.17}$$

$$X_{out}^* = -259.31176 \Rightarrow C_3 = 0.2\,pF \tag{B.18}$$
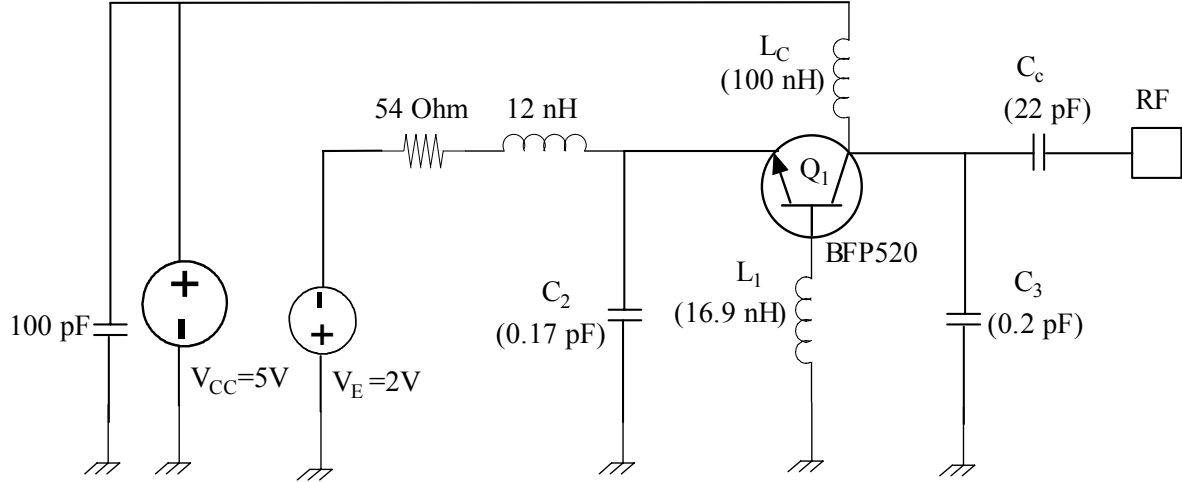

Figure B-2: Schematic of the Series feedback oscillator

Figure B-3 shows the oscillator resonance frequency of the series feedback oscillator.
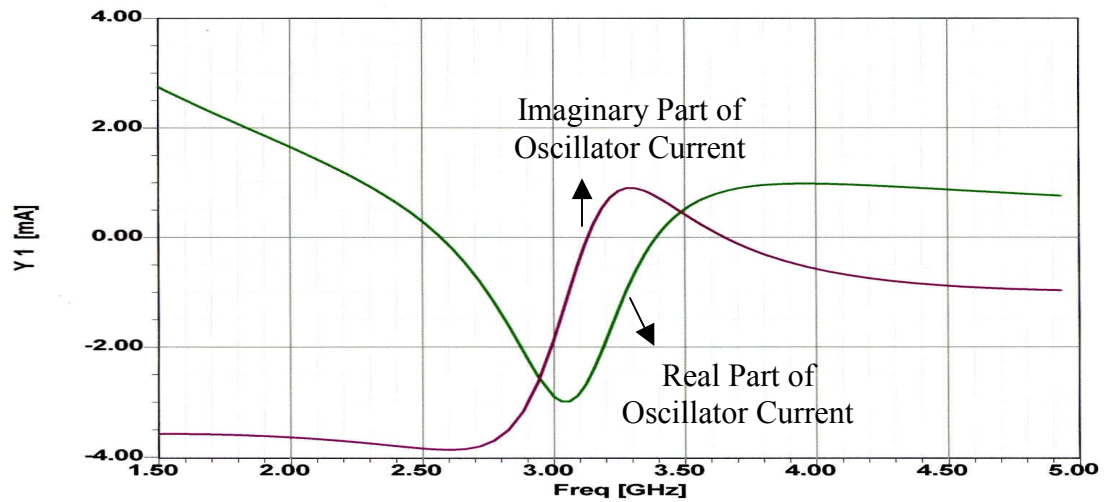

Figure B-3: Oscillator resonance frequency of the Series feedback oscillator

Frequency of the oscillator can be varied from 2000 to 4000 MHz by replacing C_2 by tuning diode, and capacitance is varied from 1.2 pF (2000 MHz) to 0.08 pf (4000 MHz).

Appendix C

Derivation of Equation (4.15)

Figure C-1 shows the equivalent representation of negative resistance portion of the circuit for the analysis of the noise voltage.
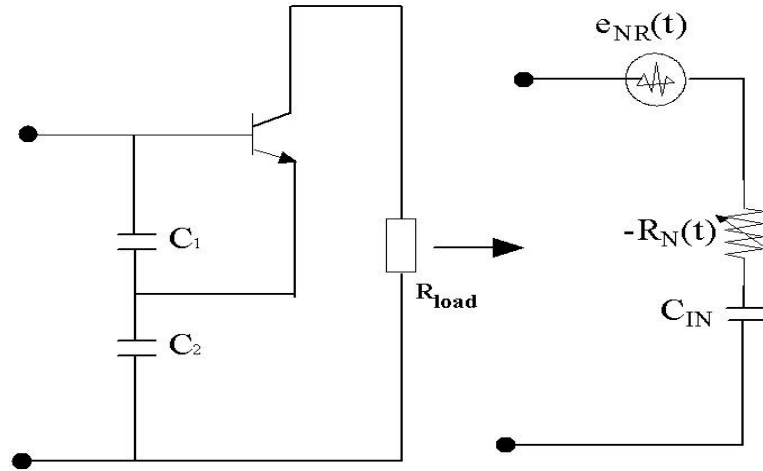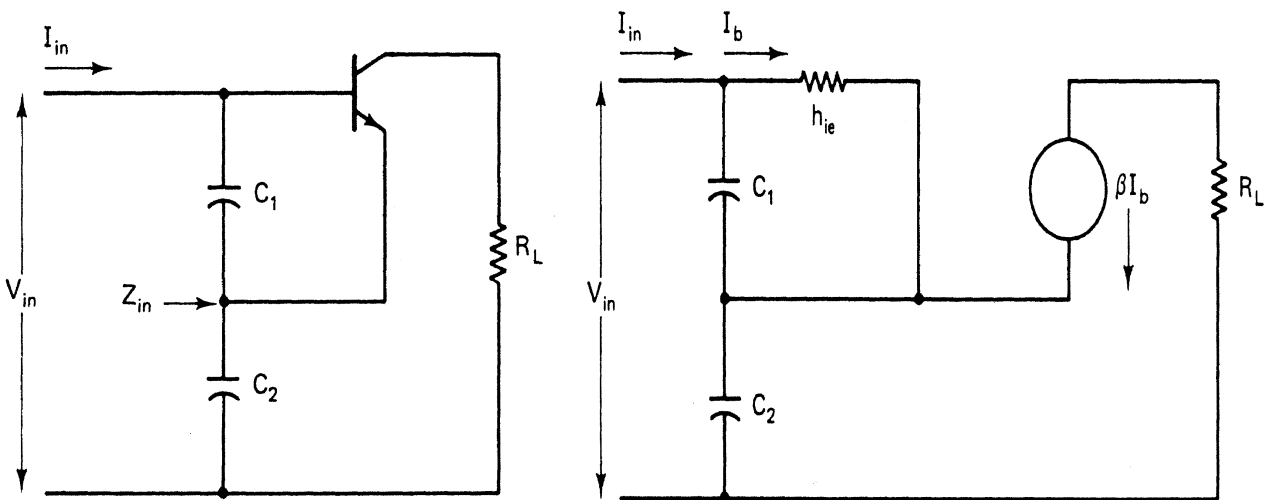

Figure C-1: Equivalent representation of negative resistance portion of the circuit

Figures C-2 illustrates the oscillator circuit for the purpose of the calculation of the negative resistance.

Figures C-2: Equivalent oscillator circuit for the purpose of the calculation of the negative resistance.

From Figure C-1, the total noise voltage power within 1 Hz bandwidth can be given as

$$\left| \overline{e_n^2(\omega)} \right|_{\omega=\omega_0} = \overline{e_R^2(\omega)} + \overline{e_{nR}^2(\omega)} \tag{C.1}$$

The first term in Equation (C.1) is the noise voltage power due to the loss resistance R, and the second term is associated with the negative resistance of the active device R_N.

From the Figure C-2, the circuit equation is given from Kirchoff's voltage law (KVL) as

$$V_{in} = I_{in}\left(X_{C_1} + X_{C_2}\right) - I_b\left(X_{C_1} - \beta X_{C_2}\right) \tag{C.2}$$

$$0 = -I_{in}\left(X_{C_1}\right) + I_b\left(X_{C_1} + h_{ie}\right) \tag{C.3}$$

Considering, $\dfrac{1}{Y_{11}} = h_{ie}$

$$Z_{in} = \frac{V_{in}}{I_{in}} = \frac{(1+\beta)X_{C_1}X_{C_2} + h_{ie}\left(X_{C_1} + X_{C_2}\right)}{X_{C_1} + h_{ie}} \tag{C.4}$$

$$Z_{in} = \frac{\left(-\dfrac{(1+\beta)}{\omega^2 C_1 C_2} + \dfrac{(C_1 + C_2)}{j\omega C_1 C_2}\dfrac{1}{Y_{11}}\right)}{\left(\dfrac{1}{Y_{11}} + \dfrac{1}{j\omega C_1}\right)} \tag{C.5}$$

$$Z_{in} = \frac{-jY_{11}(1+\beta) + \omega(C_1 + C_2)}{\omega C_2(Y_{11} + j\omega C_1)} \tag{C.6}$$

$$Z_{in} = \frac{[\omega(C_1 + C_2) - jY_{11}(1+\beta)][Y_{11} - j\omega C_1]}{\omega C_2(Y_{11}^2 + \omega^2 C_1^2)} \tag{C.7}$$

$$Z_{in} = \left[\frac{\omega Y_{11}(C_1 + C_2) - (1+\beta)\omega C_1 Y_{11}}{\omega C_2(Y_{11}^2 + \omega^2 C_1^2)}\right] - j\left[\frac{Y_{11}^2(1+\beta) + \omega^2 C_1(C_1 + C_2)}{\omega C_2(Y_{11}^2 + \omega^2 C_1^2)}\right] \tag{C.8}$$

$$Z_{in} = -R_n - jX \tag{C.9}$$

$$R_n = \frac{(1+\beta)\omega C_1 Y_{11} - \omega Y_{11}(C_1 + C_2)}{\omega C_2(Y_{11}^2 + \omega^2 C_1^2)} = \frac{(1+\beta)C_1 Y_{11} - Y_{11}(C_1 + C_2)}{C_2(Y_{11}^2 + \omega^2 C_1^2)} \tag{C.10}$$

$$R_n = \frac{\beta C_1 Y_{11} - Y_{11} C_2}{C_2 (Y_{11}^2 + \omega^2 C_1^2)} = \frac{\beta Y_{11}}{\frac{C_2}{C_1}(Y_{11}^2 + \omega^2 C_1^2)} - \frac{Y_{11}}{(Y_{11}^2 + \omega^2 C_1^2)} \tag{C-11}$$

Considering, $\beta = \dfrac{Y_{21}}{Y_{11}} \approx \dfrac{g_m}{Y_{11}}$

$$R_n = \frac{g_m \beta^2 \omega^2 C_1 C_2}{\omega^2 C_1^2 (\frac{C_2^2}{C_1^2} g_m^2 + \omega^2 \beta^2 C_2^2)} - \frac{g_m \beta \omega^2 C_2^2}{\omega^2 C_1^2 (\frac{C_2^2}{C_1^2} g_m^2 + \beta^2 \omega^2 C_2^2)} \tag{C-12}$$

$$R_n = \left[\frac{g_m^2}{\omega^2 C_1^2 (\frac{C_2^2}{C_1^2} g_m^2 + \omega^2 \beta^2 C_2^2)}\right] \left\{\frac{\beta^2 \omega^2 C_1 C_2}{g_m} - \frac{\beta \omega^2 C_2^2}{g_m}\right\} \tag{C-13}$$

$$R_n = \left[\frac{g_m^2}{\omega^2 C_1^2 (\frac{C_2^2}{C_1^2} g_m^2 + \omega^2 \beta^2 C_2^2)}\right] \left[g_m\left[\left(\frac{\omega C_1}{Y_{11}}\right)\left(\frac{\omega C_2}{Y_{11}}\right) - \frac{1}{\beta}\left(\frac{\omega C_2}{Y_{11}}\right)\left(\frac{\omega C_2}{Y_{11}}\right)\right]\right] \tag{C-14}$$

Considering, $\left(\dfrac{\omega C_1}{Y_{11}}\right)\left(\dfrac{\omega C_2}{Y_{11}}\right) \gg \dfrac{1}{\beta}\left(\dfrac{\omega C_2}{Y_{11}}\right)\left(\dfrac{\omega C_2}{Y_{11}}\right)$ and $\left(\dfrac{\omega C_1}{Y_{11}}\right)\left(\dfrac{\omega C_2}{Y_{11}}\right) \approx 1$

$$\left[g_m\left[\left(\frac{\omega C_1}{Y_{11}}\right)\left(\frac{\omega C_2}{Y_{11}}\right) - \frac{1}{\beta}\left(\frac{\omega C_2}{Y_{11}}\right)\left(\frac{\omega C_2}{Y_{11}}\right)\right]\right] \cong \frac{I_C}{V_T} = \frac{I_C}{kT/q} \Rightarrow \frac{qI_C}{kT} \tag{C-15}$$

From (C.14 and (C.15)

$$R_n = \left[\frac{g_m^2}{\omega^2 C_1^2 (\frac{C_2^2}{C_1^2} g_m^2 + \omega^2 \beta^2 C_2^2)}\right] \frac{qI_C}{kT} \tag{C-16}$$

From (C.1),

$$\left|\overline{e_n^2(f)}\right|_{\omega_0} = [4KTR] + \left[\frac{4qI_c g_m^2 + \frac{K_f I_b^{AF}}{\omega} g_m^2}{\omega_0^2 C_1^2 (\omega_0^2 (\beta^+)^2 C_2^2 + g_m^2 \frac{C_2^2}{C_1^2})}\right] \tag{C-17}$$

C3

where

$$\beta^+ = \left[\frac{Y_{21}^+}{Y_{11}^+}\right]\left[\frac{C_1}{C_2}\right]^p, \quad g_m = \left[Y_{21}^+\right]\left[\frac{C_1}{C_2}\right]^q, \text{ redefined}$$

The values of p and q depend upon the drive level.

The first term in the expression above is related to the thermal noise due to the loss resistance of the resonator tank and the second term is related to the shot noise and flicker noise in the transistor.

The flicker noise contribution in Equation (C.17) is introduced by adding term $\dfrac{K_f I_b^{AF}}{\omega}$ in I_c, where K_f is the flicker noise coefficient; AF is the flicker noise exponent, ω is the offset frequency from the carrier, and ω_0 is the oscillator frequency.

Now, the phase noise of the oscillator can be expressed as [11]

$$\left|\overline{\varphi^2(\omega)}\right|_{SSB} = \frac{\left|\overline{e_n^2(\omega)}\right|}{4\omega_0^2 L^2 I_0^2(\omega)} \tag{C-18}$$

Where L is inductance of the resonator network and I_0 is RF current. The unknown variables are $\left|e_n(\omega)\right|^2$ and $I_0^2(\omega)$, which need to be determined next. $I_0^2(\omega)$ will be transformed into $I_c^2(\omega)$ by multiplying $I_0^2(t)$ with the effective current gain $Y_{21}^+/Y_{11}^+ = \beta^+$.

From Figure C-3, the LC-series resonant circuit is in shunt between the base and the emitter with the capacitive negative conductance portion of the transistor

The oscillator collector current is given by

$$\left|I_c(t)\right| \approx \left|\frac{V_{ce}(t)}{R_L + j\left(\omega L - \dfrac{1}{\omega C_{IN}}\right)}\right| \tag{C-19}$$

$$\overline{I_c^2(\omega)} \approx \left\{\frac{\overline{V_{ce}^2(\omega)}}{[R_L]^2 + \left(\omega L - \dfrac{1}{\omega C_{IN}}\right)^2}\right\} = \left\{\frac{\overline{V_{ce}^2(\omega)}}{\left[\dfrac{\omega L}{Q}\right]^2 + \left(\omega L - \dfrac{1}{\omega C_{IN}}\right)^2}\right\} \tag{C-20}$$
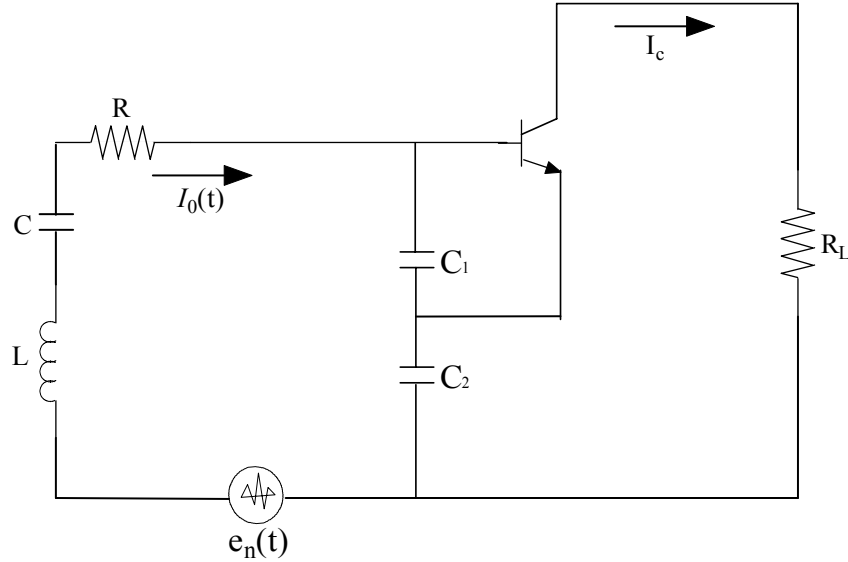
Figure C-3: Colpitts oscillator with series resonator and small signal AC equivalent circuit.

The voltage V_{ce} is the RF voltage across the collector emitter terminals of the transistor. Considering the steady-state oscillation $\omega \to \omega_0$, the total loss resistance is compensated by the negative resistance of the active device as $R_L = \overline{R_N(t)}$. The expression of $\left| \overline{I_c^2(\omega)} \right|_{\omega=\omega_0}$ is

$$\left| \overline{I_c^2(\omega)} \right|_{\omega=\omega_0} = \left| \frac{\overline{V_{ce}^2(\omega)}}{\left[\frac{\omega_0 L}{Q} \right]^2 + \left(\omega_0 L - \frac{1}{\omega_0 C_{IN}} \right)^2} \right| = \left| \frac{\overline{V_{ce}^2(\omega)}}{(\omega_0 L)^2 \left[\frac{1}{Q^2} + \left(1 - \frac{1}{\omega_0^2 LC_{IN}} \right)^2 \right]} \right| \qquad \text{(C-21)}$$

$$\left| \overline{I_{c0}^2(f)} \right|_{\omega=\omega_0} = \left| \frac{\overline{V_{ce}^2(f)}}{(\omega_0 L)^2 \left[\frac{1}{Q^2} + \left(1 - \frac{1}{\omega_0^2 L} \frac{C_1 + C_2}{C_1 C_2} \right)^2 \right]} \right| \qquad \text{(C-22)}$$

where C_{IN} is the equivalent capacitance of the negative resistor portion of the oscillator circuit.

$$C_{IN} = \frac{C_1 C_2}{C_1 + C_2}, Q = \frac{\omega L}{R_L}$$

C5

From Equation (C.18),

$$\left|\overline{\varphi^2(\omega)}\right|_{SSB} = \left\{\left[4KTR\right] + \left[\frac{4qI_c g_m^2 + \dfrac{K_f I_b^{AF}}{\omega} g_m^2}{\omega_0^2 C_1^2 (\omega_0^2 (\beta^+)^2 C_2^2 + g_m^2 \dfrac{C_2^2}{C_1^2})}\right]\right\}\left[\frac{(\omega_0)^2\left[\dfrac{1}{Q^2} + \left(1 - \dfrac{1}{\omega_0^2 L}\dfrac{C_1 + C_2}{C_1 C_2}\right)^2\right]}{4\omega^2 \left|V_{ce}^2(\omega)\right|}\right] \quad (C.23)$$

$$\left|\overline{\varphi^2(\omega)}\right|_{SSB} = \left[4KTR + \left[\frac{4qI_c g_m^2 + \dfrac{K_f I_b^{AF}}{\omega} g_m^2}{\omega_0^2 C_1^2 (\omega_0^2 (\beta^+)^2 C_2^2 + g_m^2 \dfrac{C_2^2}{C_1^2})}\right]\right]\left[\frac{\omega_0^2}{4\omega^2 V_{ce}^2}\right]\left[\frac{1}{Q^2} + \left(1 - \dfrac{1}{\omega_0^2 L}\dfrac{C_1 + C_2}{C_1 C_2}\right)^2\right] \quad (C.24)$$

Considering $\left(\dfrac{1}{\omega_0^2 L}\dfrac{C_1 + C_2}{C_1 C_2}\right) \gg 1$;

$$\pounds(\omega) = 10 Log\left\{\left[4kTR + \left[\frac{4qI_c g_m^2 + \dfrac{K_f I_b^{AF}}{\omega} g_m^2}{\omega_0^2 C_1^2 (\omega_0^2 \beta^2 C_2^2 + g_m^2 \dfrac{C_2^2}{C_1^2})}\right]\right]\left[\frac{\omega_0^2}{4\omega^2 V_{cc}^2}\right]\left[\frac{1}{Q^2} + \frac{[C_1 + C_2]^2}{C_1^2 C_2^2 \omega_0^4 L^2}\right]\right\} \quad (C-25)$$